This research was funded by Regione Lazio, Grant G06899 - 08.06.2021 “Intervento per il rafforzamento della ricerca e innovazione nel Lazio - Incentivi per i dottorati di innovazione per le imprese e per la PA" - L.R. 13/2008”

DOTTORATO DI RICERCA IN ENERGIA E AMBIENTE
PhD Program in ENERGY and ENVIRONMENT

XXXVII Cycle

Control of airborne biocontamination in HVAC systems through UV-C irradiation. An experimental and numerical study of the UV-C field.

PhD Thesis

Scuola di Dottorato in Scienze e Tecnologie per l’Innovazione Industriale
Facoltà di Ingegneria Civile e Industriale
Dipartimento di Ingegneria Astronautica, Elettrica ed Energetica

Francesca Cattai

Advisor
Annunziata. D’Orazio

A.A. 2025-2026

Extended Abstract

Indoor air quality is one of the most urgent and cross-disciplinary challenges in public health and environmental safety. It involves many sectors, from building design to systems engineering, from occupational medicine to public health. It is especially important in enclosed spaces with high occupancy or health risks, such as hospitals, offices, schools, residential areas, and public transit.

What has made this issue even more urgent in recent years is the global experience of the COVID-19 pandemic, which dramatically highlighted the importance of ventilation, natural aeration, and the control of biological pollutants in indoor spaces.

At the same time, the increasing adoption of remote work has significantly changed the purpose of home environments, turning them into both living and working spaces. This shift has led to more time spent indoors, increasing the risk of exposure to invisible pollutants such as fine particulate matter, VOCs (volatile organic compounds), chemicals from building materials or furniture, and microbiological agents. As a result, there is an urgent need to focus on indoor air quality as a health concern in both public and private spaces.

One phenomenon that highlights the complexity and significance of indoor environments is the so-called Sick Building Syndrome (SBS). Introduced by the World Health Organization in the 1980s, SBS describes a range of nonspecific symptoms, such as headaches, eye and mucous membrane irritation, dry skin, respiratory problems, fatigue, decreased concentration, or general discomfort, that occur after spending time in certain buildings. What characterizes this syndrome is that, in most cases, there is no clearly defined illness, and the symptoms tend to disappear or significantly lessen once the person leaves the environment. This shows a direct link between building features and occupant health, emphasizing a subtle but important interaction between the built environment and human response.

In recent years, numerous studies have explored the possible causes and mechanisms behind SBS. Two recent systematic reviews [1, 2] confirm that the syndrome cannot be linked to a single cause but results from an interaction of physical, chemical, biological, and psychosocial factors. Among the most involved chemical contaminants are volatile organic compounds (VOCs) emitted by construction materials, furnishings, adhesives, and paints; formaldehyde; ozone; carbon monoxide and carbon dioxide; and fine particulate matter (PM2.5 and PM10), which can penetrate the respiratory tract and cause inflammatory responses.

Besides these, physical factors such as extreme temperatures, excessive or insufficient humidity, poor ventilation, distracting ambient noise, and inadequate lighting can all harm perceived comfort and lead to symptoms.

Special attention is now focused on the microbiological contamination of indoor air, a phenomenon often overlooked but increasingly recognized as crucial, especially in sensitive environments like healthcare and social care facilities. Molds, bacteria, and bioaerosols flourish in humid, poorly ventilated spaces or areas with structural problems such as leaks and condensation, and they can cause allergic reactions, respiratory conditions, and ongoing discomfort. The reviews mentioned earlier

highlight a growing link between biological contaminants and the occurrence of SBS-related symptoms, particularly in cases where HVAC systems are poorly maintained or material quality is insufficient.

Beyond the chemical composition of the air, the literature increasingly emphasizes the importance of subjective and psychological factors, such as perceived comfort, stress levels, or the quality of workplace organization. These elements not only influence individual responses to environmental stimuli but can also amplify or diminish the appearance of symptoms. In other words, SBS is a syndrome that exists at the intersection of the physical environment and the individual's psycho-behavioral interpretation.

In such a complex and multidimensional context, the importance of developing integrated monitoring and prevention strategies becomes more evident. These strategies should not be limited to assessing the chemical-physical aspects of the air, but should also include microbiological analysis and monitoring of the occupants' physical and psychological health. Only a multidisciplinary approach that combines expertise in environmental science, engineering, healthcare, and psychology can ensure a true understanding of the phenomenon and enable effective intervention on risk factors.

In recent years, mainly due to the significant impact of the pandemic caused by the SARS-CoV-2 virus, a large number of air purifiers have entered the market. These devices operate using various physical and chemical mechanisms, some of which are combined. However, their great commercial success is often not supported by rigorous scientific research, particularly with regard to the dose of the agent supplied to biological contaminants. Some of these new devices claim to use UV-C irradiation.

The germicidal effectiveness of UV-C sources has become a major focus of research, using both experimental and numerical methods. In experimental studies, germicidal performance is most often evaluated through microbiological culture techniques, comparing the colony-forming units (CFUs) of samples exposed to UV-C radiation with those of unexposed controls. The experimental literature often provides incomplete details, often mentioning only the exposure time or the nominal radiant flux of the UV-C source. As a result, the actual dose received by microorganisms is rarely reported, making it difficult to directly compare different studies and limiting the reproducibility of the results. Additionally, factors such as spatial nonuniformity in irradiance, self-shading within samples, and the optical properties of surrounding materials can significantly affect measured inactivation but are rarely quantified.

On the numerical side, assessing UV-C effectiveness usually involves radiometric measurements and computational fluid dynamics (CFD) simulations. These methods help predict the spatial distribution of irradiance, radiant fluence, and the resulting local dose within a specific volume. When combined with models of microbial transport, they can also estimate the effective exposure of microorganisms in moving air streams. However, many numerical studies overlook the interaction between radiative transfer and fluid dynamics. In particular, airflow velocity and turbulence significantly influence how long microorganisms remain within the irradiated area, thus affecting the actual inactivation process. If the flow velocity is too high, microorganisms may pass through the UV field too quickly to receive the necessary dose for deactivation, even if the average fluence rate appears sufficient in static conditions.

Therefore, accurately evaluating UV-C germicidal effectiveness in indoor environments requires a multi-physics approach that combines radiative, fluid-dynamics, and biological-kinetics models. Such a framework should also consider the optical properties of materials, scattering effects, and potential re-emission phenomena that can influence the local fluence rate. Only by standardizing the definition of dose, carefully measuring irradiance patterns, and realistically modeling air movement can experimental and computational analyses be meaningfully compared and used to develop effective UV-C disinfection systems for indoor air quality improvement [33].

This research's novelty lies in combining experimental and numerical methods to assess the actual UV-C irradiation field in HVAC systems. Unlike most existing studies, which typically examine optical or microbiological aspects separately, this work aims to contribute to a broader approach focused on establishing a comprehensive and cumulative methodology for UV-C disinfection modeling. This overarching approach seeks to construct a unified framework that connects irradiance distribution, air flow, dose, and microbial inactivation under real-world operating conditions.

Within this context, the present work specifically focuses on the optical modeling of UV-C LED sources using ray-tracing simulations, an area still rarely explored in current research. Furthermore, the study aims to develop a robust and versatile modeling framework that can be easily reproduced and adapted to various UV-C source types, geometrical configurations, and application scenarios.

The experimental phase of the research was conducted in collaboration with Sagicofim S.p.A., a company specializing in air filtration and cleanroom technologies. A full-scale prototype of a galvanized steel duct was constructed and equipped with modular UV-C LED sources. Each module comprised thirty-two diodes arranged in an “80–110” configuration, designed to maximize uniform irradiation across the surface of a downstream HEPA filter. The LEDs emitted at three characteristic wavelengths within the germicidal range (254, 265, and 275 nm), allowing for a comparative evaluation of spectral efficiency and optical behavior.
Irradiance measurements were conducted using a Newport 918D photodiode coupled with a 1919-R precision optical power meter [112]. Before testing, the instruments were calibrated against certified standards to ensure traceability and repeatability. Measurements were performed on a grid of 494 points distributed across several planes orthogonal to the airflow, enabling the reconstruction of detailed irradiance maps that represent the spatial distribution of light within the duct.

The experimental data revealed a clear dependence of irradiance on both wavelength and geometry. The configuration operating at 265 nm exhibited the highest radiant output, consistent with the absorption peak of nucleic acids [8-10], whereas the 275 nm LEDs showed reduced power and less uniform coverage. Pronounced non-uniformities were observed near the duct corners and walls, attributed to reflection losses and shadowing effects caused by structural components. These findings underscore the necessity of numerical modeling to complement experimental analysis and guide design optimization.

To interpret these results, a detailed three-dimensional model was developed using the Ray Optics Module of COMSOL Multiphysics [114]. The model simulated the LED emission profile, accounting for angular dispersion, multiple reflections, and surface absorption. The optical properties of the duct materials were determined experimentally and implemented into the simulation to improve accuracy. The comparison between simulated and measured irradiance maps demonstrated a strong correlation, validating the model as a reliable predictive tool for UV-C system design.

Once validated, the model was used to conduct a parametric study exploring the effects of geometric and material variables. Adjusting the LED orientation, spacing, and wall reflectivity optimized light distribution. Simulations showed that coatings with reflectivity above 85% significantly improved the uniformity of the fluence rate and reduced low-irradiance zones. Even small changes in LED tilt angles or inter-module distances yielded measurable improvements in optical efficiency.

In addition to the optical analysis, the research defined repeatable procedures for measurement calibration, LED stabilization, and data processing. Each step, from voltage control to temperature monitoring, was standardized to ensure reproducibility. The combined experimental–numerical approach provided a comprehensive framework for identifying sources of non-uniformity and for predicting system performance under different configurations.

Although microbial inactivation tests and energy performance assessments were beyond the scope of this work, the study provides a solid foundation for future investigations that will extend the optical findings to biological validation. The irradiance maps and validated numerical models developed here form a database for estimating germicidal dose and for designing UV-C modules optimized for safety, efficiency, and long-term reliability.

From an engineering perspective, the study highlights the influence of wavelength, angular emission, material reflectivity, and system geometry on UV-C performance. The proposed methodology enables a quantitative assessment of each parameter, offering design guidelines for integrating LED-based disinfection technologies into HVAC systems. The approach also promotes standardization and comparability among studies, supporting the development of regulatory frameworks for UV-C systems.

In a broader context, this research contributes to the scientific effort to harmonize testing and measurement procedures for UV-C disinfection. The experimental–numerical methodology proposed here can serve as a reference for future standards, enabling reproducible, traceable, and verifiable evaluations of UV-C systems in real-world conditions.

In conclusion, the doctoral research presented in this thesis establishes an integrated framework combining experimental characterization and optical modeling for the analysis and optimization of UV-C LED systems applied to air disinfection. The results provide engineers and researchers with validated tools for designing efficient, safe, and environmentally sustainable solutions. Future developments will focus on coupling optical and thermal modeling, evaluating long-term LED stability, and integrating real-time control systems that adapt UV-C intensity to air quality variations. Ultimately, this work aims to contribute to the creation of healthier, safer indoor environments through the responsible, innovative use of UV-C technology.

Contents

List of the figures

List of tables

Introduction

Indoor air quality is one of the most urgent and cross-disciplinary challenges in public health and environmental safety. It involves many sectors, from building design to systems engineering, from occupational medicine to public health. It is especially important in enclosed spaces with high occupancy or health risks, such as hospitals, offices, schools, residential areas, and public transit.

What has made this issue even more urgent in recent years is the global experience of the COVID-19 pandemic, which dramatically highlighted the importance of ventilation, natural aeration, and the control of biological pollutants in indoor spaces.

At the same time, the increasing adoption of remote work has significantly changed the purpose of home environments, turning them into both living and working spaces. This shift has led to more time spent indoors, which raises the risk of exposure to invisible pollutants like fine particulate matter, VOCs (volatile organic compounds), chemicals from building materials or furniture, and microbiological agents. As a result, there is an urgent need to focus on indoor air quality as a health concern, both in public and private spaces.

One phenomenon that highlights the complexity and significance of indoor environments is the so-called Sick Building Syndrome (SBS). Introduced by the World Health Organization in the 1980s, SBS describes a range of nonspecific symptoms, such as headaches, eye and mucous membrane irritation, dry skin, respiratory problems, fatigue, decreased concentration, or general discomfort, that occur after spending time in certain buildings. What characterizes this syndrome is that, in most cases, there is no clearly defined illness, and the symptoms tend to disappear or significantly lessen once the person leaves the environment. This shows a direct link between building features and occupant health, emphasizing a subtle but important interaction between the built environment and human response.

In recent years, numerous studies have explored the possible causes and mechanisms behind SBS. Two recent systematic reviews [1, 2] confirm that the syndrome cannot be linked to a single cause but results from an interaction of physical, chemical, biological, and psychosocial factors. Among the most involved chemical contaminants are volatile organic compounds (VOCs) emitted by construction materials, furnishings, adhesives, and paints; formaldehyde; ozone; carbon monoxide and carbon dioxide; and fine particulate matter (PM2.5 and PM10), which can penetrate the respiratory tract and cause inflammatory responses.

Besides these, physical factors such as extreme temperatures, excessive or insufficient humidity, poor ventilation, distracting ambient noise, and inadequate lighting can all harm perceived comfort and lead to symptoms.

Special attention is now focused on the microbiological contamination of indoor air, a phenomenon often overlooked but increasingly recognized as crucial, especially in sensitive environments like healthcare and social care facilities. Molds, bacteria, and bioaerosols flourish in humid, poorly ventilated spaces or areas with structural problems such as leaks and condensation, and they can cause allergic reactions, respiratory conditions, and ongoing discomfort. The reviews mentioned earlier highlight a growing link between biological contaminants and the occurrence of SBS-related symptoms, particularly in cases where HVAC systems are poorly maintained or material quality is insufficient.

Beyond the chemical composition of the air, the literature increasingly emphasizes the importance of subjective and psychological factors, such as perceived comfort, stress levels, or the quality of workplace organization. These elements not only influence individual responses to environmental stimuli but can also amplify or diminish the symptoms' appearance. In other words, SBS is a syndrome that exists at the intersection of the physical environment and the individual's psycho-behavioral interpretation.

In such a complex and multidimensional context, the importance of developing integrated monitoring and prevention strategies becomes more evident. These strategies should not be limited to just assessing the chemical-physical aspects of the air but should also include microbiological analysis and monitoring the occupants’ physical and psychological health. Only a multidisciplinary approach that combines expertise in environmental science, engineering, healthcare, and psychology can ensure a true understanding of the phenomenon and enable effective intervention on risk factors.

The germicidal effectiveness of UV-C sources has become a major focus of research, using both experimental and numerical methods. In experimental studies, germicidal performance is most often evaluated through microbiological culture techniques, comparing the colony-forming units (CFUs) of samples exposed to UV-C radiation with those of unexposed controls. The experimental literature often provides incomplete details, usually only mentioning the exposure time or the nominal radiant flux of the UV-C source. As a result, the actual dose received by microorganisms is rarely reported, making it difficult to directly compare different studies and limiting the reproducibility of the results. Additionally, factors like the spatial non-uniformity of irradiance, self-shading within samples, and the optical properties of surrounding materials can greatly affect measured inactivation but are rarely quantified.

On the numerical side, assessing UV-C effectiveness usually involves radiometric measurements and computational fluid dynamics (CFD) simulations. These methods help predict the spatial distribution of irradiance, radiant fluence, and the resulting local dose within a specific volume. When combined with models of microbial transport, they can also estimate the effective exposure of microorganisms in moving air streams. However, many numerical studies overlook the interaction between radiative transfer and fluid dynamics. In particular, airflow velocity and turbulence significantly influence how long microorganisms remain within the irradiated area, thus affecting the actual inactivation process. If the flow velocity is too high, microorganisms may pass through the UV field too quickly to receive the necessary dose for deactivation, even if the average fluence rate appears sufficient in static conditions.

Chapter 1 – State of the Art

The quality of the air we breathe in enclosed spaces, such as homes, schools, offices, and healthcare facilities, is a key factor in both daily well-being and long-term public health. Although often invisible and overlooked, pollutants in indoor environments can be just as hazardous, if not more so, than those outdoors. Fine particulate matter, toxic gases, pathogens, and allergens build up indoors, fueled by various internal sources (like building materials, human activity, and electronic devices) and infiltration from outside, especially in urban and industrial areas.

Among the main contaminants are suspended particles (PM10, PM2.5, PM0.1), widely recognized for their harmful effects on human health: inhaling these particles is linked to cardiovascular diseases, respiratory problems, and, in the most serious cases, premature death [5]. These are accompanied by gaseous pollutants such as volatile organic compounds (VOCs), carbon monoxide (CO), nitrogen dioxide (NO_2), ozone (O_3), and radon, each with different mechanisms of action and complex impacts on occupant health.

The increasing scientific attention on Indoor Air Quality (IAQ) has driven the development of various air purification technologies, including mechanical ventilation systems, high-efficiency particulate air (HEPA) filters, portable air cleaning units (PACs), and advanced solutions based on photocatalytic oxidation (PCO), ultraviolet germicidal irradiation (UVGI), and nanostructured materials [6]. However, these technologies have limitations: some may generate potentially harmful byproducts, such as formaldehyde, ozone, or nitrogen oxides, while others depend on specific environmental conditions to work effectively, as in the case of UVGI systems, which are highly affected by humidity and air distribution [7-10].

At the same time, the global health landscape has been deeply influenced by the COVID-19 pandemic, which highlighted the importance of advanced technological solutions for limiting airborne transmission of pathogens. The disease caused by SARS-CoV-2, declared a pandemic by the World Health Organization in March 2020, has resulted in millions of deaths and raised new concerns about disinfecting air, surfaces, and objects in shared environments. In this context, a need has emerged to combine air purification strategies with engineering and healthcare approaches that can work together to reduce the risk of contagion [11,12]

Adding to this issue is a parallel public health crisis: the increasing resistance of pathogens to antibiotics. Since Fleming’s discovery of penicillin in 1928, it’s been clear that bacteria can quickly develop resistance mechanisms, making many pharmaceutical treatments ineffective. The misuse and overuse of antibiotics, both in human medicine and in animal feed, have sped up this trend, making it harder to control bacterial infections. It is estimated that in developing countries, per capita annual antibiotic consumption has increased up to tenfold, and over 200,000 tons of antibiotics are expected to be added annually to livestock feed [13].

Given these critical issues, exploring alternative, non-antibiotic strategies for infection control becomes essential. In this context, light-based therapies have shown promise as an antimicrobial solution, suitable for disinfecting surfaces as well as purifying air and water. These technologies utilize specific wavelengths, especially in the UV and visible light spectrum, to inactivate viruses, bacteria, and fungi through photochemical mechanisms. The use of UV radiation was particularly emphasized during the COVID-19 pandemic for preventing the transmission of SARS-CoV-2 in indoor settings.

In summary, the integration of air quality management, infection prevention, and the development of non-pharmacological antimicrobial technologies is a timely and multifaceted challenge. This work is positioned within this research area, aiming to contribute to the development of effective, safe, and sustainable systems for enhancing environmental health and microbiological safety in enclosed spaces.

1.1 State of the Art of UVC Applications

1.1.1 Introduction to Ultraviolet Radiation

Ultraviolet (UV) radiation is part of the electromagnetic spectrum located between visible light and X-rays, with wavelengths from 100 to 400 nanometers (nm) and photon energies between 3.10 and 12.4 electronvolts (eV). Since it lies *beyond violet* in the visible spectrum, UV radiation has higher energy than light visible to the human eye. This increased energy allows UV rays to cause various photochemical and biological effects, some of which can significantly threaten human health.

The UV spectrum is conventionally classified into the following bands:

- UVA (315–400 nm): the least energetic but still able to penetrate deeply into dermal tissues.
- UVB (280–315 nm): of intermediate energy, partially filtered by the atmosphere, responsible for both beneficial effects (e.g., vitamin D synthesis) and adverse outcomes such as erythema and DNA damage;
- UVC (100–280 nm): highly energetic and completely absorbed by the ozone layer under natural conditions, widely known for its germicidal properties.
- Vacuum UV (100–200 nm): known for strong germicidal effects but limited penetration in water, also capable of inducing ionization and ozone formation.

While the Sun remains the main natural source of UV radiation, artificial sources have greatly increased exposure opportunities. These include tanning beds (mostly UVA), phototherapy units (using narrowband UVA or UVB), mercury vapor lamps, welding arcs, plasma sources, and UVC germicidal devices. The latter are used more often for disinfecting air, water, surfaces, and equipment, taking advantage of UVC radiation's ability to inactivate many microorganisms, including viruses, bacteria, and fungi, through direct damage to their nucleic acids.

Although UV radiation is generally considered non-ionizing, some studies have shown that high-energy UV photons, especially at the lower end of the UVC spectrum, might have a weak ionizing ability, allowing them to eject electrons from atoms or molecules. This ability increases their interaction with biological materials and highlights the need to assess their potential harmful effects.

Uncontrolled or excessive exposure to UV radiation is linked to harmful health effects on the skin, eyes, and immune system. For example, UVB radiation has been associated with immune suppression, skin aging, and cancer. Conversely, UVA radiation is involved in the development of eye conditions such as cataracts and macular degeneration, as well as skin cancers. It is important to understand that various factors, including wavelength, dose, and duration of exposure, influence the biological effects of UV radiation [15].

1.2 Ultraviolet Radiation: Principles of Microbial Inactivation

Ultraviolet (UV) radiation constitutes a portion of the electromagnetic spectrum located between visible light and X-rays, with wavelengths ranging from 100 to 400 nanometers (nm).

It is typically divided into three main spectral bands: UVA (315–400 nm), UVB (280–315 nm), and UVC (100–280 nm). Among these, UVC radiation is especially important for environmental and healthcare uses because of its proven germicidal power. Irradiation around 260 nm is particularly effective, as it aligns with DNA's peak absorption, leading to disruption of nucleic acids.

The main mechanism for microbial inactivation involves nucleic acids (DNA or RNA) absorbing UV photons, which causes the formation of irreversible photochemical lesions. These changes mainly include cyclobutane pyrimidine dimers (CPDs) and 6–4 photoproducts, which disrupt key cellular functions such as replication and transcription, ultimately causing the loss of microbial viability [15,16]. Notably, CPDs make up about 75% of the damage caused by UV radiation and are the main factor in its germicidal effect [17].

The susceptibility of microbes to UV radiation varies greatly among species and depends on factors such as the type of nucleic acid (e.g., ssDNA, dsDNA, ssRNA, dsRNA) and the organism's structural complexity. Evidence shows that organisms like Escherichia coli are generally more sensitive to UV exposure than human adenoviruses [18,19]. Additionally, RNA viruses like MS2 and Qβ have similar inactivation rates, although they are less sensitive than ΦX174, a single-stranded DNA virus known for its higher vulnerability to UV [20,21].

UV disinfection efficiency is measured by fluence (mJ/cm²), which is calculated as the product of irradiance (mW/cm²) and exposure time (s). The inactivation kinetics are often modeled using the Chick-Watson first-order model, which describes a logarithmic relationship between microbial reduction and UV dose [18]:

$$log_{10}\left(\frac{N_0}{N_t}\right) = K \cdot F \tag{1.1}$$

Where:

N0 and Nt represent the initial and residual microbial concentrations (CFU/mL), while K is the inactivation rate constant (cm²/mJ), and F indicates the UV fluence delivered.

Nevertheless, deviations from this idealized linear behavior are often observed. Two commonly reported phenomena in the literature include:

- The "shoulder effect," typically observed at low fluence levels, is attributed to initial cellular resistance, shielding, or DNA repair mechanisms [22, 23].
- The "tailing effect," often observed at high fluences, is attributed to the presence of subpopulations with increased resistance or to inherent limitations of the UV treatment system [24].

In Table 1, the UV-C sensitivities of various pathogens are listed as inactivation rate constants (cm^2/mJ) across all relevant wavelengths. This table offers a comprehensive overview of how different microorganisms respond to UV radiation, enabling comparisons across species and wavelengths, and supporting the identification of suitable UV-C exposure levels for effective disinfection [25-30].

Table 1: Inactivation Rate Constant for different pathogens.

Pathogen	**Wavelength (nm)**	**Inactivation Rate Constant (k) [cm^2/mJ]**
Escherichia coli	254	0.29
Phi6 (model virus)	222	0.13
SARS-CoV-2 (OC43 variant)	222	3.8–7.1
Candida albicans	254	0.35
Mycobacterium abscessus	254	0.40

1.3 UV Radiation Technology for Disinfection and Contaminant Treatment

Ultraviolet (UV) radiation technology is one of the most established and effective methods for sterilization and the treatment of contaminants across various domains, including water purification, air sterilization, and surface disinfection. This technology is widely employed both in direct sterilization processes, which destroy pathogenic microorganisms, and in Advanced Oxidation Processes (AOPs), where UV radiation generates highly reactive species, such as hydroxyl radicals, capable of degrading persistent organic compounds [31].

1.3.1 UVC – Source

The quality and effectiveness of UV treatment largely depend on the type of light source used, as each source has a unique emission spectrum, intensity, and operational lifespan. Currently, the most common UV sources are divided into two main categories: mercury vapor lamps (both low and medium pressure) and the newer UV-C Light Emitting Diodes (UVC-LEDs).

Mercury Vapor Lamps

Mercury-vapor lamps are a long-standing, still widely used technology for UV radiation.

Low-Pressure Lamps (LP)

Low-pressure mercury-vapor lamps operate at very low mercury-vapor pressure, between 0.1 and 10 kPa. This enables nearly monochromatic emission centered at 253.7 nm, very close to the DNA absorption peak (~260 nm), making them particularly effective at damaging biomolecules and inactivating viruses, bacteria, and spores [32].

While they are energy-efficient, their performance is highly dependent on the operating temperature: optimal efficiency occurs between 40 and 60 °C, beyond which UV output drops rapidly. This limits their use in environments where precise temperature control is not feasible [33].

A high-output variant of these lamps exists, featuring enhanced UV emission density along the lamp's length, achieved through modifications to internal design and materials. These models deliver greater UV power while maintaining the same wavelength [31].

Medium-Pressure Lamps (MP)

Medium-pressure lamps operate with mercury vapor at much higher pressures (50–300 kPa), resulting in a different discharge mechanism and a polychromatic emission spectrum. This includes multiple UV spectral lines as well as infrared and visible light [32].

Unlike LP lamps, MP lamps emit across a broad wavelength range, including some wavelengths with no germicidal activity, leading to energy dispersion and lower overall efficiency. However, they offer much higher output power, making them suitable for industrial processes and large-scale water treatment. Moreover, they are less sensitive to ambient temperature changes, ensuring stable performance in uncontrolled environments [33].

Challenges of Mercury Vapor Lamps

Despite their proven effectiveness, mercury vapor lamps present several technical, operational, and environmental drawbacks:

- Toxicological risks: Mercury is a highly toxic and bioaccumulative substance. The World Health Organization [34] lists it among the top ten chemicals of major public health concern due to its severe neurological and renal effects, even at low exposure levels. Accidental breakage poses significant risks and requires stringent, costly handling and disposal procedures.

- Limited lifespan and maintenance: These lamps typically last 8,000 to 10,000 hours, significantly less than modern LED technologies. Their fragility and complex ignition systems require regular maintenance to ensure consistent performance [31]. Additionally, they need 2 to 15 minutes to reach steady-state operation, which limits their use in applications that demand frequent switching or rapid activation [33].

- High energy demand and bulkiness: Mercury lamps require high operating voltages (110 ÷ 240 V) and are relatively bulky, restricting their integration into compact or portable systems [31].

UVC - LED Technology

Ultraviolet-C Light Emitting Diodes (UVC-LEDs) are an emerging technology transforming the field of UV disinfection and sterilization.

UVC-LEDs emit radiation in the 200–300 nm range, allowing precise tuning of the emitted wavelength to maximize germicidal effectiveness. The 260–280 nm range is particularly ideal for inactivating a wide spectrum of microorganisms [31].

Structurally, UVC-LEDs are typically based on AlInGaN semiconductor materials with Multi-Quantum Well (MQW) architecture. Light is generated within thin quantum wells in the diode's active PIN region, where electron-hole recombination produces photons in the UV-C range [32]. Sapphire is commonly used as the growth substrate, while GaN layers are applied for contacts and active regions [31].

Advantages of UVC-LEDs Over Mercury Lamps

UVC-LEDs offer numerous and significant advantages over traditional mercury vapor lamps:

- Compact size and modularity: With diameters typically between 5–9 mm, LEDs can be integrated into portable devices, battery-powered modules, or disinfection systems for confined spaces [33].
- Instant ignition and no warm-up: UVC-LEDs switch on and off instantly, with no intensity variations due to ambient temperature [31].
- Low energy consumption and low-voltage operation: LEDs operate at low voltages and currents, enabling battery or renewable energy use, thereby enhancing energy efficiency and sustainability [32].
- Long lifespan and low maintenance: With operational lifespans exceeding 100,000 hours, UVC-LEDs require less maintenance and offer lower long-term operational costs [21].
- Customizable beam profile: Optical lenses and reflectors can shape the emission profile to optimize irradiation for specific applications [33].

However, technical limitations remain, especially in output power, currently in the tens of milliwatts per LED, lower than mercury vapor lamps, which emit in the watt range. Additionally, UV-C radiation has limited penetration, particularly in opaque or dense media, restricting UVC-LEDs to surface disinfection or treatment of clear liquids [26].

Table 2: Comparison between Mercury Vapor Lamps and UVC-LEDs.

Feature	Mercury Vapor Lamps (LP & MP)	UVC-LEDs
Emission Wavelength	LP: 253.7 nm (monochromatic); MP: 200–400 nm	Tunable 200–300 nm
Energy Efficiency	High (LP at 40–60 °C); Lower for MP	Constantly improving
Irradiated Power	High (Watts)	Low (tens of milliwatts)

Feature	Mercury Vapor Lamps (LP & MP)	UVC-LEDs
Operational Lifespan	Short (8,000–10,000 hours)	Very long (up to 100,000 hours)
Startup Time	2–15 minutes	Instantaneous
Size	Bulky	Compact (5–9 mm)
Maintenance	High	Low
Environmental Impact	High (toxic mercury)	Low (mercury-free)
Typical Applications	Large-scale/industrial processes	Portable/localized disinfection systems

Table Summary

The Table 2 provides a concise comparison of mercury vapor lamp technologies (both low- and medium-pressure) versus modern UVC-LED systems. Mercury lamps offer high output power and broad-spectrum UV emission, making them useful in industrial and large-volume applications, but come with significant drawbacks: a short lifespan, long warm-up times, high maintenance requirements, and environmental hazards due to their mercury content.

Conversely, UVC-LEDs offer compact size, instant activation, long operational life, and minimal environmental impact. Although their output power is currently lower, continuous technological advancements are closing the gap. UVC-LEDs are especially suitable for portable devices, low-power systems, and localized applications requiring fast, modular solutions [35].

1.3.2 Source installation

Within the scientific literature on the application of UVGI (Ultraviolet Germicidal Irradiation) technology for air and surface disinfection, multiple source installation modalities have been identified, each closely linked to the specific application context, the intended treatment objectives, and the prevailing environmental conditions. The most frequently adopted configurations include ceiling- and wall-mounted systems, commonly referred to as *upper-room* installations, primarily used to disinfect indoor air in environments occupied by individuals. The effectiveness of such systems is influenced by several factors, including ceiling height, the spatial arrangement of UV sources, the geometry of the room, and the reflective or absorbent nature of surfaces. Moreover, the interaction between airflow patterns and UV radiation distribution is a critical factor for achieving uniform irradiation of airborne particles, particularly in the presence of mechanical ventilation or forced air movement from fans.

A second widely explored application involves integrating UV sources into Air Handling Units (AHUs), with particular attention to sanitizing internal components, including heat exchange coils, internal walls, and filtration systems. These installations have demonstrated notable benefits not only in reducing microbial contamination but also in improving the operational efficiency of HVAC systems. This is achieved by inhibiting biofilm formation and thereby reducing pressure drops and energy consumption. Several studies underscore the importance of optimal lamp positioning, irradiance levels, and exposure times in ensuring effective germicidal performance within these units.

Another significant installation strategy involves placing UV sources directly within ventilation ducts to treat air in transit. In this context, disinfection efficacy is heavily influenced by operational parameters, including airflow velocity, temperature, relative humidity, and the reflective properties of the duct materials. Appropriately positioning UV sources along the airflow path maximizes the radiation dose absorbed by airborne pathogens, thereby reducing the likelihood of recirculation and re-aerosolization of infectious particles.

Lastly, increasing attention has been directed toward the use of mobile or stand-alone UVGI devices for localized sanitization of specific indoor environments, such as hospital rooms, outpatient clinics, offices, or public transport vehicles. These units, which may be stationary or portable, offer greater flexibility and are particularly advantageous in settings without centralized air-handling systems. Nonetheless, their effectiveness is closely tied to factors such as the spatial uniformity of UV radiation, the susceptibility of microorganisms to the emitted wavelength, and environmental influences, including particulate matter, physical obstructions, and ventilation conditions, whether natural or mechanical. Furthermore, it has been demonstrated that combining UVGI systems with complementary filtration technologies, such as HEPA filters, can significantly enhance the overall disinfection efficacy and broaden the spectrum of inactivated pathogens.

A systematic review was conducted, analyzing numerous articles [36-107] to evaluate the state of the art of germicidal ultraviolet (UV-C) irradiation in HVAC systems, with particular attention to both technical aspects and market positioning. The review included experimental studies, numerical analyses, and combined-method studies, covering applications in upper-room irradiation, air handling units (AHUs), and duct systems, with a limited number of studies on mobile devices. The review considered both controlled laboratory experiments and real-world operational studies to identify gaps between ideal experimental data and field performance. A critical aspect highlighted is the scarcity of information regarding dose evaluation, including the definition of irradiance, which renders the current scenario imprecise and non-quantitative. This lack of detailed data hinders the implementation of reliable operational guidelines and internationally shared regulatory standards.

UV-C irradiation is universally recognized for its ability to inactivate viruses, bacteria, and spores. However, its efficacy depends on numerous physical and environmental factors, including wavelength (typically 200–280 nm), intensity, exposure duration, and the characteristics of the target microorganisms. In HVAC applications, low-pressure mercury vapor lamps, which emit nearly monochromatically at 253.7 nm close to the DNA absorption peak, are commonly used, alongside UV-C LEDs, which offer more controllable emissions and mercury-free operation. The increasing adoption of LEDs is driven by environmental safety considerations, compact size, instant start-up, and extended operational lifetime. Nevertheless, radiation distribution and power calibration remain significant technical challenges.

One of the main issues identified is the lack of shared standards for measuring and defining the germicidal dose. Although parameters such as intensity or irradiance are commonly reported, the actual dose, defined as UV-C energy per unit area received over a given time, is rarely rigorously quantified. This limitation makes it difficult to correlate experimental results with biological outcomes, as dose is the critical parameter governing microbial inactivation. Defining standardized methodologies for dose measurement is therefore essential not only for experimental research but also for validating commercial systems.

An additional layer of complexity arises from the variability of microbial sensitivity to UV-C exposure. Some bacteria and viruses can be inactivated at relatively low doses, whereas other pathogens, including certain fungi and bacterial spores, require prolonged exposure or higher intensity. The heterogeneity of reported effective doses is further exacerbated by the lack of standardized protocols for both laboratory tests and field measurements, making it challenging to compare systems and establish general operational guidelines.

Environmental and system-specific conditions play a crucial role in determining the efficiency of UV-C disinfection. Factors such as airflow velocity, duct geometry, the presence of airborne particulates, surface reflectivity, and relative humidity influence both the penetration and uniformity of UV-C irradiation. Computational fluid dynamics (CFD) simulations have demonstrated that even minor changes in lamp placement or duct design can lead to significant variations in the dose received by the airflow, emphasizing the importance of an integrated engineering approach that combines design, measurement, and biological evaluation.

From a technological perspective, the review highlights that mercury vapor lamps continue to dominate the market due to their low cost and high output. However, UV-C LEDs are rapidly gaining ground owing to higher energy efficiency, mercury-free operation, and design flexibility. Despite these advantages, standardizing germicidal dose measurement, power calibration, and verification of radiation distribution remains an open challenge for both types of UV-C sources.

Regulatory aspects and operational guidelines are also critical for the safe and effective implementation of UV-C systems in commercial and industrial settings. Internationally, exposure limits for personnel, minimum distances for lamp installation, and integrated safety measures are still being harmonized. Adoption of rigorous and standardized protocols is essential not only to ensure microbial efficacy but also to guarantee environmental and operational safety.

In conclusion, the systematic review emphasizes that the future development and wider deployment of UV-C technology in HVAC systems critically depend on addressing current gaps in measurement standardization, optimizing engineering design, and establishing clear and harmonized operational parameters. Integrating experimental and numerical approaches, evaluating dose under real-world conditions, accounting for emerging LED devices, and analyzing market trends are key to advancing safe, effective, and sustainable UV-C applications. Only through a multidisciplinary approach combining biology, engineering, and technical management will it be possible to ensure reliable indoor air protection and support the broad adoption of this technology in the HVAC sector [35].

Chapter 2 – The aim of the research

This research project focuses on the application of UV-C radiation for air sanitation in confined environments, with particular attention to HVAC systems. The existing literature confirms the high effectiveness of UV-C radiation, with a great focus on 254 nm, in neutralizing microorganisms, including bacteria, viruses, fungi, and algae. Special importance is given to the direct irradiation of filtering surfaces, primarily HEPA filters [56], which has proven more effective than irradiating the air stream alone, both in reducing microbial levels and in limiting increases in pressure drop, thereby extending filter service life.

Despite encouraging results, the widespread implementation of these technologies is currently hindered by the lack of standardized protocols for measuring dose and irradiance, as well as by the general difficulty of ensuring the reproducibility of laboratory results. Within this context, the project aims to critically address these limitations by proposing an integrated, experimental and numerical approach to improve understanding of the underlying phenomena, particularly regarding the irradiation field, and provide tools to support the design of more effective and sustainable HVAC solutions.

The research activities include the analysis of the effectiveness of UV-C irradiation, generated by LEDs operating at different wavelengths to assessement of the actual UV-C irradiation field in HVAC systems research. Experimental tests are carried out on a scaled-down test section developed in collaboration with the industrial partner Sagicofim. In parallel, numerical simulations are performed using the ray-tracing module of COMSOL Multiphysics to reconstruct the emission solid angle of UV-C LED modules from previously conducted illuminance measurements. These numerical models allow the evaluation of actual irradiation within the geometries of interest and facilitate the comparison between simulated results and experimental data. In the future, they will be essential for identifying robust correlations between optical parameters and microbiological inactivation.

A distinctive feature of the proposed activity is the development of a detailed mathematical model to simulate the optical behavior of UV-C LED sources. This area remains relatively unexplored in the current scientific literature. This model will serve as an innovative tool to support the design of advanced HVAC systems and can be readily adapted to future studies involving new sources or plant configurations.

This study aims to provide a concrete contribution to the design of next-generation HVAC systems capable of effectively integrating UV-C technologies for air sanitation in confined environments. Through a multidisciplinary approach that combines experimental work and numerical modeling, the research seeks to address key challenges related to irradiance measurement, reproducibility of results, and their applicability at an industrial scale. The overall objective is to support the development of flexible and adaptable solutions that ensure effective disinfection performance, reduce energy consumption, and simplify system management, thereby contributing to the creation of healthier and more technologically advanced indoor environments.

Chapter 3 – Materials and Methods

In this chapter, the experimental and numerical components of the apparatus used to characterize the behavior of a prototypical device will be described. Specifically, the following aspects will be addressed:

- Illuminance measurements, aimed at quantifying the spatial distribution and intensity of the emitted radiation.
- Reconstruction of the emission solid, to determine the angular emission profile and the effective radiating volume.
- Numerical modeling, including the physical assumptions and boundary conditions adopted to simulate the device's behavior.
- Ray tracing simulations, employed to analyze the propagation of radiation within the system and validate the experimental observations.

3.1 Experimental device

The device built by the company, shown in Figures 7 and 8, is a galvanized steel duct product with a parallelepiped shape. Inside, supports are mounted on which three LED lamps are installed, each composed of 32 sources arranged according to the so-called 80-110 configuration. This configuration indicates that the upper and lower lamps are 80 mm from the filtering surface, while the central bar is 110 mm away. This geometry was chosen to achieve the largest possible irradiated area, even at the expense of the dose, and to ensure uniform power density over the surface of interest.

The dimensions of the experimental apparatus are as follows:

- Length: 100 cm
- Width: 80 cm
- Height: 26.5 cm

The net internal width, after subtracting the wall thickness, is approximately 77.5 cm. The supports on which the 32 LEDs are housed are 72 cm long and installed 0.5 cm from the left side wall and 5 cm from the right side wall. The central bar is located 22 cm from the air flow inlet, while the lower and upper bars are positioned 25 cm from it.

The side walls are movable and open outwards, facilitating the insertion of measurement instruments or obstacles into the device for various experimental tests. They are fixed to the frame of the by bolts with a wasand. Thanks to one of these openings, the sensor could be inserted and positioned optimally for measurements.

On the left wall, a lamp power supply panel is installed, allowing various sources to be disconnected and reconnected, enabling the measurements described later. The lamp's power cable ends with a three-phase plug; therefore, a two-phase adapter was used to enable operation.

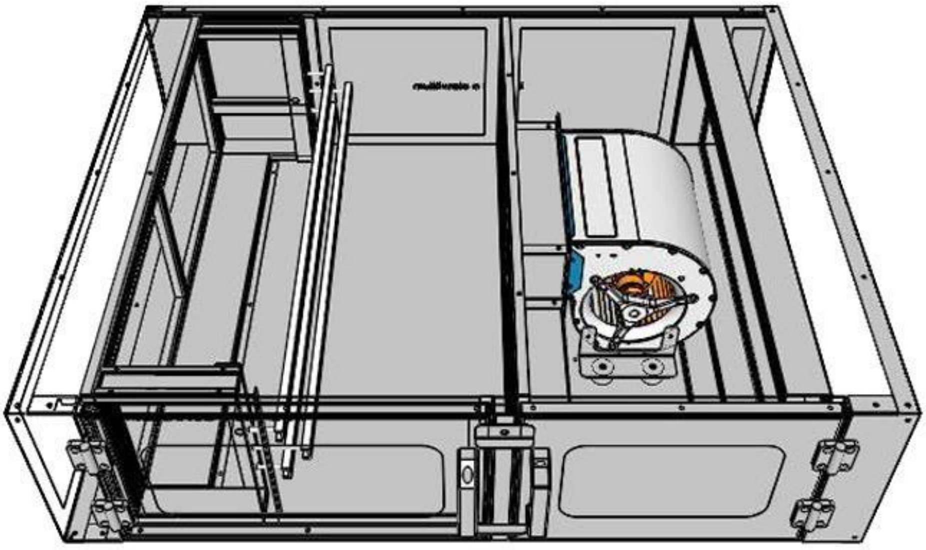

Figure 1: Top view of the test device

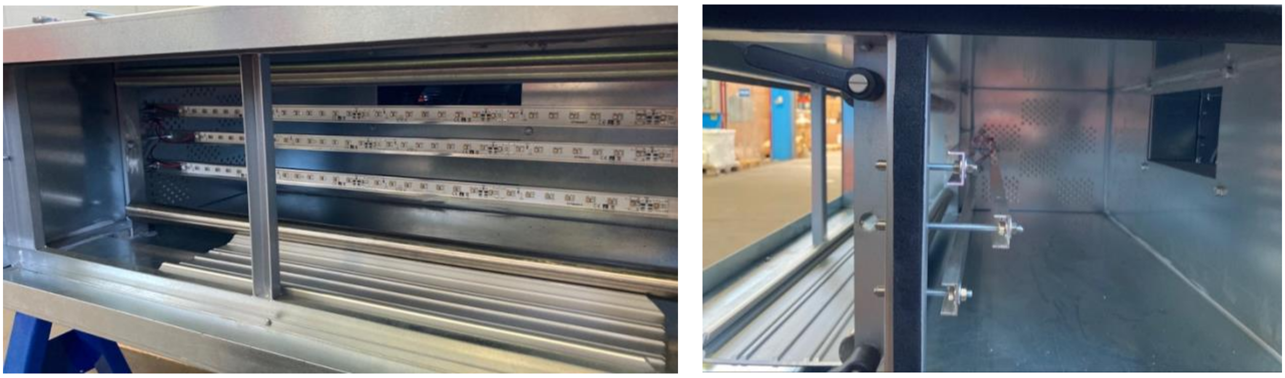

Figure 2: Frontal and lateral view of the test device

Figures 1 and 2 show two graphical representations from the device's CAD model: the first is a top view, where the fan, the three bars, and their respective distances are identified; the second is a front view, showing the 80-110 arrangement of the bars.

The front surface of the structure, measuring 60 by 21 cm, is designed to accommodate a high-efficiency particulate air (HEPA) filter. The filter system is composed of multiple microfiber sheets separated by aluminum spacers, which efficiently capture airborne particulate matter within the treated airflow.

HEPA filters are classified according to UNI EN 1822:2019 based on their fractional efficiency at the most penetrating particle size (MPPS), typically around 0.1–0.3 µm. The standard provides a precise, performance-based classification that replaces the outdated H10–H14 classes. Filters are rated accbasedeir overall efficiency and performance characteristics, ensuring that only those that meet strict filtration thresholds are used in critical applications, such as cleanrooms, healthcare facilities, and advanced HVAC systems. High-efficiency filters capture more than 99% of airborne particles at the MPPS.

This type of filter can interrupt the spread of particles depending on their size through the following mechanisms:

- Interception: larger particles following airflow lines are trapped when they come into contact with filter fibers.
- Impaction: medium-sized particles deviate from airflow streamlines due to inertia and impact the fibers directly.
- Diffusion: very small particles, influenced by Brownian motion, move randomly and are captured through prolonged interaction with the fiber matrix.

In a properly designed HEPA filter, these mechanisms act synergistically to ensure the effective removal of airborne contaminants and improve indoor air quality. The UNI EN 1822:2019 standard also specifies testing methods to verify both fractional and overall efficiency, as well as procedures for leak detection, airflow measurement, and performance validation under operational conditions [108].

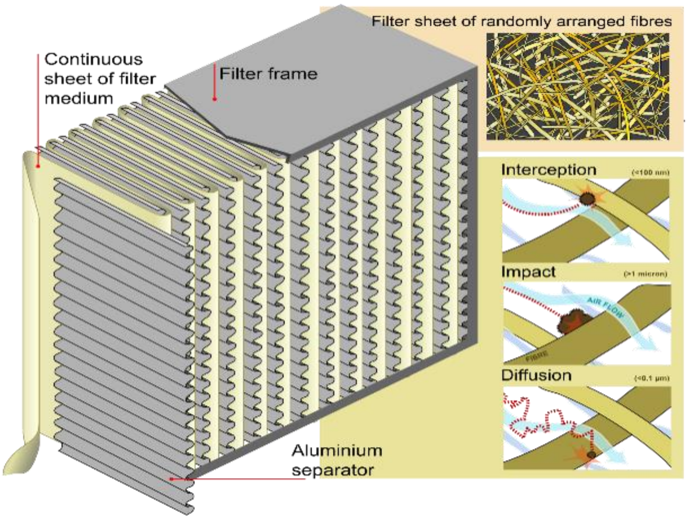

Figure 3: Configuration of a HEPA filter [109].

At the rear of the device is the fan, which manages the airflow required to maintain a constant internal temperature; the chosen device is the ROSENBERG GDSV8, which belongs to the range of double-inlet centrifugal fans with electronically commutated motors [110].

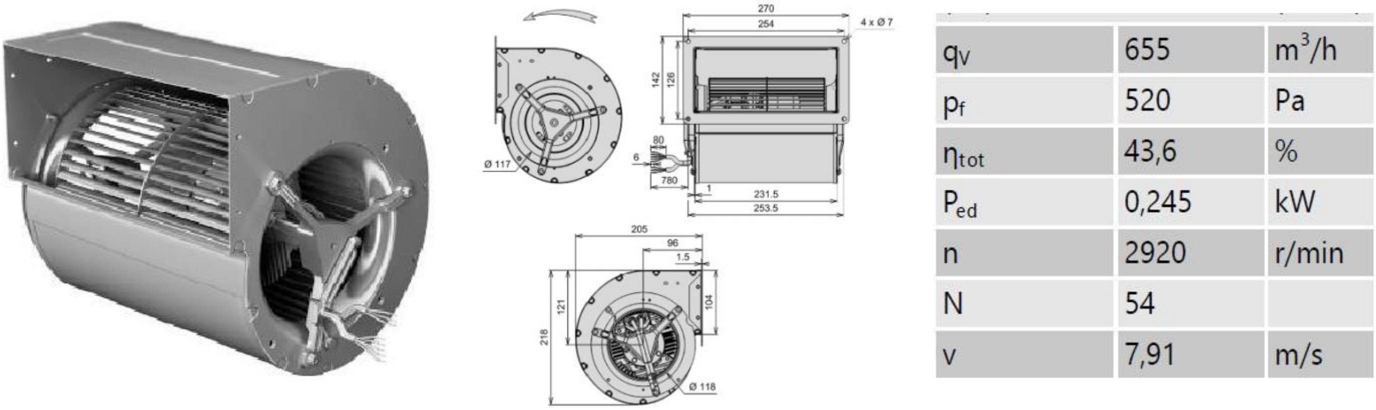

q_V	655	m^3/h
p_f	520	Pa
η_{tot}	43,6	%
P_{ed}	0,245	kW
n	2920	r/min
N	54	
v	7,91	m/s

Figure 4: Fan installed inside the test device

The experiment involved a maximum flow rate of 400 $\frac{m^3}{h}$ (equal to that expected for the prototype), corresponding to a velocity of 0.9 $\frac{m}{s}$.

3.2 Sources

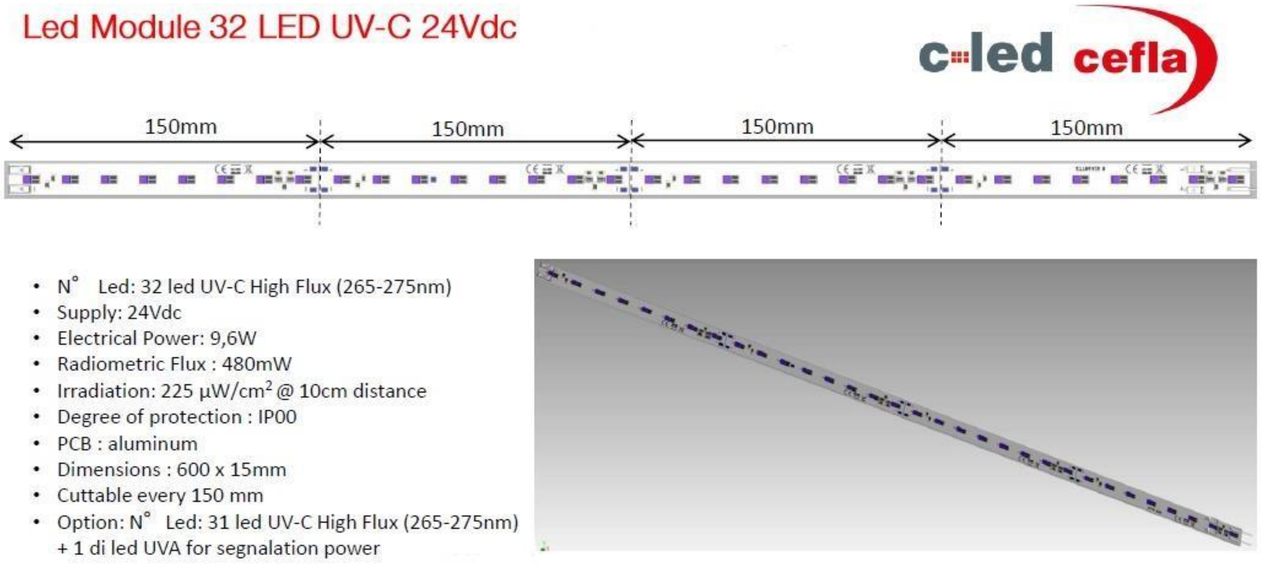

- N° Led: 32 led UV-C High Flux (265-275nm)
- Supply: 24Vdc
- Electrical Power: 9,6W
- Radiometric Flux : 480mW
- Irradiation: 225 μW/cm² @ 10cm distance
- Degree of protection : IP00
- PCB : aluminum
- Dimensions : 600 x 15mm
- Cuttable every 150 mm
- Option: N° Led: 31 led UV-C High Flux (265-275nm) + 1 di led UVA for segnalation power

Figure 5: Lamps module [111].

The three modules chosen for the experiment are the 32-LED ones, whose main characteristics are reported in Figure 5, including power supply, radiometric flux, irradiation, and dimensions. Each bar is 60 cm long and 1.5 cm high and is secured by gluing into the corresponding support mounted in the apparatus.

The 24 Vdc power supply was verified before each measurement by connecting the terminals of a digital voltmeter simultaneously to the positive pole and ground of the power wires; the air temperature was monitored using a temperature sensor inserted through a hole on the upper surface of the structure.

These modules are subject to certain acceptability conditions:

- The individual equipment has been evaluated by the manufacturer for use in an environment with pollution degree 2 and at altitudes not exceeding 2000 m.
- In the final application, the LED module must be powered by an LED driver approved separately in accordance with the IEC 61347-1 and IEC 61347-2-13 series, with a Safety Extra-Low Voltage (SELV) type output operating at a voltage below 60 Vdc.
- The maximum rated operating temperature must be maintained below 40 °C.

3.3 Sensors

3.3.1 Radiation

The UV-C illuminance measurements, aimed at determining the power density (power per unit area) reaching a detector placed at a certain distance from the source, were carried out using a photodiode coupled with a '918D High Performance' power meter, both manufactured by the American company Newport [112].

Photodiode

A photodiode consists of a semiconductor p-n junction similar to a laser diode or an LED; however, the fundamental radiation process involved is absorption. The light that strikes the junction generates electron-hole pairs. In photovoltaic mode, the generated pairs migrate to opposite sides of the junction, thereby producing a voltage. A fundamental difference between a semiconductor photon source and a photon detector lies in the fact that the former requires the use of a direct bandgap semiconductor. In contrast, the latter can use an indirect bandgap semiconductor. While the simultaneous conservation of energy and momentum makes photon emission much less likely in indirect-bandgap semiconductors, this is not the case for absorption. A readily achievable two-step process occurs when an electron is excited to a high level in the conduction band, followed by a relaxation process in which its momentum is transferred to phonons. Since this process can occur sequentially, it is much more likely than an emission process in which both steps must happen simultaneously [112].

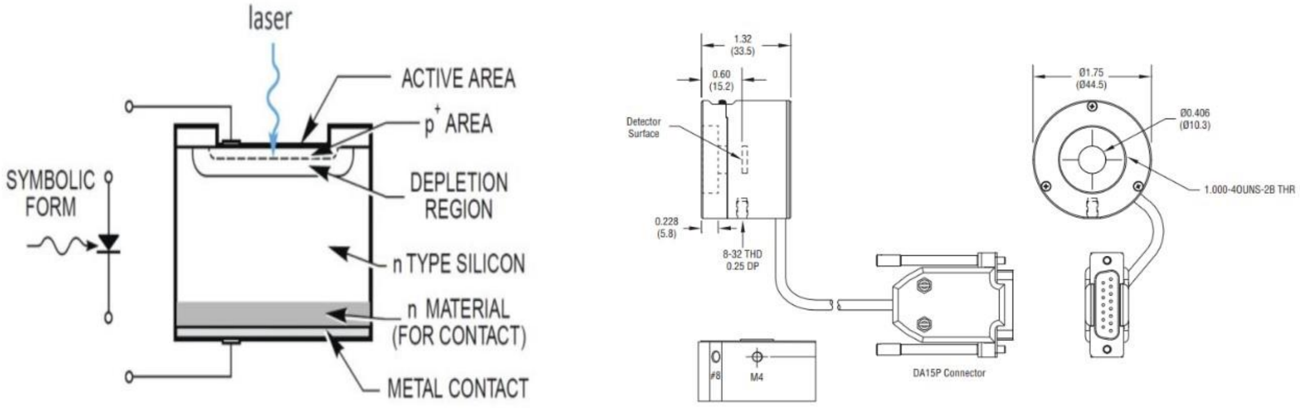

Figure 6: The photodiode structure.

Table 3: The photodiode characteristics.

Specification	**Value**
Detector material	Silicon – UV Enhanced
Spectral range	200 – 1100 nm
Active area	Ø10.3 mm
Sensor dimensions	Ø11.3 mm
Attenuator 1	OD3, integrated
Maximum power density	30 W/cm²
Max power density without attenuator	3 W/cm²
Connector type	DB15
Operating temperature	5 to 50 °C
Operating humidity	<70% relative humidity
Cable length	2 m

The 918D series photodetectors have an integrated optical attenuator that can be manually inserted or removed from the optical path using a dial located on the top of the detector housing. The "ON" and "OFF" markings on the attenuator indicate the direction of rotation.

The detector’s response depends on the wavelength of the incident light. The photodiode is transparent to photons with energies below the bandgap, which defines the infrared sensitivity limit in terms of wavelength. The photodiode’s response is typically measured in amperes of photocurrent per watt of incident optical power, and the device's response curves, shown in Figure 7, are reported in the calibration report.

To minimize the effects of ambient light during use, the room's windows were covered with reflective foil, and measurements were taken with the lights off (the measurement configuration is shown in Figure 12).

Although the photocurrent generated by ambient light can easily be zeroed out, the shot noise associated with the photocurrent will not be eliminated, nor will variations in ambient light levels caused by people moving around the room. A small electronic offset is always present in semiconductor detectors, and it can be removed using the optical meter's zeroing function. However, note that the offset depends on the temperature of both the photodiode and the amplifier inside the optical meter.

Whether the attenuator is needed depends on the amount of incoming power. Specifically, as indicated in the specifications above, if the incident power on the photodiode exceeds 300 µW, the attenuator must be used. This is because, as shown in the graph in Figure 7, once the threshold is exceeded, the sensor's characteristic curve, the output behavior as a function of the input, loses linearity, indicating that the instrument is beginning to saturate.

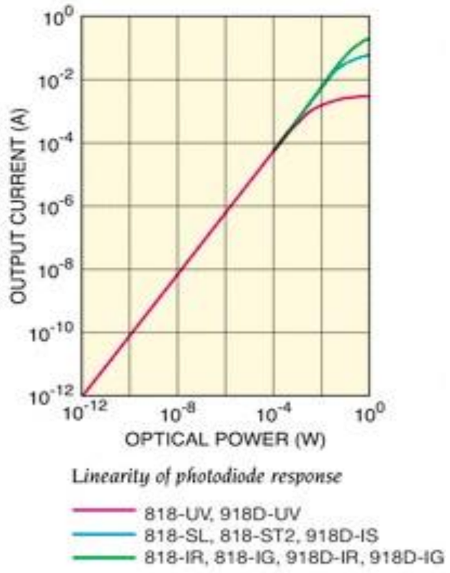

Figure 7: Sensor characteristic curve.

The maximum measurable power, therefore, depends on factors such as the wavelength of the incoming light, the photodiode's saturation level, the temperature, the use of an attenuator, and the power meter's maximum input current rating. Regarding temperature effects, the photodiode's sensitivity increases with temperature, especially for wavelengths longer than its peak response wavelength.

The temperature of the 918D series detectors is monitored with a thermistor, and the responsivity is numerically compensated to maintain accurate calibration within specifications during operation at specific wavelengths.

Returning to the attenuator, it is essentially a neutral density filter which, unlike a standard one, does not attenuate uniformly across different wavelengths, as shown in the graphs below. Its effect is wavelength-dependent. At 265 nm, where the germicidal effect of UVC LEDs is at its peak and the measurements were taken, the attenuation factor is 0.6.

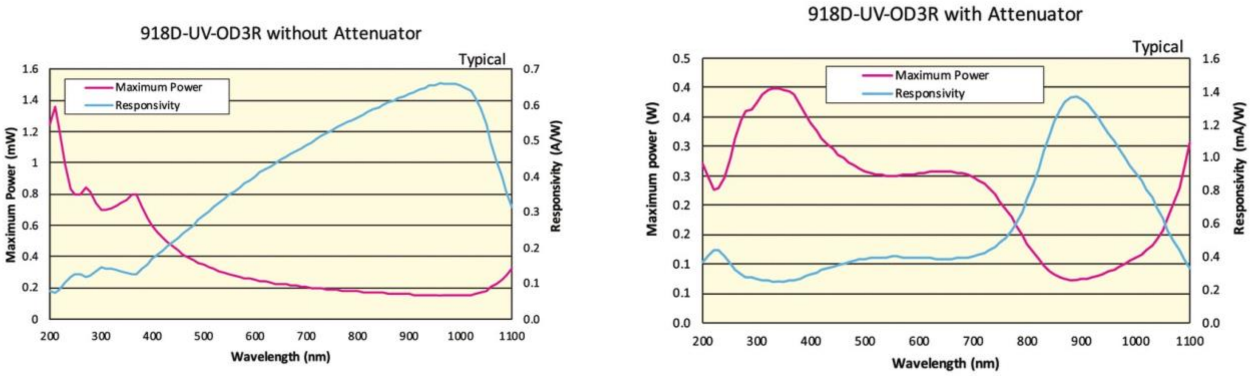

Figure 8: Comparison of characteristic curves without and with attenuator.

The Newport 1919-R is a laser power/energy meter equipped with a microprocessor that provides a wide range of measurement capabilities, display options, and data management features. It is compatible with thermopile, pyroelectric, and photodiode sensors.

Using smart connector technology, operation with a sensor requires connecting the sensor via a VGA cable and configuring and calibrating the 1919-R unit. The sensor's configuration and calibration data are stored in an EEPROM in the sensor's connector plug.

This means that when the sensor is connected, the 1919-R automatically identifies the sensor type, calibration data, and configuration settings. The 1919-R can display power or energy as a function of time and can present power measurements in both digital and analog formats. An Auto-range function is available, allowing the device to automatically select the appropriate measurement range, although manual range selection is also possible.

Although the calibration information is stored within the smart connector, it is possible to recalibrate directly from the display interface, and the updated calibration data is automatically saved to the sensor.

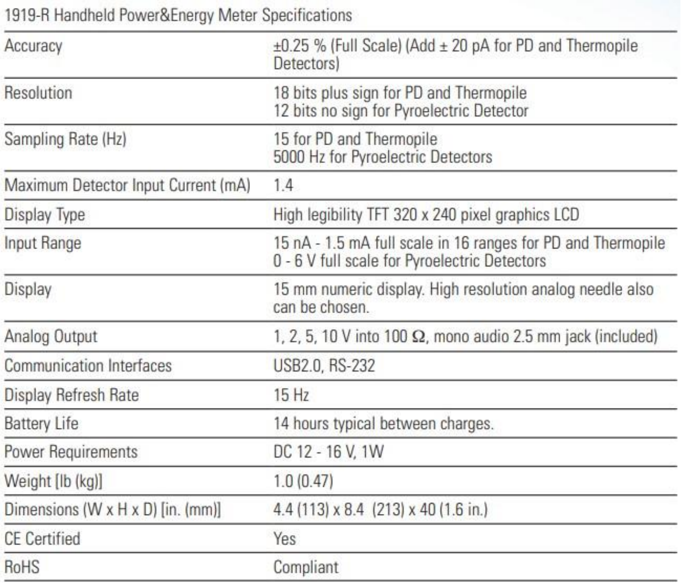

1919-R Handheld Power&Energy Meter Specifications

Accuracy	±0.25 % (Full Scale) (Add ± 20 pA for PD and Thermopile Detectors)
Resolution	18 bits plus sign for PD and Thermopile 12 bits no sign for Pyroelectric Detector
Sampling Rate (Hz)	15 for PD and Thermopile 5000 Hz for Pyroelectric Detectors
Maximum Detector Input Current (mA)	1.4
Display Type	High legibility TFT 320 x 240 pixel graphics LCD
Input Range	15 nA - 1.5 mA full scale in 16 ranges for PD and Thermopile 0 - 6 V full scale for Pyroelectric Detectors
Display	15 mm numeric display. High resolution analog needle also can be chosen.
Analog Output	1, 2, 5, 10 V into 100 Ω, mono audio 2.5 mm jack (included)
Communication Interfaces	USB2.0, RS-232
Display Refresh Rate	15 Hz
Battery Life	14 hours typical between charges.
Power Requirements	DC 12 - 16 V, 1W
Weight [lb (kg)]	1.0 (0.47)
Dimensions (W x H x D) [in. (mm)]	4.4 (113) x 8.4 (213) x 40 (1.6 in.)
CE Certified	Yes
RoHS	Compliant

Figure 9: Power meter.

Moreover, the device is compatible with PMManager, an application software that manages and records measurement data. This software effectively transforms a PC into a multichannel laser power analysis workstation. PMManager software features include extensive graphical data display, advanced measurement processing, data logging for future review, graph and data printing, and the ability to connect additional devices during active measurements. The software also allows data logging based on time intervals or the number of data points, as well as exporting data in Excel format, which can be viewed either graphically or as plain text [112].

3.3.2 Airflow and Temperature

Before each measurement, the volumetric airflow generated by the fan was evaluated to verify that the operating point was within the typical range expected for the device installed in the suspended ceiling at the terminal section of a ventilation duct (2 to 4 m/s).

The instrument used was the Testo 440 dP, manufactured by the Italian company Testo Spa, equipped with probes for measuring key environmental parameters, including a differential pressure sensor for filter monitoring. Communication between the instrument and the probe occurs via Bluetooth connection, allowing greater freedom in taking measurements, even in less accessible or uncomfortable conditions. The presence of a USB interface enables exporting measurement logs in CSV format.

Regarding the velocity probe, it is a vane type, capable of measuring 0.3 to 35 m/s, and allows the corresponding volumetric airflow to be determined.

For temperature verification within the device, critical since the lamps operate at maximum efficiency when temperatures do not exceed 40 °C, a thermo-hygrometric probe tip was employed. This probe allows simultaneous measurement of relative humidity and air temperature in indoor environments, including long-term measurements, with an accuracy of ±2 %RH and ±0.5 °C; measurement range: 0 to 100 %RH and -20 to +70 °C [113].

It should be noted that, in the current phase of this scientific research, the sensors were employed exclusively to ensure optimal operating conditions for the lamps and environmental stability, rather than to analyze the effects of temperature on light propagation. A review of the literature [114 -115] indicates that the refractive index of air varies as a function of temperature and pressure, although to an extremely limited extent. Shaheen, for pressures ranging between 88 and 107 kPa and temperatures between 303 and 338 K (≈ 30-65 °C), reported values between 1.000189 and 1.000281, with a thermal coefficient of approximately $-1.35 \times 10^{-6}\,K^{-1}$. Similarly, Dettwiller's review shows that, under typical indoor conditions (0-25 °C, 80-105 kPa), the variation remains on the order of 10^{-5}.

Based on this evidence, at this stage of the work it was considered appropriate, for the time being, not to include such variations in the simulation models, as their impact on illuminance maps was deemed negligible despite being scientifically measurable. This decision is provisional and may be revisited in future developments should a higher level of accuracy be required.

Figure 10:Flow rate and temperature meter.

3.4 Measurement points for the radiation Maps

Irradiance measurements were conducted by positioning the sensor inside the device at the same distance from the lamps where the filter will be installed, and at various positions in order to create an irradiance map. To move the sensor, a vertical rod was installed, allowing it to be placed at the desired position. The vertical rod is welded to a horizontal rod 78 cm in length at a lateral-central position, enabling horizontal movement of the sensor.

The initial measurement maps were created to obtain an order-of-magnitude estimate of the power density at 45 points, as shown in Figure 11.

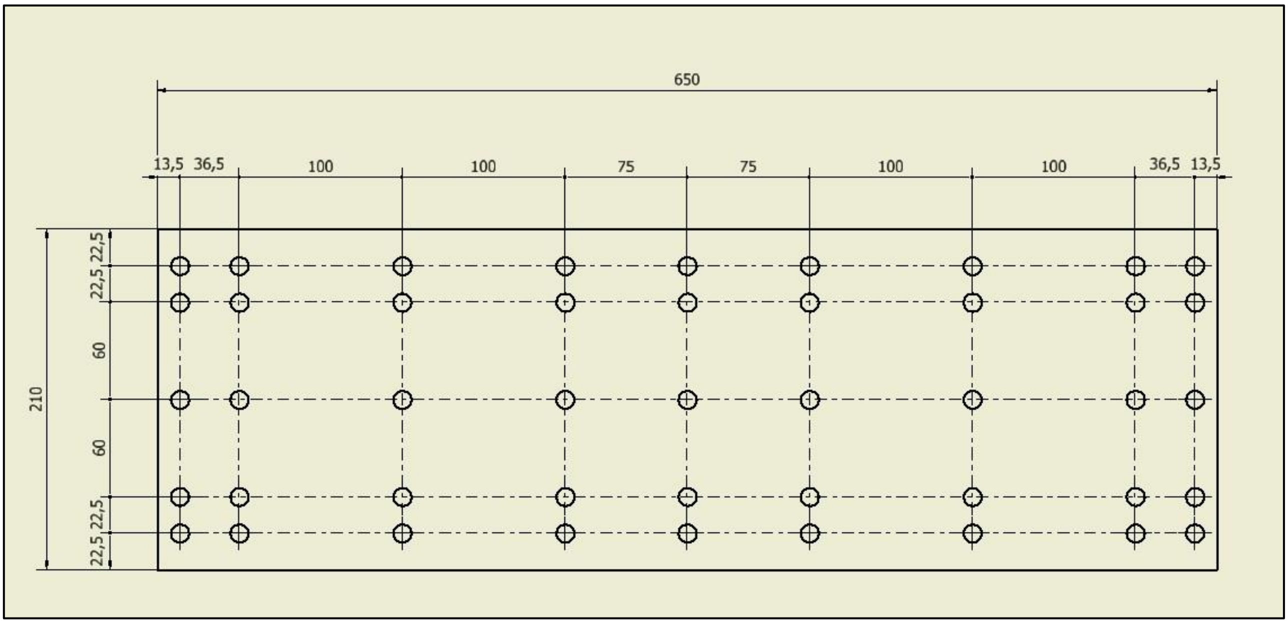

Figure 11:First measuring points map.

Since initial measurements revealed irradiance levels inconsistent with those declared by the manufacturer, more detailed maps were subsequently constructed.

- Regarding the vertical sampling step, given that the supporting vertical rod is 23.5 cm high and coincides with the midline of the box, 11 measurement points were chosen. Due to the dimensions of the support on which the sensor was mounted, the active measurement length is 16.5 cm, although the filter itself measures 21 cm. Therefore, a sampling step of 1.5 cm was selected to allow sensor placement also directly in front of the two lower and upper rods. To enable sensor placement in the central position as well, an additional measurement point was added at the center, located 0.75 cm from the immediately adjacent upper and lower points.
- For horizontal sampling, two different steps were chosen depending on whether measurements were taken at the periphery or in the central part of the device. Given that the filter length is 64 cm, a 1 cm step was deemed appropriate in the peripheral region to evaluate both the contributions from reflections off the metal walls and the reduced cooperative effect of individual illuminated modules. In the central region, a 2 cm step was selected. Specifically, a 1 cm step was used for the first 5 lateral measurement points on both the right and left sides, and 2 cm for the remaining points, resulting in a total of 38 measurement points along the horizontal axis.

The resulting irradiance matrices, therefore, comprise 494 measurement points. Sensor movement and fixation were performed manually, using graduated scales on both the vertical and horizontal rods. Vertical translation of the sensor, secured with a nut-and-bolt system, was achieved by loosening the nut as needed, while horizontal positioning was performed by sliding the metal support.

Figure 12:Sensor support and translation system.

Considering the vertical dimensions of the considered elements (box height of 26 cm, filter height of 21 cm, vertical rod height of 23.5 cm, and sampling region height of 16.5 cm), the difference Δy between the length of the support rod and the extension of the sampling region is:

$$\frac{23{,}5\ -\ 16{,}5}{2} = 3{,}5 \tag{3.4.1}$$

The distance between the extreme sensor positions and the horizontal walls, both lower and upper, of the box is:

$$\frac{26\ -\ 23{,}5}{2} + 3{,}5 = 4{,}75 \tag{3.4.2}$$

This allows the measurement points to be placed relative to the box structure, with the reference system origin at the top-left corner. The horizontal coordinate values of the points are reported in Table 4.

Table 4:Order of measurement points.

Active length of measurement [cm]	Sampling step [cm]	Distance [cm]
8.25	0	4.75
6.75	1.5	6.25
5.25	1.5	7.75
3.75	1.5	9.25
2.25	1.5	10.75
0.75	1.5	12.25
0	0.75	13
0.75	0.75	13.75
2.25	1.5	15.25
3.75	1.5	16.75
5.25	1.5	18.25
6.75	1.5	19.75
8.25	1.5	21.25

To account for the horizontal dimensions of the various elements, note that the width is 2 cm, and the sensor is positioned at the midpoint, 1 cm from the edges. When the horizontal rod is fully retracted to the left end (corresponding to the first measurement point), the scale on the small protrusion reads 71.8 cm; when the rod is fully retracted to the right end (corresponding to the last measurement point), the scale reads 7.8 cm. The total length of the measurement field to be covered is 64 cm, and, as previously stated, with the selected sampling step, there are 37 measurement points.

Table 5: Abscissas of measurement points.

Sampling step [cm]	Distance [cm]	Active length of measurement [cm]
0	5.3	31.56
1	6.3	30.56
1	7.3	29.56
1	8.3	28.56
1	9.3	27.56
2	11.3	25.56
2	13.3	23.56
2	15.3	21.56
2	17.3	19.56
2	19.3	17.56
2	21.3	15.56
2	23.3	13.56
2	25.3	11.56
2	27.3	9.56
2	29.3	7.56
2	31.3	5.56
2	33.3	3.56
2	35.3	1.56
36.86		
2	37.3	0.44
2	39.3	2.44
2	41.3	4.44
2	43.3	6.44
2	45.3	8.44
2	47.3	10.44
2	49.3	12.44
2	51.3	14.44
2	53.3	16.44
2	55.3	18.44
2	57.3	20.44
2	59.3	22.44
2	61.3	24.44
2	63.3	26.44
2	65.3	28.44
1	66.3	29.44
1	67.3	30.44
1	68.3	31.44
1	69.3	32.44

The vertical rod, when fully seated at the extreme position on the horizontal bar, is not adjacent to the device's left sidewall; the same applies when fully seated towards the right side, but at a distance of 4.3 cm. Since the sensor is positioned 1 cm from the left end of the vertical rod, the abscissa of the first measurement point, with respect to the chosen reference system, is 5.3 cm.

Figure 13 shows the front and side sections of the device, reconstructed using COMSOL Multiphysics, along with the point matrix corresponding to the sensor positions.

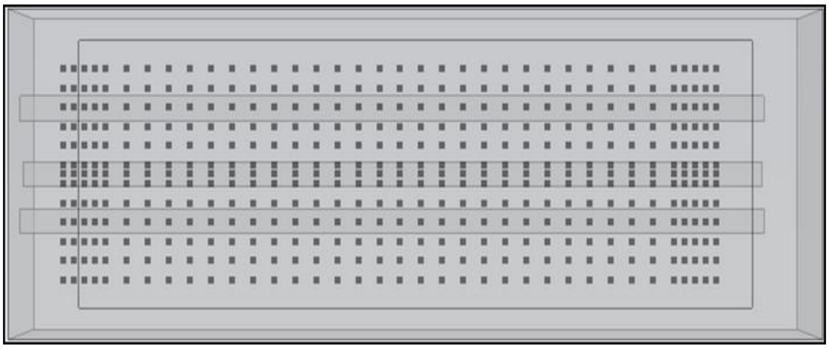

Figure 13: Representation of the 494 measuring points used in the experimental device.

Before proceeding with the construction of the irradiance maps, evaluations of irradiance at different wavelengths were conducted to verify that the wavelengths of interest fall within the range of maximum incident power. The instrument allows selecting the wavelength for which the data is to be recorded, and the procedure was as follows:

- Frequency scan of the irradiance measured at the central position (where the maximum power density is expected)
- Frequency scan of the irradiance measured at the top-left corner, which, according to preliminary results, is the most disadvantaged point, i.e., where the incident power on the sensor is significantly lower than at the central point, by an order of magnitude.

The wavelength range considered was between 200 nm and 1100 nm, with steps of 100 nm, except for three specific wavelengths, 254 nm, 265 nm, and 275 nm, which, according to the literature, correspond to the maximum germicidal effectiveness of ultraviolet radiation, depending on the source used, and exhibit their full germicidal efficacy.

Figure 14 shows the trends in power density measured at the two positions considered during simultaneous operation of the three lamps installed in the device.

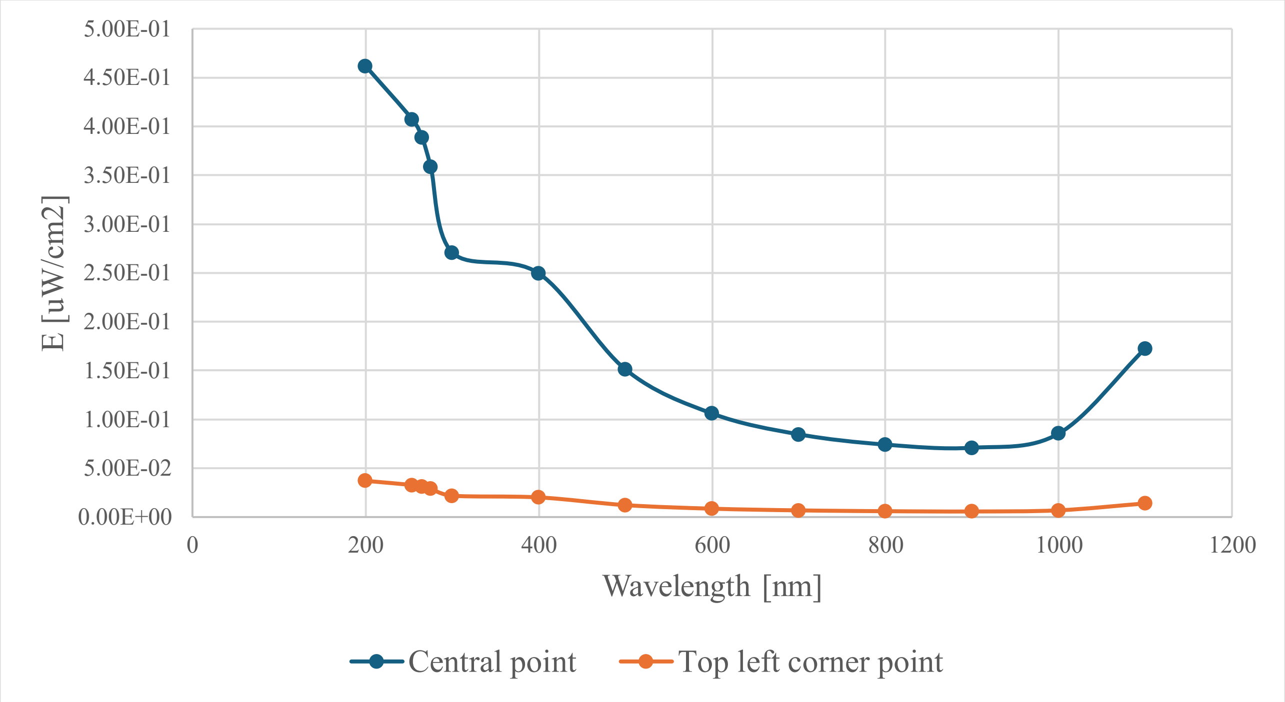

Figure 14: Measured power density as a function of wavelength for two locations of the sensor.

From Figure 15, a monotonically decreasing trend is observed at both measurement points up to 1000 nm, followed by an increase in the recorded power density. For longer wavelengths, it is evident that the maximum irradiance occurs at lower wavelengths, particularly at 200 nm, while for the wavelengths of interest, namely 254 nm and 265 nm, the difference is not significant. Therefore, it was decided to follow the literature and measure at 265 nm.

3.5 Numerical tools

3.5.1 COMSOL Multiphysics

The Ray Optics Module of COMSOL Multiphysics allows modeling light propagation using a geometric approach, considering electromagnetic radiation as a set of rays. This method is valid when the wavelength of light is negligible compared to the characteristic dimensions of the optical system:

$$\lambda \ll L\lambda \ll L\lambda \ll L \tag{3.5.1}$$

In this context, propagation follows deterministic laws based on the geometry of the medium and local optical properties, neglecting wave effects such as interference or diffraction (unless introduced in simplified form).

Ray propagation in optical media

The trajectory of a ray is determined by the spatial distribution of the refractive index. In media with uniform index, the trajectory is straight; in media with varying index, it follows a curved path governed by Hamiltonian equations:

$$\frac{dq}{dt} = \nabla_k \omega, \quad \frac{dk}{dt} = -\nabla_q \tag{3.5.2}$$

where:

- $q(t)$ is the ray position;
- k is the wave vector;
- ω is the angular frequency given by:

$$\omega = \frac{c|k|}{n(q)} \tag{3.5.3}$$

The wave number in vacuum is defined as:

$$k_0 = \frac{2\pi}{\lambda_0} \tag{3.5.4}$$

while in a medium with refractive index n, the wave number becomes:

$$k = nk_0 \tag{3.5.5}$$

Reflection, refraction, and absorbing materials

At the interface between two media, the ray direction changes according to Snell's law:

$$n_1 \sin \theta_1 = n_2 \sin \theta_2 \tag{3.5.6}$$

where:

- n_1, n_2 are the refractive indices of the two media;
- θ_1 is the angle of incidence;
- θ_2 is the angle of refraction.

In absorbing materials, the refractive index is expressed as a complex number:

$$\tilde{n} = n - i \tag{3.5.7}$$

The electric field E associated with a ray propagating along the direction $\hat{s}$ is attenuated according to:

$$|E(L)|^2 = |E_0|^2 \exp(-2k_0 \kappa L) \tag{3.5.8}$$

Where L is the distance travelled in the medium, and E_0 is the initial amplitude and κ is the extinction coefficient.

Wavefront and curvature

Each ray is associated with a three-dimensional wavefront whose geometry is described by two principal radii of curvature r_1 and r_2, which evolve according to:

$$\frac{dr_1}{ds} = 1, \quad \frac{dr_2}{ds} = -1 \tag{3.5.9}$$

The associated curvatures are:

$$\kappa_1 = \frac{1}{r_1}, \quad \kappa_2 = \frac{1}{r_2} \tag{3.5.10}$$

The matrix of principal curvatures of the wavefront is:

$$K = \kappa_1 e_1 e_1^T + \kappa_2 e_2 e_2^T \tag{3.5.11}$$

where $e_1$and e_2 are unit vectors of the principal directions orthogonal to the propagation direction.

Optical phase and electric field

The electric field along the ray trajectory is described as:

$$E(q) = a(q)\, e^{i\,\Psi(q)} \tag{3.5.12}$$

where:

- Ψ(q) is the accumulated optical phase;
- a(q) is the slowly varying complex amplitude.

In the local transverse plane, the phase can be approximated by a Taylor expansion:

$$\Psi(\Delta x, \Delta y) = \Psi_0 + k\left(n_x \Delta x + n_y \Delta y\right) + \frac{1}{2} k(\kappa_1 \Delta x^2 + \kappa_2 \Delta y^2) \tag{3.5.13}$$

This development is useful to study interference between adjacent rays and spatial phase evolution.

Accumulators and thermal ray source

COMSOL implements accumulators to collect information along ray paths. In 3D domains, the volumetric accumulator for deposited power density is defined as:

$$r_{pd} = \frac{1}{V} \sum_{i=1}^{N} R_i \tag{3.5.14}$$

where V is the volume of the mesh element and R_i is the contribution deposited by the individual ray. The power deposited by each ray in an absorbing medium can be expressed as:

$$\frac{dQ}{dt} = -\frac{dP}{dt} \tag{3.5.15}$$

and the overall volumetric source (implemented via Ray Heat Source) becomes:

$$Q_{\mathrm{src}} = \frac{1}{V}\sum_{i=1}^{N}\left(-\frac{dP_i}{dt}\right) \tag{3.5.16}$$

This source can be used as input for thermal models (Heat Transfer in Solids), allowing analysis of optical heating, ablation, thermal expansion, and other thermo-optical effects.

The theoretical formulation behind the COMSOL Ray Optics Module represents a bridge between classical optics and advanced computational analysis. The possibility to combine geometric propagation, attenuation, polarization, and thermal phenomena makes this module a powerful tool for studying and designing complex optical systems. Thanks to accumulators and integration with thermal and structural modules, the software enables high-fidelity Multiphysics simulations applicable in fields ranging from laser optics to concentrated solar energy and integrated micro-optics [116].

3.5.2 Matlab

For the pre- and post-processing phases of the acquired data, MATLAB was employed. MATLAB is a high-level programming language and interactive computing environment that is widely adopted in scientific, academic, and industrial settings for numerical analysis, signal processing, system modelling, and the simulation of complex phenomena. Its comprehensive library of built-in functions and specialized toolboxes provides robust support for data handling, visualization, and processing, while also enabling the development of customized algorithms and the automation of computational workflows.

In particular, during the source characterization phase, the Curve Fitting Toolbox was utilized. This advanced toolbox enables the implementation of interpolation and nonlinear regression techniques by iteratively fitting curves and surfaces to experimental datasets. It supports the use of a variety of predefined mathematical models, such as polynomial, exponential, and Gaussian functions, as well as the definition of user-defined models. Additionally, the toolbox offers a quantitative assessment of the fit quality through statistical metrics such as the coefficient of determination (R^2), root mean square error (RMSE), and residual analysis. The application of this toolbox allowed for the accurate extraction of the source’s characteristic parameters, thereby contributing to a more precise representation of its experimental behaviour and facilitating a more rigorous physical interpretation of the observed phenomena [117].

Chapter 4 – Experimental results

4.1 First results measurement campaign

During our stay at the company Sagicofim S.p.A., initial measurements were carried out following the first measurement point scheme (section of the second chapter), to make a preliminary assessment of the irradiance magnitude. In particular, measurements were not taken at a single frequency, but at 254 nm, 265 nm, and 275 nm to verify whether the results from the previous analysis are indeed confirmed.
The initial measurements carried have been performed with three lit lamps and the results are reported in figure 15, 16 and 17:

- 254nm

	Dev. [mm]	13,5	36,5	100	100	75	75	100	100	36,5
Dev. [mm]	Dist. [mm]	14	50	150	250	325	400	500	600	637
22,5	23	35	84	115	114	113	112	118	85	36
22,5	45	68	160	210	208	212	207	210	160	67
60	105	129	300	406	407	405	407	410	311	137
22,5	128	110	262	344	340	336	348	348	252	101
22,5	150	82	173	226	225	221	230	230	157	65

Figure 15: Irradiance map [uW/cm²] for λ=254nm with three simultaneously lit lamps.

- 265 nm

	Dev. [mm]	13,5	36,5	100	100	75	75	100	100	36,5
Dev. [mm]	Dist. [mm]	14	50	150	250	325	400	500	600	637
22,5	23	27	62	75	76	78	75	77	52	17
22,5	45	101	205	240	241	245	240	249	151	49
60	105	158	326	395	395	393	393	398	248	79
22,5	128	115	250	298	298	294	303	302	188	51
22,5	150	71	153	184	183	179	185	183	110	34

Figure 16: Irradiance map [uW/cm²] for λ=265nm with three simultaneously lit lamps.

- 275 nm

	Dev. [mm]	13,5	36,5	100	100	75	75	100	100	36,5
Dev. [mm]	Dist. [mm]	14	50	150	250	325	400	500	600	637
22,5	23	38	76	94	93	94	81	86	57	23
22,5	45	83	172	206	203	205	202	204	137	58
60	105	130	282	361	361	360	361	365	256	109
22,5	128	83	204	269	267	264	272	272	193	76
22,5	150	71	152	197	195	191	198	197	134	57

Figure 17: Irradiance map [uW/c²m] for λ=275nm with three simultaneously lit lamps.

By examining the matrices individually, a pronounced asymmetry in power density is evident. Furthermore, the findings from the emission spectrum analysis are evident in this case as well.

With regard to the matrices at 254 nm and 275 nm og figure 15 and 17, the differences are significant, whereas in the first matrices, some anomalies are observed: for most points, the irradiance values at the first frequency are higher, except for the first two columns on the left, where the 265 nm wavelength appears to be more effective.

Subsequently, it was considered appropriate to measure, at the various wavelengths of interest, the contributions due to the individual lamps being switched on.

In Figure 18, 19 and 20 the irradiance map are reported for three different frequencies of interest in case of individual switching of upper, central and lower respectively.

- Measurement with single upper lamp switched on

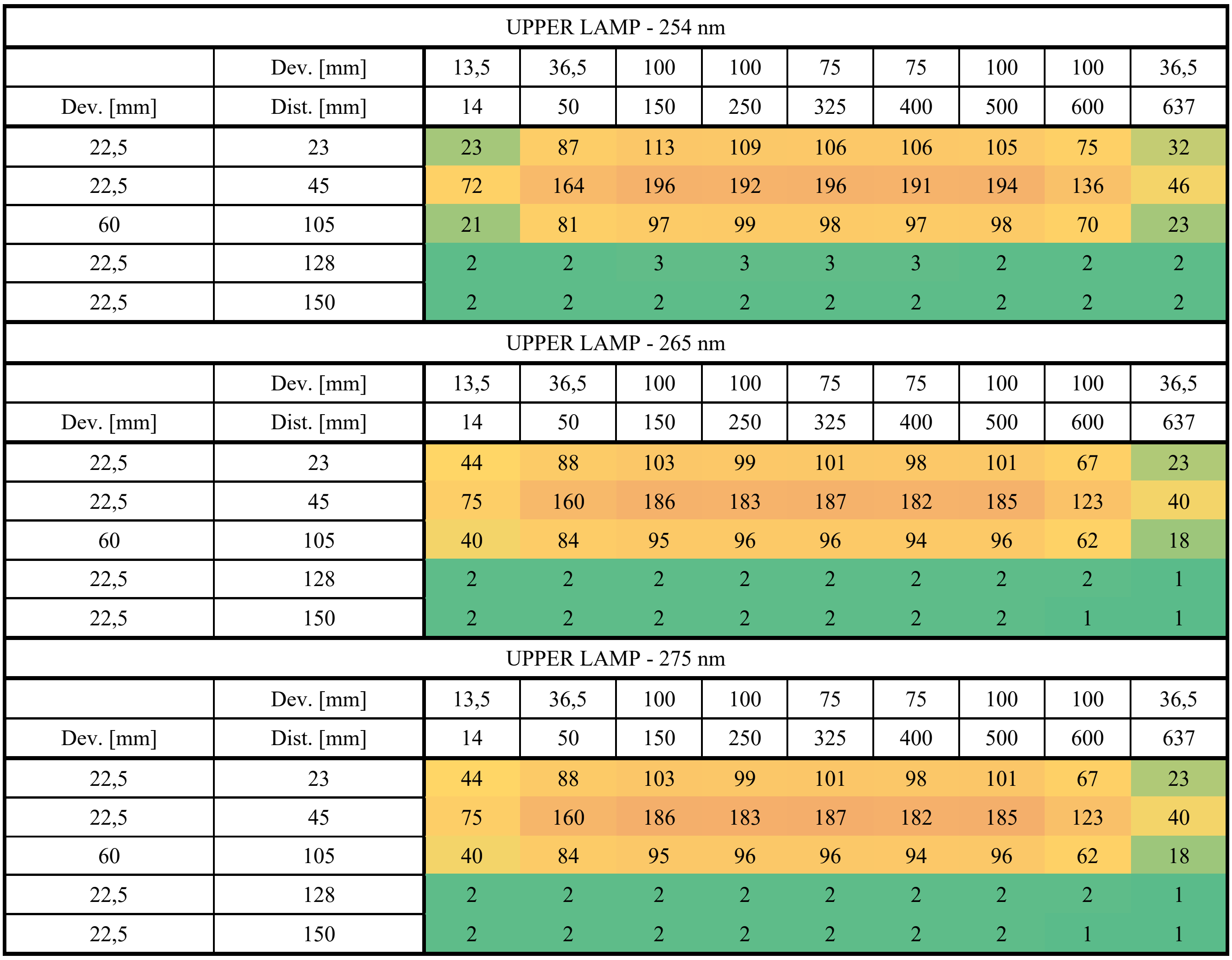

UPPER LAMP - 254 nm

	Dev. [mm]	13,5	36,5	100	100	75	75	100	100	36,5
Dev. [mm]	Dist. [mm]	14	50	150	250	325	400	500	600	637
22,5	23	23	87	113	109	106	106	105	75	32
22,5	45	72	164	196	192	196	191	194	136	46
60	105	21	81	97	99	98	97	98	70	23
22,5	128	2	2	3	3	3	3	2	2	2
22,5	150	2	2	2	2	2	2	2	2	2

UPPER LAMP - 265 nm

	Dev. [mm]	13,5	36,5	100	100	75	75	100	100	36,5
Dev. [mm]	Dist. [mm]	14	50	150	250	325	400	500	600	637
22,5	23	44	88	103	99	101	98	101	67	23
22,5	45	75	160	186	183	187	182	185	123	40
60	105	40	84	95	96	96	94	96	62	18
22,5	128	2	2	2	2	2	2	2	2	1
22,5	150	2	2	2	2	2	2	2	1	1

UPPER LAMP - 275 nm

	Dev. [mm]	13,5	36,5	100	100	75	75	100	100	36,5
Dev. [mm]	Dist. [mm]	14	50	150	250	325	400	500	600	637
22,5	23	44	88	103	99	101	98	101	67	23
22,5	45	75	160	186	183	187	182	185	123	40
60	105	40	84	95	96	96	94	96	62	18
22,5	128	2	2	2	2	2	2	2	2	1
22,5	150	2	2	2	2	2	2	2	1	1

Figure 18: Irradiance map [uW/cm²] for λ=254, 265, 275nm in case of single upper lamp switched on.

- Measurement with single central lamp switched on

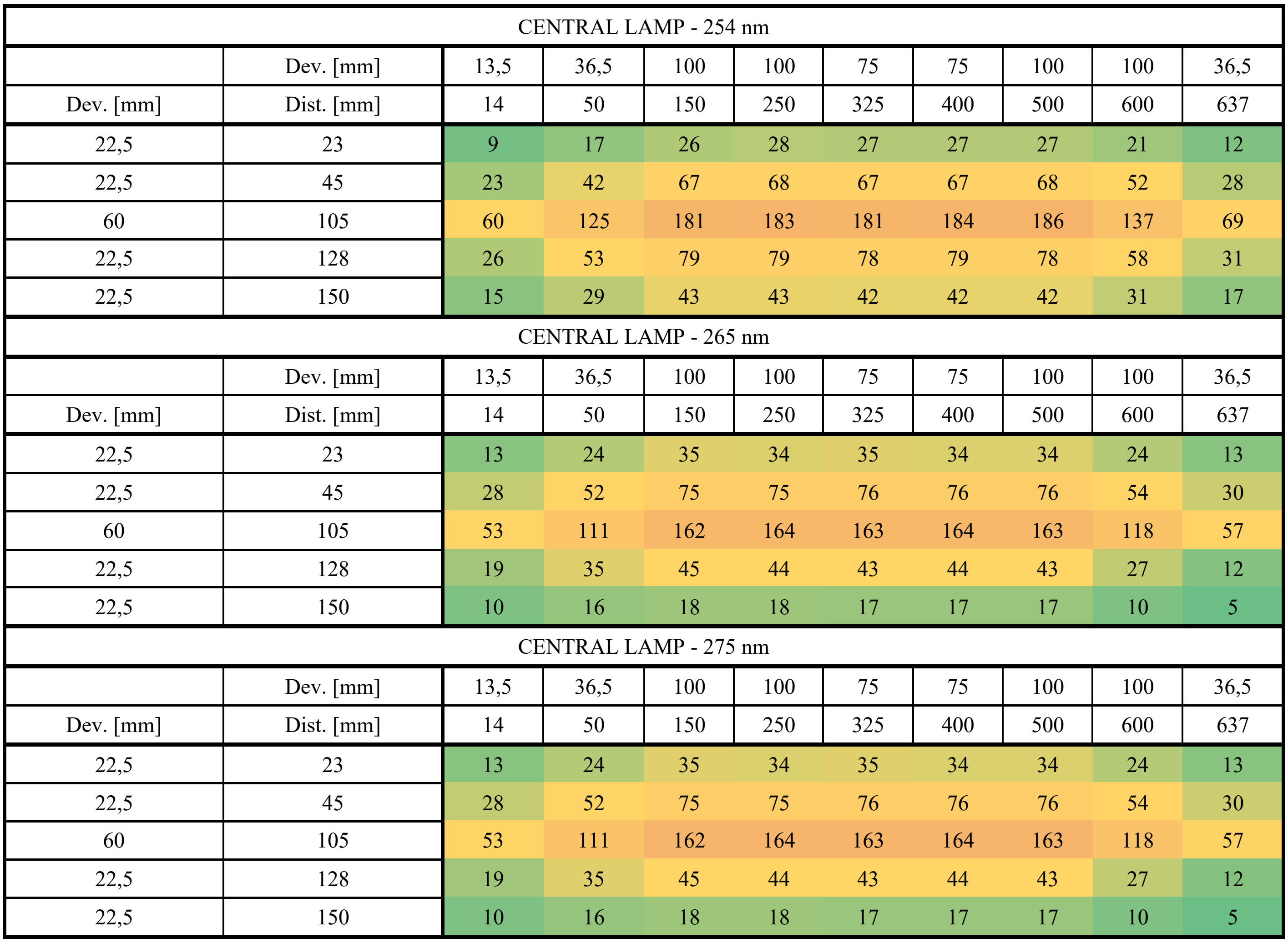

CENTRAL LAMP - 254 nm										
	Dev. [mm]	13,5	36,5	100	100	75	75	100	100	36,5
Dev. [mm]	Dist. [mm]	14	50	150	250	325	400	500	600	637
22,5	23	9	17	26	28	27	27	27	21	12
22,5	45	23	42	67	68	67	67	68	52	28
60	105	60	125	181	183	181	184	186	137	69
22,5	128	26	53	79	79	78	79	78	58	31
22,5	150	15	29	43	43	42	42	42	31	17

CENTRAL LAMP - 265 nm										
	Dev. [mm]	13,5	36,5	100	100	75	75	100	100	36,5
Dev. [mm]	Dist. [mm]	14	50	150	250	325	400	500	600	637
22,5	23	13	24	35	34	35	34	34	24	13
22,5	45	28	52	75	75	76	76	76	54	30
60	105	53	111	162	164	163	164	163	118	57
22,5	128	19	35	45	44	43	44	43	27	12
22,5	150	10	16	18	18	17	17	17	10	5

CENTRAL LAMP - 275 nm										
	Dev. [mm]	13,5	36,5	100	100	75	75	100	100	36,5
Dev. [mm]	Dist. [mm]	14	50	150	250	325	400	500	600	637
22,5	23	13	24	35	34	35	34	34	24	13
22,5	45	28	52	75	75	76	76	76	54	30
60	105	53	111	162	164	163	164	163	118	57
22,5	128	19	35	45	44	43	44	43	27	12
22,5	150	10	16	18	18	17	17	17	10	5

Figure 19: Irradiance map [uW/cm²] for λ = 254, 265, 275nm in case of single central lamp switched on.

- Measurement with single lower lamp switched on

LOWER LAMP - 254 nm

	Dev. [mm]	13,5	36,5	100	100	75	75	100	100	36,5
Dev. [mm]	Dist. [mm]	14	50	150	250	325	400	500	600	637
22,5	23	2	2	2	2	2	1	2	2	2
22,5	45	2	3	3	3	3	2	2	2	2
60	105	56	108	130	128	126	129	127	80	25
22,5	128	73	167	206	205	203	212	212	145	42
22,5	150	56	116	135	134	132	138	137	85	25

LOWER LAMP - 265 nm

	Dev. [mm]	13,5	36,5	100	100	75	75	100	100	36,5
Dev. [mm]	Dist. [mm]	14	50	150	250	325	400	500	600	637
22,5	23	2	2	2	2	1	1	1	1	1
22,5	45	2	3	3	2	2	2	2	2	2
60	105	45	96	118	114	115	118	118	80	30
22,5	128	58	127	161	160	156	163	163	108	33
22,5	150	46	89	94	92	92	94	95	48	10

LOWER LAMP - 275 nm

	Dev. [mm]	13,5	36,5	100	100	75	75	100	100	36,5
Dev. [mm]	Dist. [mm]	14	50	150	250	325	400	500	600	637
22,5	23	2	2	2	2	1	1	1	1	1
22,5	45	2	3	3	2	2	2	2	2	2
60	105	45	96	118	114	115	118	118	80	30
22,5	128	58	127	161	160	156	163	163	108	33
22,5	150	46	89	94	92	92	94	95	48	10

Figure 20: Irradiance map [uW/cm²] for λ= 254, 265, 275nm in case of single lower lamp switched on.

What we were able to observe, differently from what had emerged previously, is that for the 265 nm wavelength, particularly at the points where the sensor's position is aligned with the source, significantly higher power density values were recorded compared not only to 275 nm, but also to those measured at 254 nm, contrary to the earlier case.

These measurements were carried out not only to assess the contribution of each individual lamp, but also to allow a comparison with the data provided by the manufacturer. In particular, following discussions with representatives of the company, it became clear that the supplied data (reported in table 5 with reference to figure 21) corresponded to broadband measurements, that is, measurements performed over a wavelength range between 200 nm and 390 nm, summed together and subsequently integrated over the entire interval.

Since this information was acquired only after the measurements had already been taken, it was decided to use our data and perform an integration process, using the trapezoidal rule, over the non-uniform frequency interval in order to enable a comparison. At this stage, as it was not yet possible to accurately place the maps and lamps within a common reference system, an average was computed (based on the observed symmetry) between the values from the first and second rows (as well as the fourth and fifth rows).

- C-led measurements

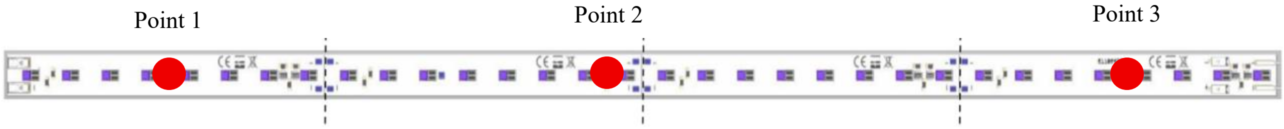

Figure 21: Measurement points declared by C-led.

Table 6: Power density declared by C-Led.

	Distance from the source	
	8 cm	11 cm
Point 1	382. 4 $\frac{uW}{cm^2}$	247.4 $\frac{uW}{cm^2}$
Point 2	405 $\frac{uW}{cm^2}$	298.5 $\frac{uW}{cm^2}$
Point 3	399 $\frac{uW}{cm^2}$	289.2 $\frac{uW}{cm^2}$

In order to enable a direct comparison with the value declared by the manufacturers, the integral was computed over the entire frequency range.

The corresponding results are presented in Table 7.

- Sapienza measurements

Table 7: Sapienza measurements.

<table>
<tr><td colspan="11">INTEGRATED UPPER LAMP - 254 nm</td></tr>
<tr><td></td><td>Dev. [mm]</td><td>13,5</td><td>36,5</td><td>100</td><td>100</td><td>75</td><td>75</td><td>100</td><td>100</td><td>36,5</td></tr>
<tr><td>Dev. [mm]</td><td>Dist. [mm]</td><td>14</td><td>50</td><td>150</td><td>250</td><td>325</td><td>400</td><td>500</td><td>600</td><td>637</td></tr>
<tr><td>22,5</td><td>34</td><td>53</td><td>123</td><td>145</td><td>141</td><td>144</td><td>140</td><td>143</td><td>95</td><td>28</td></tr>
<tr><td>60</td><td>105</td><td>37</td><td>94</td><td>11</td><td>112</td><td>11</td><td>109</td><td>111</td><td>75</td><td>23</td></tr>
<tr><td>22,5</td><td>139</td><td>2</td><td>2</td><td>2</td><td>2</td><td>2</td><td>2</td><td>2</td><td>2</td><td>2</td></tr>
<tr><td colspan="11">INTEGRATED CENTRAL LAMP - 265 nm</td></tr>
<tr><td></td><td>Dev. [mm]</td><td>13,5</td><td>36,5</td><td>100</td><td>100</td><td>75</td><td>75</td><td>100</td><td>100</td><td>36,5</td></tr>
<tr><td>Dev. [mm]</td><td>Dist. [mm]</td><td>14</td><td>50</td><td>150</td><td>250</td><td>325</td><td>400</td><td>500</td><td>600</td><td>637</td></tr>
<tr><td>22,5</td><td>34</td><td>19</td><td>35</td><td>50</td><td>50</td><td>50</td><td>50</td><td>51</td><td>35</td><td>16</td></tr>
<tr><td>60</td><td>105</td><td>64</td><td>130</td><td>179</td><td>181</td><td>179</td><td>181</td><td>182</td><td>124</td><td>57</td></tr>
<tr><td>22,5</td><td>139</td><td>16</td><td>28</td><td>39</td><td>39</td><td>38</td><td>39</td><td>38</td><td>26</td><td>14</td></tr>
<tr><td colspan="11">INTEGRATED LOWER LAMP - 275 nm</td></tr>
<tr><td></td><td>Scost. [mm]</td><td>13,5</td><td>36,5</td><td>100</td><td>100</td><td>75</td><td>75</td><td>100</td><td>100</td><td>36,5</td></tr>
<tr><td>Dev. [mm]</td><td>Dist. [mm]</td><td>14</td><td>50</td><td>150</td><td>250</td><td>325</td><td>400</td><td>500</td><td>600</td><td>637</td></tr>
<tr><td>22,5</td><td>34</td><td>2</td><td>2</td><td>2</td><td>2</td><td>2</td><td>2</td><td>2</td><td>2</td><td>2</td></tr>
<tr><td>60</td><td>105</td><td>51</td><td>102</td><td>119</td><td>115</td><td>115</td><td>119</td><td>119</td><td>72</td><td>19</td></tr>
<tr><td>22,5</td><td>139</td><td>65</td><td>137</td><td>157</td><td>156</td><td>154</td><td>160</td><td>160</td><td>96</td><td></td></tr>
</table>

The relative errors, reported in Table 7, were calculated, specifically by computing the difference between the values declared by C-LED and those measured by us and then dividing the result by the value we measured.

Table 8: Relative errors between integrated measured and manufacturer's values.

	8 cm upper lamp	11cm central lamp	8 cm lower lamp
Point 1	68%	47%	64%
Point 2	64%	40%	62%
Point 3	76%	57%	67%

As can be observed, the difference is substantial, which initially led us to believe there might be an issue with the sensor we used. However, this hypothesis was dismissed when the manufacturer allowed us to perform measurements on our device using the same photosensor they employed for their irradiance measurements. The discrepancy observed in this case was, at most, an 11% deviation between the values recorded by the company's sensor and those previously measured by us.

These discrepancies raise questions about the origin of the error, which may stem either from an overestimation by the manufacturer or from limitations in our experimental procedure. Although different photosensors were used, the internal consistency of our measurements suggests that the cause cannot be attributed solely to the instruments or to the declared data.

4.2 Second Measurement Campaign

The sources considered are incoherent sources, meaning that the phase fluctuations between two sources are statistically distributed. As a result, what is observed is the sum of the intensities of the two fields, since the interference term has an average value of zero [118].

To analyse the behaviour of the device in more detail, also in order to be able to make precise assessments about the effects of configuration changes, it was evaluated whether it is indeed possible to apply the principle of superposition within the device.

For this purpose, initial irradiance maps were obtained for the following configurations:

- Only the central lamp on
- Only the upper lamp on
- Only the lower lamp on
- All lamps on

The results are shown below using a colour scale, where:

- Red corresponds to the maximum value in all configurations
- Green corresponds to the minimum value detected

According to the following scale:

- Maximum value: 475 µW/cm²
- Minimum value: 0 µW/cm²

As expected, the maximum value was recorded when all three lamps were on, in the central region.

Central lamp on

The results are shown in Figure 22, where the left side displays an area (in green) that is significantly less illuminated than the right side. This can be explained by the fact that, during the single LED measurements, four sources, all part of the same module and located at the beginning of the bar, were burnt out. Specifically, the affected sources were LEDs number 1, 3, 5, and 7.

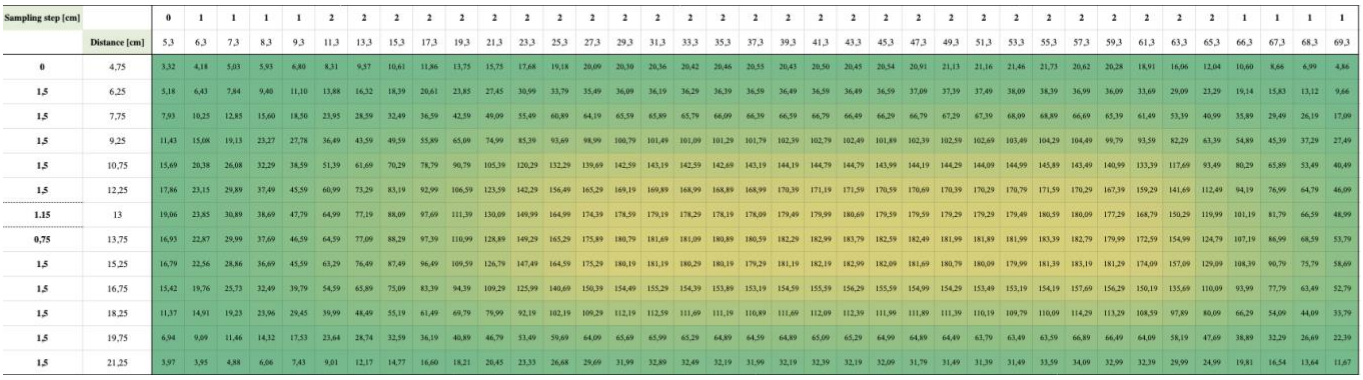

Sampling step [cm]		0	1	1	1	1	2	2	2	2	2	2	2	2	2	2	2	2	2	2	2	2	2	2	2	2	2	2	2	2	2	2	2	2	1	1	1	1
	Distance [cm]	5,3	6,3	7,3	8,3	9,3	11,3	13,3	15,3	17,3	19,3	21,3	23,3	25,3	27,3	29,3	31,3	33,3	35,3	37,3	39,3	41,3	43,3	45,3	47,3	49,3	51,3	53,3	55,3	57,3	59,3	61,3	63,3	65,3	66,3	67,3	68,3	69,3
0	4,75	3,32	4,18	5,03	5,93	6,80	8,31	9,57	10,61	11,86	13,75	15,75	17,68	19,18	20,09	20,30	20,36	20,42	20,46	20,55	20,43	20,50	20,45	20,54	20,91	21,13	21,16	21,46	21,73	20,62	20,28	18,91	16,06	12,04	10,60	8,66	6,99	4,86
1,5	6,25	5,18	6,43	7,84	9,40	11,10	13,88	16,32	18,39	20,61	23,85	27,45	30,99	33,79	35,49	36,09	36,19	36,29	36,39	36,59	36,49	36,59	36,49	36,59	37,09	37,39	37,49	38,09	38,39	36,99	36,09	33,69	29,09	23,29	19,14	15,83	13,12	9,66
1,5	7,75	7,93	10,25	12,85	15,60	18,50	23,95	28,59	32,49	36,59	42,59	49,09	55,49	60,89	64,19	65,59	65,89	65,79	66,09	66,39	66,59	66,79	66,49	66,29	66,79	67,29	67,39	68,09	68,89	66,69	65,39	61,49	53,39	40,99	35,89	29,49	26,19	17,09
1,5	9,25	11,43	15,08	19,13	23,27	27,78	36,49	43,59	49,59	55,89	65,09	74,99	85,39	93,69	98,99	100,79	101,49	101,09	101,29	101,79	102,39	102,79	102,49	101,89	102,39	102,59	102,69	103,49	104,29	104,49	99,79	93,59	82,29	63,39	54,89	45,39	37,29	27,49
1,5	10,75	15,69	20,38	26,08	32,29	38,59	51,39	61,69	70,29	78,79	90,79	105,39	120,29	132,29	139,69	142,59	143,19	142,59	142,69	143,19	144,19	144,79	144,79	143,99	144,19	144,29	144,09	144,99	145,89	143,49	140,99	133,39	117,69	93,49	80,29	65,89	53,49	40,49
1,5	12,25	17,86	23,15	29,89	37,49	45,59	60,99	73,29	83,19	92,99	106,59	123,59	142,29	156,49	165,29	169,19	169,89	168,99	168,89	168,99	170,39	171,19	171,59	170,59	170,69	170,39	170,29	170,79	171,59	170,29	167,39	159,29	141,69	112,49	94,19	76,99	64,79	46,09
1.15	13	19,06	23,85	30,89	38,69	47,79	64,99	77,19	88,09	97,69	111,39	130,09	149,99	164,99	174,39	178,59	179,19	178,29	178,19	178,09	179,49	179,99	180,69	179,59	179,59	179,29	179,29	179,49	180,59	180,09	177,29	168,79	150,29	119,99	101,19	81,79	66,59	48,99
0,75	13,75	16,93	22,87	29,99	37,69	46,59	64,59	77,09	88,29	97,39	110,99	128,89	149,29	165,29	175,89	180,79	181,69	181,09	180,89	180,59	182,29	182,99	183,79	182,59	182,49	181,99	181,89	181,99	183,39	182,79	179,99	172,59	154,99	124,79	107,19	86,99	68,59	53,79
1,5	15,25	16,79	22,56	28,86	36,69	45,59	63,29	76,49	87,49	96,49	109,59	126,79	147,49	164,59	175,29	180,19	181,19	180,29	180,19	179,29	181,19	182,19	182,99	182,09	181,69	180,79	180,09	179,99	181,39	183,19	181,29	174,09	157,09	129,09	108,39	90,79	75,79	58,69
1,5	16,75	15,42	19,76	25,73	32,49	39,79	54,59	65,89	75,09	83,39	94,39	109,29	125,99	140,69	150,39	154,49	155,29	154,39	153,89	153,19	154,59	155,59	156,29	155,59	154,99	154,29	153,49	153,19	154,19	157,69	156,29	150,19	135,69	110,09	93,99	77,79	63,49	52,79
1,5	18,25	11,37	14,91	19,23	23,96	29,45	39,99	48,49	55,19	61,49	69,79	79,99	92,19	102,19	109,29	112,19	112,59	111,69	111,19	110,89	111,69	112,09	112,39	111,99	111,89	111,39	110,19	109,79	110,09	114,29	113,29	108,59	97,89	80,09	66,29	54,09	44,09	33,79
1,5	19,75	6,94	9,09	11,46	14,32	17,53	23,64	28,74	32,59	36,19	40,89	46,79	53,49	59,69	64,09	65,69	65,99	65,29	64,89	64,59	64,89	65,09	65,29	64,99	64,89	64,49	63,79	63,49	63,59	66,89	66,49	64,09	58,19	47,69	38,89	32,29	26,69	22,39
1,5	21,25	3,97	3,95	4,88	6,06	7,43	9,01	12,17	14,77	16,60	18,21	20,45	23,33	26,68	29,69	31,99	32,89	32,49	32,19	31,99	32,19	32,39	32,19	32,09	31,79	31,49	31,39	31,49	33,59	34,09	32,99	32,39	29,99	24,99	19,81	16,54	13,64	11,67

Figure 22: Irradiance map [uW/cm²] caused by the central lamp.

Upper lamp on

The results are shown in Figure 23. Unfortunately, for this lamp as well, the shielding setup used for single-LED measurements led to the deterioration of four LEDs located at the far-right end of the lamp, specifically, those positioned at 25, 27, 29, and 31. As a result, an asymmetry in the irradiance map can also be observed in this case.

It can also be noted that the maximum irradiance (indicated by a much more intense yellow tone) corresponds to the 9.5 cm coordinate, which matches the position of the source.

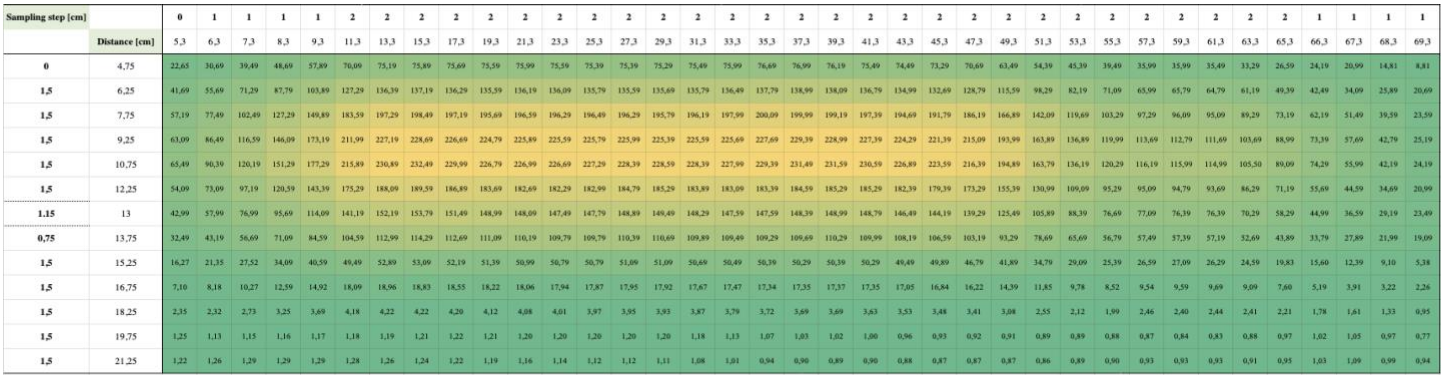

Sampling step [cm]		0	1	1	1	1	2	2	2	2	2	2	2	2	2	2	2	2	2	2	2	2	2	2	2	2	2	2	2	2	2	2	2	2	1	1	1	1
	Distance [cm]	5,3	6,3	7,3	8,3	9,3	11,3	13,3	15,3	17,3	19,3	21,3	23,3	25,3	27,3	29,3	31,3	33,3	35,3	37,3	39,3	41,3	43,3	45,3	47,3	49,3	51,3	53,3	55,3	57,3	59,3	61,3	63,3	65,3	66,3	67,3	68,3	69,3
0	4,75	22,65	30,69	39,49	48,69	57,89	70,09	75,19	75,89	75,69	75,59	75,99	75,59	75,39	75,39	75,29	75,49	75,99	76,69	76,99	76,19	75,49	74,49	73,29	70,69	63,49	54,39	45,39	39,49	35,99	35,99	35,49	33,29	26,59	24,19	20,99	14,81	8,81
1,5	6,25	41,69	55,69	71,29	87,79	103,89	127,29	136,39	137,19	136,29	135,59	136,19	136,09	135,79	135,59	135,69	135,79	136,49	137,79	138,99	138,09	136,79	134,99	132,69	128,79	115,59	98,29	82,19	71,09	65,99	65,79	64,79	61,19	49,39	42,49	34,09	25,89	20,69
1,5	7,75	57,19	77,49	102,49	127,29	149,89	183,59	197,29	198,49	197,19	195,69	196,59	196,29	196,49	196,29	195,79	196,19	197,99	200,09	199,99	199,19	197,39	194,69	191,79	186,19	166,89	142,09	119,69	103,29	97,29	96,09	95,09	89,29	73,19	62,19	51,49	39,59	23,59
1,5	9,25	63,09	86,49	116,59	146,09	173,19	211,99	227,19	228,69	226,69	224,79	225,89	225,59	225,79	225,99	225,39	225,59	225,69	227,69	229,39	228,99	227,39	224,29	221,39	215,09	193,99	163,89	136,89	119,99	113,69	112,79	111,69	103,69	88,99	73,39	57,69	42,79	25,19
1,5	10,75	65,49	90,39	120,19	151,29	177,29	215,89	230,89	232,49	229,99	226,79	226,99	226,69	227,29	228,39	228,59	228,39	227,99	229,39	231,49	231,59	230,59	226,89	223,59	216,39	194,89	163,79	136,19	120,29	116,19	115,99	114,99	105,50	89,09	74,29	55,99	42,19	24,19
1,5	12,25	54,09	73,09	97,19	120,59	143,39	175,29	188,09	189,59	186,89	183,69	182,69	182,29	182,99	184,79	185,29	183,89	183,09	183,39	184,59	185,29	185,29	182,39	179,39	173,29	155,39	130,99	109,09	95,29	95,09	94,79	93,69	86,29	71,19	55,69	44,59	34,69	20,99
1.15	13	42,99	57,99	76,99	95,69	114,09	141,19	152,19	153,79	151,49	148,99	148,09	147,49	147,79	148,89	149,49	148,29	147,59	147,59	148,39	148,99	148,79	146,49	144,19	139,29	125,49	105,89	88,39	76,69	77,09	76,39	76,39	70,29	58,29	44,99	36,59	29,19	23,49
0,75	13,75	32,49	43,19	56,69	71,09	84,59	104,59	112,99	114,29	112,69	111,09	110,19	109,79	109,79	110,39	110,69	109,89	109,49	109,29	109,69	110,29	109,99	108,19	106,59	103,19	93,29	78,69	65,69	56,79	57,49	57,39	57,19	52,69	43,89	33,79	27,89	21,99	19,09
1,5	15,25	16,27	21,35	27,52	34,09	40,59	49,49	52,89	53,09	52,19	51,39	50,99	50,79	50,79	51,09	51,09	50,69	50,49	50,39	50,29	50,39	50,29	49,49	49,89	46,79	41,89	34,79	29,09	25,39	26,59	27,09	26,29	24,59	19,83	15,60	12,39	9,10	5,38
1,5	16,75	7,10	8,18	10,27	12,59	14,92	18,09	18,96	18,83	18,55	18,22	18,06	17,94	17,87	17,95	17,92	17,67	17,47	17,34	17,35	17,37	17,35	17,05	16,84	16,22	14,39	11,85	9,78	8,52	9,54	9,59	9,69	9,09	7,60	5,19	3,91	3,22	2,26
1,5	18,25	2,35	2,32	2,73	3,25	3,69	4,18	4,22	4,22	4,20	4,12	4,08	4,01	3,97	3,95	3,93	3,87	3,79	3,72	3,69	3,69	3,63	3,53	3,48	3,41	3,08	2,55	2,12	1,99	2,46	2,40	2,44	2,41	2,21	1,78	1,61	1,33	0,95
1,5	19,75	1,25	1,13	1,15	1,16	1,17	1,18	1,19	1,21	1,22	1,21	1,20	1,20	1,20	1,20	1,20	1,18	1,13	1,07	1,03	1,02	1,00	0,96	0,93	0,92	0,91	0,89	0,89	0,88	0,87	0,84	0,83	0,88	0,97	1,02	1,05	0,97	0,77
1,5	21,25	1,22	1,26	1,29	1,29	1,29	1,28	1,26	1,24	1,22	1,19	1,16	1,14	1,12	1,12	1,11	1,08	1,01	0,94	0,90	0,89	0,90	0,88	0,87	0,87	0,87	0,86	0,89	0,90	0,93	0,93	0,93	0,91	0,95	1,03	1,09	0,99	0,94

Figure 23: Irradiance map [uW/cm²] caused by the upper lamp.

Lower lamp on

The results are shown in Figure 24. As described in Chapter 2, the distances between the upper and lower bars relative to the central bar are not the same; in particular, the lower bar is positioned 1.5 cm farther away.

This explains the chromatic map in Figure 24, which shows a more intense yellow marking toward the lower wall and less toward the center, in contrast to the map for the upper lamp previously shown.

The maximum illuminance, in fact, does not occur at the 16.75 cm ordinate (which would correspond to a symmetrical position), but rather at 18.25 cm. At this coordinate, the sensor records a higher power because it is directly facing the light sources.

As with the upper lamp, the single-LED measurements for this lamp also led to the failure of four LEDs, which, as can be seen from the map, are located in the central-right area. Specifically, the malfunctioning LEDs are those in positions 18, 20, 22, and 24.

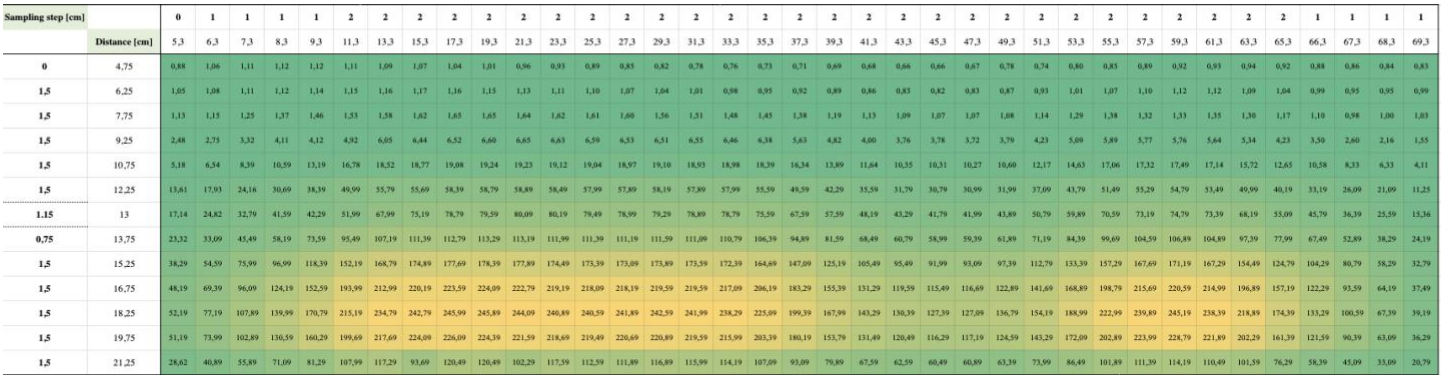

Sampling step [cm]		0	1	1	1	1	2	2	2	2	2	2	2	2	2	2	2	2	2	2	2	2	2	2	2	2	2	2	2	2	2	2	2	2	1	1	1	1
	Distance [cm]	5,3	6,3	7,3	8,3	9,3	11,3	13,3	15,3	17,3	19,3	21,3	23,3	25,3	27,3	29,3	31,3	33,3	35,3	37,3	39,3	41,3	43,3	45,3	47,3	49,3	51,3	53,3	55,3	57,3	59,3	61,3	63,3	65,3	66,3	67,3	68,3	69,3
0	4,75	0,88	1,06	1,11	1,12	1,12	1,11	1,09	1,07	1,04	1,01	0,96	0,93	0,89	0,85	0,82	0,78	0,76	0,73	0,71	0,69	0,68	0,66	0,66	0,67	0,78	0,74	0,80	0,85	0,89	0,92	0,93	0,94	0,92	0,88	0,86	0,84	0,83
1,5	6,25	1,05	1,08	1,11	1,12	1,14	1,15	1,16	1,17	1,16	1,15	1,13	1,11	1,10	1,07	1,04	1,01	0,98	0,95	0,92	0,89	0,86	0,83	0,82	0,83	0,87	0,93	1,01	1,07	1,10	1,12	1,12	1,09	1,04	0,99	0,95	0,95	0,99
1,5	7,75	1,13	1,15	1,25	1,37	1,46	1,53	1,58	1,62	1,65	1,65	1,64	1,62	1,61	1,60	1,56	1,51	1,48	1,45	1,38	1,19	1,13	1,09	1,07	1,07	1,08	1,14	1,29	1,38	1,32	1,33	1,35	1,30	1,17	1,10	0,98	1,00	1,03
1,5	9,25	2,48	2,75	3,32	4,11	4,12	4,92	6,05	6,44	6,52	6,60	6,65	6,63	6,59	6,53	6,51	6,55	6,46	6,38	5,63	4,82	4,00	3,76	3,78	3,72	3,79	4,23	5,09	5,89	5,77	5,76	5,64	5,34	4,23	3,50	2,60	2,16	1,55
1,5	10,75	5,18	6,54	8,39	10,59	13,19	16,78	18,52	18,77	19,08	19,24	19,23	19,12	19,04	18,97	19,10	18,93	18,98	18,39	16,34	13,89	11,64	10,35	10,31	10,27	10,60	12,17	14,63	17,06	17,32	17,49	17,14	15,72	12,65	10,58	8,33	6,33	4,11
1,5	12,25	13,61	17,93	24,16	30,69	38,39	49,99	55,79	55,69	58,39	58,79	58,89	58,49	57,99	57,89	58,19	57,89	57,99	55,59	49,59	42,29	35,59	31,79	30,79	30,99	31,99	37,09	43,79	51,49	55,29	54,79	53,49	49,99	40,19	33,19	26,09	21,09	11,25
1.15	13	17,14	24,82	32,79	41,59	42,29	51,99	67,99	75,19	78,79	79,59	80,09	80,19	79,49	78,99	79,29	78,89	78,79	75,59	67,59	57,59	48,19	43,29	41,79	41,99	43,89	50,79	59,89	70,59	73,19	74,79	73,39	68,19	55,09	45,79	36,39	25,59	15,36
0,75	13,75	23,32	33,09	45,49	58,19	73,59	95,49	107,19	111,39	112,79	113,29	113,19	111,99	111,39	111,19	111,59	111,09	110,79	106,39	94,89	81,59	68,49	60,79	58,99	59,39	61,89	71,19	84,39	99,69	104,59	106,89	104,89	97,39	77,99	67,49	52,89	38,29	24,19
1,5	15,25	38,29	54,59	75,99	96,99	118,39	152,19	168,79	174,89	177,69	178,39	177,89	174,49	173,39	173,09	173,89	173,59	172,39	164,69	147,09	125,19	105,49	95,49	91,99	93,09	97,39	112,79	133,39	157,29	167,69	171,19	167,29	154,49	124,79	104,29	80,79	58,29	32,79
1,5	16,75	48,19	69,39	96,09	124,19	152,59	193,99	212,99	220,19	223,59	224,09	222,79	219,19	218,09	218,19	219,59	219,59	217,09	206,19	183,29	155,39	131,29	119,59	115,49	116,69	122,89	141,69	168,89	198,79	215,69	220,59	214,99	196,89	157,19	122,29	93,59	64,19	37,49
1,5	18,25	52,19	77,19	107,89	139,99	170,79	215,19	234,79	242,79	245,99	245,89	244,09	240,89	240,59	241,89	242,59	241,99	238,29	225,09	199,39	167,99	143,29	130,39	127,39	127,09	136,79	154,19	188,99	222,99	239,89	245,19	238,39	218,89	174,39	133,29	100,59	67,39	39,19
1,5	19,75	51,19	73,99	102,89	130,59	160,29	199,69	217,69	224,09	226,09	224,39	221,59	218,69	219,49	220,69	220,89	219,59	215,99	203,39	180,19	153,79	131,49	120,49	116,29	117,19	124,59	143,29	172,09	202,89	223,99	228,79	221,89	202,29	161,39	121,59	90,39	63,09	36,29
1,5	21,25	28,62	40,89	55,89	71,09	81,29	107,99	117,29	93,69	120,49	120,49	102,29	117,59	112,59	111,89	116,89	115,99	114,19	107,09	93,09	79,89	67,59	62,59	60,49	60,89	63,39	73,99	86,49	101,89	111,39	114,19	110,49	101,59	76,29	58,39	45,09	33,09	20,79

Figure 24: Irradiance map [uW/cm²] caused by the lower lamp.

We report below the experimental map obtained with all three lamps turned on simultaneously:

Experimental map with all three lamps on simultaneously

The results are shown in Figure 25. Naturally, the map recorded with all three lamps operating at the same time is affected by the malfunction of the twelve LEDs, four from each lamp, previously mentioned.

Because of this, what we expect are irradiance maps that, especially in the central area, will not display a uniformly red tone.

Below, we present both the experimental and the reconstructed maps, which will later be compared. It is important to note that both maps share the same scale.

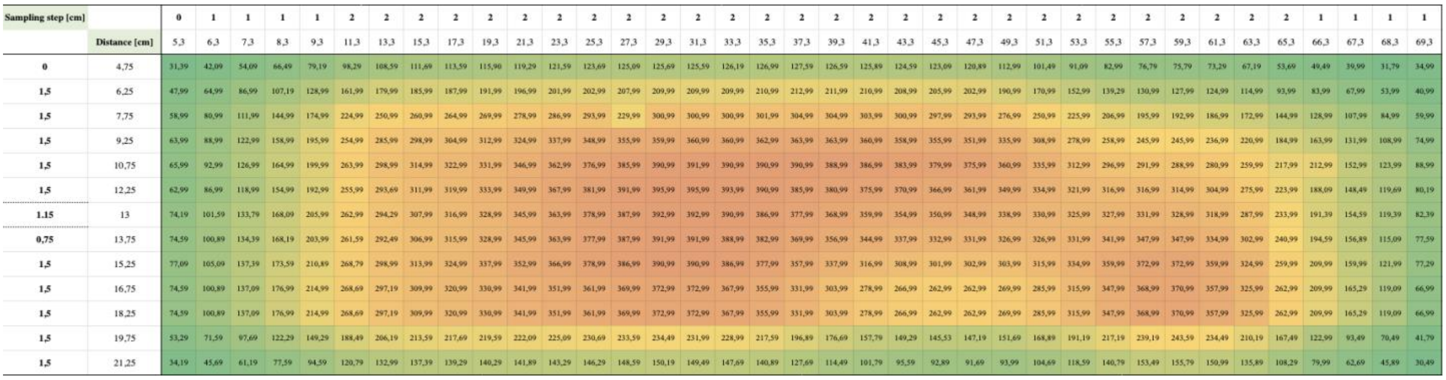

Sampling step [cm]		0	1	1	1	1	2	2	2	2	2	2	2	2	2	2	2	2	2	2	2	2	2	2	2	2	2	2	2	2	2	2	2	2	1	1	1	1
	Distance [cm]	5,3	6,3	7,3	8,3	9,3	11,3	13,3	15,3	17,3	19,3	21,3	23,3	25,3	27,3	29,3	31,3	33,3	35,3	37,3	39,3	41,3	43,3	45,3	47,3	49,3	51,3	53,3	55,3	57,3	59,3	61,3	63,3	65,3	66,3	67,3	68,3	69,3
0	4,75	31,39	42,09	54,09	66,49	79,19	98,29	108,59	111,69	113,59	115,90	119,29	121,59	123,69	125,09	125,69	125,59	126,19	126,99	127,59	126,59	125,89	124,59	123,09	120,89	112,99	101,49	91,09	82,99	76,79	75,79	73,29	67,19	53,69	49,49	39,99	31,79	34,99
1,5	6,25	47,99	64,99	86,99	107,19	128,99	161,99	179,99	185,99	187,99	191,99	196,99	201,99	202,99	207,99	209,99	209,99	209,99	210,99	212,99	211,99	210,99	208,99	205,99	202,99	190,99	170,99	152,99	139,29	130,99	127,99	124,99	114,99	93,99	83,99	67,99	53,99	40,99
1,5	7,75	58,99	80,99	111,99	144,99	174,99	224,99	250,99	260,99	264,99	269,99	278,99	286,99	293,99	229,99	300,99	300,99	300,99	301,99	304,99	304,99	303,99	300,99	297,99	293,99	276,99	250,99	225,99	206,99	195,99	192,99	186,99	172,99	144,99	128,99	107,99	84,99	59,99
1,5	9,25	63,99	88,99	122,99	158,99	195,99	254,99	285,99	298,99	304,99	312,99	324,99	337,99	348,99	355,99	359,99	360,99	360,99	362,99	363,99	363,99	360,99	358,99	355,99	351,99	335,99	308,99	278,99	258,99	245,99	245,99	236,99	220,99	184,99	163,99	131,99	108,99	74,99
1,5	10,75	65,99	92,99	126,99	164,99	199,99	263,99	298,99	314,99	322,99	331,99	346,99	362,99	376,99	385,99	390,99	391,99	390,99	390,99	390,99	388,99	386,99	383,99	379,99	375,99	360,99	335,99	312,99	296,99	291,99	288,99	280,99	259,99	217,99	212,99	152,99	123,99	88,99
1,5	12,25	62,99	86,99	118,99	154,99	192,99	255,99	293,69	311,99	319,99	333,99	349,99	367,99	381,99	391,99	395,99	395,99	393,99	390,99	385,99	380,99	375,99	370,99	366,99	361,99	349,99	334,99	321,99	316,99	316,99	314,99	304,99	275,99	223,99	188,09	148,49	119,69	80,19
1.15	13	74,19	101,59	133,79	168,09	205,99	262,99	294,29	307,99	316,99	328,99	345,99	363,99	378,99	387,99	392,99	392,99	390,99	386,99	377,99	368,99	359,99	354,99	350,99	348,99	338,99	330,99	325,99	327,99	331,99	328,99	318,99	287,99	233,99	191,39	154,59	119,39	82,39
0,75	13,75	74,59	100,89	134,39	168,19	203,99	261,59	292,49	306,99	315,99	328,99	345,99	363,99	377,99	387,99	391,99	391,99	388,99	382,99	369,99	356,99	344,99	337,99	332,99	331,99	326,99	326,99	331,99	341,99	347,99	347,99	334,99	302,99	240,99	194,59	156,89	115,09	77,59
1,5	15,25	77,09	105,09	137,39	173,59	210,89	268,79	298,99	313,99	324,99	337,99	352,99	366,99	378,99	386,99	390,99	390,99	386,99	377,99	357,99	337,99	316,99	308,99	301,99	302,99	303,99	315,99	334,99	359,99	372,99	372,99	359,99	324,99	259,99	209,99	159,99	121,99	77,29
1,5	16,75	74,59	100,89	137,09	176,99	214,99	268,69	297,19	309,99	320,99	330,99	341,99	351,99	361,99	369,99	372,99	372,99	367,99	355,99	331,99	303,99	278,99	266,99	262,99	262,99	269,99	285,99	315,99	347,99	368,99	370,99	357,99	325,99	262,99	209,99	165,29	119,09	66,99
1,5	18,25	74,59	100,89	137,09	176,99	214,99	268,69	297,19	309,99	320,99	330,99	341,99	351,99	361,99	369,99	372,99	372,99	367,99	355,99	331,99	303,99	278,99	266,99	262,99	262,99	269,99	285,99	315,99	347,99	368,99	370,99	357,99	325,99	262,99	209,99	165,29	119,09	66,99
1,5	19,75	53,29	71,59	97,69	122,29	149,29	188,49	206,19	213,59	217,69	219,59	222,09	225,09	230,69	233,59	234,49	231,99	228,99	217,59	196,89	176,69	157,79	149,29	145,53	147,19	151,69	168,89	191,19	217,19	239,19	243,59	234,49	210,19	167,49	122,99	93,49	70,49	41,79
1,5	21,25	34,19	45,69	61,19	77,59	94,59	120,79	132,99	137,39	139,29	140,29	141,89	143,29	146,29	148,59	150,19	149,49	147,69	140,89	127,69	114,49	101,79	95,59	92,89	91,69	93,99	104,69	118,59	140,79	153,49	155,79	150,99	135,89	108,29	79,99	62,69	45,89	30,49

Figure 25: Irradiance map [uW/cm²] caused by three lamps lit simultaneously.

Reconstructed Map with Three Lamps On

In order to verify that the system within the device is linear, and therefore that it is possible to apply the principle of superposition of effects, the map corresponding to three lamps turned on was reconstructed as the sum of the maps obtained with the individual bars. This reconstructed map was then compared with the experimentally measured map with three lamps on.

The results are shown in Figure 26.

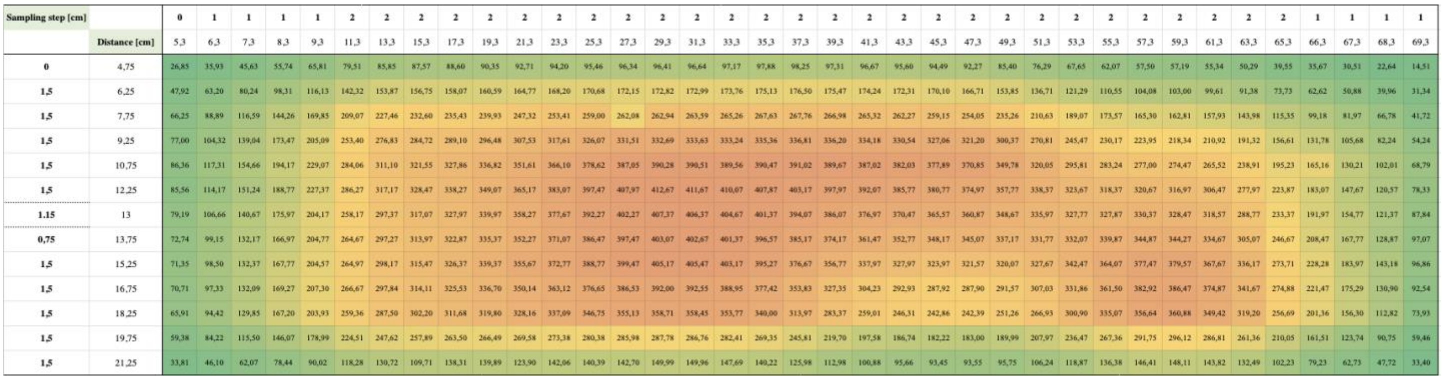

Sampling step [cm]		0	1	1	1	1	2	2	2	2	2	2	2	2	2	2	2	2	2	2	2	2	2	2	2	2	2	2	2	2	2	2	2	2	1	1	1	1
	Distance [cm]	5,3	6,3	7,3	8,3	9,3	11,3	13,3	15,3	17,3	19,3	21,3	23,3	25,3	27,3	29,3	31,3	33,3	35,3	37,3	39,3	41,3	43,3	45,3	47,3	49,3	51,3	53,3	55,3	57,3	59,3	61,3	63,3	65,3	66,3	67,3	68,3	69,3
0	4,75	26,85	35,93	45,63	55,74	65,81	79,51	85,85	87,57	88,60	90,35	92,71	94,20	95,46	96,34	96,41	96,64	97,17	97,88	98,25	97,31	96,67	95,60	94,49	92,27	85,40	76,29	67,65	62,07	57,50	57,19	55,34	50,29	39,55	35,67	30,51	22,64	14,51
1,5	6,25	47,92	63,20	80,24	98,31	116,13	142,32	153,87	156,75	158,07	160,59	164,77	168,20	170,68	172,15	172,82	172,99	173,76	175,13	176,50	175,47	174,24	172,31	170,10	166,71	153,85	136,71	121,29	110,55	104,08	103,00	99,61	91,38	73,73	62,62	50,88	39,96	31,34
1,5	7,75	66,25	88,89	116,59	144,26	169,85	209,07	227,46	232,60	235,43	239,93	247,32	253,41	259,00	262,08	262,94	263,59	265,26	267,63	267,76	266,98	265,32	262,27	259,15	254,05	235,26	210,63	189,07	173,57	165,30	162,81	157,93	143,98	115,35	99,18	81,97	66,78	41,72
1,5	9,25	77,00	104,32	139,04	173,47	205,09	253,40	276,83	284,72	289,10	296,48	307,53	317,61	326,07	331,51	332,69	333,63	333,24	335,36	336,81	336,20	334,18	330,54	327,06	321,20	300,37	270,81	245,47	230,17	223,95	218,34	210,92	191,32	156,61	131,78	105,68	82,24	54,24
1,5	10,75	86,36	117,31	154,66	194,17	229,07	284,06	311,10	321,55	327,86	336,82	351,61	366,10	378,62	387,05	390,28	390,51	389,56	390,47	391,02	389,67	387,02	382,03	377,89	370,85	349,78	320,05	295,81	283,24	277,00	274,47	265,52	238,91	195,23	165,16	130,21	102,01	68,79
1,5	12,25	85,56	114,17	151,24	188,77	227,37	286,27	317,17	328,47	338,27	349,07	365,17	383,07	397,47	407,97	412,67	411,67	410,07	407,87	403,17	397,97	392,07	385,77	380,77	374,97	357,77	338,37	323,67	318,37	320,67	316,97	306,47	277,97	223,87	183,07	147,67	120,57	78,33
1.15	13	79,19	106,66	140,67	175,97	204,17	258,17	297,37	317,07	327,97	339,97	358,27	377,67	392,27	402,27	407,37	406,37	404,67	401,37	394,07	386,07	376,97	370,47	365,57	360,87	348,67	335,97	327,77	327,87	330,37	328,47	318,57	288,77	233,37	191,97	154,77	121,37	87,84
0,75	13,75	72,74	99,15	132,17	166,97	204,77	264,67	297,27	313,97	322,87	335,37	352,27	371,07	386,47	397,47	403,07	402,67	401,37	396,57	385,17	374,17	361,47	352,77	348,17	345,07	337,17	331,77	332,07	339,87	344,87	344,27	334,67	305,07	246,67	208,47	167,77	128,87	97,07
1,5	15,25	71,35	98,50	132,37	167,77	204,57	264,97	298,17	315,47	326,37	339,37	355,67	372,77	388,77	399,47	405,17	405,47	403,17	395,27	376,67	356,77	337,97	327,97	323,97	321,57	320,07	327,67	342,47	364,07	377,47	379,57	367,67	336,17	273,71	228,28	183,97	143,18	96,86
1,5	16,75	70,71	97,33	132,09	169,27	207,30	266,67	297,84	314,11	325,53	336,70	350,14	363,12	376,65	386,53	392,00	392,55	388,95	377,42	353,83	327,35	304,23	292,93	287,92	287,90	291,57	307,03	331,86	361,50	382,92	386,47	374,87	341,67	274,88	221,47	175,29	130,90	92,54
1,5	18,25	65,91	94,42	129,85	167,20	203,93	259,36	287,50	302,20	311,68	319,80	328,16	337,09	346,75	355,13	358,71	358,45	353,77	340,00	313,97	283,37	259,01	246,31	242,86	242,39	251,26	266,93	300,90	335,07	356,64	360,88	349,42	319,20	256,69	201,36	156,30	112,82	73,93
1,5	19,75	59,38	84,22	115,50	146,07	178,99	224,51	247,62	257,89	263,50	266,49	269,58	273,38	280,38	285,98	287,78	286,76	282,41	269,35	245,81	219,70	197,58	186,74	182,22	183,00	189,99	207,97	236,47	267,36	291,75	296,12	286,81	261,36	210,05	161,51	123,74	90,75	59,46
1,5	21,25	33,81	46,10	62,07	78,44	90,02	118,28	130,72	109,71	138,31	139,89	123,90	142,06	140,39	142,70	149,99	149,96	147,69	140,22	125,98	112,98	100,88	95,66	93,45	93,55	95,75	106,24	118,87	136,38	146,41	148,11	143,82	132,49	102,23	79,23	62,73	47,72	33,40

Figure 26: Irradiance map [uW/cm²] caused by three lamps lit simultaneously reconstructed from maps of single lamps lit.

A more or less similar distribution can be observed in the reconstructed map, with a certain chromatic symmetry, aside from a few slightly more intense small areas. Considering that the Δy between the upper and lower bars relative to the central one is not the same, we can observe in the maps shown in Figures 25 and 26 how the reflection phenomena have a positive influence, with the area near the lower wall displaying a more intense coloration compared to the upper one. Following the visual comparison, a quantitative analysis was carried out, including an evaluation of the relative error between the two cases.

$$\varepsilon = \frac{reconstructed\ value\ -\ experimental\ value}{experimental\ value} \tag{4.2.1}$$

By setting a color scale in which the maximum value is equal to 1 and the minimum value is equal to zero, highlighted respectively in red and green, the result shown in Figure 27 is obtained.

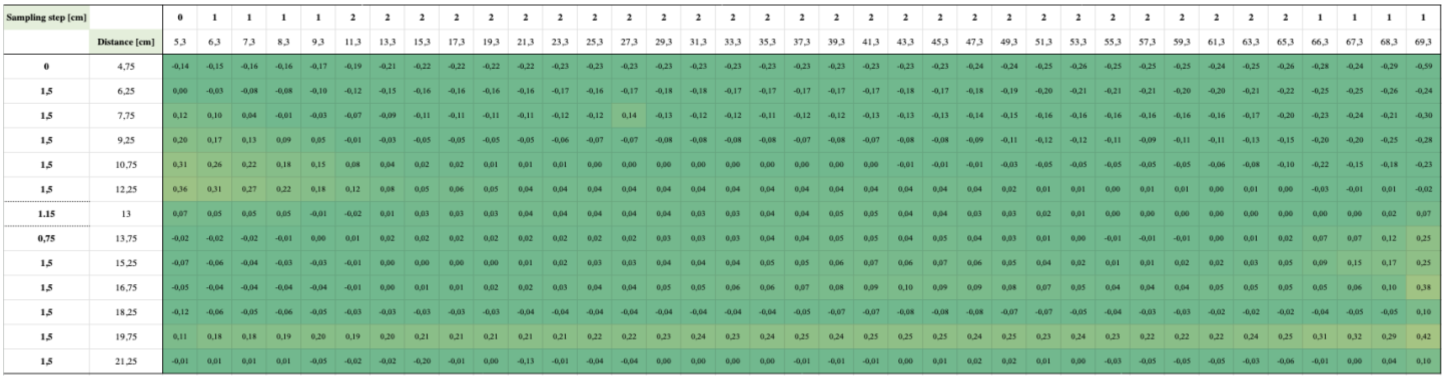

Sampling step [cm]		0	1	1	1	1	2	2	2	2	2	2	2	2	2	2	2	2	2	2	2	2	2	2	2	2	2	2	2	2	2	2	2	2	1	1	1	1
	Distance [cm]	5,3	6,3	7,3	8,3	9,3	11,3	13,3	15,3	17,3	19,3	21,3	23,3	25,3	27,3	29,3	31,3	33,3	35,3	37,3	39,3	41,3	43,3	45,3	47,3	49,3	51,3	53,3	55,3	57,3	59,3	61,3	63,3	65,3	66,3	67,3	68,3	69,3
0	4,75	-0,14	-0,15	-0,16	-0,16	-0,17	-0,19	-0,21	-0,22	-0,22	-0,22	-0,22	-0,23	-0,23	-0,23	-0,23	-0,23	-0,23	-0,23	-0,23	-0,23	-0,23	-0,23	-0,23	-0,24	-0,24	-0,25	-0,26	-0,25	-0,25	-0,25	-0,24	-0,25	-0,26	-0,28	-0,24	-0,29	-0,59
1,5	6,25	0,00	-0,03	-0,08	-0,08	-0,10	-0,12	-0,15	-0,16	-0,16	-0,16	-0,16	-0,17	-0,16	-0,17	-0,18	-0,18	-0,17	-0,17	-0,17	-0,17	-0,17	-0,18	-0,17	-0,18	-0,19	-0,20	-0,21	-0,21	-0,21	-0,20	-0,20	-0,21	-0,22	-0,25	-0,25	-0,26	-0,24
1,5	7,75	0,12	0,10	0,04	-0,01	-0,03	-0,07	-0,09	-0,11	-0,11	-0,11	-0,11	-0,12	-0,12	0,14	-0,13	-0,12	-0,12	-0,11	-0,12	-0,12	-0,13	-0,13	-0,13	-0,14	-0,15	-0,16	-0,16	-0,16	-0,16	-0,16	-0,16	-0,17	-0,20	-0,23	-0,24	-0,21	-0,30
1,5	9,25	0,20	0,17	0,13	0,09	0,05	-0,01	-0,03	-0,05	-0,05	-0,05	-0,05	-0,06	-0,07	-0,07	-0,08	-0,08	-0,08	-0,08	-0,07	-0,08	-0,07	-0,08	-0,08	-0,09	-0,11	-0,12	-0,12	-0,11	-0,09	-0,11	-0,11	-0,13	-0,15	-0,20	-0,20	-0,25	-0,28
1,5	10,75	0,31	0,26	0,22	0,18	0,15	0,08	0,04	0,02	0,02	0,01	0,01	0,01	0,00	0,00	0,00	0,00	0,00	0,00	0,00	0,00	0,00	-0,01	-0,01	-0,01	-0,03	-0,05	-0,05	-0,05	-0,05	-0,05	-0,06	-0,08	-0,10	-0,22	-0,15	-0,18	-0,23
1,5	12,25	0,36	0,31	0,27	0,22	0,18	0,12	0,08	0,05	0,06	0,05	0,04	0,04	0,04	0,04	0,04	0,04	0,04	0,04	0,04	0,04	0,04	0,04	0,04	0,04	0,02	0,01	0,01	0,00	0,01	0,01	0,00	0,01	0,00	-0,03	-0,01	0,01	-0,02
1.15	13	0,07	0,05	0,05	0,05	-0,01	-0,02	0,01	0,03	0,03	0,03	0,04	0,04	0,04	0,04	0,04	0,03	0,03	0,04	0,04	0,05	0,05	0,04	0,04	0,03	0,03	0,02	0,01	0,00	0,00	0,00	0,00	0,00	0,00	0,00	0,00	0,02	0,07
0,75	13,75	-0,02	-0,02	-0,02	-0,01	0,00	0,01	0,02	0,02	0,02	0,02	0,02	0,02	0,02	0,02	0,03	0,03	0,03	0,04	0,04	0,05	0,05	0,04	0,05	0,04	0,03	0,01	0,00	-0,01	-0,01	-0,01	0,00	0,01	0,02	0,07	0,07	0,12	0,25
1,5	15,25	-0,07	-0,06	-0,04	-0,03	-0,03	-0,01	0,00	0,00	0,00	0,00	0,01	0,02	0,03	0,03	0,04	0,04	0,04	0,05	0,05	0,06	0,07	0,06	0,07	0,06	0,05	0,04	0,02	0,01	0,01	0,02	0,02	0,03	0,05	0,09	0,15	0,17	0,25
1,5	16,75	-0,05	-0,04	-0,04	-0,04	-0,04	-0,01	0,00	0,01	0,01	0,02	0,02	0,03	0,04	0,04	0,05	0,05	0,06	0,06	0,07	0,08	0,09	0,10	0,09	0,09	0,08	0,07	0,05	0,04	0,04	0,04	0,05	0,05	0,05	0,05	0,06	0,10	0,38
1,5	18,25	-0,12	-0,06	-0,05	-0,06	-0,05	-0,03	-0,03	-0,03	-0,03	-0,03	-0,04	-0,04	-0,04	-0,04	-0,04	-0,04	-0,04	-0,04	-0,05	-0,07	-0,07	-0,08	-0,08	-0,08	-0,07	-0,07	-0,05	-0,04	-0,03	-0,03	-0,02	-0,02	-0,02	-0,04	-0,05	-0,05	0,10
1,5	19,75	0,11	0,18	0,18	0,19	0,20	0,19	0,20	0,21	0,21	0,21	0,21	0,21	0,22	0,22	0,23	0,24	0,23	0,24	0,25	0,24	0,25	0,25	0,25	0,24	0,25	0,23	0,24	0,23	0,22	0,22	0,22	0,24	0,25	0,31	0,32	0,29	0,42
1,5	21,25	-0,01	0,01	0,01	0,01	-0,05	-0,02	-0,02	-0,20	-0,01	0,00	-0,13	-0,01	-0,04	-0,04	0,00	0,00	0,00	0,00	-0,01	-0,01	-0,01	0,00	0,01	0,02	0,02	0,01	0,00	-0,03	-0,05	-0,05	-0,05	-0,03	-0,06	-0,01	0,00	0,04	0,10

Figure 27: Relative error between reconstructed and experimental.

Within the map, the error between the reconstruction and the experimental data does not exceed 8%.

In the upper right area and along an entire strip in the lower part, an error ranging between 10% and

30% is observed.

There are isolated points, mainly located on the sides, where the error reaches 40%, and one measurement point in the upper right corner where an error of 59% is recorded. To better assess the actual impact of reflection phenomena, whether positive or negative, on irradiance levels, further reconstructed maps were produced.

4.2.1 Single – LED measurements

Following the acquisition of experimental illuminance measurements under both single-lamp and three-lamp simultaneous activation conditions, additional measurements were conducted with only one lamp switched on, in order to gain a deeper understanding of the internal photometric behavior of the system. Specifically, for a lamp equipped with 32 discrete light sources, as shown in figure 29, the illuminance contribution of the first, the last, and the central source was measured for the central lamp and the first and the central source for the upper and lower lamp.

These measurements were systematically repeated for each of the three lamps, enabling a comparative analysis of the spatial distribution of luminous flux along the lamp axis. To support this analysis, the corresponding illuminance maps for the different activation configurations are reported below.

It should be noted that, compared to the previously reported maps obtained under three-lamp activation, the color scale used in the present case is not aligned with the former. This is due to the significantly lower peak illuminance values observed when only a single source is active, which would otherwise result in maps with insufficient contrast and unreadable spatial information.

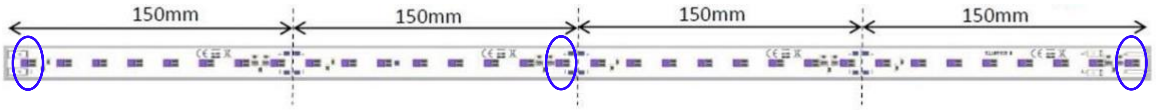

Figure 28: Position of the sources 1 - 16 – 32.

The results are presented below using a color scale in which red corresponds to the maximum value in all cases considered and green represents the minimum value.

Central Lamp

The results are shown in Figures 29, 30, and 31.

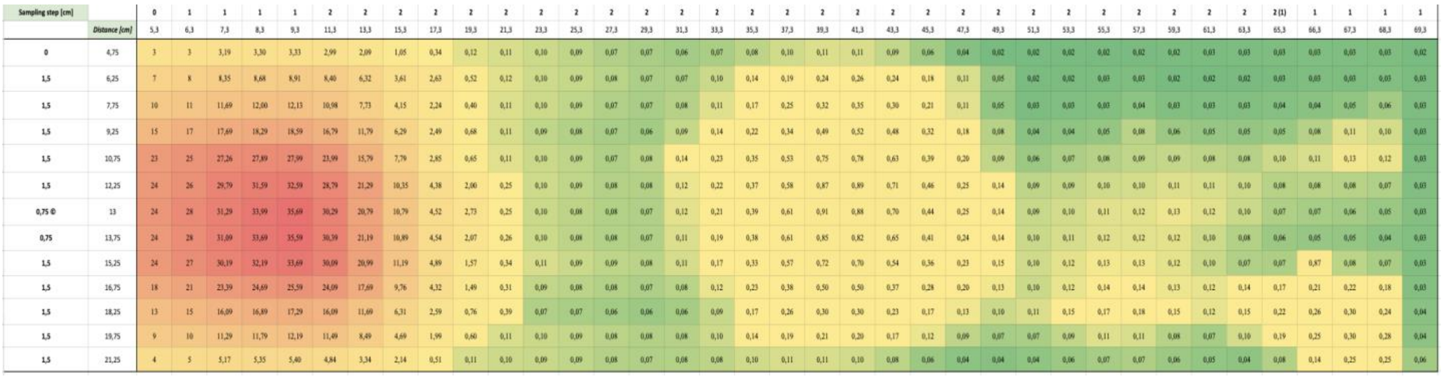

Sampling step [cm]		0	1	1	1	1	2	2	2	2	2	2	2	2	2	2	2	2	2	2	2	2	2	2	2	2	2	2	2	2	2	2	2	2 (1)	1	1	1	1
	Distance [cm]	5,3	6,3	7,3	8,3	9,3	11,3	13,3	15,3	17,3	19,3	21,3	23,3	25,3	27,3	29,3	31,3	33,3	35,3	37,3	39,3	41,3	43,3	45,3	47,3	49,3	51,3	53,3	55,3	57,3	59,3	61,3	63,3	65,3	66,3	67,3	68,3	69,3
0	4,75	3	3	3,19	3,30	3,33	2,99	2,09	1,05	0,34	0,12	0,11	0,10	0,09	0,07	0,07	0,06	0,07	0,08	0,10	0,11	0,11	0,09	0,06	0,04	0,02	0,02	0,02	0,02	0,02	0,02	0,03	0,03	0,03	0,03	0,03	0,03	0,02
1,5	6,25	7	8	8,35	8,68	8,91	8,40	6,32	3,61	2,63	0,52	0,12	0,10	0,09	0,08	0,07	0,07	0,10	0,14	0,19	0,24	0,26	0,24	0,18	0,11	0,05	0,02	0,02	0,03	0,03	0,02	0,02	0,02	0,03	0,03	0,03	0,03	0,03
1,5	7,75	10	11	11,69	12,00	12,13	10,98	7,73	4,15	2,24	0,40	0,11	0,10	0,09	0,07	0,07	0,08	0,11	0,17	0,25	0,32	0,35	0,30	0,21	0,11	0,05	0,03	0,03	0,03	0,04	0,03	0,03	0,03	0,04	0,04	0,05	0,06	0,03
1,5	9,25	15	17	17,69	18,29	18,59	16,79	11,79	6,29	2,49	0,68	0,11	0,09	0,08	0,07	0,06	0,09	0,14	0,22	0,34	0,49	0,52	0,48	0,32	0,18	0,08	0,04	0,04	0,05	0,08	0,06	0,05	0,05	0,05	0,08	0,11	0,10	0,03
1,5	10,75	23	25	27,26	27,89	27,99	23,99	15,79	7,79	2,85	0,65	0,11	0,10	0,09	0,07	0,08	0,14	0,23	0,35	0,53	0,75	0,78	0,63	0,39	0,20	0,09	0,06	0,07	0,08	0,09	0,09	0,08	0,08	0,10	0,11	0,13	0,12	0,03
1,5	12,25	24	26	29,79	31,59	32,59	28,79	21,29	10,35	4,38	2,00	0,25	0,10	0,09	0,08	0,08	0,12	0,22	0,37	0,58	0,87	0,89	0,71	0,46	0,25	0,14	0,09	0,09	0,10	0,10	0,11	0,11	0,10	0,08	0,08	0,08	0,07	0,03
0,75 ©	13	24	28	31,29	33,99	35,69	30,29	20,79	10,79	4,52	2,73	0,25	0,10	0,08	0,08	0,07	0,12	0,21	0,39	0,61	0,91	0,88	0,70	0,44	0,25	0,14	0,09	0,10	0,11	0,12	0,13	0,12	0,10	0,07	0,07	0,06	0,05	0,03
0,75	13,75	24	28	31,09	33,69	35,59	30,39	21,19	10,89	4,54	2,07	0,26	0,10	0,08	0,08	0,07	0,11	0,19	0,38	0,61	0,85	0,82	0,65	0,41	0,24	0,14	0,10	0,11	0,12	0,12	0,12	0,10	0,08	0,06	0,05	0,05	0,04	0,03
1,5	15,25	24	27	30,19	32,19	33,69	30,09	20,99	11,19	4,89	1,57	0,34	0,11	0,09	0,09	0,08	0,11	0,17	0,33	0,57	0,72	0,70	0,54	0,36	0,23	0,15	0,10	0,12	0,13	0,13	0,12	0,10	0,07	0,07	0,87	0,08	0,07	0,03
1,5	16,75	18	21	23,39	24,69	25,59	24,09	17,69	9,76	4,32	1,49	0,31	0,09	0,08	0,08	0,07	0,08	0,12	0,23	0,38	0,50	0,50	0,37	0,28	0,20	0,13	0,10	0,12	0,14	0,14	0,13	0,12	0,14	0,17	0,21	0,22	0,18	0,03
1,5	18,25	13	15	16,09	16,89	17,29	16,09	11,69	6,31	2,59	0,76	0,39	0,07	0,07	0,06	0,06	0,06	0,09	0,17	0,26	0,30	0,30	0,23	0,17	0,13	0,10	0,11	0,15	0,17	0,18	0,15	0,12	0,15	0,22	0,26	0,30	0,24	0,04
1,5	19,75	9	10	11,29	11,79	12,19	11,49	8,49	4,69	1,99	0,60	0,11	0,10	0,09	0,08	0,08	0,08	0,10	0,14	0,19	0,21	0,20	0,17	0,12	0,09	0,07	0,07	0,09	0,11	0,11	0,08	0,07	0,10	0,19	0,25	0,30	0,28	0,04
1,5	21,25	4	5	5,17	5,35	5,40	4,84	3,34	2,14	0,51	0,11	0,10	0,09	0,09	0,08	0,07	0,08	0,08	0,10	0,11	0,11	0,10	0,08	0,06	0,04	0,04	0,04	0,06	0,07	0,07	0,06	0,05	0,04	0,08	0,14	0,25	0,25	0,06

Figure 29: Experimental map related to led 1 of the central lamp. The maximum result is equal to ~ 36 uW/cm².

Sampling step [cm]		0	1	1	1	1	2	2	2	2	2	2	2	2	2	2	2	2	2	2	2	2	2	2	2	2	2	2	2	2	2	2	2	2 (1)	1	1	1	1
	Distance [cm]	5,3	6,3	7,3	8,3	9,3	11,3	13,3	15,3	17,3	19,3	21,3	23,3	25,3	27,3	29,3	31,3	33,3	35,3	37,3	39,3	41,3	43,3	45,3	47,3	49,3	51,3	53,3	55,3	57,3	59,3	61,3	63,3	65,3	66,3	67,3	68,3	69,3
0	4,75	0,09	0,09	0,08	0,07	0,07	0,06	0,06	0,06	0,05	0,05	0,05	0,05	0,06	0,09	0,55	1,52	2,66	3,46	3,64	3,21	2,22	2,00	0,32	0,06	0,05	0,05	0,05	0,05	0,05	0,05	0,05	0,05	0,06	0,06	0,05	0,05	0,05
1,5	6,25	0,20	0,15	0,11	0,09	0,08	0,07	0,06	0,05	0,05	0,06	0,06	0,07	0,09	0,59	1,94	4,10	6,59	8,31	8,51	7,47	5,19	2,63	0,97	0,17	0,07	0,06	0,05	0,05	0,05	0,05	0,05	0,05	0,05	0,06	0,06	0,05	0,05
1,5	7,75	0,35	0,24	0,16	0,12	0,10	0,07	0,06	0,05	0,05	0,06	0,06	0,07	0,16	1,01	3,04	6,63	10,79	13,79	14,09	12,49	8,69	4,42	2,01	0,41	0,07	0,06	0,06	0,05	0,05	0,05	0,05	0,06	0,06	0,06	0,07	0,08	0,05
1,5	9,25	0,59	0,39	0,23	0,15	0,11	0,07	0,05	0,05	0,04	0,05	0,06	0,07	0,10	0,93	3,30	8,04	14,09	18,89	19,99	18,09	12,69	6,62	2,77	0,80	0,11	0,07	0,06	0,06	0,05	0,06	0,06	0,06	0,07	0,10	0,12	0,11	0,05
1,5	10,75	1,17	0,76	0,42	0,27	0,19	0,11	0,07	0,06	0,06	0,06	0,07	0,08	0,30	1,64	5,06	11,69	20,01	26,89	28,49	25,19	17,09	8,89	3,62	1,05	0,16	0,08	0,07	0,06	0,06	0,07	0,07	0,08	0,10	0,11	0,12	0,12	0,05
1,5	12,25	1,82	1,20	0,62	0,37	0,25	0,14	0,08	0,06	0,06	0,07	0,08	0,09	0,33	1,75	5,50	12,69	22,19	30,59	33,29	28,49	18,59	9,33	3,75	1,08	0,15	0,08	0,08	0,07	0,07	0,07	0,08	0,09	0,09	0,09	0,09	0,09	0,05
0,75 ©	13	2,00	1,42	0,73	0,43	0,29	0,16	0,09	0,06	0,06	0,07	0,08	0,09	0,20	1,41	4,75	11,43	20,64	29,59	33,79	29,29	20,01	10,59	4,69	1,99	0,35	0,09	0,08	0,07	0,07	0,07	0,07	0,07	0,08	0,07	0,07	0,07	0,05
0,75	13,75	1,92	1,43	0,77	0,43	0,29	0,16	0,09	0,06	0,06	0,06	0,08	0,09	0,16	1,95	6,01	13,04	22,49	30,49	32,39	27,29	18,09	9,07	3,63	2,21	0,31	0,09	0,08	0,07	0,07	0,07	0,07	0,07	0,07	0,08	0,08	0,07	0,05
1,5	15,25	1,84	1,44	0,82	0,44	0,29	0,16	0,10	0,06	0,06	0,06	0,07	0,08	0,11	0,99	3,83	9,93	17,49	22,49	24,59	23,49	17,69	10,29	4,96	1,82	0,26	0,09	0,08	0,07	0,07	0,06	0,06	0,06	0,07	0,08	0,08	0,07	0,05
1,5	16,75	1,59	1,25	0,75	0,37	0,23	0,15	0,12	0,08	0,06	0,06	0,07	0,08	0,10	0,80	3,18	8,17	16,39	19,89	20,89	19,06	13,49	7,10	2,94	0,84	0,10	0,07	0,06	0,06	0,06	0,06	0,07	0,10	0,13	0,15	0,16	0,13	0,05
1,5	18,25	0,92	0,78	0,56	0,34	0,23	0,17	0,11	0,07	0,05	0,05	0,06	0,07	0,08	0,24	1,47	4,38	8,38	11,53	12,36	11,39	8,09	4,16	1,97	0,37	0,06	0,06	0,05	0,05	0,05	0,05	0,06	0,08	0,13	0,16	0,18	0,16	0,04
1,5	19,75	0,57	0,49	0,40	0,29	0,22	0,16	0,11	0,07	0,06	0,05	0,06	0,07	0,07	0,09	0,80	2,68	5,31	7,60	8,37	7,93	6,00	3,35	1,40	0,37	0,07	0,06	0,06	0,06	0,06	0,05	0,05	0,07	0,10	0,13	0,15	0,16	0,05
1,5	21,25	0,30	0,28	0,25	0,20	0,16	0,12	0,09	0,07	0,06	0,05	0,06	0,06	0,07	0,07	0,34	1,36	2,91	4,26	4,77	4,58	3,52	2,04	0,80	0,18	0,06	0,06	0,06	0,06	0,06	0,06	0,06	0,06	0,06	0,08	0,10	0,12	0,05

Figure 30: Experimental map related to led 16 of the central lamp. The maximum result is equal to ~ 33 uW/cm².

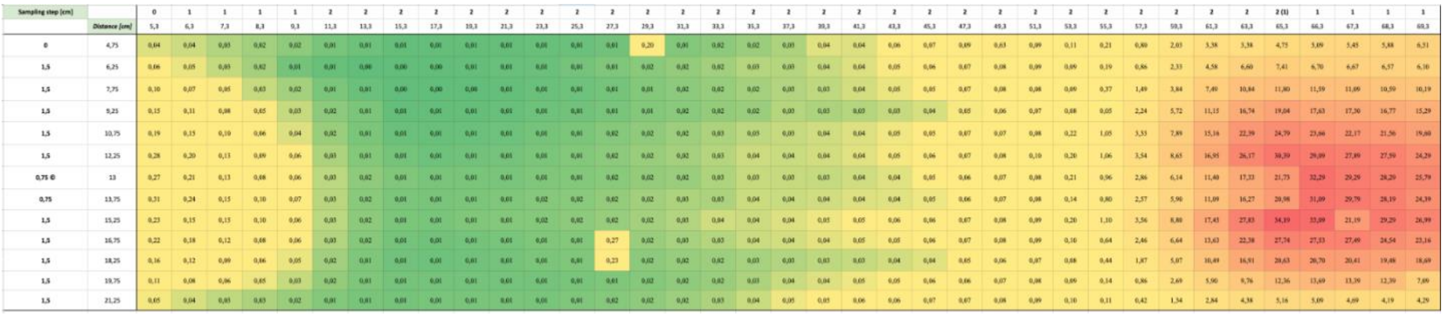

Sampling step [cm]		0	1	1	1	1	2	2	2	2	2	2	2	2	2	2	2	2	2	2	2	2	2	2	2	2	2	2	2	2	2	2	2	2 (1)	1	1	1	1
	Distance [cm]	5,3	6,3	7,3	8,3	9,3	11,3	13,3	15,3	17,3	19,3	21,3	23,3	25,3	27,3	29,3	31,3	33,3	35,3	37,3	39,3	41,3	43,3	45,3	47,3	49,3	51,3	53,3	55,3	57,3	59,3	61,3	63,3	65,3	66,3	67,3	68,3	69,3
0	4,75	0,04	0,04	0,03	0,02	0,02	0,01	0,01	0,01	0,01	0,01	0,01	0,01	0,01	0,01	0,20	0,01	0,02	0,02	0,03	0,04	0,04	0,06	0,07	0,09	0,63	0,09	0,11	0,21	0,80	2,03	3,38	3,38	4,75	5,09	5,45	5,88	6,51
1,5	6,25	0,06	0,05	0,03	0,02	0,01	0,01	0,00	0,00	0,00	0,01	0,01	0,01	0,01	0,01	0,02	0,02	0,02	0,03	0,03	0,04	0,04	0,05	0,06	0,07	0,08	0,09	0,09	0,19	0,86	2,33	4,58	6,60	7,41	6,70	6,67	6,57	6,10
1,5	7,75	0,10	0,07	0,05	0,03	0,02	0,01	0,01	0,00	0,00	0,00	0,01	0,01	0,01	0,01	0,01	0,02	0,02	0,02	0,03	0,03	0,04	0,05	0,05	0,07	0,08	0,08	0,09	0,37	1,49	3,84	7,49	10,84	11,80	11,59	11,09	10,59	10,19
1,5	9,25	0,15	0,11	0,08	0,05	0,03	0,02	0,01	0,01	0,01	0,01	0,01	0,01	0,01	0,01	0,01	0,02	0,02	0,02	0,03	0,03	0,03	0,03	0,04	0,05	0,06	0,07	0,08	0,05	2,24	5,72	11,15	16,74	19,04	17,63	17,30	16,77	15,29
1,5	10,75	0,19	0,15	0,10	0,06	0,04	0,02	0,01	0,01	0,01	0,01	0,01	0,01	0,01	0,02	0,02	0,02	0,03	0,03	0,03	0,04	0,04	0,05	0,05	0,07	0,07	0,08	0,22	1,05	3,33	7,89	15,16	22,39	24,79	23,66	22,17	21,56	19,60
1,5	12,25	0,28	0,20	0,13	0,09	0,06	0,03	0,01	0,01	0,01	0,01	0,01	0,01	0,01	0,02	0,02	0,02	0,03	0,04	0,04	0,04	0,04	0,05	0,06	0,07	0,08	0,10	0,20	1,06	3,54	8,65	16,95	26,17	30,39	29,09	27,89	27,59	24,29
0,75 ©	13	0,27	0,21	0,13	0,08	0,06	0,03	0,02	0,01	0,01	0,01	0,01	0,01	0,01	0,02	0,02	0,02	0,03	0,03	0,03	0,03	0,04	0,04	0,05	0,06	0,07	0,08	0,21	0,96	2,86	6,14	11,40	17,33	21,73	32,29	29,29	28,29	25,79
0,75	13,75	0,31	0,24	0,15	0,10	0,07	0,03	0,02	0,01	0,01	0,01	0,01	0,02	0,02	0,02	0,02	0,03	0,03	0,04	0,04	0,04	0,04	0,04	0,05	0,06	0,07	0,08	0,14	0,80	2,57	5,90	11,09	16,27	20,98	31,09	29,79	28,19	24,39
1,5	15,25	0,23	0,15	0,13	0,10	0,06	0,03	0,02	0,01	0,01	0,01	0,01	0,02	0,02	0,02	0,02	0,03	0,04	0,04	0,04	0,05	0,05	0,06	0,06	0,07	0,08	0,09	0,20	1,10	3,56	8,80	17,45	27,83	34,19	33,09	21,19	29,29	26,99
1,5	16,75	0,22	0,18	0,12	0,08	0,06	0,03	0,02	0,01	0,01	0,01	0,01	0,01	0,01	0,27	0,02	0,03	0,03	0,04	0,04	0,04	0,05	0,05	0,06	0,07	0,08	0,09	0,10	0,64	2,46	6,64	13,63	22,38	27,74	27,33	27,49	24,54	23,16
1,5	18,25	0,16	0,12	0,09	0,06	0,05	0,02	0,01	0,01	0,01	0,01	0,01	0,01	0,01	0,23	0,02	0,02	0,02	0,03	0,03	0,03	0,03	0,04	0,04	0,05	0,06	0,07	0,08	0,44	1,87	5,07	10,49	16,91	20,63	20,70	20,41	19,48	18,69
1,5	19,75	0,11	0,08	0,06	0,05	0,03	0,02	0,01	0,01	0,01	0,01	0,01	0,01	0,01	0,01	0,02	0,02	0,02	0,03	0,04	0,04	0,05	0,05	0,06	0,06	0,07	0,08	0,09	0,14	0,86	2,69	5,90	9,76	12,36	13,69	13,39	12,39	7,89
1,5	21,25	0,05	0,04	0,03	0,03	0,02	0,01	0,01	0,01	0,01	0,01	0,01	0,01	0,01	0,02	0,02	0,02	0,03	0,04	0,05	0,05	0,06	0,06	0,07	0,07	0,08	0,09	0,10	0,11	0,42	1,34	2,84	4,38	5,16	5,09	4,69	4,19	4,29

Figure 31: Experimental map related to led 32 of the central lamp. The maximum result is equal to ~ 35 uW/cm².

Upper Lamp

The results are shown in Figures 32 and 33.

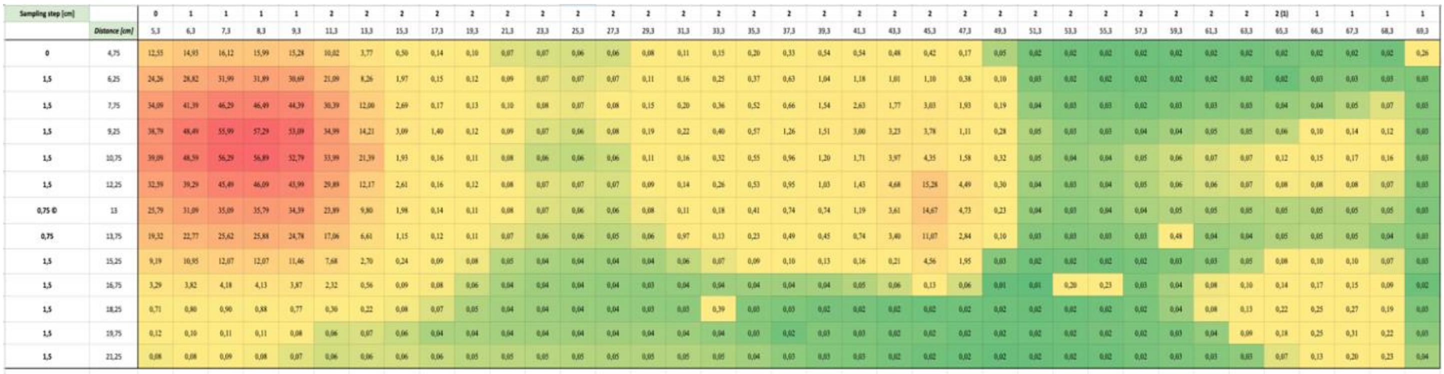

Sampling step [cm]		0	1	1	1	1	2	2	2	2	2	2	2	2	2	2	2	2	2	2	2	2	2	2	2	2	2	2	2	2	2	2	2	2 (1)	1	1	1	1
	Distance [cm]	5,3	6,3	7,3	8,3	9,3	11,3	13,3	15,3	17,3	19,3	21,3	23,3	25,3	27,3	29,3	31,3	33,3	35,3	37,3	39,3	41,3	43,3	45,3	47,3	49,3	51,3	53,3	55,3	57,3	59,3	61,3	63,3	65,3	66,3	67,3	68,3	69,3
0	4,75	12,55	14,93	16,12	15,99	15,28	10,02	3,77	0,50	0,14	0,10	0,07	0,07	0,06	0,06	0,08	0,11	0,15	0,20	0,33	0,54	0,54	0,48	0,42	0,17	0,05	0,02	0,02	0,02	0,02	0,02	0,02	0,02	0,02	0,02	0,02	0,02	0,26
1,5	6,25	24,26	28,82	31,99	31,89	30,69	21,09	8,26	1,97	0,15	0,12	0,09	0,07	0,07	0,07	0,11	0,16	0,25	0,37	0,63	1,04	1,18	1,01	1,10	0,38	0,10	0,03	0,02	0,02	0,02	0,02	0,02	0,02	0,02	0,03	0,03	0,03	0,03
1,5	7,75	34,09	41,39	46,29	46,49	44,39	30,39	12,00	2,69	0,17	0,13	0,10	0,08	0,07	0,08	0,15	0,20	0,36	0,52	0,66	1,54	2,63	1,77	3,03	1,93	0,19	0,04	0,03	0,03	0,02	0,03	0,03	0,03	0,04	0,04	0,05	0,07	0,03
1,5	9,25	38,79	48,49	55,99	57,29	53,09	34,99	14,21	3,09	1,40	0,12	0,09	0,07	0,06	0,08	0,19	0,22	0,40	0,57	1,26	1,51	3,00	3,23	3,78	1,11	0,28	0,05	0,03	0,03	0,04	0,04	0,05	0,05	0,06	0,10	0,14	0,12	0,03
1,5	10,75	39,09	48,59	56,29	56,89	52,79	33,99	21,39	1,93	0,16	0,11	0,08	0,06	0,06	0,06	0,11	0,16	0,32	0,55	0,96	1,20	1,71	3,97	4,35	1,58	0,32	0,05	0,04	0,04	0,05	0,06	0,07	0,07	0,12	0,15	0,17	0,16	0,03
1,5	12,25	32,59	39,29	45,49	46,09	45,99	29,89	12,17	2,61	0,16	0,12	0,08	0,07	0,07	0,07	0,09	0,14	0,26	0,53	0,95	1,03	1,43	4,68	15,28	4,49	0,30	0,04	0,03	0,04	0,05	0,06	0,06	0,07	0,08	0,08	0,08	0,07	0,03
0,75 ©	13	25,79	31,09	35,09	35,79	34,39	23,89	9,80	1,98	0,14	0,11	0,08	0,07	0,06	0,06	0,08	0,11	0,18	0,41	0,74	0,74	1,19	3,61	14,67	4,73	0,23	0,04	0,03	0,04	0,04	0,05	0,05	0,05	0,05	0,05	0,05	0,05	0,03
0,75	13,75	19,32	22,77	25,62	25,88	24,78	17,06	6,61	1,15	0,12	0,11	0,07	0,06	0,06	0,05	0,06	0,97	0,13	0,23	0,49	0,45	0,74	3,40	11,07	2,84	0,10	0,03	0,03	0,03	0,03	0,48	0,04	0,04	0,05	0,05	0,05	0,04	0,03
1,5	15,25	9,19	10,95	12,07	12,07	11,46	7,68	2,70	0,24	0,09	0,08	0,05	0,04	0,04	0,04	0,04	0,06	0,07	0,09	0,10	0,13	0,16	0,21	4,56	1,95	0,03	0,02	0,02	0,02	0,02	0,03	0,03	0,05	0,08	0,10	0,10	0,07	0,03
1,5	16,75	3,29	3,82	4,18	4,13	3,87	2,32	0,56	0,09	0,08	0,06	0,04	0,04	0,04	0,04	0,03	0,04	0,04	0,04	0,04	0,04	0,05	0,06	0,13	0,06	0,01	0,01	0,20	0,23	0,03	0,04	0,08	0,10	0,14	0,17	0,15	0,09	0,02
1,5	18,25	0,71	0,80	0,90	0,88	0,77	0,30	0,22	0,08	0,07	0,05	0,04	0,04	0,04	0,04	0,03	0,03	0,39	0,03	0,03	0,02	0,02	0,02	0,02	0,02	0,02	0,02	0,02	0,02	0,02	0,04	0,08	0,13	0,22	0,25	0,27	0,19	0,03
1,5	19,75	0,12	0,10	0,11	0,11	0,08	0,06	0,07	0,06	0,04	0,04	0,04	0,04	0,04	0,04	0,04	0,04	0,04	0,03	0,02	0,03	0,03	0,02	0,02	0,02	0,02	0,02	0,02	0,02	0,02	0,03	0,04	0,09	0,18	0,25	0,31	0,22	0,03
1,5	21,25	0,08	0,08	0,09	0,08	0,07	0,06	0,06	0,06	0,06	0,05	0,05	0,05	0,05	0,05	0,05	0,05	0,05	0,04	0,03	0,03	0,03	0,02	0,02	0,02	0,02	0,02	0,02	0,02	0,02	0,03	0,03	0,03	0,07	0,13	0,20	0,23	0,04

Figure 32: Experimental map related to led 1 of the upper lamp. The maximum result is equal to ~ 57 uW/cm².

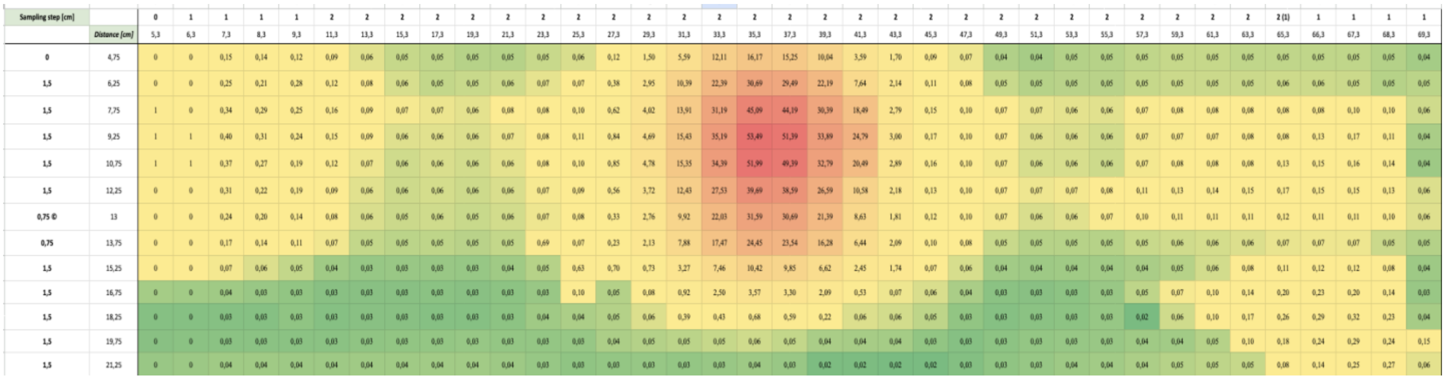

Sampling step [cm]		0	1	1	1	1	2	2	2	2	2	2	2	2	2	2	2	2	2	2	2	2	2	2	2	2	2	2	2	2	2	2	2	2 (1)	1	1	1	1
	Distance [cm]	5,3	6,3	7,3	8,3	9,3	11,3	13,3	15,3	17,3	19,3	21,3	23,3	25,3	27,3	29,3	31,3	33,3	35,3	37,3	39,3	41,3	43,3	45,3	47,3	49,3	51,3	53,3	55,3	57,3	59,3	61,3	63,3	65,3	66,3	67,3	68,3	69,3
0	4,75	0	0	0,15	0,14	0,12	0,09	0,06	0,05	0,05	0,05	0,05	0,05	0,06	0,12	1,50	5,59	12,11	16,17	15,25	10,04	3,59	1,70	0,09	0,07	0,04	0,04	0,05	0,05	0,05	0,05	0,05	0,05	0,05	0,05	0,05	0,05	0,04
1,5	6,25	0	0	0,25	0,21	0,28	0,12	0,08	0,06	0,05	0,05	0,06	0,07	0,07	0,38	2,95	10,39	22,39	30,69	29,49	22,19	7,64	2,14	0,11	0,08	0,05	0,05	0,05	0,05	0,05	0,05	0,05	0,05	0,06	0,06	0,05	0,05	0,05
1,5	7,75	1	0	0,34	0,29	0,25	0,16	0,09	0,07	0,07	0,06	0,08	0,08	0,10	0,62	4,02	13,91	31,19	45,09	44,19	30,39	18,49	2,79	0,15	0,10	0,07	0,07	0,06	0,06	0,07	0,08	0,08	0,08	0,08	0,08	0,10	0,10	0,06
1,5	9,25	1	1	0,40	0,31	0,24	0,15	0,09	0,06	0,06	0,06	0,07	0,08	0,11	0,84	4,69	15,43	35,19	53,49	51,39	33,89	24,79	3,00	0,17	0,10	0,07	0,06	0,06	0,06	0,07	0,07	0,07	0,08	0,08	0,13	0,17	0,11	0,04
1,5	10,75	1	1	0,37	0,27	0,19	0,12	0,07	0,06	0,06	0,06	0,06	0,08	0,10	0,85	4,78	15,35	34,39	51,99	49,39	32,79	20,49	2,89	0,16	0,10	0,07	0,06	0,06	0,06	0,07	0,08	0,08	0,08	0,13	0,15	0,16	0,14	0,04
1,5	12,25	0	0	0,31	0,22	0,19	0,09	0,06	0,06	0,06	0,06	0,06	0,07	0,09	0,56	3,72	12,43	27,53	39,69	38,59	26,59	10,58	2,18	0,13	0,10	0,07	0,07	0,07	0,08	0,11	0,13	0,14	0,15	0,17	0,15	0,15	0,13	0,06
0,75 ©	13	0	0	0,24	0,20	0,14	0,08	0,06	0,05	0,06	0,05	0,06	0,07	0,08	0,33	2,76	9,92	22,03	31,59	30,69	21,39	8,63	1,81	0,12	0,10	0,07	0,06	0,06	0,07	0,10	0,11	0,11	0,11	0,12	0,11	0,11	0,10	0,06
0,75	13,75	0	0	0,17	0,14	0,11	0,07	0,05	0,05	0,05	0,05	0,05	0,69	0,07	0,23	2,13	7,88	17,47	24,45	23,54	16,28	6,44	2,09	0,10	0,08	0,05	0,05	0,05	0,05	0,05	0,06	0,06	0,06	0,07	0,07	0,07	0,05	0,05
1,5	15,25	0	0	0,07	0,06	0,05	0,04	0,03	0,03	0,03	0,03	0,04	0,05	0,63	0,70	0,73	3,27	7,46	10,42	9,85	6,62	2,45	1,74	0,07	0,06	0,04	0,04	0,04	0,04	0,04	0,05	0,06	0,08	0,11	0,12	0,12	0,08	0,04
1,5	16,75	0	0	0,04	0,03	0,03	0,03	0,03	0,03	0,03	0,03	0,03	0,03	0,10	0,05	0,08	0,92	2,50	3,57	3,30	2,09	0,53	0,07	0,06	0,04	0,03	0,03	0,03	0,03	0,05	0,07	0,10	0,14	0,20	0,23	0,20	0,14	0,03
1,5	18,25	0	0	0,03	0,03	0,03	0,03	0,03	0,03	0,03	0,03	0,03	0,04	0,04	0,05	0,06	0,39	0,43	0,68	0,59	0,22	0,06	0,06	0,05	0,03	0,03	0,03	0,03	0,03	0,02	0,06	0,10	0,17	0,26	0,29	0,32	0,23	0,04
1,5	19,75	0	0	0,03	0,03	0,03	0,03	0,03	0,03	0,03	0,03	0,03	0,03	0,03	0,04	0,05	0,05	0,05	0,06	0,05	0,04	0,04	0,04	0,03	0,03	0,03	0,03	0,03	0,03	0,04	0,04	0,05	0,10	0,18	0,24	0,29	0,24	0,15
1,5	21,25	0	0	0,04	0,04	0,04	0,04	0,04	0,04	0,04	0,04	0,04	0,03	0,03	0,03	0,03	0,03	0,03	0,04	0,03	0,02	0,02	0,02	0,02	0,03	0,03	0,03	0,04	0,04	0,04	0,05	0,05	0,05	0,08	0,14	0,25	0,27	0,06

Figure 33 Experimental map related to led 16 of the upper lamp. The maximum result is equal to ~ 54 uW/cm²

Lower Lamp

The results are shown in Figures 34 and 35.

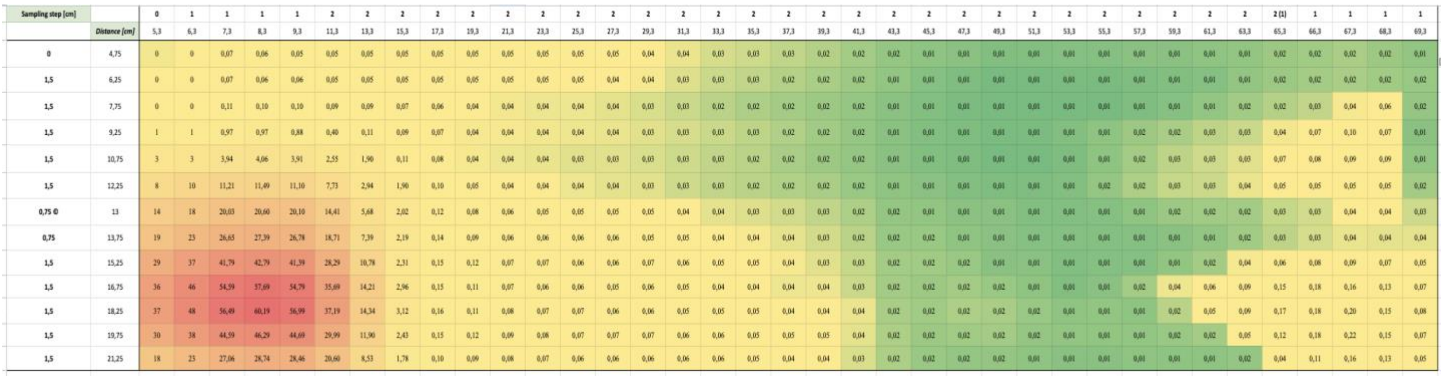

Sampling step [cm]		0	1	1	1	1	2	2	2	2	2	2	2	2	2	2	2	2	2	2	2	2	2	2	2	2	2	2	2	2	2	2	2	2 (1)	1	1	1	1
	Distance [cm]	5,3	6,3	7,3	8,3	9,3	11,3	13,3	15,3	17,3	19,3	21,3	23,3	25,3	27,3	29,3	31,3	33,3	35,3	37,3	39,3	41,3	43,3	45,3	47,3	49,3	51,3	53,3	55,3	57,3	59,3	61,3	63,3	65,3	66,3	67,3	68,3	69,3
0	4,75	0	0	0,07	0,06	0,05	0,05	0,05	0,05	0,05	0,05	0,05	0,05	0,05	0,05	0,04	0,04	0,03	0,03	0,03	0,02	0,02	0,02	0,01	0,01	0,01	0,01	0,01	0,01	0,01	0,01	0,01	0,01	0,02	0,02	0,02	0,02	0,01
1,5	6,25	0	0	0,07	0,06	0,06	0,05	0,05	0,05	0,05	0,05	0,05	0,05	0,05	0,04	0,04	0,03	0,03	0,03	0,02	0,02	0,02	0,01	0,01	0,01	0,01	0,01	0,01	0,01	0,01	0,01	0,01	0,01	0,02	0,02	0,02	0,02	0,02
1,5	7,75	0	0	0,11	0,10	0,10	0,09	0,09	0,07	0,06	0,04	0,04	0,04	0,04	0,04	0,03	0,03	0,02	0,02	0,02	0,02	0,02	0,01	0,01	0,01	0,01	0,01	0,01	0,01	0,01	0,01	0,01	0,02	0,02	0,03	0,04	0,06	0,02
1,5	9,25	1	1	0,97	0,97	0,88	0,40	0,11	0,09	0,07	0,04	0,04	0,04	0,04	0,04	0,03	0,03	0,03	0,03	0,02	0,02	0,02	0,01	0,01	0,01	0,01	0,01	0,01	0,01	0,02	0,02	0,03	0,03	0,04	0,07	0,10	0,07	0,01
1,5	10,75	3	3	3,94	4,06	3,91	2,55	1,90	0,11	0,08	0,04	0,04	0,04	0,03	0,03	0,03	0,03	0,03	0,02	0,02	0,02	0,02	0,01	0,01	0,01	0,01	0,01	0,01	0,01	0,02	0,03	0,03	0,03	0,07	0,08	0,09	0,09	0,01
1,5	12,25	8	10	11,21	11,49	11,10	7,73	2,94	1,90	0,10	0,05	0,04	0,04	0,04	0,04	0,03	0,03	0,03	0,02	0,02	0,02	0,02	0,01	0,01	0,01	0,01	0,01	0,01	0,02	0,02	0,03	0,03	0,04	0,05	0,05	0,05	0,05	0,02
0,75 ©	13	14	18	20,03	20,60	20,10	14,41	5,68	2,02	0,12	0,08	0,06	0,05	0,05	0,05	0,05	0,04	0,04	0,03	0,03	0,03	0,02	0,02	0,01	0,01	0,01	0,01	0,01	0,01	0,01	0,02	0,02	0,02	0,03	0,03	0,04	0,04	0,03
0,75	13,75	19	23	26,65	27,39	26,78	18,71	7,39	2,19	0,14	0,09	0,06	0,06	0,06	0,06	0,05	0,05	0,04	0,04	0,04	0,03	0,02	0,02	0,02	0,01	0,01	0,01	0,01	0,01	0,01	0,01	0,01	0,02	0,03	0,03	0,04	0,04	0,04
1,5	15,25	29	37	41,79	42,79	41,39	28,29	10,78	2,31	0,15	0,12	0,07	0,07	0,06	0,06	0,07	0,06	0,05	0,05	0,04	0,03	0,03	0,02	0,02	0,02	0,01	0,01	0,01	0,01	0,01	0,01	0,02	0,04	0,06	0,08	0,09	0,07	0,05
1,5	16,75	36	46	54,59	57,69	54,79	35,69	14,21	2,96	0,15	0,11	0,07	0,06	0,06	0,05	0,06	0,05	0,04	0,04	0,04	0,04	0,03	0,02	0,02	0,02	0,02	0,01	0,01	0,01	0,02	0,04	0,06	0,09	0,15	0,18	0,16	0,13	0,07
1,5	18,25	37	48	56,49	60,19	56,99	37,19	14,34	3,12	0,16	0,11	0,08	0,07	0,07	0,06	0,06	0,05	0,05	0,05	0,04	0,04	0,04	0,02	0,02	0,02	0,02	0,02	0,01	0,01	0,01	0,02	0,05	0,09	0,17	0,18	0,20	0,15	0,08
1,5	19,75	30	38	44,59	46,29	44,69	29,99	11,90	2,43	0,15	0,12	0,09	0,08	0,07	0,07	0,07	0,06	0,06	0,05	0,05	0,05	0,04	0,02	0,02	0,02	0,02	0,02	0,01	0,01	0,01	0,02	0,02	0,05	0,12	0,18	0,22	0,15	0,07
1,5	21,25	18	23	27,06	28,74	28,46	20,60	8,53	1,78	0,10	0,09	0,08	0,07	0,06	0,06	0,06	0,06	0,06	0,05	0,04	0,04	0,03	0,02	0,02	0,02	0,02	0,01	0,01	0,01	0,01	0,01	0,01	0,02	0,04	0,11	0,16	0,13	0,05

Figure 34: Experimental map related to led 1 of the lower lamp. The maximum result is equal to ~ 60 uW/cm².

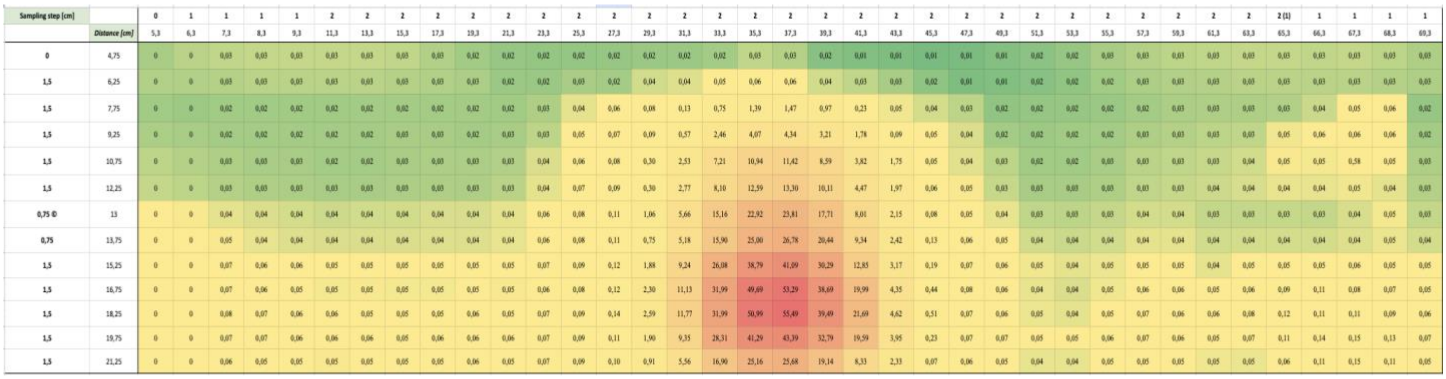

Sampling step [cm]		0	1	1	1	1	2	2	2	2	2	2	2	2	2	2	2	2	2	2	2	2	2	2	2	2	2	2	2	2	2	2	2	2 (1)	1	1	1	1
	Distance [cm]	5,3	6,3	7,3	8,3	9,3	11,3	13,3	15,3	17,3	19,3	21,3	23,3	25,3	27,3	29,3	31,3	33,3	35,3	37,3	39,3	41,3	43,3	45,3	47,3	49,3	51,3	53,3	55,3	57,3	59,3	61,3	63,3	65,3	66,3	67,3	68,3	69,3
0	4,75	0	0	0,03	0,03	0,03	0,03	0,03	0,03	0,03	0,02	0,02	0,02	0,02	0,02	0,02	0,02	0,02	0,03	0,03	0,02	0,01	0,01	0,01	0,01	0,01	0,02	0,02	0,03	0,03	0,03	0,03	0,03	0,03	0,03	0,03	0,03	0,03
1,5	6,25	0	0	0,03	0,03	0,03	0,03	0,03	0,03	0,03	0,03	0,02	0,02	0,03	0,02	0,04	0,04	0,05	0,06	0,06	0,04	0,03	0,03	0,02	0,01	0,01	0,02	0,02	0,02	0,03	0,03	0,03	0,03	0,03	0,03	0,03	0,03	0,03
1,5	7,75	0	0	0,02	0,02	0,02	0,02	0,02	0,02	0,02	0,02	0,02	0,03	0,04	0,06	0,08	0,13	0,75	1,39	1,47	0,97	0,23	0,05	0,04	0,03	0,02	0,02	0,02	0,02	0,02	0,03	0,03	0,03	0,03	0,04	0,05	0,06	0,02
1,5	9,25	0	0	0,02	0,02	0,02	0,02	0,02	0,03	0,03	0,02	0,03	0,03	0,05	0,07	0,09	0,57	2,46	4,07	4,34	3,21	1,78	0,09	0,05	0,04	0,02	0,02	0,02	0,02	0,03	0,03	0,03	0,03	0,05	0,06	0,06	0,06	0,02
1,5	10,75	0	0	0,03	0,03	0,03	0,02	0,02	0,03	0,03	0,03	0,03	0,04	0,06	0,08	0,30	2,53	7,21	10,94	11,42	8,59	3,82	1,75	0,05	0,04	0,03	0,02	0,02	0,03	0,03	0,03	0,03	0,04	0,05	0,05	0,58	0,05	0,03
1,5	12,25	0	0	0,03	0,03	0,03	0,03	0,03	0,03	0,03	0,03	0,03	0,04	0,07	0,09	0,30	2,77	8,10	12,59	13,30	10,11	4,47	1,97	0,06	0,05	0,03	0,03	0,03	0,03	0,03	0,03	0,04	0,04	0,04	0,04	0,05	0,04	0,03
0,75 ©	13	0	0	0,04	0,04	0,04	0,04	0,04	0,04	0,04	0,04	0,04	0,06	0,08	0,11	1,06	5,66	15,16	22,92	23,81	17,71	8,01	2,15	0,08	0,05	0,04	0,03	0,03	0,03	0,04	0,04	0,03	0,03	0,03	0,03	0,04	0,05	0,03
0,75	13,75	0	0	0,05	0,04	0,04	0,04	0,04	0,04	0,04	0,04	0,04	0,06	0,08	0,11	0,75	5,18	15,90	25,00	26,78	20,44	9,34	2,42	0,13	0,06	0,05	0,04	0,04	0,04	0,04	0,04	0,04	0,04	0,04	0,04	0,04	0,05	0,04
1,5	15,25	0	0	0,07	0,06	0,06	0,05	0,05	0,05	0,05	0,05	0,05	0,07	0,09	0,12	1,88	9,24	26,08	38,79	41,09	30,29	12,85	3,17	0,19	0,07	0,06	0,05	0,04	0,05	0,05	0,05	0,04	0,05	0,05	0,05	0,06	0,05	0,05
1,5	16,75	0	0	0,07	0,06	0,05	0,05	0,05	0,05	0,05	0,05	0,05	0,06	0,08	0,12	2,30	11,13	31,99	49,69	53,29	38,69	19,99	4,35	0,44	0,08	0,06	0,04	0,04	0,05	0,06	0,06	0,05	0,06	0,09	0,11	0,08	0,07	0,05
1,5	18,25	0	0	0,08	0,07	0,06	0,06	0,05	0,05	0,05	0,06	0,05	0,07	0,09	0,14	2,59	11,77	31,99	50,99	55,49	39,49	21,69	4,62	0,51	0,07	0,06	0,05	0,04	0,05	0,07	0,06	0,06	0,08	0,12	0,11	0,11	0,09	0,06
1,5	19,75	0	0	0,07	0,07	0,06	0,06	0,06	0,05	0,06	0,06	0,06	0,07	0,09	0,11	1,90	9,35	28,31	41,29	43,39	32,79	19,59	3,95	0,23	0,07	0,07	0,05	0,05	0,06	0,07	0,06	0,05	0,07	0,11	0,14	0,15	0,13	0,07
1,5	21,25	0	0	0,06	0,05	0,05	0,05	0,05	0,05	0,05	0,06	0,05	0,07	0,09	0,10	0,91	5,56	16,90	25,16	25,68	19,14	8,33	2,33	0,07	0,06	0,05	0,04	0,04	0,05	0,05	0,05	0,05	0,05	0,06	0,11	0,15	0,11	0,05

Figure 35: Experimental map related to led 16 of the lower lamp. The maximum result is equal to ~ 55 uW/cm².

4.3 Third Measurement Campaign

After the second measurement campaign carried out in 2022, a new campaign was conducted in 2025. The acquisition process, described in Chapter 3, was kept unchanged in order to ensure proper repeatability and adequate spatial resolution.

In contrast to the methodology adopted during the previous campaign, the present phase began with measurements performed using a single active source, followed by configurations with one lamp switched on, and finally with all three lamps operating simultaneously.

4.3.1 Measurements with single LED switched on

The experimental procedure was structured as follows:

- Frequency scan (265 nm) of the irradiance generated by the source positioned at the center of the central bar, where a more uniform distribution is expected, with minimal influence from reflective contributions. This analysis was also extended to the central positions of the upper and lower bars, where irradiance is more significantly affected by the presence of reflective material.
- Frequency scan (265 nm) of the irradiance produced by the sources placed at the first and last positions (i.e., at the ends of the bars), where the distribution is strongly influenced by reflection phenomena.

The results are presented below using a colour scale in which red corresponds to the maximum value in all cases considered and green represents the minimum value.

Upper Lamp

The results are shown in Figures 36, 37, and 38.

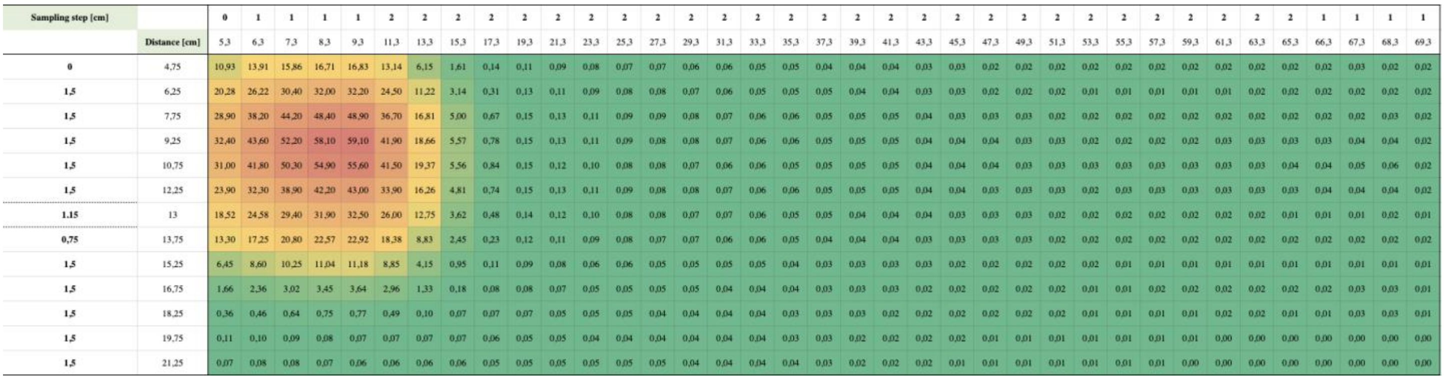

Sampling step [cm]		0	1	1	1	1	2	2	2	2	2	2	2	2	2	2	2	2	2	2	2	2	2	2	2	2	2	2	2	2	2	2	2	2	1	1	1	1
	Distance [cm]	5,3	6,3	7,3	8,3	9,3	11,3	13,3	15,3	17,3	19,3	21,3	23,3	25,3	27,3	29,3	31,3	33,3	35,3	37,3	39,3	41,3	43,3	45,3	47,3	49,3	51,3	53,3	55,3	57,3	59,3	61,3	63,3	65,3	66,3	67,3	68,3	69,3
0	4,75	10,93	13,91	15,86	16,71	16,83	13,14	6,15	1,61	0,14	0,11	0,09	0,08	0,07	0,07	0,06	0,06	0,05	0,05	0,04	0,04	0,04	0,03	0,03	0,02	0,02	0,02	0,02	0,02	0,02	0,02	0,02	0,02	0,02	0,02	0,03	0,02	0,02
1,5	6,25	20,28	26,22	30,40	32,00	32,20	24,50	11,22	3,14	0,31	0,13	0,11	0,09	0,08	0,08	0,07	0,06	0,05	0,05	0,05	0,04	0,04	0,03	0,03	0,02	0,02	0,02	0,01	0,01	0,01	0,01	0,01	0,02	0,02	0,02	0,02	0,02	0,02
1,5	7,75	28,90	38,20	44,20	48,40	48,90	36,70	16,81	5,00	0,67	0,15	0,13	0,11	0,09	0,09	0,08	0,07	0,06	0,06	0,05	0,05	0,05	0,04	0,03	0,03	0,03	0,02	0,02	0,02	0,02	0,02	0,02	0,02	0,02	0,02	0,02	0,03	0,02
1,5	9,25	32,40	43,60	52,20	58,10	59,10	41,90	18,66	5,57	0,78	0,15	0,13	0,11	0,09	0,08	0,08	0,07	0,06	0,06	0,05	0,05	0,05	0,04	0,04	0,04	0,03	0,03	0,02	0,02	0,02	0,02	0,03	0,03	0,03	0,03	0,04	0,04	0,02
1,5	10,75	31,00	41,80	50,30	54,90	55,60	41,50	19,37	5,56	0,84	0,15	0,12	0,10	0,08	0,08	0,07	0,06	0,06	0,05	0,05	0,05	0,05	0,04	0,04	0,04	0,03	0,03	0,03	0,03	0,03	0,03	0,03	0,03	0,04	0,04	0,05	0,06	0,02
1,5	12,25	23,90	32,30	38,90	42,20	43,00	33,90	16,26	4,81	0,74	0,15	0,13	0,11	0,09	0,08	0,08	0,07	0,06	0,06	0,05	0,05	0,05	0,04	0,04	0,03	0,03	0,03	0,02	0,03	0,03	0,03	0,03	0,03	0,03	0,04	0,04	0,04	0,02
1.15	13	18,52	24,58	29,40	31,90	32,50	26,00	12,75	3,62	0,48	0,14	0,12	0,10	0,08	0,08	0,07	0,07	0,06	0,05	0,05	0,04	0,04	0,04	0,03	0,03	0,03	0,02	0,02	0,02	0,02	0,02	0,02	0,02	0,01	0,01	0,01	0,02	0,01
0,75	13,75	13,30	17,25	20,80	22,57	22,92	18,38	8,83	2,45	0,23	0,12	0,11	0,09	0,08	0,07	0,07	0,06	0,06	0,05	0,04	0,04	0,04	0,03	0,03	0,03	0,03	0,02	0,02	0,02	0,02	0,02	0,02	0,02	0,02	0,02	0,02	0,02	0,02
1,5	15,25	6,45	8,60	10,25	11,04	11,18	8,85	4,15	0,95	0,11	0,09	0,08	0,06	0,06	0,05	0,05	0,05	0,05	0,04	0,03	0,03	0,03	0,03	0,02	0,02	0,02	0,02	0,02	0,01	0,01	0,01	0,01	0,01	0,01	0,01	0,01	0,01	0,01
1,5	16,75	1,66	2,36	3,02	3,45	3,64	2,96	1,33	0,18	0,08	0,08	0,07	0,05	0,05	0,05	0,05	0,04	0,04	0,04	0,03	0,03	0,03	0,02	0,02	0,02	0,02	0,02	0,01	0,01	0,02	0,02	0,02	0,02	0,02	0,02	0,03	0,03	0,01
1,5	18,25	0,36	0,46	0,64	0,75	0,77	0,49	0,10	0,07	0,07	0,07	0,05	0,05	0,05	0,04	0,04	0,04	0,04	0,03	0,03	0,03	0,02	0,02	0,02	0,02	0,02	0,02	0,01	0,01	0,01	0,01	0,02	0,02	0,01	0,01	0,03	0,03	0,01
1,5	19,75	0,11	0,10	0,09	0,08	0,07	0,07	0,07	0,07	0,06	0,05	0,05	0,04	0,04	0,04	0,04	0,04	0,04	0,03	0,03	0,02	0,02	0,02	0,02	0,01	0,01	0,01	0,01	0,01	0,01	0,01	0,00	0,00	0,00	0,00	0,00	0,00	0,00
1,5	21,25	0,07	0,08	0,08	0,07	0,06	0,06	0,06	0,06	0,05	0,05	0,05	0,05	0,05	0,05	0,04	0,04	0,04	0,04	0,03	0,02	0,02	0,02	0,01	0,01	0,01	0,01	0,01	0,01	0,01	0,00	0,00	0,00	0,00	0,00	0,00	0,00	0,00

Figure 36: Experimental map related to led 1 of the upper lamp. The maximum result is equal to ~ 55 uW/cm².

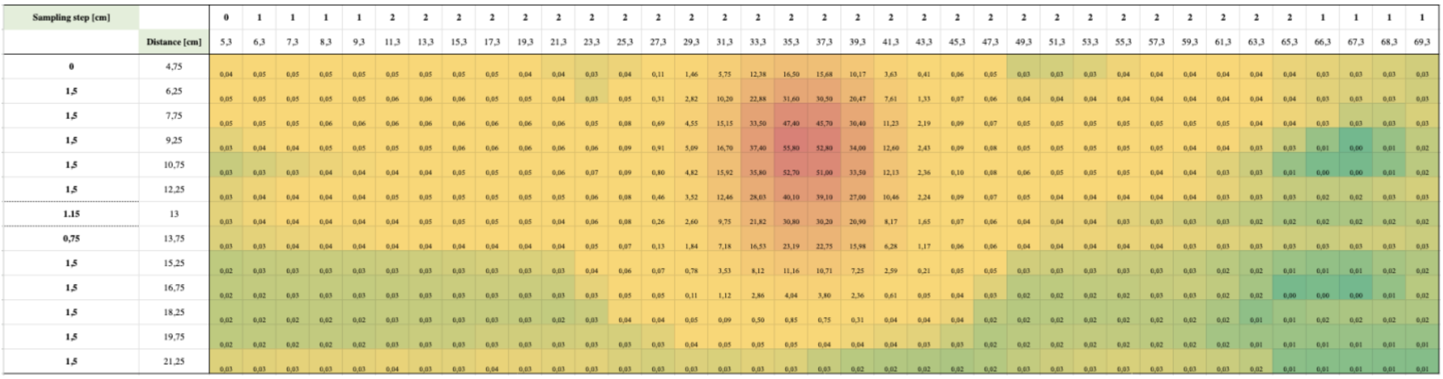

Sampling step [cm]		0	1	1	1	1	2	2	2	2	2	2	2	2	2	2	2	2	2	2	2	2	2	2	2	2	2	2	2	2	2	2	2	2	1	1	1	1
	Distance [cm]	5,3	6,3	7,3	8,3	9,3	11,3	13,3	15,3	17,3	19,3	21,3	23,3	25,3	27,3	29,3	31,3	33,3	35,3	37,3	39,3	41,3	43,3	45,3	47,3	49,3	51,3	53,3	55,3	57,3	59,3	61,3	63,3	65,3	66,3	67,3	68,3	69,3
0	4,75	0,04	0,05	0,05	0,05	0,05	0,05	0,05	0,05	0,05	0,04	0,04	0,03	0,04	0,11	1,46	5,75	12,38	16,50	15,68	10,17	3,63	0,41	0,06	0,05	0,03	0,03	0,03	0,04	0,04	0,04	0,04	0,04	0,04	0,03	0,03	0,03	0,03
1,5	6,25	0,05	0,05	0,05	0,05	0,05	0,06	0,06	0,06	0,05	0,05	0,04	0,03	0,05	0,31	2,82	10,20	22,88	31,60	30,50	20,47	7,61	1,33	0,07	0,06	0,04	0,04	0,04	0,04	0,04	0,04	0,04	0,04	0,04	0,03	0,03	0,03	0,03
1,5	7,75	0,05	0,05	0,05	0,06	0,06	0,06	0,06	0,06	0,06	0,06	0,06	0,05	0,08	0,69	4,55	15,15	33,50	47,40	45,70	30,40	11,23	2,19	0,09	0,07	0,05	0,05	0,05	0,05	0,05	0,05	0,05	0,04	0,04	0,03	0,03	0,03	0,03
1,5	9,25	0,03	0,04	0,04	0,05	0,05	0,05	0,05	0,06	0,06	0,06	0,06	0,06	0,09	0,91	5,09	16,70	37,40	55,80	52,80	34,00	12,60	2,43	0,09	0,08	0,05	0,05	0,05	0,05	0,05	0,04	0,04	0,03	0,03	0,01	0,00	0,01	0,02
1,5	10,75	0,03	0,03	0,03	0,04	0,04	0,04	0,04	0,05	0,05	0,05	0,06	0,07	0,09	0,80	4,82	15,92	35,80	52,70	51,00	33,50	12,13	2,36	0,10	0,08	0,06	0,05	0,05	0,05	0,04	0,04	0,03	0,03	0,01	0,00	0,00	0,01	0,02
1,5	12,25	0,03	0,04	0,04	0,04	0,04	0,05	0,05	0,05	0,05	0,05	0,05	0,06	0,08	0,46	3,52	12,46	28,03	40,10	39,10	27,00	10,46	2,24	0,09	0,07	0,05	0,04	0,04	0,04	0,04	0,04	0,03	0,03	0,03	0,02	0,02	0,03	0,03
1.15	13	0,03	0,04	0,04	0,04	0,04	0,04	0,05	0,05	0,05	0,05	0,04	0,06	0,08	0,26	2,60	9,75	21,82	30,80	30,20	20,90	8,17	1,65	0,07	0,06	0,04	0,04	0,04	0,03	0,03	0,03	0,03	0,02	0,02	0,02	0,02	0,02	0,02
0,75	13,75	0,03	0,03	0,04	0,04	0,04	0,04	0,04	0,04	0,04	0,04	0,04	0,05	0,07	0,13	1,84	7,18	16,53	23,19	22,75	15,98	6,28	1,17	0,06	0,06	0,04	0,04	0,04	0,04	0,04	0,03	0,03	0,03	0,03	0,03	0,03	0,03	0,03
1,5	15,25	0,02	0,03	0,03	0,03	0,03	0,03	0,03	0,03	0,03	0,03	0,03	0,04	0,06	0,07	0,78	3,53	8,12	11,16	10,71	7,25	2,59	0,21	0,05	0,05	0,03	0,03	0,03	0,03	0,03	0,03	0,02	0,02	0,01	0,01	0,01	0,02	0,02
1,5	16,75	0,02	0,02	0,03	0,03	0,03	0,03	0,03	0,03	0,03	0,03	0,03	0,03	0,05	0,05	0,11	1,12	2,86	4,04	3,80	2,36	0,61	0,05	0,04	0,03	0,02	0,02	0,02	0,02	0,03	0,03	0,02	0,02	0,00	0,00	0,00	0,01	0,02
1,5	18,25	0,02	0,02	0,02	0,02	0,02	0,03	0,03	0,03	0,03	0,03	0,02	0,03	0,04	0,04	0,05	0,09	0,50	0,85	0,75	0,31	0,04	0,04	0,04	0,02	0,02	0,02	0,02	0,02	0,02	0,02	0,02	0,01	0,01	0,02	0,02	0,02	0,02
1,5	19,75	0,02	0,02	0,02	0,02	0,02	0,03	0,03	0,03	0,03	0,03	0,03	0,03	0,03	0,03	0,04	0,05	0,05	0,05	0,04	0,04	0,04	0,03	0,03	0,02	0,02	0,02	0,02	0,02	0,02	0,02	0,02	0,01	0,01	0,01	0,01	0,01	0,01
1,5	21,25	0,03	0,03	0,03	0,03	0,03	0,04	0,03	0,03	0,04	0,03	0,03	0,03	0,03	0,03	0,03	0,03	0,03	0,03	0,03	0,02	0,02	0,02	0,02	0,02	0,03	0,03	0,03	0,03	0,03	0,03	0,03	0,02	0,01	0,01	0,01	0,01	0,01

Figure 37: Experimental map related to led 16 of the upper lamp. The maximum result is equal to ~ 56 uW/cm².

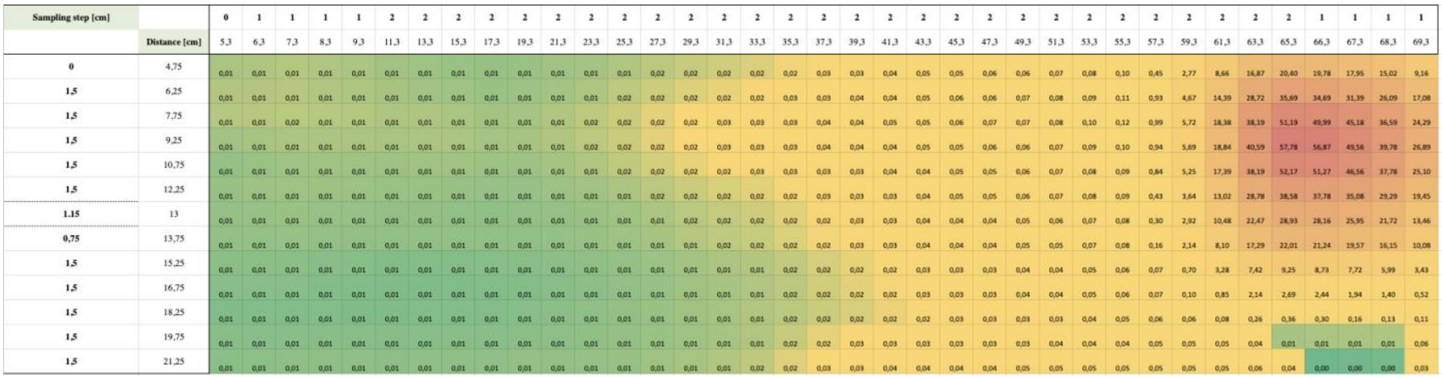

Sampling step [cm]		0	1	1	1	1	2	2	2	2	2	2	2	2	2	2	2	2	2	2	2	2	2	2	2	2	2	2	2	2	2	2	2	2	1	1	1	1
	Distance [cm]	5,3	6,3	7,3	8,3	9,3	11,3	13,3	15,3	17,3	19,3	21,3	23,3	25,3	27,3	29,3	31,3	33,3	35,3	37,3	39,3	41,3	43,3	45,3	47,3	49,3	51,3	53,3	55,3	57,3	59,3	61,3	63,3	65,3	66,3	67,3	68,3	69,3
0	4,75	0,01	0,01	0,01	0,01	0,01	0,01	0,01	0,01	0,01	0,01	0,01	0,01	0,01	0,02	0,02	0,02	0,02	0,02	0,03	0,03	0,04	0,05	0,05	0,06	0,06	0,07	0,08	0,10	0,45	2,77	8,66	16,87	20,40	19,78	17,95	15,02	9,16
1,5	6,25	0,01	0,01	0,01	0,01	0,01	0,01	0,01	0,01	0,01	0,01	0,01	0,01	0,02	0,02	0,02	0,02	0,02	0,03	0,03	0,04	0,04	0,05	0,06	0,06	0,07	0,08	0,09	0,11	0,93	4,67	14,39	28,72	35,69	34,69	31,39	26,09	17,08
1,5	7,75	0,01	0,01	0,02	0,01	0,01	0,01	0,01	0,01	0,01	0,01	0,01	0,02	0,02	0,02	0,02	0,03	0,03	0,03	0,04	0,04	0,05	0,05	0,06	0,07	0,07	0,08	0,10	0,12	0,99	5,72	18,38	38,19	51,19	49,99	45,18	36,59	24,29
1,5	9,25	0,01	0,01	0,01	0,01	0,01	0,01	0,01	0,01	0,01	0,01	0,01	0,02	0,02	0,02	0,02	0,03	0,03	0,03	0,04	0,04	0,04	0,05	0,05	0,06	0,06	0,07	0,09	0,10	0,94	5,69	18,84	40,59	57,78	56,87	49,56	39,78	26,89
1,5	10,75	0,01	0,01	0,01	0,01	0,01	0,01	0,01	0,01	0,01	0,01	0,01	0,01	0,02	0,02	0,02	0,02	0,03	0,03	0,03	0,03	0,04	0,04	0,05	0,05	0,06	0,07	0,08	0,09	0,84	5,25	17,39	38,19	52,17	51,27	46,56	37,78	25,10
1,5	12,25	0,01	0,01	0,01	0,01	0,01	0,01	0,01	0,01	0,01	0,01	0,01	0,01	0,01	0,02	0,02	0,02	0,02	0,02	0,03	0,03	0,03	0,04	0,05	0,05	0,06	0,07	0,08	0,09	0,43	3,64	13,02	28,78	38,58	37,78	35,08	29,29	19,45
1.15	13	0,01	0,01	0,01	0,01	0,01	0,01	0,01	0,01	0,01	0,01	0,01	0,01	0,01	0,01	0,02	0,02	0,02	0,02	0,02	0,03	0,03	0,04	0,04	0,04	0,05	0,06	0,07	0,08	0,30	2,92	10,48	22,47	28,93	28,16	25,95	21,72	13,46
0,75	13,75	0,01	0,01	0,01	0,01	0,01	0,01	0,01	0,01	0,01	0,01	0,01	0,01	0,01	0,01	0,01	0,02	0,02	0,02	0,02	0,03	0,03	0,04	0,04	0,04	0,05	0,05	0,07	0,08	0,16	2,14	8,10	17,29	22,01	21,24	19,57	16,15	10,08
1,5	15,25	0,01	0,01	0,01	0,01	0,01	0,01	0,01	0,01	0,01	0,01	0,01	0,01	0,01	0,01	0,01	0,01	0,01	0,02	0,02	0,02	0,02	0,03	0,03	0,03	0,04	0,04	0,05	0,06	0,07	0,70	3,28	7,42	9,25	8,73	7,72	5,99	3,43
1,5	16,75	0,01	0,01	0,01	0,01	0,01	0,01	0,01	0,01	0,01	0,01	0,01	0,01	0,01	0,01	0,01	0,01	0,01	0,02	0,02	0,02	0,02	0,03	0,03	0,03	0,04	0,04	0,05	0,06	0,07	0,10	0,85	2,14	2,69	2,44	1,94	1,40	0,52
1,5	18,25	0,01	0,01	0,01	0,01	0,01	0,01	0,01	0,01	0,01	0,01	0,01	0,01	0,01	0,01	0,01	0,01	0,01	0,02	0,02	0,02	0,02	0,02	0,03	0,03	0,03	0,03	0,04	0,05	0,06	0,06	0,08	0,26	0,36	0,30	0,16	0,13	0,11
1,5	19,75	0,01	0,01	0,01	0,01	0,01	0,01	0,01	0,01	0,01	0,01	0,01	0,01	0,01	0,01	0,01	0,01	0,01	0,02	0,02	0,03	0,03	0,03	0,03	0,03	0,03	0,04	0,04	0,04	0,05	0,05	0,05	0,04	0,01	0,01	0,01	0,01	0,06
1,5	21,25	0,01	0,01	0,01	0,01	0,01	0,01	0,01	0,01	0,01	0,01	0,01	0,01	0,01	0,01	0,01	0,01	0,02	0,02	0,03	0,03	0,04	0,04	0,04	0,04	0,05	0,05	0,05	0,05	0,05	0,05	0,05	0,06	0,04	0,00	0,00	0,00	0,03

Figure 38: Experimental map related to led 32 of the upper lamp. The maximum result is equal to ~ 57 uW/cm².

Central Lamp

The results are presented in Figures 39, 40, and 41. It should be noted that, during the acquisition campaign, the first LED experienced degradation that compromised its functionality. Therefore, to ensure the continuity of the measurements, the second LED on the same bar was selected as an alternative reference.

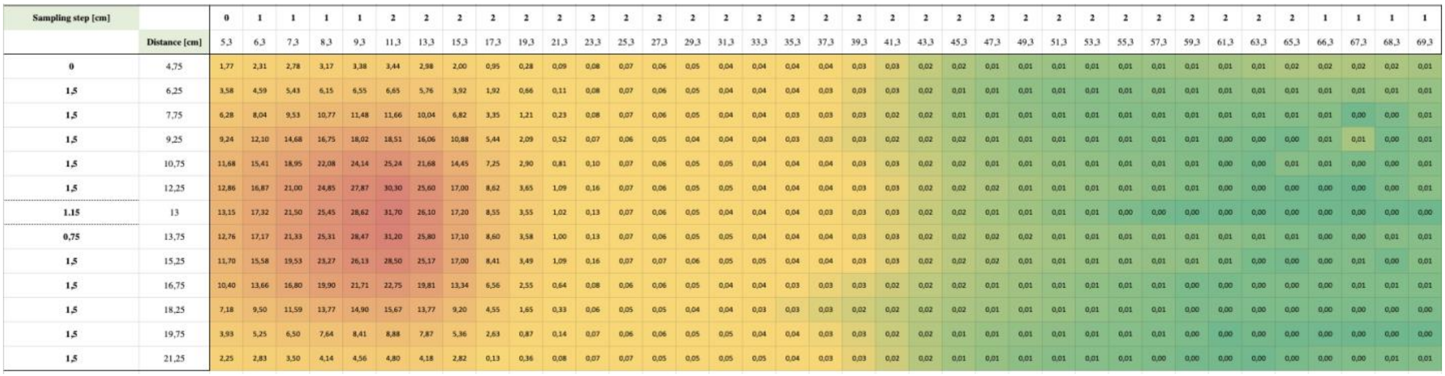

Sampling step [cm]		0	1	1	1	1	2	2	2	2	2	2	2	2	2	2	2	2	2	2	2	2	2	2	2	2	2	2	2	2	2	2	2	2	1	1	1	1
	Distance [cm]	5,3	6,3	7,3	8,3	9,3	11,3	13,3	15,3	17,3	19,3	21,3	23,3	25,3	27,3	29,3	31,3	33,3	35,3	37,3	39,3	41,3	43,3	45,3	47,3	49,3	51,3	53,3	55,3	57,3	59,3	61,3	63,3	65,3	66,3	67,3	68,3	69,3
0	4,75	1,77	2,31	2,78	3,17	3,38	3,44	2,98	2,00	0,95	0,28	0,09	0,08	0,07	0,06	0,05	0,04	0,04	0,04	0,04	0,03	0,03	0,02	0,02	0,01	0,01	0,01	0,01	0,01	0,01	0,01	0,01	0,01	0,02	0,02	0,02	0,02	0,01
1,5	6,25	3,58	4,59	5,43	6,15	6,55	6,65	5,76	3,92	1,92	0,66	0,11	0,08	0,07	0,06	0,05	0,04	0,04	0,04	0,03	0,03	0,03	0,02	0,01	0,01	0,01	0,01	0,01	0,01	0,01	0,01	0,01	0,01	0,01	0,01	0,01	0,01	0,01
1,5	7,75	6,28	8,04	9,53	10,77	11,48	11,66	10,04	6,82	3,35	1,21	0,23	0,08	0,07	0,06	0,05	0,04	0,04	0,03	0,03	0,03	0,02	0,02	0,01	0,01	0,01	0,01	0,01	0,01	0,01	0,01	0,01	0,01	0,01	0,01	0,00	0,00	0,01
1,5	9,25	9,24	12,10	14,68	16,75	18,02	18,51	16,06	10,88	5,44	2,09	0,52	0,07	0,06	0,05	0,04	0,04	0,04	0,03	0,03	0,03	0,02	0,02	0,02	0,01	0,01	0,01	0,01	0,01	0,01	0,01	0,00	0,00	0,00	0,01	0,01	0,00	0,01
1,5	10,75	11,68	15,41	18,95	22,08	24,14	25,24	21,68	14,45	7,25	2,90	0,81	0,10	0,07	0,06	0,05	0,05	0,04	0,04	0,04	0,03	0,03	0,02	0,02	0,01	0,01	0,01	0,01	0,01	0,01	0,01	0,00	0,00	0,01	0,01	0,00	0,00	0,01
1,5	12,25	12,86	16,87	21,00	24,85	27,87	30,30	25,60	17,00	8,62	3,65	1,09	0,16	0,07	0,06	0,05	0,05	0,04	0,04	0,04	0,03	0,03	0,02	0,02	0,02	0,01	0,01	0,01	0,01	0,01	0,01	0,00	0,00	0,00	0,00	0,00	0,00	0,01
1.15	13	13,15	17,32	21,50	25,45	28,62	31,70	26,10	17,20	8,55	3,55	1,02	0,13	0,07	0,06	0,05	0,04	0,04	0,04	0,03	0,03	0,03	0,02	0,02	0,01	0,01	0,01	0,01	0,00	0,00	0,00	0,00	0,00	0,00	0,00	0,00	0,00	0,00
0,75	13,75	12,76	17,17	21,33	25,31	28,47	31,20	25,80	17,10	8,60	3,58	1,00	0,13	0,07	0,06	0,05	0,05	0,04	0,04	0,04	0,03	0,03	0,02	0,02	0,02	0,02	0,01	0,01	0,01	0,01	0,01	0,01	0,01	0,01	0,00	0,00	0,01	0,01
1,5	15,25	11,70	15,58	19,53	23,27	26,13	28,50	25,17	17,00	8,41	3,49	1,09	0,16	0,07	0,07	0,06	0,05	0,05	0,04	0,04	0,03	0,03	0,02	0,02	0,02	0,01	0,01	0,01	0,01	0,01	0,01	0,01	0,00	0,00	0,00	0,01	0,00	0,01
1,5	16,75	10,40	13,66	16,80	19,90	21,71	22,75	19,81	13,34	6,56	2,55	0,64	0,08	0,06	0,06	0,05	0,04	0,04	0,03	0,03	0,03	0,02	0,02	0,02	0,01	0,01	0,01	0,01	0,01	0,01	0,00	0,00	0,00	0,00	0,00	0,01	0,01	0,01
1,5	18,25	7,18	9,50	11,59	13,77	14,90	15,67	13,77	9,20	4,55	1,65	0,33	0,06	0,05	0,05	0,04	0,04	0,03	0,03	0,03	0,02	0,02	0,02	0,02	0,01	0,01	0,01	0,01	0,01	0,01	0,00	0,00	0,00	0,00	0,00	0,00	0,00	0,00
1,5	19,75	3,93	5,25	6,50	7,64	8,41	8,88	7,87	5,36	2,63	0,87	0,14	0,07	0,06	0,06	0,05	0,05	0,04	0,04	0,03	0,03	0,02	0,02	0,01	0,01	0,01	0,01	0,01	0,01	0,01	0,00	0,00	0,00	0,00	0,00	0,00	0,00	0,00
1,5	21,25	2,25	2,83	3,50	4,14	4,56	4,80	4,18	2,82	0,13	0,36	0,08	0,07	0,07	0,05	0,05	0,05	0,05	0,04	0,03	0,03	0,02	0,02	0,01	0,01	0,01	0,01	0,01	0,01	0,00	0,00	0,00	0,00	0,00	0,00	0,00	0,01	0,01

Figure 39: Experimental map related to led 2 of the central lamp. The maximum result is equal to ~ 32 uW/cm².

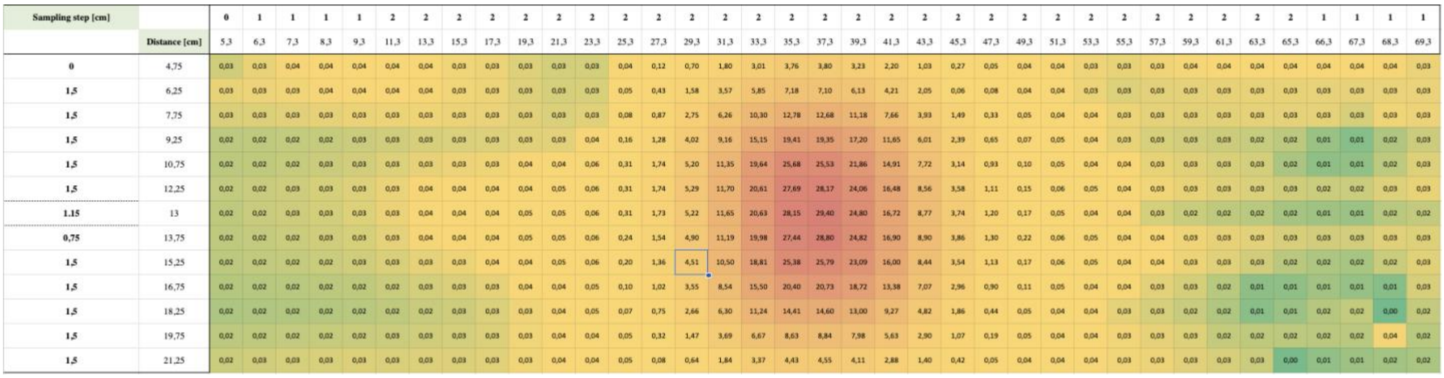

Sampling step [cm]		0	1	1	1	1	2	2	2	2	2	2	2	2	2	2	2	2	2	2	2	2	2	2	2	2	2	2	2	2	2	2	2	2	1	1	1	1
	Distance [cm]	5,3	6,3	7,3	8,3	9,3	11,3	13,3	15,3	17,3	19,3	21,3	23,3	25,3	27,3	29,3	31,3	33,3	35,3	37,3	39,3	41,3	43,3	45,3	47,3	49,3	51,3	53,3	55,3	57,3	59,3	61,3	63,3	65,3	66,3	67,3	68,3	69,3
0	4,75	0,03	0,03	0,04	0,04	0,04	0,04	0,04	0,03	0,03	0,03	0,03	0,03	0,04	0,12	0,70	1,80	3,01	3,76	3,80	3,23	2,20	1,03	0,27	0,05	0,04	0,04	0,03	0,03	0,03	0,04	0,04	0,04	0,04	0,04	0,04	0,04	0,03
1,5	6,25	0,03	0,03	0,03	0,04	0,04	0,04	0,04	0,03	0,03	0,03	0,03	0,03	0,05	0,43	1,58	3,57	5,85	7,18	7,10	6,13	4,21	2,05	0,06	0,08	0,04	0,04	0,03	0,03	0,03	0,03	0,03	0,03	0,03	0,03	0,03	0,03	0,03
1,5	7,75	0,03	0,03	0,03	0,03	0,03	0,03	0,03	0,03	0,03	0,03	0,03	0,03	0,08	0,87	2,75	6,26	10,30	12,78	12,68	11,18	7,66	3,93	1,49	0,33	0,05	0,04	0,04	0,03	0,03	0,03	0,03	0,03	0,03	0,03	0,03	0,03	0,03
1,5	9,25	0,02	0,02	0,02	0,02	0,03	0,03	0,03	0,03	0,03	0,03	0,03	0,04	0,16	1,28	4,02	9,16	15,15	19,41	19,35	17,20	11,65	6,01	2,39	0,65	0,07	0,05	0,04	0,03	0,03	0,03	0,03	0,02	0,02	0,01	0,01	0,02	0,03
1,5	10,75	0,02	0,02	0,02	0,03	0,03	0,03	0,03	0,03	0,03	0,04	0,04	0,06	0,31	1,74	5,20	11,35	19,64	25,68	25,53	21,86	14,91	7,72	3,14	0,93	0,10	0,05	0,04	0,04	0,03	0,03	0,03	0,03	0,02	0,01	0,01	0,02	0,03
1,5	12,25	0,02	0,02	0,03	0,03	0,03	0,03	0,04	0,04	0,04	0,04	0,05	0,06	0,31	1,74	5,29	11,70	20,61	27,69	28,17	24,06	16,48	8,56	3,58	1,11	0,15	0,06	0,05	0,04	0,03	0,03	0,03	0,03	0,03	0,02	0,02	0,03	0,03
1.15	13	0,02	0,02	0,03	0,03	0,03	0,03	0,04	0,04	0,04	0,05	0,05	0,06	0,31	1,73	5,22	11,65	20,63	28,15	29,40	24,80	16,72	8,77	3,74	1,20	0,17	0,05	0,04	0,04	0,03	0,02	0,02	0,02	0,02	0,01	0,01	0,02	0,02
0,75	13,75	0,02	0,02	0,02	0,03	0,03	0,03	0,04	0,04	0,04	0,05	0,05	0,06	0,24	1,54	4,90	11,19	19,98	27,44	28,80	24,82	16,90	8,90	3,86	1,30	0,22	0,06	0,05	0,04	0,04	0,03	0,03	0,03	0,03	0,03	0,03	0,03	0,03
1,5	15,25	0,02	0,02	0,02	0,02	0,03	0,03	0,03	0,03	0,04	0,04	0,05	0,06	0,20	1,36	4,51	10,50	18,81	25,38	25,79	23,09	16,00	8,44	3,54	1,13	0,17	0,06	0,05	0,04	0,04	0,03	0,03	0,03	0,02	0,02	0,02	0,02	0,03
1,5	16,75	0,02	0,02	0,02	0,02	0,02	0,02	0,03	0,03	0,03	0,04	0,04	0,05	0,10	1,02	3,55	8,54	15,50	20,40	20,73	18,72	13,38	7,07	2,96	0,90	0,11	0,05	0,04	0,04	0,03	0,03	0,02	0,01	0,01	0,01	0,01	0,01	0,03
1,5	18,25	0,02	0,02	0,02	0,02	0,02	0,02	0,02	0,03	0,03	0,03	0,04	0,05	0,07	0,75	2,66	6,30	11,24	14,41	14,60	13,00	9,27	4,82	1,86	0,44	0,05	0,04	0,04	0,03	0,03	0,02	0,02	0,01	0,01	0,02	0,02	0,00	0,02
1,5	19,75	0,02	0,02	0,02	0,02	0,02	0,03	0,03	0,03	0,03	0,03	0,04	0,04	0,05	0,32	1,47	3,69	6,67	8,63	8,84	7,98	5,63	2,90	1,07	0,19	0,05	0,04	0,04	0,03	0,03	0,03	0,02	0,02	0,02	0,02	0,02	0,04	0,02
1,5	21,25	0,02	0,03	0,03	0,03	0,03	0,03	0,03	0,03	0,03	0,03	0,04	0,04	0,05	0,08	0,64	1,84	3,37	4,43	4,55	4,11	2,88	1,40	0,42	0,05	0,04	0,04	0,04	0,03	0,03	0,03	0,03	0,03	0,00	0,01	0,01	0,02	0,02

Figure 40: Experimental map related to led 16 of the central lamp. The maximum result is equal to ~ 30 uW/cm².

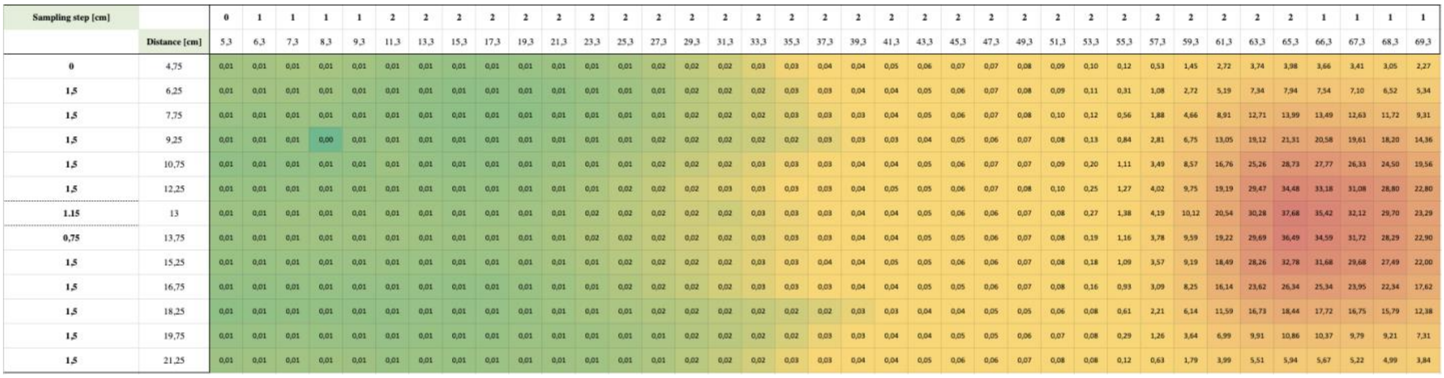

Sampling step [cm]		0	1	1	1	1	2	2	2	2	2	2	2	2	2	2	2	2	2	2	2	2	2	2	2	2	2	2	2	2	2	2	2	2	1	1	1	1
	Distance [cm]	5,3	6,3	7,3	8,3	9,3	11,3	13,3	15,3	17,3	19,3	21,3	23,3	25,3	27,3	29,3	31,3	33,3	35,3	37,3	39,3	41,3	43,3	45,3	47,3	49,3	51,3	53,3	55,3	57,3	59,3	61,3	63,3	65,3	66,3	67,3	68,3	69,3
0	4,75	0,01	0,01	0,01	0,01	0,01	0,01	0,01	0,01	0,01	0,01	0,01	0,01	0,01	0,02	0,02	0,02	0,03	0,03	0,04	0,04	0,05	0,06	0,07	0,07	0,08	0,09	0,10	0,12	0,53	1,45	2,72	3,74	3,98	3,66	3,41	3,05	2,27
1,5	6,25	0,01	0,01	0,01	0,01	0,01	0,01	0,01	0,01	0,01	0,01	0,01	0,01	0,01	0,01	0,02	0,02	0,02	0,03	0,03	0,04	0,04	0,05	0,06	0,07	0,08	0,09	0,11	0,31	1,08	2,72	5,19	7,34	7,94	7,54	7,10	6,52	5,34
1,5	7,75	0,01	0,01	0,01	0,01	0,01	0,01	0,01	0,01	0,01	0,01	0,01	0,01	0,01	0,01	0,02	0,02	0,02	0,03	0,03	0,03	0,04	0,05	0,06	0,07	0,08	0,10	0,12	0,56	1,88	4,66	8,91	12,71	13,99	13,49	12,63	11,72	9,31
1,5	9,25	0,01	0,01	0,01	0,00	0,01	0,01	0,01	0,01	0,01	0,01	0,01	0,01	0,01	0,02	0,02	0,02	0,02	0,02	0,03	0,03	0,03	0,04	0,05	0,06	0,07	0,08	0,13	0,84	2,81	6,75	13,05	19,12	21,31	20,58	19,61	18,20	14,36
1,5	10,75	0,01	0,01	0,01	0,01	0,01	0,01	0,01	0,01	0,01	0,01	0,01	0,01	0,01	0,02	0,02	0,02	0,03	0,03	0,03	0,04	0,04	0,05	0,06	0,07	0,07	0,09	0,20	1,11	3,49	8,57	16,76	25,26	28,73	27,77	26,33	24,50	19,56
1,5	12,25	0,01	0,01	0,01	0,01	0,01	0,01	0,01	0,01	0,01	0,01	0,01	0,01	0,02	0,02	0,02	0,03	0,03	0,03	0,03	0,04	0,05	0,05	0,06	0,07	0,08	0,10	0,25	1,27	4,02	9,75	19,19	29,47	34,48	33,18	31,08	28,80	22,80
1.15	13	0,01	0,01	0,01	0,01	0,01	0,01	0,01	0,01	0,01	0,01	0,01	0,02	0,02	0,02	0,02	0,02	0,03	0,03	0,03	0,04	0,04	0,05	0,06	0,06	0,07	0,08	0,27	1,38	4,19	10,12	20,54	30,28	37,68	35,42	32,12	29,70	23,29
0,75	13,75	0,01	0,01	0,01	0,01	0,01	0,01	0,01	0,01	0,01	0,01	0,01	0,02	0,02	0,02	0,02	0,02	0,03	0,03	0,03	0,04	0,04	0,05	0,05	0,06	0,07	0,08	0,19	1,16	3,78	9,59	19,22	29,69	36,49	34,59	31,72	28,29	22,90
1,5	15,25	0,01	0,01	0,01	0,01	0,01	0,01	0,01	0,01	0,01	0,01	0,01	0,01	0,02	0,02	0,02	0,02	0,03	0,03	0,04	0,04	0,05	0,05	0,06	0,06	0,07	0,08	0,18	1,09	3,57	9,19	18,49	28,26	32,78	31,68	29,68	27,49	22,00
1,5	16,75	0,01	0,01	0,01	0,01	0,01	0,01	0,01	0,01	0,01	0,01	0,01	0,01	0,02	0,02	0,02	0,02	0,03	0,03	0,03	0,04	0,04	0,05	0,05	0,06	0,07	0,08	0,16	0,93	3,09	8,25	16,14	23,62	26,34	25,34	23,95	22,34	17,62
1,5	18,25	0,01	0,01	0,01	0,01	0,01	0,01	0,01	0,01	0,01	0,01	0,01	0,01	0,01	0,02	0,02	0,02	0,02	0,02	0,02	0,03	0,03	0,04	0,04	0,05	0,05	0,06	0,08	0,61	2,21	6,14	11,59	16,73	18,44	17,72	16,75	15,79	12,38
1,5	19,75	0,01	0,01	0,01	0,01	0,01	0,01	0,01	0,01	0,01	0,01	0,01	0,01	0,01	0,01	0,02	0,02	0,02	0,02	0,03	0,03	0,04	0,04	0,05	0,05	0,06	0,07	0,08	0,29	1,26	3,64	6,99	9,91	10,86	10,37	9,79	9,21	7,31
1,5	21,25	0,01	0,01	0,01	0,01	0,01	0,01	0,01	0,01	0,01	0,01	0,01	0,01	0,01	0,01	0,02	0,02	0,02	0,03	0,03	0,04	0,04	0,05	0,06	0,06	0,07	0,08	0,08	0,12	0,63	1,79	3,99	5,51	5,94	5,67	5,22	4,99	3,84

Figure 41: Experimental map related to led 32 of the central lamp. The maximum result is equal to ~ 38 uW/cm².

Lower Lamp

The results are shown in Figures 42, 43, and 44.

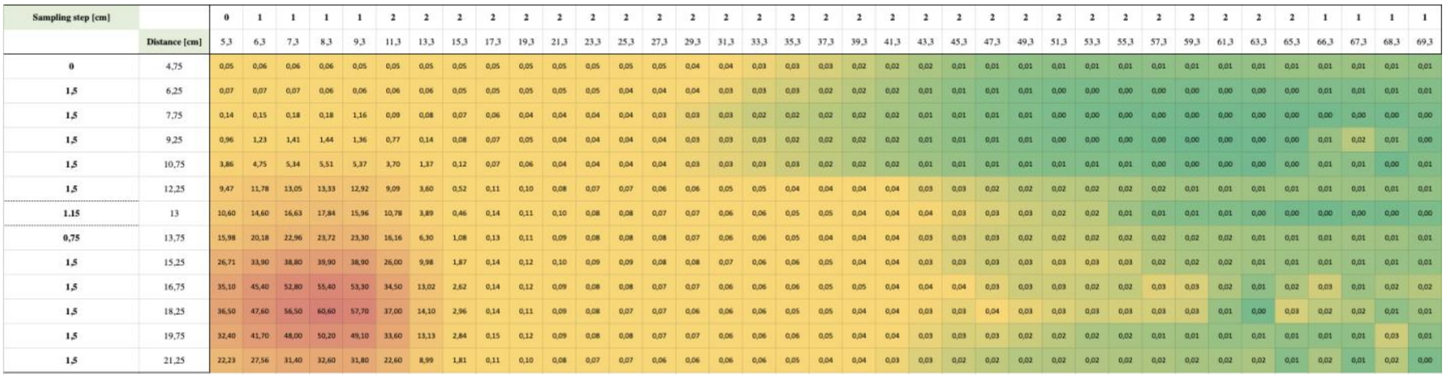

Sampling step [cm]		0	1	1	1	1	2	2	2	2	2	2	2	2	2	2	2	2	2	2	2	2	2	2	2	2	2	2	2	2	2	2	2	2	1	1	1	1
	Distance [cm]	5,3	6,3	7,3	8,3	9,3	11,3	13,3	15,3	17,3	19,3	21,3	23,3	25,3	27,3	29,3	31,3	33,3	35,3	37,3	39,3	41,3	43,3	45,3	47,3	49,3	51,3	53,3	55,3	57,3	59,3	61,3	63,3	65,3	66,3	67,3	68,3	69,3
0	4,75	0,05	0,06	0,06	0,06	0,05	0,05	0,05	0,05	0,05	0,05	0,05	0,05	0,05	0,05	0,04	0,04	0,03	0,03	0,03	0,02	0,02	0,02	0,01	0,01	0,01	0,01	0,01	0,01	0,01	0,01	0,01	0,01	0,01	0,01	0,01	0,01	0,01
1,5	6,25	0,07	0,07	0,07	0,06	0,06	0,06	0,06	0,05	0,05	0,05	0,05	0,05	0,04	0,04	0,04	0,03	0,03	0,03	0,02	0,02	0,02	0,01	0,01	0,01	0,01	0,00	0,00	0,00	0,00	0,00	0,00	0,00	0,00	0,01	0,01	0,01	0,01
1,5	7,75	0,14	0,15	0,18	0,18	1,16	0,09	0,08	0,07	0,06	0,04	0,04	0,04	0,04	0,03	0,03	0,03	0,02	0,02	0,02	0,02	0,02	0,01	0,01	0,01	0,01	0,00	0,00	0,00	0,00	0,00	0,00	0,00	0,00	0,00	0,00	0,00	0,00
1,5	9,25	0,96	1,23	1,41	1,44	1,36	0,77	0,14	0,08	0,07	0,05	0,04	0,04	0,04	0,04	0,03	0,03	0,03	0,02	0,02	0,02	0,02	0,01	0,01	0,01	0,01	0,00	0,00	0,00	0,00	0,00	0,00	0,00	0,00	0,01	0,02	0,01	0,00
1,5	10,75	3,86	4,75	5,34	5,51	5,37	3,70	1,37	0,12	0,07	0,06	0,04	0,04	0,04	0,04	0,03	0,03	0,03	0,03	0,02	0,02	0,02	0,01	0,01	0,01	0,01	0,01	0,01	0,01	0,00	0,00	0,00	0,00	0,00	0,01	0,01	0,00	0,01
1,5	12,25	9,47	11,78	13,05	13,33	12,92	9,09	3,60	0,52	0,11	0,10	0,08	0,07	0,07	0,06	0,06	0,05	0,05	0,04	0,04	0,04	0,04	0,03	0,03	0,02	0,02	0,02	0,02	0,02	0,02	0,01	0,01	0,01	0,01	0,01	0,01	0,01	0,01
1.15	13	10,60	14,60	16,63	17,84	15,96	10,78	3,89	0,46	0,14	0,11	0,10	0,08	0,08	0,07	0,07	0,06	0,06	0,05	0,05	0,04	0,04	0,04	0,03	0,03	0,03	0,02	0,02	0,01	0,01	0,01	0,01	0,00	0,00	0,00	0,00	0,00	0,00
0,75	13,75	15,98	20,18	22,96	23,72	23,30	16,16	6,30	1,08	0,13	0,11	0,09	0,08	0,08	0,08	0,07	0,06	0,06	0,05	0,04	0,04	0,04	0,03	0,03	0,03	0,02	0,02	0,02	0,02	0,02	0,02	0,02	0,01	0,01	0,01	0,01	0,01	0,01
1,5	15,25	26,71	33,90	38,80	39,90	38,90	26,00	9,98	1,87	0,14	0,12	0,10	0,09	0,09	0,08	0,08	0,07	0,06	0,06	0,05	0,04	0,04	0,03	0,03	0,03	0,03	0,03	0,03	0,03	0,02	0,02	0,02	0,01	0,01	0,01	0,01	0,01	0,01
1,5	16,75	35,10	45,40	52,80	55,40	53,30	34,50	13,02	2,62	0,14	0,12	0,09	0,08	0,08	0,07	0,07	0,06	0,06	0,06	0,05	0,05	0,04	0,04	0,04	0,03	0,03	0,03	0,02	0,02	0,03	0,03	0,02	0,01	0,02	0,03	0,01	0,02	0,02
1,5	18,25	36,50	47,60	56,50	60,60	57,70	37,00	14,10	2,96	0,14	0,11	0,09	0,08	0,07	0,07	0,06	0,06	0,06	0,05	0,05	0,04	0,04	0,03	0,03	0,04	0,03	0,03	0,03	0,03	0,03	0,03	0,01	0,00	0,03	0,02	0,02	0,01	0,01
1,5	19,75	32,40	41,70	48,00	50,20	49,10	33,60	13,13	2,84	0,15	0,12	0,09	0,08	0,08	0,07	0,07	0,06	0,06	0,06	0,05	0,04	0,04	0,03	0,03	0,03	0,02	0,02	0,02	0,02	0,01	0,01	0,01	0,01	0,01	0,01	0,01	0,03	0,01
1,5	21,25	22,23	27,56	31,40	32,60	31,80	22,60	8,99	1,81	0,11	0,10	0,08	0,07	0,07	0,06	0,06	0,06	0,06	0,05	0,04	0,04	0,03	0,03	0,02	0,02	0,02	0,02	0,02	0,02	0,02	0,02	0,02	0,02	0,01	0,02	0,01	0,02	0,00

Figure 42: Experimental map related to led 1 of th lower lamp. The maximum result is equal to ~ 60 uW/cm².

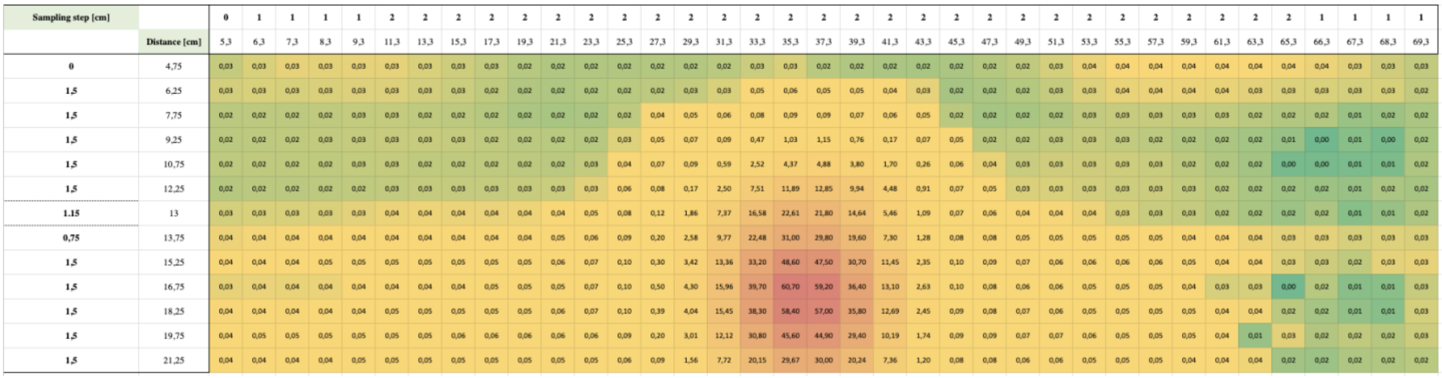

Sampling step [cm]		0	1	1	1	1	2	2	2	2	2	2	2	2	2	2	2	2	2	2	2	2	2	2	2	2	2	2	2	2	2	2	2	2	1	1	1	1
	Distance [cm]	5,3	6,3	7,3	8,3	9,3	11,3	13,3	15,3	17,3	19,3	21,3	23,3	25,3	27,3	29,3	31,3	33,3	35,3	37,3	39,3	41,3	43,3	45,3	47,3	49,3	51,3	53,3	55,3	57,3	59,3	61,3	63,3	65,3	66,3	67,3	68,3	69,3
0	4,75	0,03	0,03	0,03	0,03	0,03	0,03	0,03	0,03	0,03	0,02	0,02	0,02	0,02	0,02	0,02	0,02	0,03	0,03	0,02	0,02	0,02	0,02	0,02	0,02	0,02	0,03	0,04	0,04	0,04	0,04	0,04	0,04	0,04	0,04	0,03	0,03	0,03
1,5	6,25	0,03	0,03	0,03	0,03	0,03	0,03	0,03	0,03	0,02	0,02	0,02	0,02	0,02	0,02	0,03	0,03	0,05	0,06	0,05	0,05	0,04	0,03	0,02	0,02	0,02	0,03	0,03	0,04	0,04	0,04	0,04	0,03	0,03	0,03	0,03	0,03	0,02
1,5	7,75	0,02	0,02	0,02	0,02	0,03	0,03	0,02	0,02	0,02	0,02	0,02	0,02	0,02	0,04	0,05	0,06	0,08	0,09	0,09	0,07	0,06	0,05	0,02	0,02	0,02	0,02	0,03	0,03	0,03	0,03	0,03	0,02	0,02	0,02	0,01	0,02	0,02
1,5	9,25	0,02	0,02	0,02	0,03	0,03	0,03	0,03	0,03	0,02	0,02	0,02	0,02	0,03	0,05	0,07	0,09	0,47	1,03	1,15	0,76	0,17	0,07	0,05	0,02	0,02	0,03	0,03	0,03	0,02	0,02	0,02	0,02	0,01	0,00	0,01	0,00	0,02
1,5	10,75	0,02	0,02	0,02	0,02	0,03	0,03	0,02	0,02	0,02	0,02	0,02	0,03	0,04	0,07	0,09	0,59	2,52	4,37	4,88	3,80	1,70	0,26	0,06	0,04	0,03	0,03	0,03	0,03	0,03	0,02	0,02	0,02	0,00	0,00	0,01	0,01	0,02
1,5	12,25	0,02	0,02	0,02	0,02	0,02	0,03	0,03	0,03	0,03	0,03	0,03	0,03	0,06	0,08	0,17	2,50	7,51	11,89	12,85	9,94	4,48	0,91	0,07	0,05	0,03	0,03	0,03	0,03	0,03	0,03	0,02	0,02	0,02	0,02	0,01	0,02	0,02
1.15	13	0,03	0,03	0,03	0,03	0,03	0,04	0,04	0,04	0,04	0,04	0,04	0,05	0,08	0,12	1,86	7,37	16,58	22,61	21,80	14,64	5,46	1,09	0,07	0,06	0,04	0,04	0,04	0,03	0,03	0,03	0,02	0,02	0,02	0,02	0,01	0,01	0,02
0,75	13,75	0,04	0,04	0,04	0,04	0,04	0,04	0,04	0,04	0,04	0,04	0,05	0,06	0,09	0,20	2,58	9,77	22,48	31,00	29,80	19,60	7,30	1,28	0,08	0,08	0,05	0,05	0,05	0,05	0,05	0,04	0,04	0,04	0,03	0,03	0,03	0,03	0,03
1,5	15,25	0,04	0,04	0,04	0,05	0,05	0,05	0,05	0,05	0,05	0,05	0,06	0,07	0,10	0,30	3,42	13,36	33,20	48,60	47,50	30,70	11,45	2,35	0,10	0,09	0,07	0,06	0,06	0,06	0,06	0,05	0,04	0,04	0,03	0,03	0,02	0,03	0,03
1,5	16,75	0,03	0,04	0,04	0,04	0,04	0,04	0,04	0,04	0,05	0,05	0,05	0,07	0,10	0,50	4,30	15,96	39,70	60,70	59,20	36,40	13,10	2,63	0,10	0,08	0,06	0,06	0,05	0,05	0,05	0,04	0,03	0,03	0,00	0,02	0,01	0,01	0,03
1,5	18,25	0,04	0,04	0,04	0,04	0,04	0,05	0,05	0,05	0,05	0,05	0,06	0,07	0,10	0,39	4,04	15,45	38,30	58,40	57,00	35,80	12,69	2,45	0,09	0,08	0,07	0,06	0,05	0,05	0,05	0,05	0,04	0,04	0,02	0,02	0,01	0,01	0,03
1,5	19,75	0,04	0,05	0,05	0,05	0,05	0,05	0,05	0,06	0,06	0,06	0,06	0,06	0,09	0,20	3,01	12,12	30,80	45,60	44,90	29,40	10,19	1,74	0,09	0,09	0,07	0,07	0,06	0,05	0,05	0,05	0,04	0,01	0,03	0,02	0,02	0,02	0,03
1,5	21,25	0,04	0,04	0,04	0,04	0,05	0,05	0,05	0,05	0,05	0,05	0,05	0,05	0,06	0,09	1,56	7,72	20,15	29,67	30,00	20,24	7,36	1,20	0,08	0,08	0,06	0,06	0,05	0,05	0,05	0,04	0,04	0,04	0,02	0,02	0,02	0,02	0,02

Figure 43: Experimental map related to led 16 of th lower lamp. The maximum result is equal to ~ 61 uW/cm².

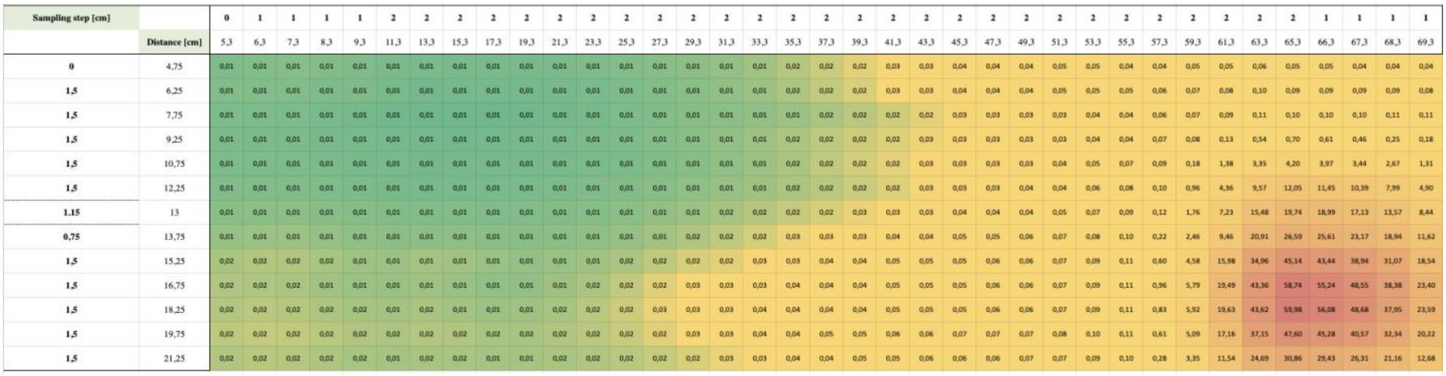

Sampling step [cm]		0	1	1	1	1	2	2	2	2	2	2	2	2	2	2	2	2	2	2	2	2	2	2	2	2	2	2	2	2	2	2	2	2	1	1	1	1
	Distance [cm]	5,3	6,3	7,3	8,3	9,3	11,3	13,3	15,3	17,3	19,3	21,3	23,3	25,3	27,3	29,3	31,3	33,3	35,3	37,3	39,3	41,3	43,3	45,3	47,3	49,3	51,3	53,3	55,3	57,3	59,3	61,3	63,3	65,3	66,3	67,3	68,3	69,3
0	4,75	0,01	0,01	0,01	0,01	0,01	0,01	0,01	0,01	0,01	0,01	0,01	0,01	0,01	0,01	0,01	0,01	0,01	0,02	0,02	0,02	0,03	0,03	0,04	0,04	0,04	0,05	0,05	0,04	0,04	0,05	0,05	0,06	0,05	0,05	0,04	0,04	0,04
1,5	6,25	0,01	0,01	0,01	0,01	0,01	0,01	0,01	0,01	0,01	0,01	0,01	0,01	0,01	0,01	0,01	0,01	0,01	0,02	0,02	0,02	0,03	0,03	0,04	0,04	0,04	0,05	0,05	0,05	0,06	0,07	0,08	0,10	0,09	0,09	0,09	0,09	0,08
1,5	7,75	0,01	0,01	0,01	0,01	0,01	0,01	0,01	0,01	0,01	0,01	0,01	0,01	0,01	0,01	0,01	0,01	0,01	0,01	0,02	0,02	0,02	0,02	0,03	0,03	0,03	0,03	0,04	0,04	0,06	0,07	0,09	0,11	0,10	0,10	0,10	0,11	0,11
1,5	9,25	0,01	0,01	0,01	0,01	0,01	0,01	0,01	0,01	0,01	0,01	0,01	0,01	0,01	0,01	0,01	0,01	0,01	0,02	0,02	0,02	0,02	0,03	0,03	0,03	0,03	0,03	0,04	0,04	0,07	0,08	0,13	0,54	0,70	0,61	0,46	0,25	0,18
1,5	10,75	0,01	0,01	0,01	0,01	0,01	0,01	0,01	0,01	0,01	0,01	0,01	0,01	0,01	0,01	0,01	0,01	0,01	0,02	0,02	0,02	0,02	0,03	0,03	0,03	0,03	0,04	0,05	0,07	0,09	0,18	1,38	3,35	4,20	3,97	3,44	2,67	1,31
1,5	12,25	0,01	0,01	0,01	0,01	0,01	0,01	0,01	0,01	0,01	0,01	0,01	0,01	0,01	0,01	0,01	0,01	0,01	0,02	0,02	0,02	0,02	0,03	0,03	0,03	0,04	0,04	0,06	0,08	0,10	0,96	4,36	9,57	12,05	11,45	10,39	7,99	4,90
1.15	13	0,01	0,01	0,01	0,01	0,01	0,01	0,01	0,01	0,01	0,01	0,01	0,01	0,01	0,01	0,01	0,02	0,02	0,02	0,02	0,03	0,03	0,03	0,04	0,04	0,04	0,05	0,07	0,09	0,12	1,76	7,23	15,48	19,74	18,99	17,13	13,57	8,44
0,75	13,75	0,01	0,01	0,01	0,01	0,01	0,01	0,01	0,01	0,01	0,01	0,01	0,01	0,01	0,01	0,02	0,02	0,02	0,03	0,03	0,03	0,04	0,04	0,05	0,05	0,06	0,07	0,08	0,10	0,22	2,46	9,46	20,91	26,59	25,61	23,17	18,94	11,62
1,5	15,25	0,02	0,02	0,02	0,02	0,01	0,01	0,01	0,01	0,01	0,01	0,01	0,01	0,02	0,02	0,02	0,02	0,03	0,03	0,04	0,04	0,05	0,05	0,05	0,06	0,06	0,07	0,09	0,11	0,60	4,58	15,98	34,96	45,14	43,44	38,94	31,07	18,54
1,5	16,75	0,02	0,02	0,02	0,01	0,01	0,01	0,01	0,01	0,01	0,01	0,01	0,02	0,02	0,02	0,03	0,03	0,03	0,04	0,04	0,04	0,05	0,05	0,05	0,06	0,06	0,07	0,09	0,11	0,96	5,79	19,49	43,36	58,74	55,24	48,55	38,38	23,40
1,5	18,25	0,02	0,02	0,02	0,02	0,02	0,01	0,02	0,01	0,01	0,01	0,02	0,02	0,02	0,03	0,03	0,03	0,04	0,04	0,04	0,04	0,05	0,05	0,05	0,06	0,06	0,07	0,09	0,11	0,83	5,92	19,63	43,62	59,98	56,08	48,68	37,95	23,59
1,5	19,75	0,02	0,02	0,02	0,02	0,02	0,02	0,02	0,02	0,02	0,02	0,02	0,02	0,02	0,02	0,03	0,03	0,04	0,04	0,05	0,05	0,06	0,06	0,07	0,07	0,07	0,08	0,10	0,11	0,61	5,09	17,16	37,15	47,60	45,28	40,57	32,34	20,22
1,5	21,25	0,02	0,02	0,02	0,02	0,02	0,01	0,02	0,02	0,01	0,01	0,02	0,02	0,02	0,02	0,02	0,03	0,03	0,04	0,04	0,05	0,05	0,06	0,06	0,06	0,07	0,07	0,09	0,10	0,28	3,35	11,54	24,69	30,86	29,43	26,31	21,16	12,68

Figure 44: Experimental map related to led 32 of th lower lamp. The maximum result is equal to ~ 60 uW/cm².

This second analysis, in continuity with the observations made in the previous paragraph, confirms a marked difference in power density between the sources located on the upper and lower bars compared to those on the central bar. The irradiance maps clearly show that in case of the LEDs on the outer lamps the effects are more strongly affected by internal reflection phenomena caused by the device's reflective surfaces. As a result, significantly higher irradiance values are recorded, both for central and peripheral LEDs, than those observed on the central bar.

Additionally, the geometric asymmetry of the system, already noted in the single-LED measurements and even more evident in the results of the second measurement campaign, further contributes to this behaviour. The lower lamp, positioned approximately 1.5 cm farther from the central axis than the upper one, produces an irradiance distribution that is less centered and more directed toward the lower wall of the device. This structural configuration is reflected in the color maps, where a higher intensity is observed near the wall, with a reduced spread toward the center. Conversely, the LEDs on the upper lamp, being closer to the system's optical axis, generate more symmetrical and centrally concentrated beams, consistent with their geometric positioning.

4.3.2 Measurements with lamps switched on

As in the previous campaign, measurements were carried out both with a single lamp turned on and with three lamps turned on simultaneously. The objective was to assess the repeatability over time of the recorded irradiance maps and to evaluate the consistency of the results with those obtained in the previous campaign. However, unlike the earlier campaign, the use of shielding during the measurements with a single source turned on caused several sources to malfunction, thus preventing the comparison of some matrices, including the one corresponding to the configuration with three lamps turned on simultaneously.

As in the previous case, the results are shown below using a color scale, where:

- Red corresponds to the maximum value in all configurations
- Green corresponds to the minimum value detected

According to the following scale:

- Maximum value: 379 µW/cm²
- Minimum value: 0 µW/cm²

Upper lamp on

The results are shown in Figure 45, where a less illuminated area stands out in correspondence with the final sampling steps of the map. Unfortunately, the shielding mode used for single-LED measurements led to the degradation of four LEDs located on the right side of the lamp, specifically at positions 25, 27, 29, and 31.

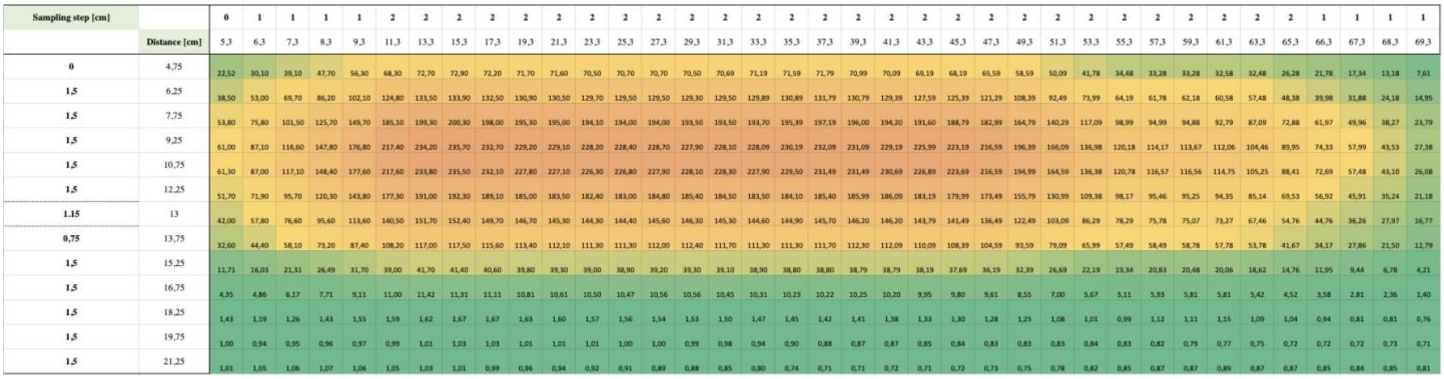

Sampling step [cm]		0	1	1	1	1	2	2	2	2	2	2	2	2	2	2	2	2	2	2	2	2	2	2	2	2	2	2	2	2	2	2	2	2	1	1	1	1
	Distance [cm]	5,3	6,3	7,3	8,3	9,3	11,3	13,3	15,3	17,3	19,3	21,3	23,3	25,3	27,3	29,3	31,3	33,3	35,3	37,3	39,3	41,3	43,3	45,3	47,3	49,3	51,3	53,3	55,3	57,3	59,3	61,3	63,3	65,3	66,3	67,3	68,3	69,3
0	4,75	22,52	30,10	39,10	47,70	56,30	68,30	72,70	72,90	72,20	71,70	71,60	70,50	70,70	70,70	70,50	70,69	71,19	71,59	71,79	70,99	70,09	69,19	68,19	65,59	58,59	50,09	41,78	34,48	33,28	33,28	32,58	32,48	26,28	21,78	17,34	13,18	7,61
1,5	6,25	38,50	53,00	69,70	86,20	102,10	124,80	133,50	133,90	132,50	130,90	130,50	129,70	129,50	129,50	129,30	129,50	129,89	130,89	131,79	130,79	129,39	127,59	125,39	121,29	108,39	92,49	73,99	64,19	61,78	62,18	60,58	57,48	48,38	39,98	31,88	24,18	14,95
1,5	7,75	53,80	75,80	101,50	125,70	149,70	185,10	199,30	200,30	198,00	195,30	195,00	194,10	194,00	194,00	193,50	193,50	193,70	195,39	197,19	196,00	194,20	191,60	188,79	182,99	164,79	140,29	117,09	98,99	94,99	94,88	92,79	87,09	72,88	61,97	49,96	38,27	23,79
1,5	9,25	61,00	87,10	116,60	147,80	176,80	217,40	234,20	235,70	232,70	229,20	229,10	228,20	228,40	228,70	227,90	228,10	228,09	230,19	232,09	231,09	229,19	225,99	223,19	216,59	196,39	166,09	136,98	120,18	114,17	113,67	112,06	104,46	89,95	74,33	57,99	43,53	27,38
1,5	10,75	61,30	87,00	117,10	148,40	177,60	217,60	233,80	235,50	232,10	227,80	227,10	226,30	226,80	227,90	228,10	228,30	227,90	229,50	231,49	231,49	230,69	226,89	223,69	216,59	194,99	164,59	136,38	120,78	116,57	116,56	114,75	105,25	88,41	72,69	57,48	43,10	26,08
1,5	12,25	51,70	71,90	95,70	120,30	143,80	177,30	191,00	192,30	189,10	185,00	183,50	182,40	183,00	184,80	185,40	184,50	183,50	184,10	185,40	185,99	186,09	183,19	179,99	173,49	155,79	130,99	109,38	98,17	95,46	95,25	94,35	85,14	69,53	56,92	45,91	35,24	21,18
1.15	13	42,00	57,80	76,60	95,60	113,60	140,50	151,70	152,40	149,70	146,70	145,30	144,30	144,40	145,60	146,30	145,30	144,60	144,90	145,70	146,20	146,20	143,79	141,49	136,49	122,49	103,09	86,29	78,29	75,78	75,07	73,27	67,46	54,76	44,76	36,26	27,97	16,77
0,75	13,75	32,60	44,40	58,10	73,20	87,40	108,20	117,00	117,50	115,60	113,40	112,10	111,30	111,30	112,00	112,40	111,70	111,30	111,30	111,70	112,30	112,09	110,09	108,39	104,59	93,59	79,09	65,99	57,49	58,49	58,78	57,78	53,78	41,67	34,17	27,86	21,50	12,79
1,5	15,25	11,71	16,03	21,31	26,49	31,70	39,00	41,70	41,40	40,60	39,80	39,30	39,00	38,90	39,20	39,30	39,10	38,90	38,80	38,80	38,79	38,79	38,19	37,69	36,19	32,39	26,69	22,19	19,34	20,83	20,48	20,06	18,62	14,76	11,95	9,44	6,78	4,21
1,5	16,75	4,35	4,86	6,17	7,71	9,11	11,00	11,42	11,31	11,11	10,81	10,61	10,50	10,47	10,56	10,56	10,45	10,31	10,23	10,22	10,25	10,20	9,95	9,80	9,61	8,55	7,00	5,67	5,11	5,93	5,81	5,81	5,42	4,52	3,58	2,81	2,36	1,40
1,5	18,25	1,43	1,19	1,26	1,43	1,55	1,59	1,62	1,67	1,67	1,63	1,60	1,57	1,56	1,54	1,53	1,50	1,47	1,45	1,42	1,41	1,38	1,33	1,30	1,28	1,25	1,08	1,01	0,99	1,12	1,11	1,15	1,09	1,04	0,94	0,81	0,81	0,76
1,5	19,75	1,00	0,94	0,95	0,96	0,97	0,99	1,01	1,03	1,03	1,01	1,01	1,01	1,00	1,00	0,99	0,98	0,94	0,90	0,88	0,87	0,87	0,85	0,84	0,83	0,83	0,83	0,84	0,83	0,82	0,79	0,77	0,75	0,72	0,72	0,72	0,73	0,71
1,5	21,25	1,01	1,05	1,06	1,07	1,06	1,05	1,03	1,01	0,99	0,96	0,94	0,92	0,91	0,89	0,88	0,85	0,80	0,74	0,71	0,71	0,72	0,71	0,72	0,73	0,75	0,78	0,82	0,85	0,87	0,87	0,89	0,87	0,87	0,85	0,84	0,85	0,81

Figure 45: Experimental map related to the upper lamp. The maximum result is equal to ~ 230 uW/cm².

Central lamp on

The results are shown in Figure 46, where a significantly less illuminated area can be observed on the left side compared to the right. This is due to the fact that, during and after the single-LED measurements, several sources burned out.

These belonged to the same module in groups of four and were located in the initial and central parts of the light bar.

The affected LEDs are numbers 1, 3, 5, 7; 10, 12, 14, 16; and 18, 20, 22, 24.

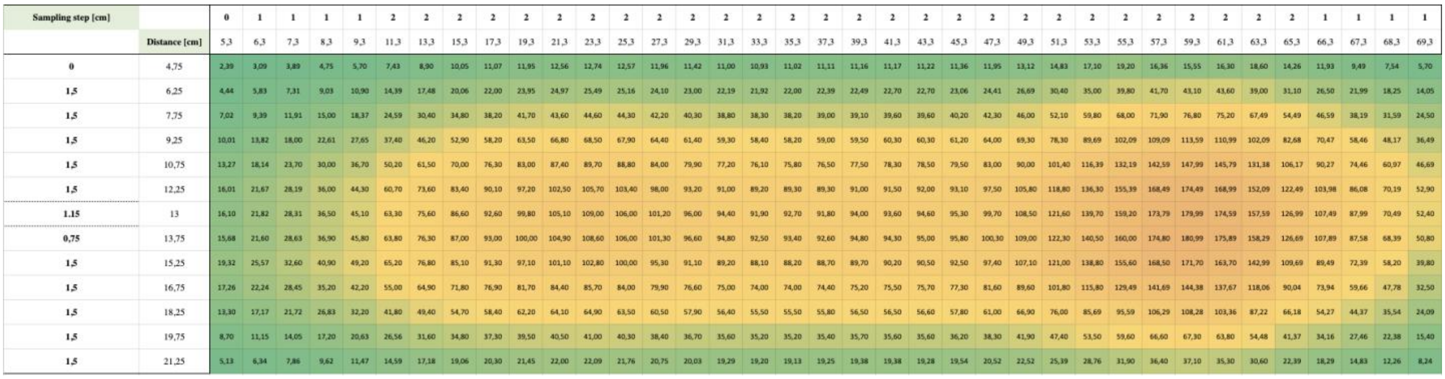

Sampling step [cm]		0	1	1	1	1	2	2	2	2	2	2	2	2	2	2	2	2	2	2	2	2	2	2	2	2	2	2	2	2	2	2	2	2	1	1	1	1
	Distance [cm]	5,3	6,3	7,3	8,3	9,3	11,3	13,3	15,3	17,3	19,3	21,3	23,3	25,3	27,3	29,3	31,3	33,3	35,3	37,3	39,3	41,3	43,3	45,3	47,3	49,3	51,3	53,3	55,3	57,3	59,3	61,3	63,3	65,3	66,3	67,3	68,3	69,3
0	4,75	2,39	3,09	3,89	4,75	5,70	7,43	8,90	10,05	11,07	11,95	12,56	12,74	12,57	11,96	11,42	11,00	10,93	11,02	11,11	11,16	11,17	11,22	11,36	11,95	13,12	14,83	17,10	19,20	16,36	15,55	16,30	18,60	14,26	11,93	9,49	7,54	5,70
1,5	6,25	4,44	5,83	7,31	9,03	10,90	14,39	17,48	20,06	22,00	23,95	24,97	25,49	25,16	24,10	23,00	22,19	21,92	22,00	22,39	22,49	22,70	22,70	23,06	24,41	26,69	30,40	35,00	39,80	41,70	43,10	43,60	39,00	31,10	26,50	21,99	18,25	14,05
1,5	7,75	7,02	9,39	11,91	15,00	18,37	24,59	30,40	34,80	38,20	41,70	43,60	44,60	44,30	42,20	40,30	38,80	38,30	38,20	39,00	39,10	39,60	39,60	40,20	42,30	46,00	52,10	59,80	68,00	71,90	76,80	75,20	67,49	54,49	46,59	38,19	31,59	24,50
1,5	9,25	10,01	13,82	18,00	22,61	27,65	37,40	46,20	52,90	58,20	63,50	66,80	68,50	67,90	64,40	61,40	59,30	58,40	58,20	59,00	59,50	60,30	60,30	61,20	64,00	69,30	78,30	89,69	102,09	109,09	113,59	110,99	102,09	82,68	70,47	58,46	48,17	36,49
1,5	10,75	13,27	18,14	23,70	30,00	36,70	50,20	61,50	70,00	76,30	83,00	87,40	89,70	88,80	84,00	79,90	77,20	76,10	75,80	76,50	77,50	78,30	78,50	79,50	83,00	90,00	101,40	116,39	132,19	142,59	147,99	145,79	131,38	106,17	90,27	74,46	60,97	46,69
1,5	12,25	16,01	21,67	28,19	36,00	44,30	60,70	73,60	83,40	90,10	97,20	102,50	105,70	103,40	98,00	93,20	91,00	89,20	89,30	89,30	91,00	91,50	92,00	93,10	97,50	105,80	118,80	136,30	155,39	168,49	174,49	168,99	152,09	122,49	103,98	86,08	70,19	52,90
1.15	13	16,10	21,82	28,31	36,50	45,10	63,30	75,60	86,60	92,60	99,80	105,10	109,00	106,00	101,20	96,00	94,40	91,90	92,70	91,80	94,00	93,60	94,60	95,30	99,70	108,50	121,60	139,70	159,20	173,79	179,99	174,59	157,59	126,99	107,49	87,99	70,49	52,40
0,75	13,75	15,68	21,60	28,63	36,90	45,80	63,80	76,30	87,00	93,00	100,00	104,90	108,60	106,00	101,30	96,60	94,80	92,50	93,40	92,60	94,80	94,30	95,00	95,80	100,30	109,00	122,30	140,50	160,00	174,80	180,99	175,89	158,29	126,69	107,89	87,58	68,39	50,80
1,5	15,25	19,32	25,57	32,60	40,90	49,20	65,20	76,80	85,10	91,30	97,10	101,10	102,80	100,00	95,30	91,10	89,20	88,10	88,20	88,70	89,70	90,20	90,50	92,50	97,40	107,10	121,00	138,80	155,60	168,50	171,70	163,70	142,99	109,69	89,49	72,39	58,20	39,80
1,5	16,75	17,26	22,24	28,45	35,20	42,20	55,00	64,90	71,80	76,90	81,70	84,40	85,70	84,00	79,90	76,60	75,00	74,00	74,00	74,40	75,20	75,50	75,70	77,30	81,60	89,60	101,80	115,80	129,49	141,69	144,38	137,67	118,06	90,04	73,94	59,66	47,78	32,50
1,5	18,25	13,30	17,17	21,72	26,83	32,20	41,80	49,40	54,70	58,40	62,20	64,10	64,90	63,50	60,50	57,90	56,40	55,50	55,50	55,80	56,50	56,50	56,60	57,80	61,00	66,90	76,00	85,69	95,59	106,29	108,28	103,36	87,22	66,18	54,27	44,37	35,54	24,09
1,5	19,75	8,70	11,15	14,05	17,20	20,63	26,56	31,60	34,80	37,30	39,50	40,50	41,00	40,30	38,40	36,70	35,60	35,20	35,20	35,40	35,70	35,60	35,60	36,20	38,30	41,90	47,40	53,50	59,60	66,60	67,30	63,80	54,48	41,37	34,16	27,46	22,38	15,40
1,5	21,25	5,13	6,34	7,86	9,62	11,47	14,59	17,18	19,06	20,30	21,45	22,00	22,09	21,76	20,75	20,03	19,29	19,20	19,13	19,25	19,38	19,38	19,28	19,54	20,52	22,52	25,39	28,76	31,90	36,40	37,10	35,30	30,60	22,39	18,29	14,83	12,26	8,24

Figure 46: Experimental map related to the central lamp. The maximum result is equal to ~ 180 uW/cm².

Lower lamp on

The results are shown in Figure 47. As described in Chapter 2 and discussed in the previous paragraph, the distances between the upper and lower bars and the central bar are not equal, but rather asymmetric, with the lower bar positioned 1.5 cm farther away. This condition explains the color map shown, which is characterized by a more pronounced illumination toward the lower part and less toward the center, opposite to what was observed in the map of the upper bar.
For this lamp as well, several LEDs were damaged following the first measurement campaign, particularly those in positions: 2, 4, 6, 8; 10, 12, 14, 16; and 18, 20, 22, 24.

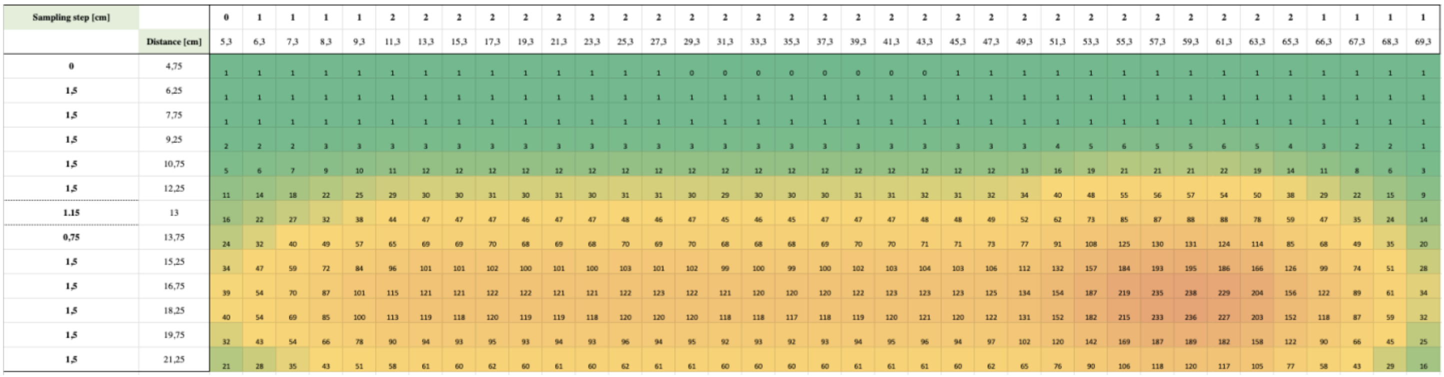

Sampling step [cm]		0	1	1	1	1	2	2	2	2	2	2	2	2	2	2	2	2	2	2	2	2	2	2	2	2	2	2	2	2	2	2	2	2	1	1	1	1
	Distance [cm]	5,3	6,3	7,3	8,3	9,3	11,3	13,3	15,3	17,3	19,3	21,3	23,3	25,3	27,3	29,3	31,3	33,3	35,3	37,3	39,3	41,3	43,3	45,3	47,3	49,3	51,3	53,3	55,3	57,3	59,3	61,3	63,3	65,3	66,3	67,3	68,3	69,3
0	4,75	1	1	1	1	1	1	1	1	1	1	1	1	1	1	0	0	0	0	0	0	0	0	1	1	1	1	1	1	1	1	1	1	1	1	1	1	1
1,5	6,25	1	1	1	1	1	1	1	1	1	1	1	1	1	1	1	1	1	1	1	1	1	1	1	1	1	1	1	1	1	1	1	1	1	1	1	1	1
1,5	7,75	1	1	1	1	1	1	1	1	1	1	1	1	1	1	1	1	1	1	1	1	1	1	1	1	1	1	1	1	1	1	1	1	1	1	1	1	1
1,5	9,25	2	2	2	3	3	3	3	3	3	3	3	3	3	3	3	3	3	3	3	3	3	3	3	3	3	4	5	6	5	5	6	5	4	3	2	2	1
1,5	10,75	5	6	7	9	10	11	12	12	12	12	12	12	12	12	12	12	12	12	12	12	12	12	12	12	13	16	19	21	21	21	22	19	14	11	8	6	3
1,5	12,25	11	14	18	22	25	29	30	30	31	30	31	30	31	31	30	29	30	30	30	31	31	32	31	32	34	40	48	55	56	57	54	50	38	29	22	15	9
1.15	13	16	22	27	32	38	44	47	47	47	46	47	47	48	46	47	45	46	45	47	47	47	48	48	49	52	62	73	85	87	88	88	78	59	47	35	24	14
0,75	13,75	24	32	40	49	57	65	69	69	70	68	69	68	70	69	70	68	68	68	69	70	70	71	71	73	77	91	108	125	130	131	124	114	85	68	49	35	20
1,5	15,25	34	47	59	72	84	96	101	101	102	100	101	100	103	101	102	99	100	99	100	102	103	104	103	106	112	132	157	184	193	195	186	166	126	99	74	51	28
1,5	16,75	39	54	70	87	101	115	121	121	122	122	121	121	122	123	122	121	120	120	120	122	123	123	123	125	134	154	187	219	235	238	229	204	156	122	89	61	34
1,5	18,25	40	54	69	85	100	113	119	118	120	119	119	118	120	120	120	118	118	117	118	119	120	121	120	122	131	152	182	215	233	236	227	203	152	118	87	59	32
1,5	19,75	32	43	54	66	78	90	94	93	95	93	94	93	96	94	95	92	93	92	93	94	95	96	94	97	102	120	142	169	187	189	182	158	122	90	66	45	25
1,5	21,25	21	28	35	43	51	58	61	60	62	60	61	60	62	61	61	60	60	60	60	61	61	61	60	62	65	76	90	106	118	120	117	105	77	58	43	29	16

Figure 47: Experimental map related to the lower lamp. The maximum result is equal to ~ 238 uW/cm².

All lamps on simultaneously

The experimental map recorded with all three lamps turned on simultaneously, shown in Figure 48, reflects the influence of the malfunctioning LEDs mentioned earlier. For this reason, it is expected that the central area, in particular, does not exhibit a uniform red tone.

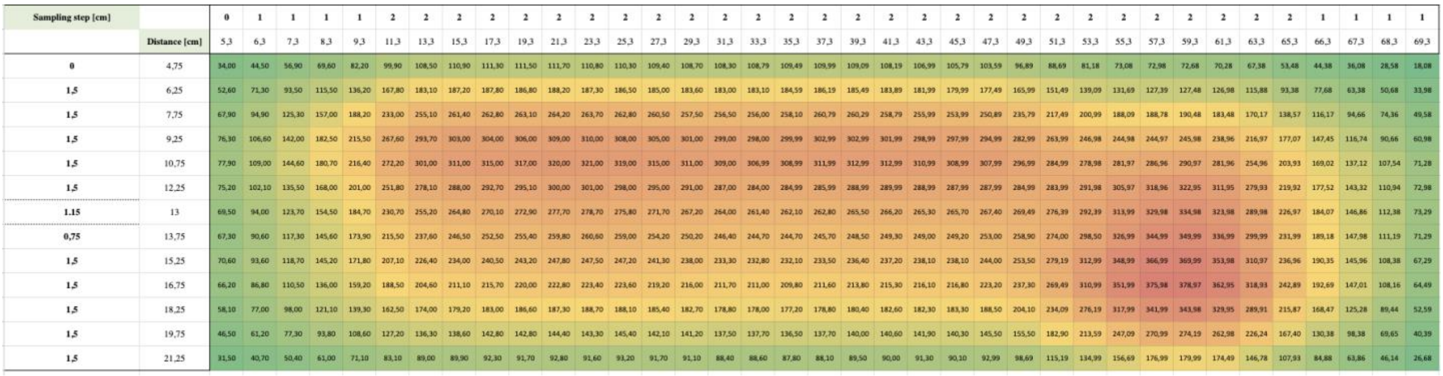

Sampling step [cm]		0	1	1	1	1	2	2	2	2	2	2	2	2	2	2	2	2	2	2	2	2	2	2	2	2	2	2	2	2	2	2	2	2	1	1	1	1
	Distance [cm]	5,3	6,3	7,3	8,3	9,3	11,3	13,3	15,3	17,3	19,3	21,3	23,3	25,3	27,3	29,3	31,3	33,3	35,3	37,3	39,3	41,3	43,3	45,3	47,3	49,3	51,3	53,3	55,3	57,3	59,3	61,3	63,3	65,3	66,3	67,3	68,3	69,3
0	4,75	34,00	44,50	56,90	69,60	82,20	99,90	108,50	110,90	111,30	111,50	111,70	110,80	110,30	109,40	108,70	108,30	108,79	109,49	109,99	109,09	108,19	106,99	105,79	103,59	96,89	88,69	81,18	73,08	72,98	72,68	70,28	67,38	53,48	44,38	36,08	28,58	18,08
1,5	6,25	52,60	71,30	93,50	115,50	136,20	167,80	183,10	187,20	187,80	186,80	188,20	187,30	186,50	185,00	183,60	183,00	183,10	184,59	186,19	185,49	183,89	181,99	179,99	177,49	165,99	151,49	139,09	131,69	127,39	127,48	126,98	115,88	93,38	77,68	63,38	50,68	33,98
1,5	7,75	67,90	94,90	125,30	157,00	188,20	233,00	255,10	261,40	262,80	263,10	264,20	263,70	262,80	260,50	257,50	256,50	256,00	258,10	260,79	260,29	258,79	255,99	253,99	250,89	235,79	217,49	200,99	188,09	188,78	190,48	183,48	170,17	138,57	116,17	94,66	74,36	49,58
1,5	9,25	76,30	106,60	142,00	182,50	215,50	267,60	293,70	303,00	304,00	306,00	309,00	310,00	308,00	305,00	301,00	299,00	298,00	299,99	302,99	302,99	301,99	298,99	297,99	294,99	282,99	263,99	246,98	244,98	244,97	245,98	238,96	216,97	177,07	147,45	116,74	90,66	60,98
1,5	10,75	77,90	109,00	144,60	180,70	216,40	272,20	301,00	311,00	315,00	317,00	320,00	321,00	319,00	315,00	311,00	309,00	306,99	308,99	311,99	312,99	312,99	310,99	308,99	307,99	296,99	284,99	278,98	281,97	286,96	290,97	281,96	254,96	203,93	169,02	137,12	107,54	71,28
1,5	12,25	75,20	102,10	135,50	168,00	201,00	251,80	278,10	288,00	292,70	295,10	300,00	301,00	298,00	295,00	291,00	287,00	284,00	284,99	285,99	288,99	289,99	288,99	287,99	287,99	284,99	283,99	291,98	305,97	318,96	322,95	311,95	279,93	219,92	177,52	143,32	110,94	72,98
1.15	13	69,50	94,00	123,70	154,50	184,70	230,70	255,20	264,80	270,10	272,90	277,70	278,70	275,80	271,70	267,20	264,00	261,40	262,10	262,80	265,50	266,20	265,30	265,70	267,40	269,49	276,39	292,39	313,99	329,98	334,98	323,98	289,98	226,97	184,07	146,86	112,38	73,29
0,75	13,75	67,30	90,60	117,30	145,60	173,90	215,50	237,60	246,50	252,50	255,40	259,80	260,60	259,00	254,20	250,20	246,40	244,70	244,70	245,70	248,50	249,30	249,00	249,20	253,00	258,90	274,00	298,50	326,99	344,99	349,99	336,99	299,99	231,99	189,18	147,98	111,19	71,29
1,5	15,25	70,60	93,60	118,70	145,20	171,80	207,10	226,40	234,00	240,50	243,20	247,80	247,50	247,20	241,30	238,00	233,30	232,80	232,10	233,50	236,40	237,20	238,10	238,10	244,00	253,50	279,19	312,99	348,99	366,99	369,99	353,98	310,97	236,96	190,35	145,96	108,38	67,29
1,5	16,75	66,20	86,80	110,50	136,00	159,20	188,50	204,60	211,10	215,70	220,00	222,80	223,40	223,60	219,20	216,00	211,70	211,00	209,80	211,60	213,80	215,30	216,10	216,80	223,20	237,30	269,49	310,99	351,99	375,98	378,97	362,95	318,93	242,89	192,69	147,01	108,16	64,49
1,5	18,25	58,10	77,00	98,00	121,10	139,30	162,50	174,00	179,20	183,00	186,60	187,30	188,70	188,10	185,40	182,70	178,80	178,00	177,20	178,80	180,40	182,60	182,30	183,30	188,50	204,10	234,09	276,19	317,99	341,99	343,98	329,95	289,91	215,87	168,47	125,28	89,44	52,59
1,5	19,75	46,50	61,20	77,30	93,80	108,60	127,20	136,30	138,60	142,80	142,80	144,40	143,30	145,40	142,10	141,20	137,50	137,70	136,50	137,70	140,00	140,60	141,90	140,30	145,50	155,50	182,90	213,59	247,09	270,99	274,19	262,98	226,24	167,40	130,38	98,38	69,65	40,39
1,5	21,25	31,50	40,70	50,40	61,00	71,10	83,10	89,00	89,90	92,30	91,70	92,80	91,60	93,20	91,70	91,10	88,40	88,60	87,80	88,10	89,50	90,00	91,30	90,10	92,99	98,69	115,19	134,99	156,69	176,99	179,99	174,49	146,78	107,93	84,88	63,86	46,14	26,68

Figure 48: Experimental map related to three lamps turned on simultaneously. The maximum value is equal to ~ 380 uW/cm².

As already done in the previous campaign, this second phase of measurements also aimed to verify the system's behavior under linear conditions, in order to apply the principle of superposition of effects. This approach enables the prediction of irradiance resulting from various source activation configurations.

Once the experimental maps for the individual lamps were obtained, attention was focused on reconstructing a combined irradiance map by summing the contributions of each single source. This reconstructed map is then compared with the experimental one recorded with all lamps turned on simultaneously, using the same color scale to ensure visual and interpretative consistency between the two representations.

To verify that the device behaves as a linear system, making it possible to apply the principle of superposition of effects, the map corresponding to three lamps turned on was reconstructed as the sum of the maps of the individual bars, shown in Figure 49.

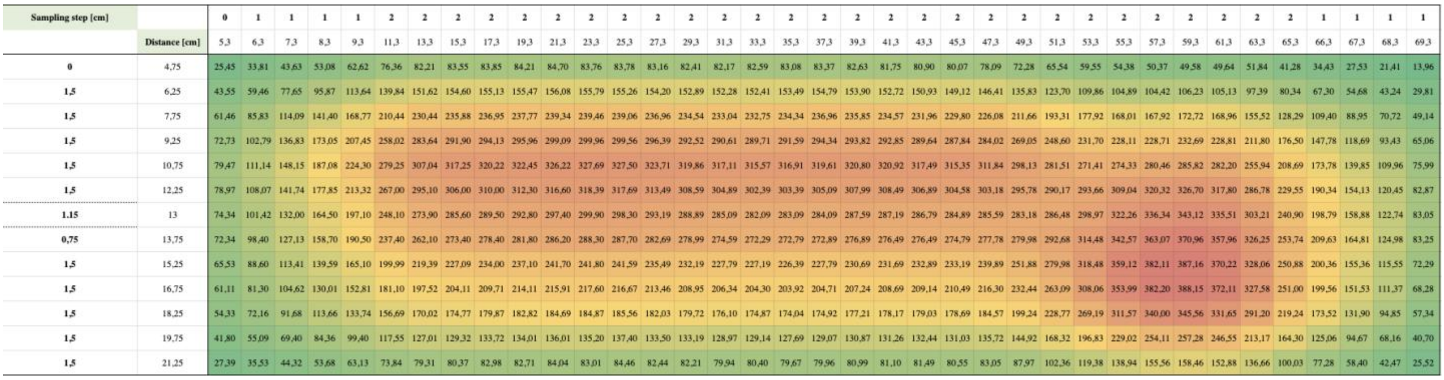

Sampling step [cm]		0	1	1	1	1	2	2	2	2	2	2	2	2	2	2	2	2	2	2	2	2	2	2	2	2	2	2	2	2	2	2	2	2	1	1	1	1
	Distance [cm]	5,3	6,3	7,3	8,3	9,3	11,3	13,3	15,3	17,3	19,3	21,3	23,3	25,3	27,3	29,3	31,3	33,3	35,3	37,3	39,3	41,3	43,3	45,3	47,3	49,3	51,3	53,3	55,3	57,3	59,3	61,3	63,3	65,3	66,3	67,3	68,3	69,3
0	4,75	25,45	33,81	43,63	53,08	62,62	76,36	82,21	83,55	83,85	84,21	84,70	83,76	83,78	83,16	82,41	82,17	82,59	83,08	83,37	82,63	81,75	80,90	80,07	78,09	72,28	65,54	59,55	54,38	50,37	49,58	49,64	51,84	41,28	34,43	27,53	21,41	13,96
1,5	6,25	43,55	59,46	77,65	95,87	113,64	139,84	151,62	154,60	155,13	155,47	156,08	155,79	155,26	154,20	152,89	152,28	152,41	153,49	154,79	153,90	152,72	150,93	149,12	146,41	135,83	123,70	109,86	104,89	104,42	106,23	105,13	97,39	80,34	67,30	54,68	43,24	29,81
1,5	7,75	61,46	85,83	114,09	141,40	168,77	210,44	230,44	235,88	236,95	237,77	239,34	239,46	239,06	236,96	234,54	233,04	232,75	234,34	236,96	235,85	234,57	231,96	229,80	226,08	211,66	193,31	177,92	168,01	167,92	172,72	168,96	155,52	128,29	109,40	88,95	70,72	49,14
1,5	9,25	72,73	102,79	136,83	173,05	207,45	258,02	283,64	291,90	294,13	295,96	299,09	299,96	299,56	296,39	292,52	290,61	289,71	291,59	294,34	293,82	292,85	289,64	287,84	284,02	269,05	248,60	231,70	228,11	228,71	232,69	228,81	211,80	176,50	147,78	118,69	93,43	65,06
1,5	10,75	79,47	111,14	148,15	187,08	224,30	279,25	307,04	317,25	320,22	322,45	326,22	327,69	327,50	323,71	319,86	317,11	315,57	316,91	319,61	320,80	320,92	317,49	315,35	311,84	298,13	281,51	271,41	274,33	280,46	285,82	282,20	255,94	208,69	173,78	139,85	109,96	75,99
1,5	12,25	78,97	108,07	141,74	177,85	213,32	267,00	295,10	306,00	310,00	312,30	316,60	318,39	317,69	313,49	308,59	304,89	302,39	303,39	305,09	307,99	308,49	306,89	304,58	303,18	295,78	290,17	293,66	309,04	320,32	326,70	317,80	286,78	229,55	190,34	154,13	120,45	82,87
1.15	13	74,34	101,42	132,00	164,50	197,10	248,10	273,90	285,60	289,50	292,80	297,40	299,90	298,30	293,19	288,89	285,09	282,09	283,09	284,09	287,59	287,19	286,79	284,89	285,59	283,18	286,48	298,97	322,26	336,34	343,12	335,51	303,21	240,90	198,79	158,88	122,74	83,05
0,75	13,75	72,34	98,40	127,13	158,70	190,50	237,40	262,10	273,40	278,40	281,80	286,20	288,30	287,70	282,69	278,99	274,59	272,29	272,79	272,89	276,89	276,49	276,49	274,79	277,78	279,98	292,68	314,48	342,57	363,07	370,96	357,96	326,25	253,74	209,63	164,81	124,98	83,25
1,5	15,25	65,53	88,60	113,41	139,59	165,10	199,99	219,39	227,09	234,00	237,10	241,70	241,80	241,59	235,49	232,19	227,79	227,19	226,39	227,79	230,69	231,69	232,89	233,19	239,89	251,88	279,98	318,48	359,12	382,11	387,16	370,22	328,06	250,88	200,36	155,36	115,55	72,29
1,5	16,75	61,11	81,30	104,62	130,01	152,81	181,10	197,52	204,11	209,71	214,11	215,91	217,60	216,67	213,46	208,95	206,34	204,30	203,92	204,71	207,24	208,69	209,14	210,49	216,30	232,44	263,09	308,06	353,99	382,20	388,15	372,11	327,58	251,00	199,56	151,53	111,37	68,28
1,5	18,25	54,33	72,16	91,68	113,66	133,74	156,69	170,02	174,77	179,87	182,82	184,69	184,87	185,56	182,03	179,72	176,10	174,87	174,04	174,92	177,21	178,17	179,03	178,69	184,57	199,24	228,77	269,19	311,57	340,00	345,56	331,65	291,20	219,24	173,52	131,90	94,85	57,34
1,5	19,75	41,80	55,09	69,40	84,36	99,40	117,55	127,01	129,32	133,72	134,01	136,01	135,20	137,40	133,50	133,19	128,97	129,14	127,69	129,07	130,87	131,26	132,44	131,03	135,72	144,92	168,32	196,83	229,02	254,11	257,28	246,55	213,17	164,30	125,06	94,67	68,16	40,70
1,5	21,25	27,39	35,53	44,32	53,68	63,13	73,84	79,31	80,37	82,98	82,71	84,04	83,01	84,46	82,44	82,21	79,94	80,40	79,67	79,96	80,99	81,10	81,49	80,55	83,05	87,97	102,36	119,38	138,94	155,56	158,46	152,88	136,66	100,03	77,28	58,40	42,47	25,52

Figure 49: Reconstruction of the map related to three lamps lit simultaneously starting from maps related to single lamps lit.

The reconstructed map exhibits a distribution that is largely similar to the experimental map, also displaying a certain degree of color symmetry. Following this visual comparison, a quantitative analysis was performed by evaluating the relative error between the two maps. The results, expressed as absolute value, are shown in Figure 50.

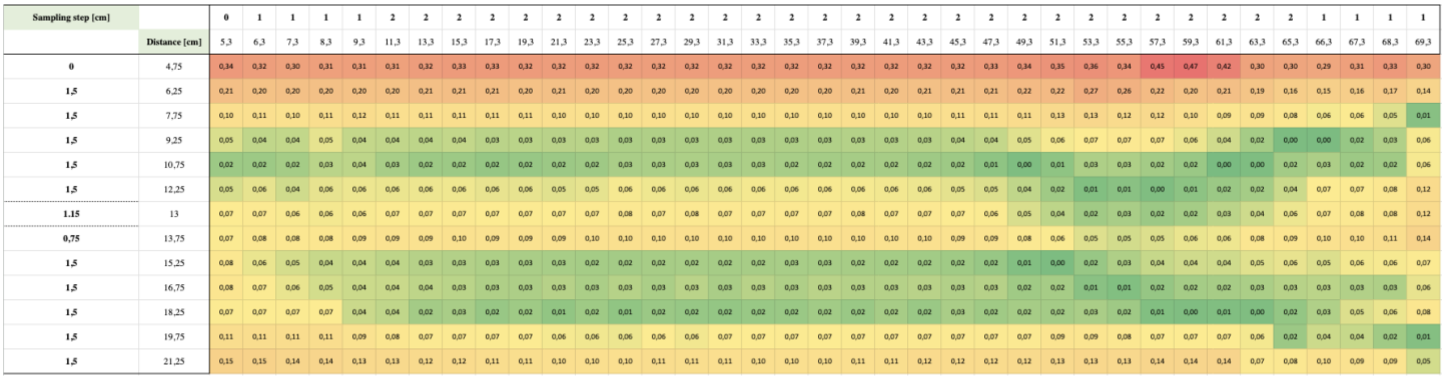

Sampling step [cm]		0	1	1	1	1	2	2	2	2	2	2	2	2	2	2	2	2	2	2	2	2	2	2	2	2	2	2	2	2	2	2	2	2	1	1	1	1
	Distance [cm]	5,3	6,3	7,3	8,3	9,3	11,3	13,3	15,3	17,3	19,3	21,3	23,3	25,3	27,3	29,3	31,3	33,3	35,3	37,3	39,3	41,3	43,3	45,3	47,3	49,3	51,3	53,3	55,3	57,3	59,3	61,3	63,3	65,3	66,3	67,3	68,3	69,3
0	4,75	0,34	0,32	0,30	0,31	0,31	0,31	0,32	0,33	0,33	0,32	0,32	0,32	0,32	0,32	0,32	0,32	0,32	0,32	0,32	0,32	0,32	0,32	0,32	0,33	0,34	0,35	0,36	0,34	0,45	0,47	0,42	0,30	0,30	0,29	0,31	0,33	0,30
1,5	6,25	0,21	0,20	0,20	0,20	0,20	0,20	0,21	0,21	0,21	0,20	0,21	0,20	0,20	0,20	0,20	0,20	0,20	0,20	0,20	0,21	0,20	0,21	0,21	0,21	0,22	0,22	0,27	0,26	0,22	0,20	0,21	0,19	0,16	0,15	0,16	0,17	0,14
1,5	7,75	0,10	0,11	0,10	0,11	0,12	0,11	0,11	0,11	0,11	0,11	0,10	0,10	0,10	0,10	0,10	0,10	0,10	0,10	0,10	0,10	0,10	0,10	0,11	0,11	0,11	0,13	0,13	0,12	0,12	0,10	0,09	0,09	0,08	0,06	0,06	0,05	0,01
1,5	9,25	0,05	0,04	0,04	0,05	0,04	0,04	0,04	0,04	0,03	0,03	0,03	0,03	0,03	0,03	0,03	0,03	0,03	0,03	0,03	0,03	0,03	0,03	0,04	0,04	0,05	0,06	0,07	0,07	0,07	0,06	0,04	0,02	0,00	0,00	0,02	0,03	0,06
1,5	10,75	0,02	0,02	0,02	0,03	0,04	0,03	0,02	0,02	0,02	0,02	0,02	0,02	0,03	0,03	0,03	0,03	0,03	0,02	0,02	0,02	0,02	0,02	0,02	0,01	0,00	0,01	0,03	0,03	0,02	0,02	0,00	0,00	0,02	0,03	0,02	0,02	0,06
1,5	12,25	0,05	0,06	0,04	0,06	0,06	0,06	0,06	0,06	0,06	0,06	0,05	0,05	0,06	0,06	0,06	0,06	0,06	0,06	0,06	0,06	0,06	0,06	0,05	0,05	0,04	0,02	0,01	0,01	0,00	0,01	0,02	0,02	0,04	0,07	0,07	0,08	0,12
1.15	13	0,07	0,07	0,06	0,06	0,06	0,07	0,07	0,07	0,07	0,07	0,07	0,07	0,08	0,07	0,08	0,07	0,07	0,07	0,07	0,08	0,07	0,07	0,07	0,06	0,05	0,04	0,02	0,03	0,02	0,02	0,03	0,04	0,06	0,07	0,08	0,08	0,12
0,75	13,75	0,07	0,08	0,08	0,08	0,09	0,09	0,09	0,10	0,09	0,09	0,09	0,10	0,10	0,10	0,10	0,10	0,10	0,10	0,10	0,10	0,10	0,10	0,09	0,09	0,08	0,06	0,05	0,05	0,05	0,06	0,06	0,08	0,09	0,10	0,10	0,11	0,14
1,5	15,25	0,08	0,06	0,05	0,04	0,04	0,04	0,03	0,03	0,03	0,03	0,03	0,02	0,02	0,02	0,02	0,02	0,02	0,03	0,03	0,02	0,02	0,02	0,02	0,02	0,01	0,00	0,02	0,03	0,04	0,04	0,04	0,05	0,06	0,05	0,06	0,06	0,07
1,5	16,75	0,08	0,07	0,06	0,05	0,04	0,04	0,04	0,03	0,03	0,03	0,03	0,03	0,03	0,03	0,03	0,03	0,03	0,03	0,03	0,03	0,03	0,03	0,03	0,03	0,02	0,02	0,01	0,01	0,02	0,02	0,02	0,03	0,03	0,03	0,03	0,03	0,06
1,5	18,25	0,07	0,07	0,07	0,07	0,04	0,04	0,02	0,03	0,02	0,02	0,01	0,02	0,01	0,02	0,02	0,02	0,02	0,02	0,02	0,02	0,02	0,02	0,03	0,02	0,02	0,02	0,03	0,02	0,01	0,00	0,01	0,00	0,02	0,03	0,05	0,06	0,08
1,5	19,75	0,11	0,11	0,11	0,11	0,09	0,08	0,07	0,07	0,07	0,07	0,06	0,06	0,06	0,06	0,06	0,07	0,07	0,07	0,07	0,07	0,07	0,07	0,07	0,07	0,07	0,09	0,09	0,08	0,07	0,07	0,07	0,06	0,02	0,04	0,04	0,02	0,01
1,5	21,25	0,15	0,15	0,14	0,14	0,13	0,13	0,12	0,12	0,11	0,11	0,10	0,10	0,10	0,11	0,11	0,11	0,10	0,10	0,10	0,11	0,11	0,12	0,12	0,12	0,12	0,13	0,13	0,13	0,14	0,14	0,14	0,07	0,08	0,10	0,09	0,09	0,05

Figure 50: Absolut value of the relative error betweenth reconstructed map of figure 49 and the experimental map of figure 48.

The relative error is strongly negative, indicating that the experimental results are higher than the reconstructed ones. To better understand these effects, a color scale was set up where the minimum value is highlighted in green (negative) and the maximum value in red (positive).

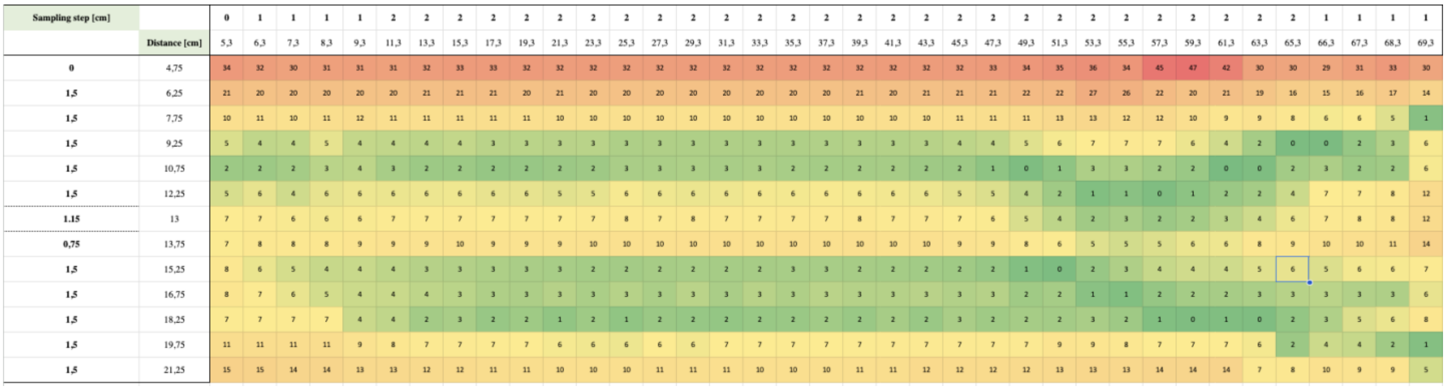

Sampling step [cm]		0	1	1	1	1	2	2	2	2	2	2	2	2	2	2	2	2	2	2	2	2	2	2	2	2	2	2	2	2	2	2	2	2	1	1	1	1
	Distance [cm]	5,3	6,3	7,3	8,3	9,3	11,3	13,3	15,3	17,3	19,3	21,3	23,3	25,3	27,3	29,3	31,3	33,3	35,3	37,3	39,3	41,3	43,3	45,3	47,3	49,3	51,3	53,3	55,3	57,3	59,3	61,3	63,3	65,3	66,3	67,3	68,3	69,3
0	4,75	34	32	30	31	31	31	32	33	33	32	32	32	32	32	32	32	32	32	32	32	32	32	32	33	34	35	36	34	45	47	42	30	30	29	31	33	30
1,5	6,25	21	20	20	20	20	20	21	21	21	20	21	20	20	20	20	20	20	20	20	21	20	21	21	21	22	22	27	26	22	20	21	19	16	15	16	17	14
1,5	7,75	10	11	10	11	12	11	11	11	11	11	10	10	10	10	10	10	10	10	10	10	10	10	11	11	11	13	13	12	12	10	9	9	8	6	6	5	1
1,5	9,25	5	4	4	5	4	4	4	4	3	3	3	3	3	3	3	3	3	3	3	3	3	3	4	4	5	6	7	7	7	6	4	2	0	0	2	3	6
1,5	10,75	2	2	2	3	4	3	2	2	2	2	2	2	3	3	3	3	3	2	2	2	2	2	2	1	0	1	3	3	2	2	0	0	2	3	2	2	6
1,5	12,25	5	6	4	6	6	6	6	6	6	6	5	5	6	6	6	6	6	6	6	6	6	6	5	5	4	2	1	1	0	1	2	2	4	7	7	8	12
1.15	13	7	7	6	6	6	7	7	7	7	7	7	7	8	7	8	7	7	7	7	8	7	7	7	6	5	4	2	3	2	2	3	4	6	7	8	8	12
0,75	13,75	7	8	8	8	9	9	9	10	9	9	9	10	10	10	10	10	10	10	10	10	10	10	9	9	8	6	5	5	5	6	6	8	9	10	10	11	14
1,5	15,25	8	6	5	4	4	4	3	3	3	3	3	2	2	2	2	2	2	3	3	2	2	2	2	2	1	0	2	3	4	4	4	5	6	5	6	6	7
1,5	16,75	8	7	6	5	4	4	4	3	3	3	3	3	3	3	3	3	3	3	3	3	3	3	3	3	2	2	1	1	2	2	2	3	3	3	3	3	6
1,5	18,25	7	7	7	7	4	4	2	3	2	2	1	2	1	2	2	2	2	2	2	2	2	2	3	2	2	2	3	2	1	0	1	0	2	3	5	6	8
1,5	19,75	11	11	11	11	9	8	7	7	7	7	6	6	6	6	6	7	7	7	7	7	7	7	7	7	7	9	9	8	7	7	7	6	2	4	4	2	1
1,5	21,25	15	15	14	14	13	13	12	12	11	11	10	10	10	11	11	11	10	10	10	11	11	12	12	12	12	13	13	13	14	14	14	7	8	10	9	9	5

Figure 51: Absolut percentage value of the relative error betweenth reconstructed map of figure 49 and the experimental map of figure 48.

The error between the reconstruction and the experimental data is most evident in the upper part, ranging between 20% and 30%, but also in isolated points where the error reaches 45 – 47%. Other areas are noticeable as well, including a whole strip at the bottom and scattered spots throughout the map, where the error reaches about 10%. The reconstruction, on the other hand, proves to be more reliable moving towards the central areas, both from above and below.

4.4 Comparison between the second and third measurement campaigns

A detailed comparison between the first (2022) and second (2025) measurement campaigns highlights both methodological consistencies and significant differences in the experimental outcomes, primarily due to hardware degradation and the adoption of more refined acquisition strategies. In both campaigns, irradiance maps were acquired with identical spatial resolution and measurement protocols to ensure repeatability. However, in the 2025 campaign, the measurement sequence was reverse, starting with single-LED acquisitions, followed by single-lamp configurations, and finally with all lamps turned on, in order to reduce cumulative thermal and electrical stress on the sources.

It should also be noted that the two campaigns were conducted under different ambient lighting conditions. In particular, the third campaign was performed in a darker environment, which may have slightly influenced the perception and measurement of low-intensity irradiance regions.

In the 2022 campaign, irradiance maps obtained with individual lamps and their sum were used to validate the linearity of the system. The reconstructed map, obtained by summing the single-lamp maps, showed good agreement with the experimental map acquired with all lamps on, with a relative error generally below 8%, except for some localized regions where it reached up to 59%. These discrepancies were attributed to LED failures and geometric asymmetries, particularly the 1.5 cm offset of the lower bar relative to the central axis, which caused a shift in the irradiance peak toward the lower wall.

In contrast, the 2025 campaign was affected by more extensive LED degradation, mainly due to the shielding used during single-LED measurements. This led to the malfunction of numerous LEDs across all bars,up to 12 in the central lamp alone, compromising the uniformity of the irradiance distribution. Despite these limitations, the reconstructed map again showed a distribution similar to the experimental one, confirming the system's approximate linearity. However, the relative error was more pronounced in this campaign, with values ranging from 20% to 30% in the upper region and isolated peaks up to 47%. These deviations suggest a stronger influence of reflective phenomena and source degradation, particularly in peripheral regions.

Due to discrepancies in LED functionality between the two campaigns, reliable quantitative comparisons are limited to configurations with a single LED on and with an entire bar activated. Specifically, the comparison focused on the experimental data from the central LED of the central lamp (LED no. 16) and the configuration with only the upper lamp turned on, as in both cases the number and position of faulty LEDs remained unchanged between the two campaigns.

The comparison was based on an analysis of the relative error, calculated as:

$$\varepsilon = \left| \frac{I_{2022} - I_{2025}}{I_{2022}} \right| * 100 \tag{4.4.1}$$

where I_{2022} and I_{2025} represent the irradiance values measured in the second and third campaigns, respectively. The relative error maps are shown in Figure 52 (upper lamp on) and Figure 53 (central LED on).

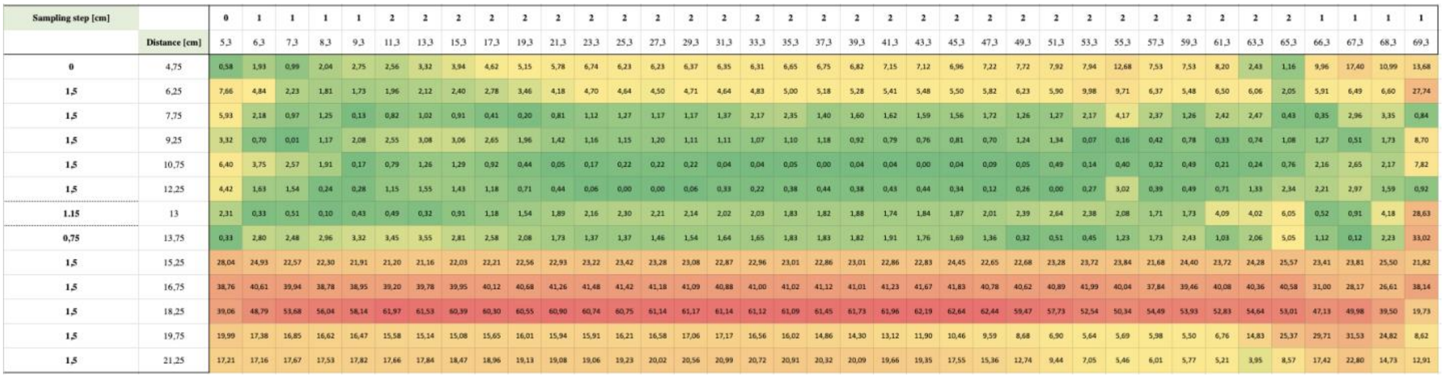

Sampling step [cm]		0	1	1	1	1	2	2	2	2	2	2	2	2	2	2	2	2	2	2	2	2	2	2	2	2	2	2	2	2	2	2	2	2	1	1	1	1
	Distance [cm]	5,3	6,3	7,3	8,3	9,3	11,3	13,3	15,3	17,3	19,3	21,3	23,3	25,3	27,3	29,3	31,3	33,3	35,3	37,3	39,3	41,3	43,3	45,3	47,3	49,3	51,3	53,3	55,3	57,3	59,3	61,3	63,3	65,3	66,3	67,3	68,3	69,3
0	4,75	0,58	1,93	0,99	2,04	2,75	2,56	3,32	3,94	4,62	5,15	5,78	6,74	6,23	6,23	6,37	6,35	6,31	6,65	6,75	6,82	7,15	7,12	6,96	7,22	7,72	7,92	7,94	12,68	7,53	7,53	8,20	2,43	1,16	9,96	17,40	10,99	13,68
1,5	6,25	7,66	4,84	2,23	1,81	1,73	1,96	2,12	2,40	2,78	3,46	4,18	4,70	4,64	4,50	4,71	4,64	4,83	5,00	5,18	5,28	5,41	5,48	5,50	5,82	6,23	5,90	9,98	9,71	6,37	5,48	6,50	6,06	2,05	5,91	6,49	6,60	27,74
1,5	7,75	5,93	2,18	0,97	1,25	0,13	0,82	1,02	0,91	0,41	0,20	0,81	1,12	1,27	1,17	1,17	1,37	2,17	2,35	1,40	1,60	1,62	1,59	1,56	1,72	1,26	1,27	2,17	4,17	2,37	1,26	2,42	2,47	0,43	0,35	2,96	3,35	0,84
1,5	9,25	3,32	0,70	0,01	1,17	2,08	2,55	3,08	3,06	2,65	1,96	1,42	1,16	1,15	1,20	1,11	1,11	1,07	1,10	1,18	0,92	0,79	0,76	0,81	0,70	1,24	1,34	0,07	0,16	0,42	0,78	0,33	0,74	1,08	1,27	0,51	1,73	8,70
1,5	10,75	6,40	3,75	2,57	1,91	0,17	0,79	1,26	1,29	0,92	0,44	0,05	0,17	0,22	0,22	0,22	0,04	0,04	0,05	0,00	0,04	0,04	0,00	0,04	0,09	0,05	0,49	0,14	0,40	0,32	0,49	0,21	0,24	0,76	2,16	2,65	2,17	7,82
1,5	12,25	4,42	1,63	1,54	0,24	0,28	1,15	1,55	1,43	1,18	0,71	0,44	0,06	0,00	0,00	0,06	0,33	0,22	0,38	0,44	0,38	0,43	0,44	0,34	0,12	0,26	0,00	0,27	3,02	0,39	0,49	0,71	1,33	2,34	2,21	2,97	1,59	0,92
1.15	13	2,31	0,33	0,51	0,10	0,43	0,49	0,32	0,91	1,18	1,54	1,89	2,16	2,30	2,21	2,14	2,02	2,03	1,83	1,82	1,88	1,74	1,84	1,87	2,01	2,39	2,64	2,38	2,08	1,71	1,73	4,09	4,02	6,05	0,52	0,91	4,18	28,63
0,75	13,75	0,33	2,80	2,48	2,96	3,32	3,45	3,55	2,81	2,58	2,08	1,73	1,37	1,37	1,46	1,54	1,64	1,65	1,83	1,83	1,82	1,91	1,76	1,69	1,36	0,32	0,51	0,45	1,23	1,73	2,43	1,03	2,06	5,05	1,12	0,12	2,23	33,02
1,5	15,25	28,04	24,93	22,57	22,30	21,91	21,20	21,16	22,03	22,21	22,56	22,93	23,22	23,42	23,28	23,08	22,87	22,96	23,01	22,86	23,01	22,86	22,83	24,45	22,65	22,68	23,28	23,72	23,84	21,68	24,40	23,72	24,28	25,57	23,41	23,81	25,50	21,82
1,5	16,75	38,76	40,61	39,94	38,78	38,95	39,20	39,78	39,95	40,12	40,68	41,26	41,48	41,42	41,18	41,09	40,88	41,00	41,02	41,12	41,01	41,23	41,67	41,83	40,78	40,62	40,89	41,99	40,04	37,84	39,46	40,08	40,36	40,58	31,00	28,17	26,61	38,14
1,5	18,25	39,06	48,79	53,68	56,04	58,14	61,97	61,53	60,39	60,30	60,55	60,90	60,74	60,75	61,14	61,17	61,14	61,12	61,09	61,45	61,73	61,96	62,19	62,64	62,44	59,47	57,73	52,54	50,34	54,49	53,93	52,83	54,64	53,01	47,13	49,98	39,50	19,73
1,5	19,75	19,99	17,38	16,85	16,62	16,47	15,58	15,14	15,08	15,65	16,01	15,94	15,91	16,21	16,58	17,06	17,17	16,56	16,02	14,86	14,30	13,12	11,90	10,46	9,59	8,68	6,90	5,64	5,69	5,98	5,50	6,76	14,83	25,37	29,71	31,53	24,82	8,62
1,5	21,25	17,21	17,16	17,67	17,53	17,82	17,66	17,84	18,47	18,96	19,13	19,08	19,06	19,23	20,02	20,56	20,99	20,72	20,91	20,32	20,09	19,66	19,35	17,55	15,36	12,74	9,44	7,05	5,46	6,01	5,77	5,21	3,95	8,57	17,42	22,80	14,73	12,91

Figure 52: Relative absolute percentage error map for the configuration with the upper lamp turned on.

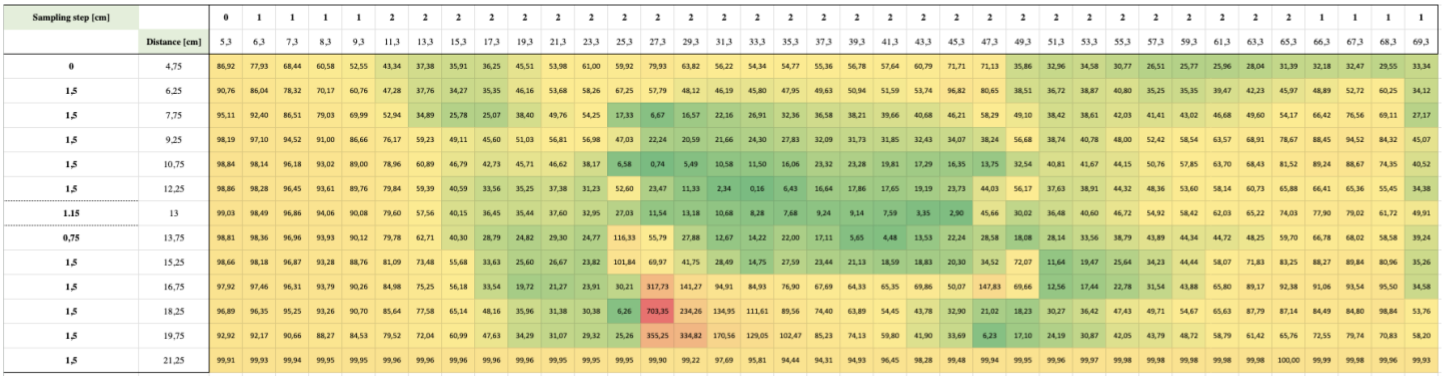

Sampling step [cm]		0	1	1	1	1	2	2	2	2	2	2	2	2	2	2	2	2	2	2	2	2	2	2	2	2	2	2	2	2	2	2	2	2	1	1	1	1
	Distance [cm]	5,3	6,3	7,3	8,3	9,3	11,3	13,3	15,3	17,3	19,3	21,3	23,3	25,3	27,3	29,3	31,3	33,3	35,3	37,3	39,3	41,3	43,3	45,3	47,3	49,3	51,3	53,3	55,3	57,3	59,3	61,3	63,3	65,3	66,3	67,3	68,3	69,3
0	4,75	86,92	77,93	68,44	60,58	52,55	43,34	37,38	35,91	36,25	45,51	53,98	61,00	59,92	79,93	63,82	56,22	54,34	54,77	55,36	56,78	57,64	60,79	71,71	71,13	35,86	32,96	34,58	30,77	26,51	25,77	25,96	28,04	31,39	32,18	32,47	29,55	33,34
1,5	6,25	90,76	86,04	78,32	70,17	60,76	47,28	37,76	34,27	35,35	46,16	53,68	58,26	67,25	57,79	48,12	46,19	45,80	47,95	49,63	50,94	51,59	53,74	96,82	80,65	38,51	36,72	38,87	40,80	35,25	35,35	39,47	42,23	45,97	48,89	52,72	60,25	34,12
1,5	7,75	95,11	92,40	86,51	79,03	69,99	52,94	34,89	25,78	25,07	38,40	49,76	54,25	17,33	6,67	16,57	22,16	26,91	32,36	36,58	38,21	39,66	40,68	46,21	58,29	49,10	38,42	38,61	42,03	41,41	43,02	46,68	49,60	54,17	66,42	76,56	69,11	27,17
1,5	9,25	98,19	97,10	94,52	91,00	86,66	76,17	59,23	49,11	45,60	51,03	56,81	56,98	47,03	22,24	20,59	21,66	24,30	27,83	32,09	31,73	31,85	32,43	34,07	38,24	56,68	38,74	40,78	48,00	52,42	58,54	63,57	68,91	78,67	88,45	94,52	84,32	45,07
1,5	10,75	98,84	98,14	96,18	93,02	89,00	78,96	60,89	46,79	42,73	45,71	46,62	38,17	6,58	0,74	5,49	10,58	11,50	16,06	23,32	23,28	19,81	17,29	16,35	13,75	32,54	40,81	41,67	44,15	50,76	57,85	63,70	68,43	81,52	89,24	88,67	74,35	40,52
1,5	12,25	98,86	98,28	96,45	93,61	89,76	79,84	59,39	40,59	33,56	35,25	37,38	31,23	52,60	23,47	11,33	2,34	0,16	6,43	16,64	17,86	17,65	19,19	23,73	44,03	56,17	37,63	38,91	44,32	48,36	53,60	58,14	60,73	65,88	66,41	65,36	55,45	34,38
1.15	13	99,03	98,49	96,86	94,06	90,08	79,60	57,56	40,15	36,45	35,44	37,60	32,95	27,03	11,54	13,18	10,68	8,28	7,68	9,24	9,14	7,59	3,35	2,90	45,66	30,02	36,48	40,60	46,72	54,92	58,42	62,03	65,22	74,03	77,90	79,02	61,72	49,91
0,75	13,75	98,81	98,36	96,96	93,93	90,12	79,78	62,71	40,30	28,79	24,82	29,30	24,77	116,33	55,79	27,88	12,67	14,22	22,00	17,11	5,65	4,48	13,53	22,24	28,58	18,08	28,14	33,56	38,79	43,89	44,34	44,72	48,25	59,70	66,78	68,02	58,58	39,24
1,5	15,25	98,66	98,18	96,87	93,28	88,76	81,09	73,48	55,68	33,63	25,60	26,67	23,82	101,84	69,97	41,75	28,49	14,75	27,59	23,44	21,13	18,59	18,83	20,30	34,52	72,07	11,64	19,47	25,64	34,23	44,44	58,07	71,83	83,25	88,27	89,84	80,96	35,26
1,5	16,75	97,92	97,46	96,31	93,79	90,26	84,98	75,25	56,18	33,54	19,72	21,27	23,91	30,21	317,73	141,27	94,91	84,93	76,90	67,69	64,33	65,35	69,86	50,07	147,83	69,66	12,56	17,44	22,78	31,54	43,88	65,80	89,17	92,38	91,06	93,54	95,50	34,58
1,5	18,25	96,89	96,35	95,25	93,26	90,70	85,64	77,58	65,14	48,16	35,96	31,38	30,38	6,26	703,35	234,26	134,95	111,61	89,56	74,40	63,89	54,45	43,78	32,90	21,02	18,23	30,27	36,42	47,43	49,71	54,67	65,63	87,79	87,14	84,49	84,80	98,84	53,76
1,5	19,75	92,92	92,17	90,66	88,27	84,53	79,52	72,04	60,99	47,63	34,29	31,07	29,32	25,26	355,25	334,82	170,56	129,05	102,47	85,23	74,13	59,80	41,90	33,69	6,23	17,10	24,19	30,87	42,05	43,79	48,72	58,79	61,42	65,76	72,55	79,74	70,83	58,20
1,5	21,25	99,91	99,93	99,94	99,95	99,95	99,96	99,96	99,96	99,96	99,96	99,95	99,95	99,95	99,90	99,22	97,69	95,81	94,44	94,31	94,93	96,45	98,28	99,48	99,94	99,95	99,96	99,97	99,98	99,98	99,98	99,98	99,98	100,00	99,99	99,98	99,96	99,93

Figure 53: Relative absolute percentage error map for the configuration with the central LED turned on.

In the case of the upper lamp configuration, the illuminated region, namely the upper central and left part of the map, shows a maximum relative error of approximately 13%. However, in the less illuminated areas, where the power density is very low, the error increases significantly, reaching much higher values.

A different behaviour is observed in the configuration with the single central LED on; in the strongly illuminated region, the relative error is around 22%, but it increases rapidly as one moves away from the central area. In these peripheral zones, the error reaches very high values, indicating greater sensitivity of the measurement to local conditions and internal reflections.

It is important to note that the high discrepancies observed in the single-LED comparison may be attributed to a deterioration of the source during the third measurement campaign, as the LED in question ceased functioning shortly after the acquisition. This suggests that the source was already in a degraded state at the time of measurement, negatively affecting the reliability of the acquired data.

Overall, these results confirm the validity of the comparison between the two campaigns only under well-controlled and symmetric conditions and emphasize the importance of preserving source integrity to ensure the repeatability and reliability of the measurements.

4.5 Source characterization

In the context of experimental analysis, an accurate characterization of the spatial emission of the UVC LEDs employed in the device is of paramount importance.

To this end, a three-dimensional emission model, referred to as the emission solid, was constructed to precisely represent the angular distribution of the irradiated power density. This model was developed with the specific aim of faithfully reproducing the optical behavior of the source within a simulated environment.

The resulting emission solid will serve as the reference for the subsequent numerical implementation within the COMSOL Multiphysics® environment, as detailed in the following chapter.

Starting from the second measurement campaign, and in particular from the analysis of data acquired with a single active source, the reconstruction of the emission solid was based on the irradiance map corresponding to the sixteenth LED, positioned at the center of the array.

4.5.1 Reconstruction of the Emission Solid Based on Experimental Data

In the context of a luminous source (possibly point-like), the illuminance E_v at a point on the receiving surface is defined as follows:

$$E_v = \frac{d\phi_v}{dA} \tag{4.5.1}$$

Where $d\phi_v$ represents the infinitesimal variation of the incident radiant flux, expressed in watts [W], dA denotes the area of the receiving surface element [m²].

Luminous intensity I, emitted by the source in a given direction, is defined as the ratio between the infinitesimal variation of the radiant flux and the size of the solid angle element dΩ, expressed in steradians [sr]:

$$\mathrm{I} = \frac{d\phi_v}{d\Omega} \tag{4.5.2}$$

Therefore, luminous intensity is intrinsically independent of the distance from the source, depending solely on the direction around which the solid angle element $d\Omega$ is derived.

Considering a polar coordinate system r, θ, φ, any generic straight direction around which each solid angle element is defined can be specified by a pair of angles θ, φ. The map $I(\theta, \varphi)$ is traditionally referred to as the "emission solid" of the source.

In the present study, the following polar coordinate system will be considered:

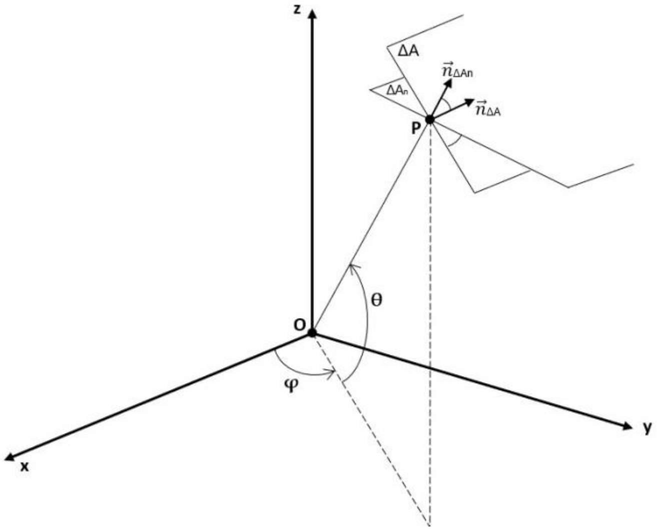

Figure 54: Polar coordinate system.

Where the following equations describe the coordinate transformations with respect to the Cartesian system:

$$\begin{cases} x = r\cos\vartheta\cos\varphi \\ y = r\cos\vartheta\sin\varphi \\ z = r\sin\vartheta \end{cases} \tag{4.5.3}$$

By integrating the illuminance over a receiving surface A, the total received radiant flux is obtained:

$$\phi_v = \int E_v dA \tag{4.5.4}$$

Similarly, the radiant flux emitted by the source in all directions can be expressed as an integral of the luminous intensity over the entire solid angle:

$$\phi_v = \int_0^{4\pi} I(\Omega)d\Omega = \int I\,(\vartheta,\ \varphi)\ dA_{sfera} \int_{\vartheta=0}^{\pi}\int_{\varphi=0}^{2\pi} I(\vartheta,\varphi)sin(\vartheta)\ d\vartheta d\varphi \tag{4.5.5}$$

Recalling that, in the polar coordinate system previously introduced, the surface element on a sphere is expressed as $dA = r^2 cos\theta d\varphi d\theta$, and considering the differential definition of solid angle $d\Omega = \frac{dA}{r^2}$ the integral of the luminous intensity can be rewritten as:

$$\phi_v = \int_{\vartheta=-\pi}^{\pi}\int_{\varphi=0}^{2\pi} I(\vartheta,\varphi)cos(\vartheta)\ d\vartheta d\varphi \tag{4.5.6}$$

In the present study, the source under investigation has a characteristic dimension on the order of 3 mm and is positioned at a distance of 11 cm from the measurement surface. Since this distance exceeds the maximum dimension of the source by more than a factor of five, it is reasonable to approximate the source, with sufficient accuracy, as a point source.

Let R denote the distance between a point source O and a surface element ΔS, and Let α denote the angle between the direction of radiation propagation and the normal vector to the surface element, $\overrightarrow{n_{\Delta S}}$, the projection of the surface ΔS onto the sphere centered at point A with radius R is given by:

$$\Delta S_n = \Delta S\ *\cos\alpha \tag{4.5.7}$$

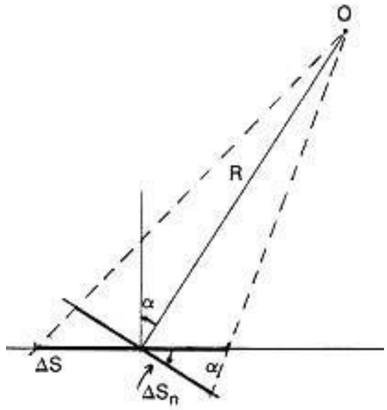

Figure 55: Surface projection.

The solid angle subtended by this projection is:

$$\Delta\Omega = \frac{\Delta S_n}{r^2} = \frac{\Delta S \ * \ \cos\alpha}{r^2} \tag{4.5.8}$$

The radiant flux emitted within the solid angle is:

$$\Delta\phi = I * \Delta\Omega = I * \frac{\Delta S \ * \ \cos\alpha}{r^2} \tag{4.5.9}$$

From which the expression for illuminance is derived:

$$E_v = \frac{\Delta\phi}{\Delta S} = \frac{I * \ \cos\alpha}{R^2} \tag{4.5.10}$$

In order to reconstruct the directional luminous intensity $I(\theta, \varphi)$ from known illuminance values measured on an arbitrarily oriented surface element ΔS it is necessary to express the term $\cos\alpha$as a function of the polar angles (φ, θ), which define the direction of the incident radiation with respect to the source-surface geometry.

Let us consider a surface ΔS on which illuminance is evaluated, and a generic point P on this surface, located at a distance from a luminous source positioned at point O. The point P is associated with a position vector $\overrightarrow{OP}$. Let ΔS_nbe a surface normal to $\overrightarrow{OP}$; evidently, the unit normal vector to ΔS_n, denoted $\vec{n}_{\Delta S_n}$, coincides with the unit vector of $\overrightarrow{OP}$: $\widehat{n_{\Delta S_n}} = \frac{\overrightarrow{OP}}{\|OP\|}$. Let $\widehat{n_{\Delta S}}$ be the normal vector to the surface ΔScontaining the point on which the radiation is incident. The angle α, defined as the angle between the planes $\Delta S$and ΔS_n, coincides with the angle between their respective normal vector $\widehat{n_{\Delta S}}$ e $\widehat{n_{\Delta S_n}}$, and is expressed by the scalar product:

$$\cos\alpha \ = \ \widehat{n_{\Delta A}} \cdot \widehat{n_{\Delta A_n}} \tag{4.5.11}$$

Starting from the coordinate transformation formula (4.5.3) and denoting by (φ, θ) the angular parameters characterizing the normal vector $\widehat{n_{\Delta S_n}}$ and by (φ', θ')those corresponding to the normal vector $\widehat{n_{\Delta S}}$, the unit vectors $\widehat{n_{\Delta S_n}}$ e $\widehat{n_{\Delta S}}$ can be expressed as follows:

$$\widehat{n_{\Delta S_n}} = \frac{\overrightarrow{OP}}{\|OP\|} = \frac{x\hat{\imath}+y\hat{\jmath}+\widehat{x\hat{k}}}{\sqrt{x^2+y^2+z^2}} = \frac{r\ \cos\vartheta\cos\varphi\hat{\imath}+r\ \cos\vartheta\sin\varphi\hat{\jmath}+r\ \sin\vartheta\hat{k}}{r} = \cos\vartheta\cos\varphi\,\hat{\imath} + \cos\vartheta\sin\varphi\,\hat{\jmath} + \sin\vartheta\,\hat{k} \tag{4.5.12}$$

$$\widehat{n_{\Delta S}} = \cos\vartheta'\cos\varphi'\,\hat{\imath} + \cos\vartheta'^{\sin\varphi'\hat{\jmath}} + \sin\vartheta'\hat{k} \tag{4.5.13}$$

We can therefore express $\cos\alpha$ as:

$$\begin{aligned}\cos\alpha &= \widehat{n_{\Delta A}}\cdot\widehat{n_{\Delta A_n}} \\ &= \cos\vartheta\cos\varphi\cos\vartheta'\cos\varphi' + \cos\vartheta\sin\varphi\cos\vartheta'\sin\varphi' + \sin\vartheta\sin\vartheta'\end{aligned} \tag{4.5.14}$$

In the configuration relevant to this study, where the goal is to reconstruct the UV-C irradiation intensity from known illuminance values on a surface orthogonal to the x-axis, the normal vector $\widehat{n_{\Delta A}}$ coincides with the unit vector along the x-axis:

$$\widehat{n_{\Delta A}} \equiv \hat{\imath} = \begin{pmatrix}1\\0\\0\end{pmatrix} \tag{4.5.15}$$

It therefore follows that the relation holds:

$$\begin{aligned}\cos\alpha &= \widehat{n_{\Delta A}}\cdot\widehat{n_{\Delta A_n}} = \widehat{n_x}\cdot\frac{\overrightarrow{OP}}{\|OP\|} \\ &= \left(1\hat{\imath}+0\hat{\jmath}+0\hat{k}\right)\cdot\frac{\left(\cos\vartheta\cos\varphi\,\hat{\imath}+\cos\vartheta\sin\varphi\,\hat{\jmath}+\sin\vartheta\,\hat{k}\right)}{r} \\ &= \cos\vartheta\ \cos\varphi\end{aligned} \tag{4.5.16}$$

Ultimately, the following relation holds:

$$\cos\alpha = \cos\vartheta\ \cos\varphi \tag{4.5.17}$$

We can therefore express the illuminance as:

$$\mathrm{E} = \frac{I * \cos\vartheta\ \cos\varphi}{r^2} \tag{4.5.18}$$

This relationship was employed to reconstruct the irradiation intensity, that is, to determine the value of the intensity emitted by the source in a given direction, based on the illuminance measurements taken on surface elements. For this purpose, given the coordinates of the measurement points, the angles ϑ and φ were computed for each point in the experimental map.

Finally, by inverting the relationship:

$$\mathrm{I} = \frac{E * r^2}{\cos \vartheta \, \cos \varphi} \tag{4.5.19}$$

The angular distribution of the luminous intensity is obtained, which is essential for reconstructing the LED emission solid.

Therefore, once the data from the experimental map had been retrieved, it was necessary to evaluate the horizontal and vertical opening angles. For the reconstruction of the emission solid, a coordinate transformation was performed from the Cartesian system (x, y, z) to the spherical reference system (r, θ, φ), deriving, from the known coordinates of the various measurement points, the corresponding angular. values.
For each measurement point, r is expressed as:

$$r^2 = {r_{xy}}^2 + z^2 = x^2 + y^2 + z^2 \tag{4.5.20}$$

where x, y, and $z$are the Cartesian coordinates of the point.

The angles (θ, φ) can similarly be determined from the Cartesian coordinates (x, y, z) of the points at which the sensor is located.

In the adopted reference system, where the x-axis coincides with the direction of wave propagation, the azimuthal angle $\varphi$is defined as the angle between the x-axis and the projection of the ray direction onto the xy-plane, whereas the elevation angle $\theta$is defined as the angle between the ray direction and the xy-plane.

Under these assumptions, the two angles can be expressed as:

$$\vartheta = \tan^{-1} \frac{z}{x^2 + y^2} \tag{4.5.21}$$

$$\varphi = \tan^{-1} \frac{y}{x} \tag{4.5.22}$$

For the construction of the emission solid, as previously mentioned at the beginning of the paragraph, the experimental map corresponding to the power density distribution emitted by LED 16, located on the central bar, was selected.

This phase of the study was conducted using the MATLAB environment, which enabled the reconstruction of a three-dimensional matrix representing the emission profile of the LED as a function of the angles ϑ and φ.

Starting from the experimental irradiation maps, the corresponding luminance distribution was derived, understood as a three-dimensional representation of the source's emission solid. The resulting luminance describes the intensity of the emission as a function of the elevation angle ϑ and the azimuthal angle φ, forming the basis for modeling the angular behavior of the LED, as reported in figure 57.

Regarding the angle φ, the available experimental data covered a sufficiently wide range to include regions where the distribution vanishes. To complete the coverage of the entire emission hemisphere, the interval was synthetically extended to $[-\pi, \pi]$ by controlled addition of the missing angular values, preserving consistency with the observed trend.

Conversely, for the angle ϑ, the density of experimental measurement points was limited to a narrower interval due to the geometric configuration of the sensors. To ensure full coverage of the hemisphere and guarantee that the emission function vanishes at the boundaries of the angular domain, synthetic data corresponding to larger angles were added, consistent with a physically plausible behavior of the source. This extension enabled the modeling of the luminance distribution over the entire upper hemisphere, while maintaining continuity and coherence with the actual experimental data.

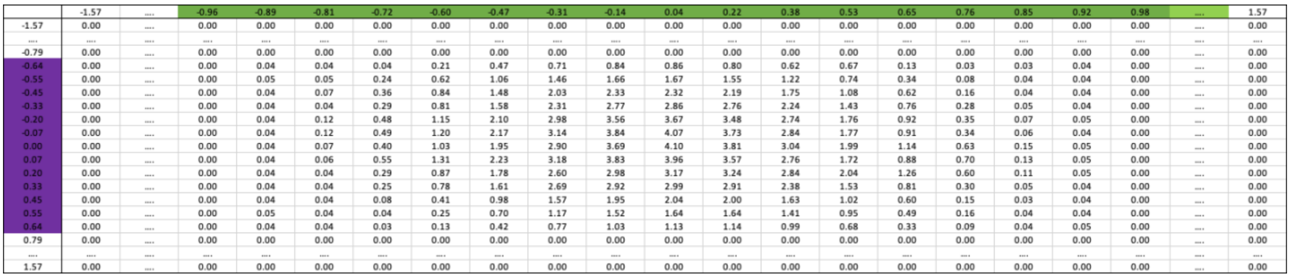

	-1.57	....	-0.96	-0.89	-0.81	-0.72	-0.60	-0.47	-0.31	-0.14	0.04	0.22	0.38	0.53	0.65	0.76	0.85	0.92	0.98	....	1.57
-1.57	0.00	....	0.00	0.00	0.00	0.00	0.00	0.00	0.00	0.00	0.00	0.00	0.00	0.00	0.00	0.00	0.00	0.00	0.00	....	0.00
....	....	....	....	....	....	....	....	....	....	....	....	....	....	....	....	....	....	....	....	....	....
-0.79	0.00	....	0.00	0.00	0.00	0.00	0.00	0.00	0.00	0.00	0.00	0.00	0.00	0.00	0.00	0.00	0.00	0.00	0.00	....	0.00
-0.64	0.00	....	0.00	0.04	0.04	0.04	0.21	0.47	0.71	0.84	0.86	0.80	0.62	0.67	0.13	0.03	0.03	0.04	0.00	....	0.00
-0.55	0.00	....	0.00	0.05	0.05	0.24	0.62	1.06	1.46	1.66	1.67	1.55	1.22	0.74	0.34	0.08	0.04	0.04	0.00	....	0.00
-0.45	0.00	....	0.00	0.04	0.07	0.36	0.84	1.48	2.03	2.33	2.32	2.19	1.75	1.08	0.62	0.16	0.04	0.04	0.00	....	0.00
-0.33	0.00	....	0.00	0.04	0.04	0.29	0.81	1.58	2.31	2.77	2.86	2.76	2.24	1.43	0.76	0.28	0.05	0.04	0.00	....	0.00
-0.20	0.00	....	0.00	0.04	0.12	0.48	1.15	2.10	2.98	3.56	3.67	3.48	2.74	1.76	0.92	0.35	0.07	0.05	0.00	....	0.00
-0.07	0.00	....	0.00	0.04	0.12	0.49	1.20	2.17	3.14	3.84	4.07	3.73	2.84	1.77	0.91	0.34	0.06	0.04	0.00	....	0.00
0.00	0.00	....	0.00	0.04	0.07	0.40	1.03	1.95	2.90	3.69	4.10	3.81	3.04	1.99	1.14	0.63	0.15	0.05	0.00	....	0.00
0.07	0.00	....	0.00	0.04	0.06	0.55	1.31	2.23	3.18	3.83	3.96	3.57	2.76	1.72	0.88	0.70	0.13	0.05	0.00	....	0.00
0.20	0.00	....	0.00	0.04	0.04	0.29	0.87	1.78	2.60	2.98	3.17	3.24	2.84	2.04	1.26	0.60	0.11	0.05	0.00	....	0.00
0.33	0.00	....	0.00	0.04	0.04	0.25	0.78	1.61	2.69	2.92	2.99	2.91	2.38	1.53	0.81	0.30	0.05	0.04	0.00	....	0.00
0.45	0.00	....	0.00	0.04	0.04	0.08	0.41	0.98	1.57	1.95	2.04	2.00	1.63	1.02	0.60	0.15	0.03	0.04	0.00	....	0.00
0.55	0.00	....	0.00	0.05	0.04	0.04	0.25	0.70	1.17	1.52	1.64	1.64	1.41	0.95	0.49	0.16	0.04	0.04	0.00	....	0.00
0.64	0.00	....	0.00	0.04	0.04	0.03	0.13	0.42	0.77	1.03	1.13	1.14	0.99	0.68	0.33	0.09	0.04	0.05	0.00	....	0.00
0.79	0.00	....	0.00	0.00	0.00	0.00	0.00	0.00	0.00	0.00	0.00	0.00	0.00	0.00	0.00	0.00	0.00	0.00	0.00	....	0.00
....	....	....	....	....	....	....	....	....	....	....	....	....	....	....	....	....	....	....	....	....	....
1.57	0.00	....	0.00	0.00	0.00	0.00	0.00	0.00	0.00	0.00	0.00	0.00	0.00	0.00	0.00	0.00	0.00	0.00	0.00	....	0.00

Figure 56: Emission solid data.

Figure 58 illustrates the angular interval selected for the analysis, highlighting how the boundary values were forced to zero in order to suppress emission outside the domain of interest. Specifically, the visible dots indicate columns of zeros along the φ direction that were present in the experimental data, whereas for ϑ, such zeros were manually added to artificially extend the domain and ensure a consistent closure of the angular distribution.

4.6 Mathematical Model of the Emission Solid

The resulting matrix, together with the corresponding values of the angles ϑ and φ, was subsequently imported into the MATLAB environment for the reconstruction of the emission solid. Among the tools available in MATLAB, the Curve Fitter application proved particularly effective for the analysis and modeling of the experimental luminous emission data. This tool enables the fitting of curves and surfaces to discrete data sets, offering a wide range of fitting models, including polynomial, Gaussian, rational, and user-defined functions, with the capability to automatically optimize parameters to minimize the error with respect to the observed data.

In the specific context of this study, Curve Fitter was employed to obtain a continuous and analytical representation of the emission solid from the experimental luminance matrix. The objective was to identify a bidimensional function $f(\vartheta, \varphi)$ capable of accurately approximating the luminous emission profile over the entire angular domain.

To this end, various functional families were explored: in particular, polynomial models of different orders were tested, and, where necessary, more complex custom-built functional expressions were employed to capture the specific features of the distribution. The fitting procedure yielded the optimal parameters for each considered model, allowing the selection of the function that best represented the experimental data, based on goodness-of-fit criteria such as the root mean square error and the coefficient of determination R^2.

This procedure enabled the derivation of a mathematical model of the emission solid that preserves the actual irradiance profile and is readily integrable into subsequent simulation environments.

For the reconstruction of the emission solid from the experimental data, the initial choice of fitting equations was based on well-established models from the literature, to adopt analytical representations capable of accurately describing the angular behavior of the intensity distribution. In particular, the primary reference was the study by "*Moreno, I.; Sun, C.-C. 2008*" [119], which proposes a phenomenological approach that is both simple and accurate for modeling the radiation pattern of LED sources under far-field conditions.

According to this work, the radiation pattern can be described as the sum of a maximum of two or three elementary functions, selected from the following:

1 **Gaussian function** (Eq. 1 of the reference), employed to represent angular distributions characterized by symmetric and regular decay:

$$\mathrm{I}(\theta, \phi) = \sum_i g_{1i} \exp\left[-(\ln 2)(\theta - g_{2i})^2 \left(\frac{\cos^2 \phi}{(g_{3i})^2} + \frac{\sin^2 \phi}{(g_{4i})^2}\right)\right] \tag{4.6.1}$$

2 **Cosine power function** (Eq. 2 of the reference), suitable for modelling behaviours close to Lambertian emission or with sharper decay at the edges:

$$\mathrm{I}(\theta, \phi) = \sum_i c_{1i} \cos^{c_{4i}}[\theta - (c_{2i} \cos^2 \phi + c_{3i} \sin^2 \phi)] \tag{4.6.2}$$

These functions are derived from physical considerations related to light propagation from the emitting chip, reflection within the reflecting cup, and refraction/lensing effects of the optical enclosure. They apply to a wide range of LED types, including Lambertian, batwing, and side-emitter configurations.

In our work, to complement the two formulations drawn from the literature, a third type of function was introduced, purely polynomial in nature and not derived from physical models or bibliographic sources. This approach was implemented using exclusively the functionalities of MATLAB's Curve Fitter toolbox, which enables the identification of a best-fit polynomial model based on the available experimental data. This empirical model allowed for the exploration of the adaptability of a representation free from theoretical constraints, thereby enabling a performance comparison with more physically motivated models.

The combination of these three approaches enabled a thorough comparative evaluation between methodologies based on known physical models and purely numerical solutions, allowing for the identification of the limitations and advantages of each in terms of fitting quality, model robustness, and ease of implementation in subsequent solid reconstruction processes.

For an initial preliminary assessment and to identify the equation most representative of the emission solid, a numerical-experimental comparison was conducted at a reference wavelength of 265 nm. To this end, a fictitious quadratic mesh was adopted, with elements of 1 cm², corresponding to the target surface on which the quantity of interest, namely, the incident power density, was evaluated. For the spatial discretization of the emission solid, a total of 64,000 rays was employed.

The approximation surfaces obtained via MATLAB are reported below, together with the initial results of the numerical-experimental comparison, in figure 58, 59, 60 for gaussian, cosine and polynomial function respectively.

The Gaussian function result

$$\mathrm{f}(\varphi,\varphi) = \mathrm{a}\cdot\exp\left(-ln(2)(|\vartheta|-b)^2\left(\left(cos(\varphi)\right)^2/c^2+\left(sin(\varphi)\right)^2/d^2\right)\right)+a_1 \cdot exp\left(-ln(2)(|\vartheta|-b_1)^2\left(\left(cos(\varphi)\right)^2/c_1^2+\left(sin(\varphi)\right)^2/d_1^2\right)\right) \quad (4.6.3)$$

and it is shown in figure 57.

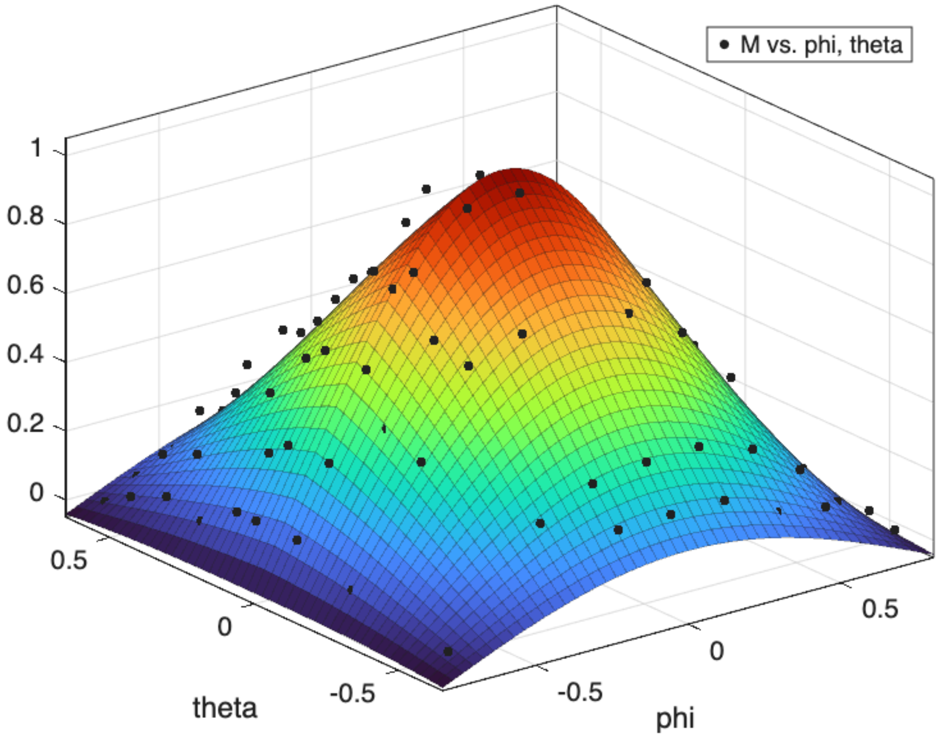

Value of the coefficients

a	1.4105
a1	-1.4945
b	0.9623
b1	1.0341
c	601.53
c1	0.7462
d	0.6933
d1	2.0727

R-square 0.9723

Tolerance 10^{-6}

Figure 57: Gaussian function fitting of the intensity matrix of figure 56.

The Cosine power function

$$\begin{aligned} f(\varphi, \vartheta) \;=\; & a\,cos^2\left(|\vartheta| - \left(bcos^2(\varphi) + csin^2(\varphi)\right)\right) + \\ & a^1 cos^2\left(|\vartheta| - \left(b^1 cos^2(\varphi) + c^1 sin^2(\varphi)\right)\right) \end{aligned} \tag{4.6.4}$$

and it is shown in figure 58.

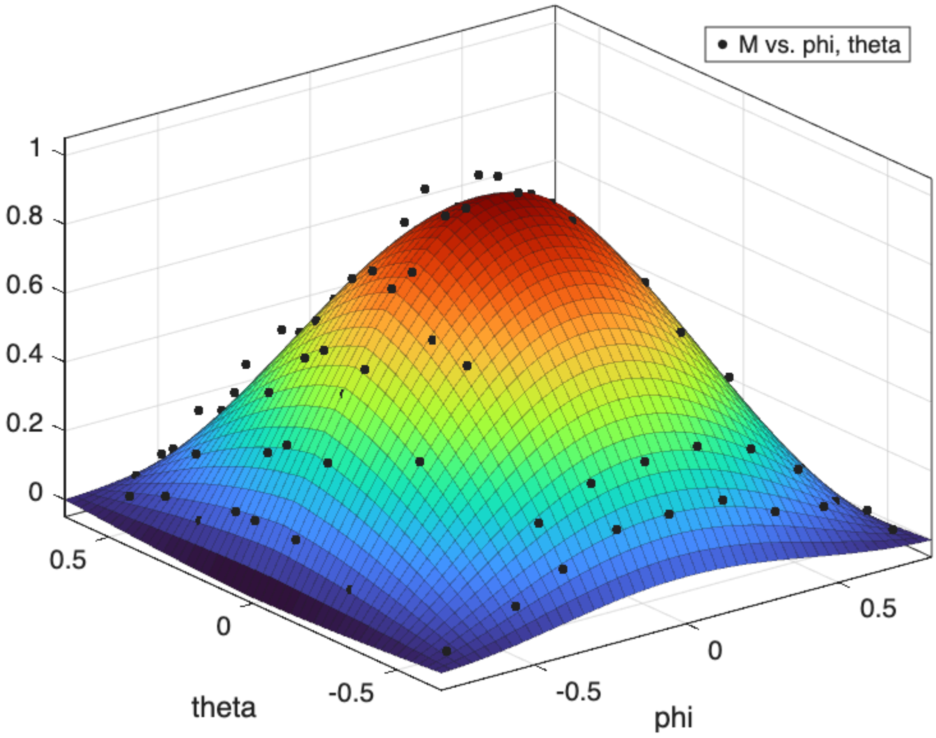

Value of the coefficients

a	9.5382
a1	-9.5376
b	0.6475
b1	0.7482
c	0.6784
c1	0.5787

R-square 0.9658

Tolerance 10^{-5}

Figure 58: Cosine function fitting of the intensity matrix of figure 56.

The Polynomial function

$$f(\varphi,\ \theta) = p^{00} + p^{10}\cdot\varphi + p^{01}\cdot\theta + p^{20}\cdot\varphi^2 + p^{11}\cdot\varphi\cdot\theta + p^{02}\cdot\theta^2 + p^{30} \cdot\varphi^3 + p^{21}\cdot\varphi^2\cdot\theta + p^{12}\cdot\varphi\cdot\theta^2 + p^{03}\cdot\theta^3 + p^{40}\cdot\varphi^4 + p^{31} \cdot\varphi^3\cdot\theta + p^{22}\cdot\varphi^2\cdot\theta^2 + p^{13}\cdot\varphi\cdot\theta^3 + p^{04}\cdot\theta^4 \tag{4.6.5}$$

and it is shown in figure 59.

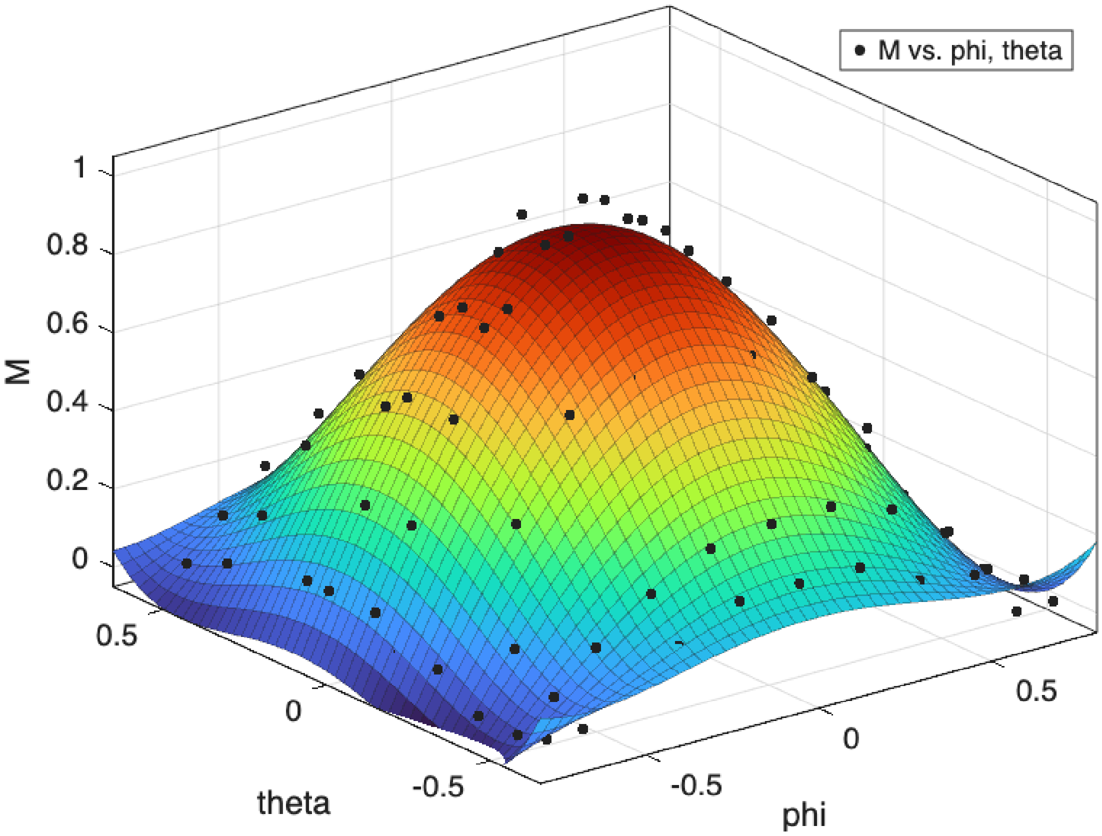

Value of the coefficients

p00	0.9175
p10	-0.1176
p01	0.0757
p20	-1.7528
p11	-0.1886
p02	-2.7716
p30	0.1894
p21	0.0136
p12	0.1449
p03	-0.2547
p40	0.5018
p31	0.161
p22	3.2497
p13	0.2949
p04	2.3393
R-square	0.974
Tolerance	10^{-6}

Figure 59: Polynomial function fitting of the intensity matrix of figure 56.

As can be observed from the graphs shown, the peak values of the curves are equal to 1. This is because the curves were normalized with respect to the maximum of the measured power data, to make the different distributions comparable without altering the relative shape of each curve. The normalization is defined as:

$$\tilde{f}(\varphi,\theta) = f(\varphi,\theta)/f_{max} \tag{4.6.6}$$

where f_{max} represents the maximum value of the power measured experimentally.

The source characterization was implemented in COMSOL by inserting the characteristic curve as a function dependent on an initial parameter, identified as the total power P_{tot} emitted by the source. In this context, the source function can be formalized as:

$$f(\varphi, \theta; P_{tot}) = P_{tot} \cdot \tilde{f}(\varphi, \theta) \tag{4.6.7}$$

This approach allows for consistency between the experimental data and the numerical model. The determination of P_{tot} was carried out using the trapezoidal rule applied to the intensity data measured with a photometer, according to the following formula:

$$P_{tot} \approx \sum_{i=1}^{n-1} \left(\frac{I_i + I_{i+1}}{2}\right) \cdot \Delta\Omega_i \tag{4.6.8}$$

where I_i represents the intensity measured within the solid angle sector $\Delta\Omega_i$.

Subsequently, the area under the non-normalized curve was computed, corresponding to the integral of the parameterized function over the entire emission solid:

$$A = \int_{\Omega} f(\varphi, \theta)\ d\Omega \tag{4.6.9}$$

With

$$d\Omega = cos(\theta)\ d\theta\ d\varphi \tag{4.6.10}$$

In this expression, φ and θ denote the azimuthal and polar angles of the source, respectively. This calculation enables the determination of the total emitted power distribution and serves to verify the consistency between the experimental measurements and the parameterized function used in the simulation.
Even from a preliminary visual analysis, it can be observed that the Gaussian function proposed in the reference article approximates the experimental data with greater accuracy compared to the other tested functions.

This occurs because the cosine function, as evident from the graphs, tends to underestimate the experimental values. Such underestimation directly affects the numerical results, introducing a discrepancy between the simulation and the actual measurements.

Regarding the representation using a fourth-degree polynomial in $\varphi$and θ, it is noticeable that the curve tends to rise at the lateral edges, a phenomenon that leads to significant errors in the peripheral regions of the diagram, which are already critical due to the low relative intensity and the sensitivity of the sensor.

This initial visual analysis is confirmed by the preliminary numerical-experimental comparisons. In particular, the behavior of the power distribution is evaluated in the frontal region with respect to the source, where the normals to the sensor plane and those to the source plane are aligned. In this configuration, the curve is expected to reach its intensity peak, corresponding to the principal emission direction of the source.

In mathematical terms, for the Gaussian function $f_G(\varphi,\theta)$, the cosine function $f_C(\varphi,\theta)$, or the polynomial function $f_P(\varphi,\theta)$, the distribution along the direction normal to the source ($\varphi = 0, \theta = 0$) must satisfy:

$$f(0,0) \approx I_{max} \tag{4.6.11}$$

where $I_{\max}$ represents the maximum value of intensity measured experimentally. The lateral discrepancies observed in the cosine and polynomial functions manifest as deviations from the expected peak, highlighting the influence of the chosen parametric function on the numerical model.

Once the most representative parametric function was identified and all relevant parameters were determined, it was implemented in COMSOL Multiphysics as a weighting function within the Ray Optics module. The corresponding simulation was then executed, and the extracted irradiance data were subsequently compared with the experimental measurements to assess the model's reliability and accuracy.

Below are the comparisons between numerical and experimental data, considering the measurements acquired and subsequently simulated at the wavelength of 265 nm:

Gaussian function

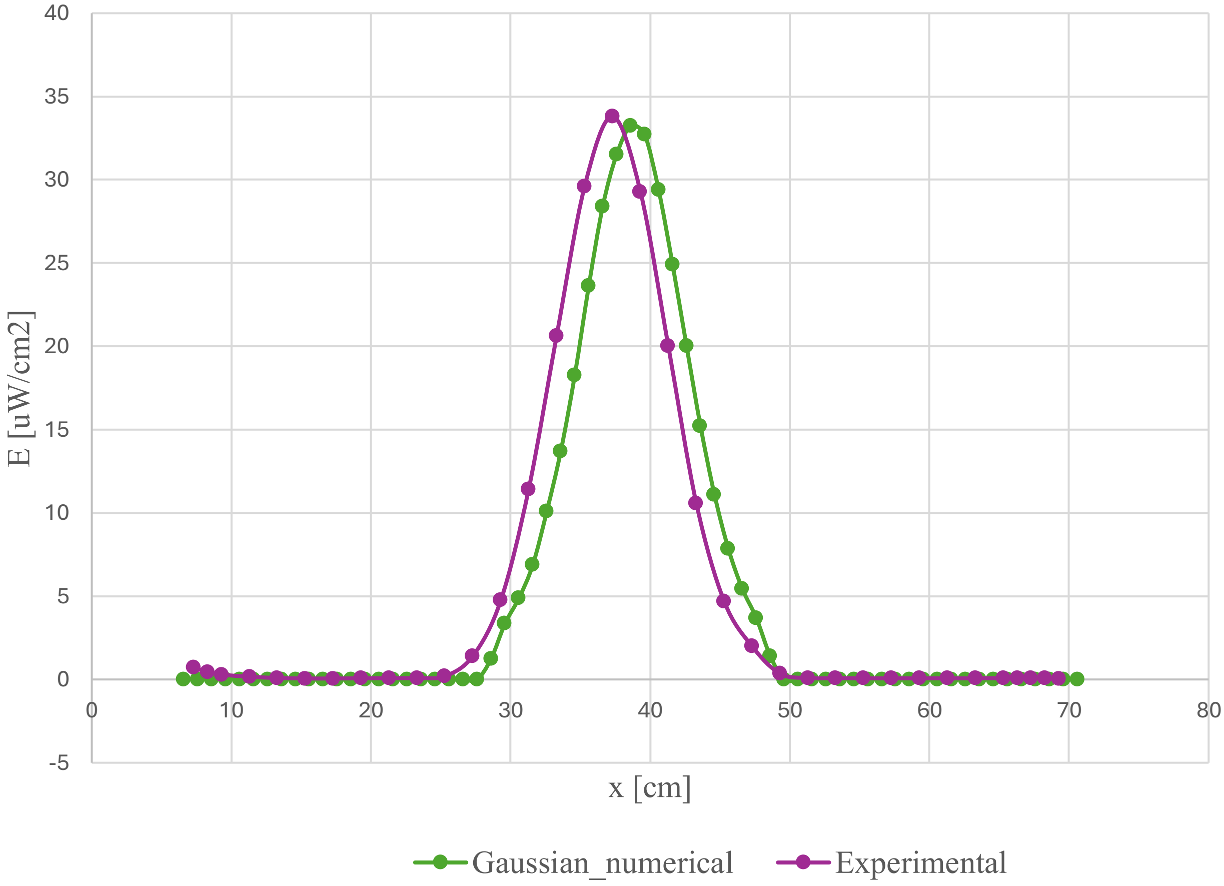

Figure 60: Comparison between the power density profile along the x-axis from a numerical gaussian emission distribution and experimental data.

Cosine power function

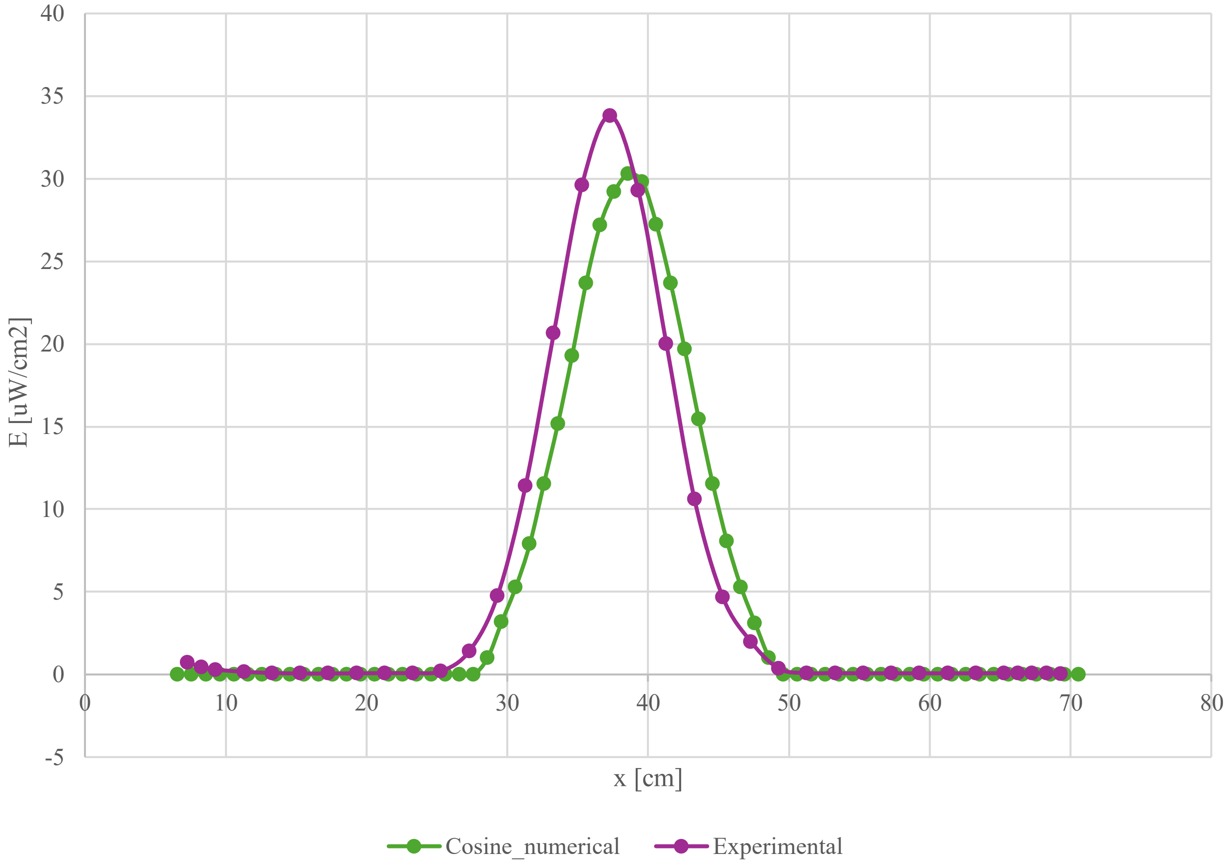

Figure 61: Comparison between the power density profile along the x-axis from a numerical cosine emission distribution and experimental data.

Polynomial function

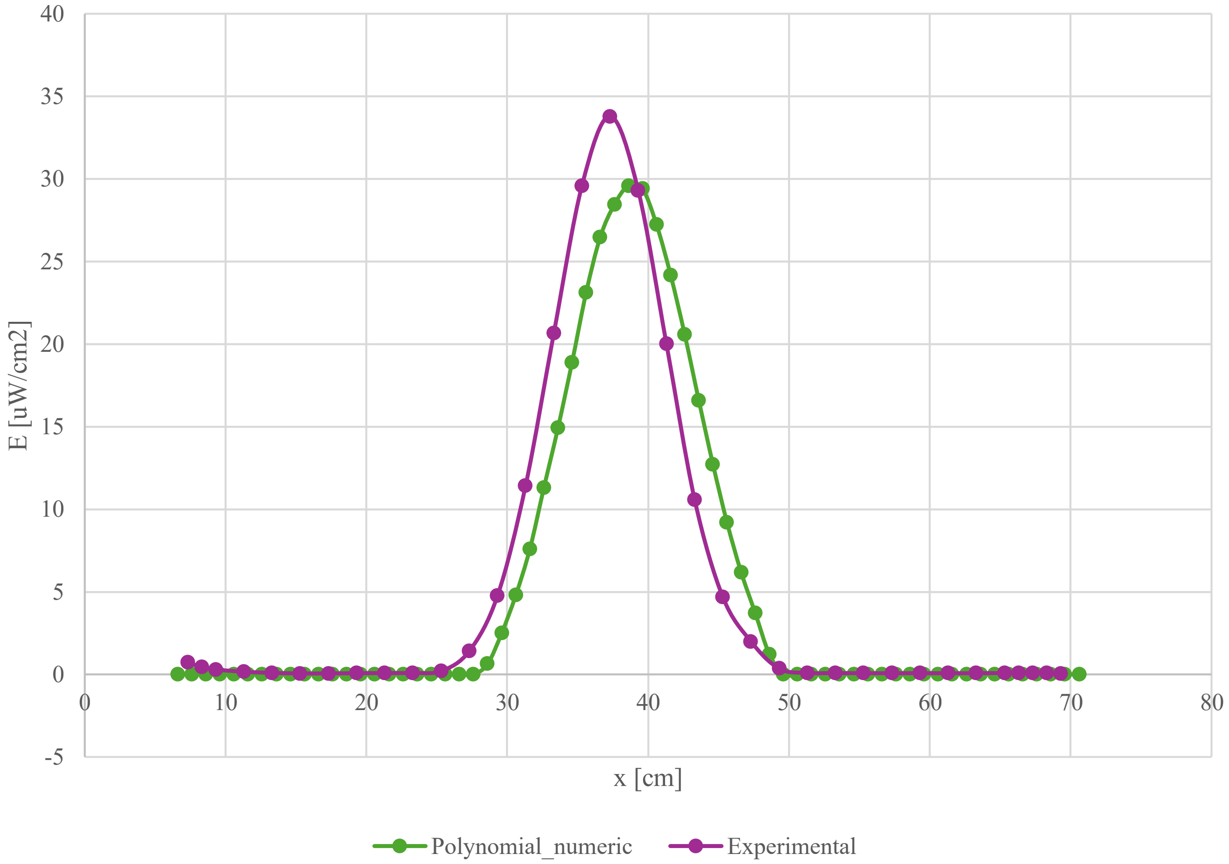

Figure 62: Comparison between the power density profile along the x-axis from a numerical polynomial emission distribution and experimental data.

As can be observed from the reported trends, the previously discussed conclusions are confirmed. In particular, it is evident that both the polynomial function and the cosine function consistently tend to underestimate the experimental values.

This discrepancy is not negligible: the underestimation introduces significant errors in the numerical modeling and reduces the reliability of the results. These findings indicate that such choices of parametric functions are less accurate in reproducing the actual behavior of the source, especially in peak regions and peripheral areas, where the intensity distribution is more sensitive. For this reason, the Gaussian function proposed in the reference article was initially selected, as it demonstrated greater consistency with the experimental data and a better ability to faithfully reproduce the shape of the source's power distribution.

In contrast, alternative functions such as the polynomial and cosine models proved to be less reliable in the numerical-experimental comparisons, exhibiting significant discrepancies, particularly in the critical regions of maximum intensity.

Best-Fitting Analytical Model

The function initially adopted to describe the model behavior was the Gaussian function proposed in the reference article, selected for its ability to approximate the experimental distribution in a first-order approach. However, as highlighted in Figure 63, this function exhibits certain structural limitations: the resulting surface displays a periodic trend along the horizontal axis (corresponding to the φ axis), while along the θ axis (corresponding to the vertical axis), it tends asymptotically toward a non-zero constant value outside the domain of interest.

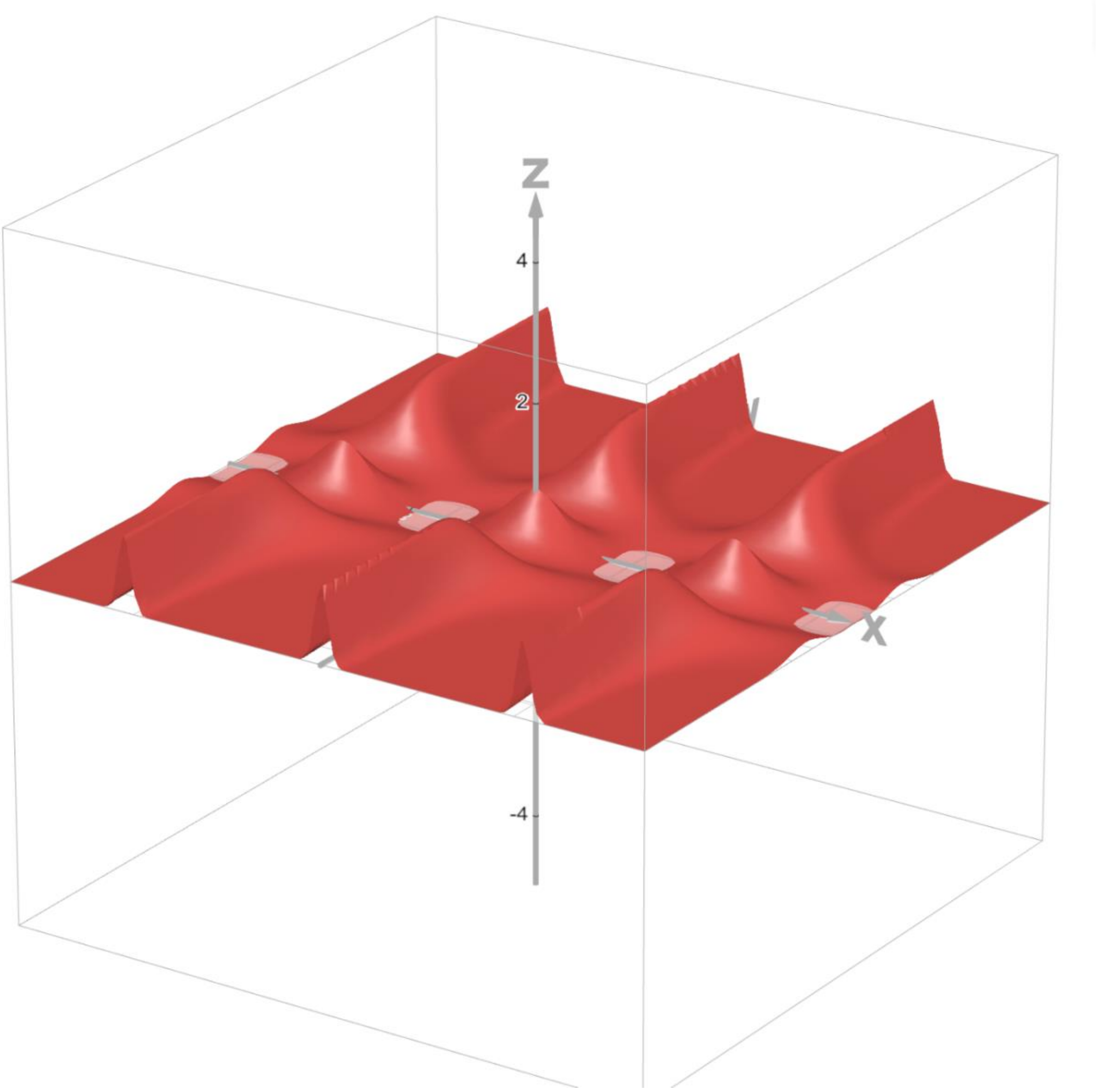

Figure 63: Three-dimensional emission pattern regard to gaussian distribution.

These artifacts compromise the accuracy of the phenomenon's description, as the periodicity and the presence of a non-zero asymptotic limit do not reflect the expected physical behaviour. For this reason, instead of retaining the formulation proposed in the article, the surface was modelled using a combination of Gaussian functions. Specifically, a summation of Gaussians up to the second order was considered, capable of more faithfully capturing the experimental characteristics and eliminating the distortions introduced by the original model.

- The Pure Gaussian function, shown in figure 65, results as

$$f(\vartheta,\varphi) = ae^{(-((\frac{\varphi^2}{b^2})+(\frac{\vartheta^2}{c^2})))} + a_1e^{(-((\frac{\varphi^2}{b_1{}^2})+(\frac{\vartheta^2}{c_1{}^2})))} \tag{4.7.1}$$

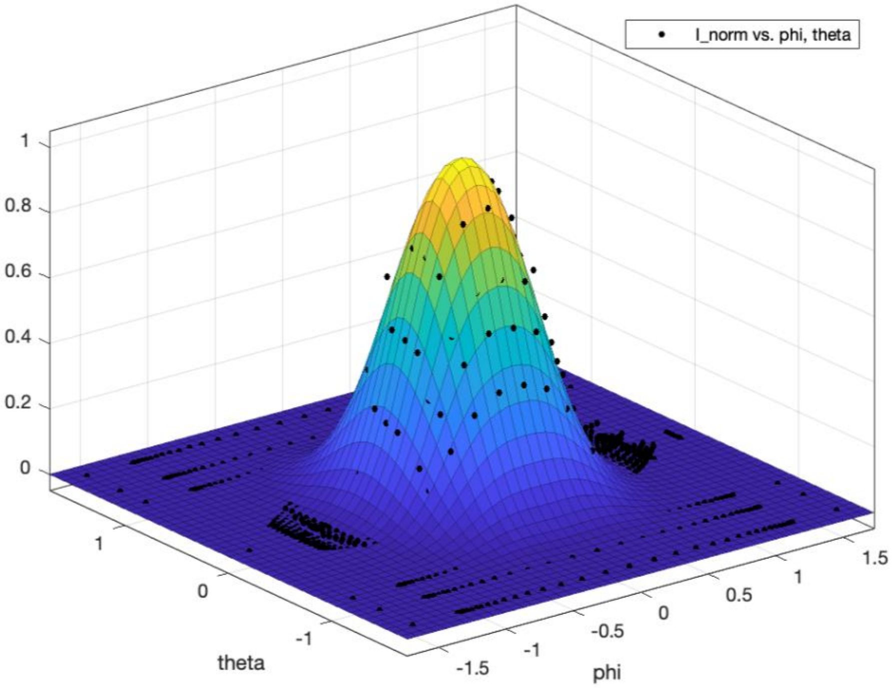

Value of the coefficients

a	-117.5637
a1	118.5901
b	0.4097
b1	0.4109
c	0.5998
c1	0.5992

R-square 0.9841

Tolerance 10^{-6}

Figure 64: Pure gaussian function fitting of the intensity matrix of figure 56.

The fitting obtained shows a higher coefficient of determination R^2 compared to that reported in Figure 64. Moreover, unlike the previously parameterized curve, the new approximation tends to slightly overestimate the experimental values rather than underestimate them. This behavior is particularly appropriate when considering the data acquisition methodology: photometric measurements were performed using a mapping system with discrete and fixed observation points. Specifically, it was not possible to carry out measurements directly along the LED axis (i.e., for $\theta = 0$ and $\varphi = 0$). Instead, acquisitions were conducted in a position close to the axis, with $\theta = 0$ and a slight misalignment of 0.3 cm to the right with respect to the principal emission direction.

In this context, the fact that the best fit tends to overestimate the experimental data can be interpreted as a desirable effect, as it partially compensates for the geometric deviation introduced by the experimental configuration. Consequently, the resulting parameterization can be considered adequate and physically consistent with the measurement conditions.

To assess the accuracy of the theoretical model, it is necessary to compare the simulation results with the experimental measurements. The following section describes this comparison, highlighting similarities and discrepancies between the simulated data and actual observations.

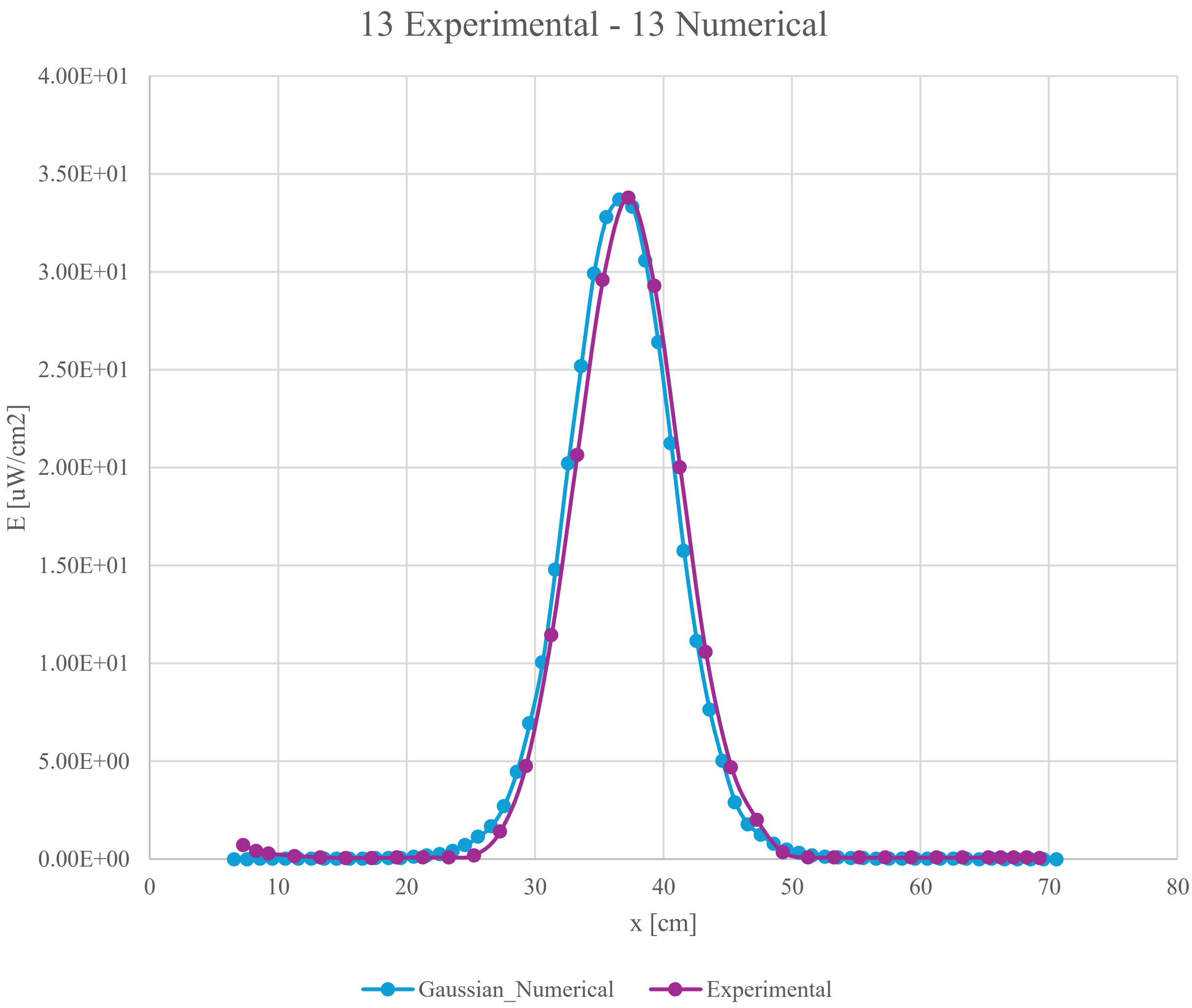

Figure 65:Comparison of the power density profile along the x-axis between a numerically simulated pure Gaussian emission and experimental measurements taken on the side opposite to the source.

To quantitatively assess the quality of the fitting, the numerical data (light blue curve) were interpolated at the same points as the experimental measurements (purple curve), allowing for a direct estimation of the relative error at each point:

$$\varepsilon_i = \frac{|y_{num} - y_{exp}|}{y_{exp}} \tag{4.7.2}$$

The analysis reveals that, in the central region of the distribution near the emission peak, the agreement between the model and the experimental data is satisfactory, with a relative error ranging between 5% and 11%. This indicates that the numerical parametrization adequately captures the main trend of the distribution.

In contrast, more pronounced discrepancies are observed in the peripheral regions. In particular, on the left side of the distribution, the experimental data tend to rise relative to the expected decay. This behavior appears to be attributable to light leakage, which may have artificially increased the signal in regions where the intensity should be negligible. It is important to emphasize that, under these conditions, the relative error is amplified by the fact that the experimental values are very small, such that even minimal absolute differences become significant in percentage terms.

Overall, despite these deviations in the marginal regions, the model maintains good consistency with the experimental data in the central region, which represents the most relevant aspect for beam characterization.

Chapter 5 – Numerical results

After identifying the function that best describes the emission solid of the light source, the work focused on validating the numerical model developed in COMSOL Multiphysics. In this phase, a simplified geometric model was created in order to retain the essential elements of the system while minimizing computational complexity. This was followed by the characterization of the materials, a fundamental step to ensure consistency between the simulation and the actual physical phenomenon. The source was then discretized to more accurately reproduce its emission distribution, while particular attention was paid to mesh construction and convergence verification, both essential to ensure numerical stability and the reliability of the results.

This process enabled the development of a robust predictive model, which was subsequently compared with experimental luminance measurements acquired using a photometer, in order to assess its descriptive capability and actual reliability.

5.1 Numerical Model (Geometry)

The initial phase involved the construction of a simplified geometric model of the test device. As illustrated in Figure 66, two parallelepipeds were created: the smaller one represents the air inlet duct in the section illuminated by ultraviolet radiation, while the larger one corresponds to the section housing the lamps and subsequently the HEPA filter.

In this phase of the analysis, the latter was modeled solely as a surface, since the focus was placed on the amount of radiation incident on its filtering surface, rather than on its subsequent propagation within the material. This surface was represented with an area smaller than that of the metallic structure enclosing it, and it serves as the basis for the analysis of the parameter of interest, namely, the surface radiation density.

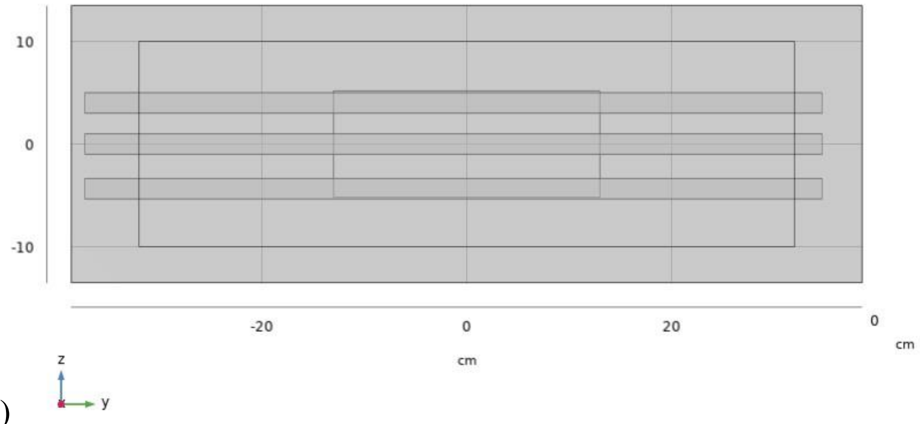

a)

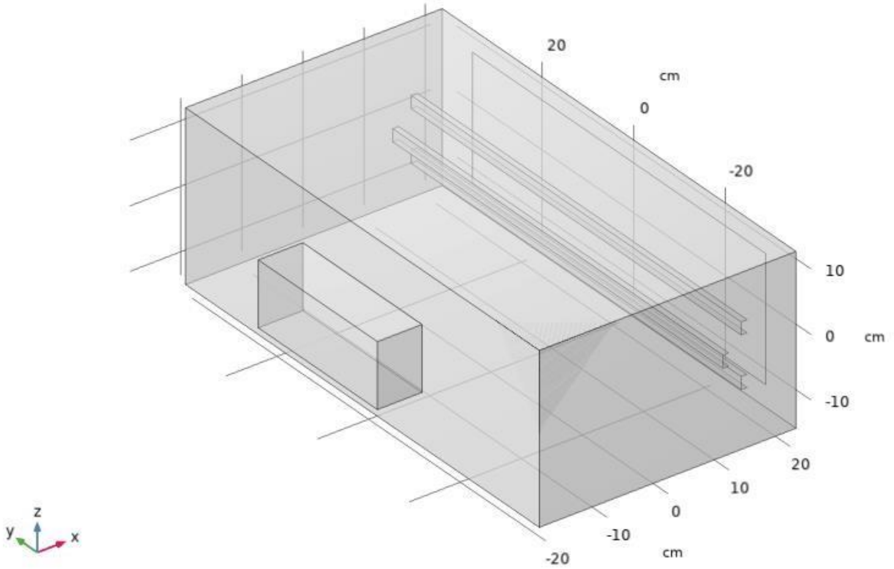

b)

Figure 66: Test device reconstruction in Comsol Multiphysics: a) Front section of the reconstructed device, b) 3D top view of the reconstructed device.

5.2 Mesh (Filtering Surface)

The first phase of the analysis focused on evaluating the discretization of the emission domain and the filtering surface, considering only the central LED of the lamp located 11 cm from the filtering surface as active. Particular attention was given to two complementary aspects:

- identifying an appropriate number of rays for the discretization of the emission solid angle, while keeping the mesh of the filtering surface fixed;
- for a fixed number of rays, assessing the effect of mesh refinement on the filtering surface on the convergence of the results.

For the convergence study of the illuminance field, two square meshes with grid steps of 1 cm and 0.5 cm were considered. The number of rays was progressively increased from 1,000 up to 2,048,000, doubling at each simulation.

The data exported from COMSOL were organized into a matrix, where each column represents the illuminance field (power density) on the filtering surface for a given number of rays, and each row corresponds to a node of the spatial grid. The first column contains the results obtained with 1,000 rays, the second with 2,000 rays, the third with 4,000 rays, and so on, up to the last column, corresponding to 2,048,000 rays.

The error analysis was conducted incrementally: for each simulation, the values $I_i(k)$in the current column were compared with those in the subsequent column, taken as the reference I_{ref}. In other words, the reference was not exclusively the most refined simulation, but progressively the one obtained with the immediately higher number of rays, in order to evaluate convergence step by step.

To quantify the error, the Normalized Root Mean Square Error (NRMSE) was used, in the form where normalization is performed inside the square root:

$$\mathrm{NRMSE_k} = \sqrt{\frac{1}{\mathrm{N}}\sum_{\mathrm{i=1}}^{\mathrm{N}}\left(\frac{\mathrm{I_i(k)} - I_i(k+1)}{\mathrm{I_i(k)}}\right)^2} \tag{5.2.1}$$

The following definitions apply:

- $I_i(k)$: power density at node $i$obtained from the simulation with $N_{\text{rays}} = 2k \cdot 1000$;
- $I_i(k+1)$: corresponding value from the simulation with twice the number of rays;
- N: number of grid nodes;
- $\bar{I}(k+1)$: average power density from the more refined simulation (column $k+1$), used for normalization.

This formulation yields a dimensionless and robust indicator that remains well-defined even in the presence of nodes with very low or null intensity values. Normalization with respect to the global average avoids numerical instabilities and allows the error to be interpreted as a percentage deviation from the characteristic level of the field.

Operationally, at the end of each simulation, COMSOL generated a file containing the incident power density at each node. The data were subsequently processed in MATLAB: after reconstructing the field matrix, the NRMSE was computed between consecutive columns, thereby measuring the relative variation between one simulation and the next.

This procedure enabled a quantitative verification of numerical convergence as the number of rays increased and the mesh element size decreased. In particular, it was observed that the error progressively decreased with the increasing number of rays, eventually stabilizing, indicating the attainment of a convergence condition. Simultaneously, reducing the mesh element size allowed for a more accurate spatial description of the illuminance field, further reducing the residual error.

The adoption of the NRMSE, computed incrementally between consecutive simulations, provided an objective and easily interpretable measure of the model's numerical stability, synthesizing the combined influence of the number of rays and spatial discretization, and offering a clear criterion for determining the required level of accuracy in the simulations.

The trends obtained from the analysis are presented below. Specifically, the NRMSE values computed between consecutive simulations are shown as a function of the number of rays and the discretization of the filtering surface, in order to highlight the asymptotic behavior of the error and the numerical stability of the model.

In figure 67 results are reported for element size: 0.5 cm, figure 68 refers to on element size equal to 1 cm.

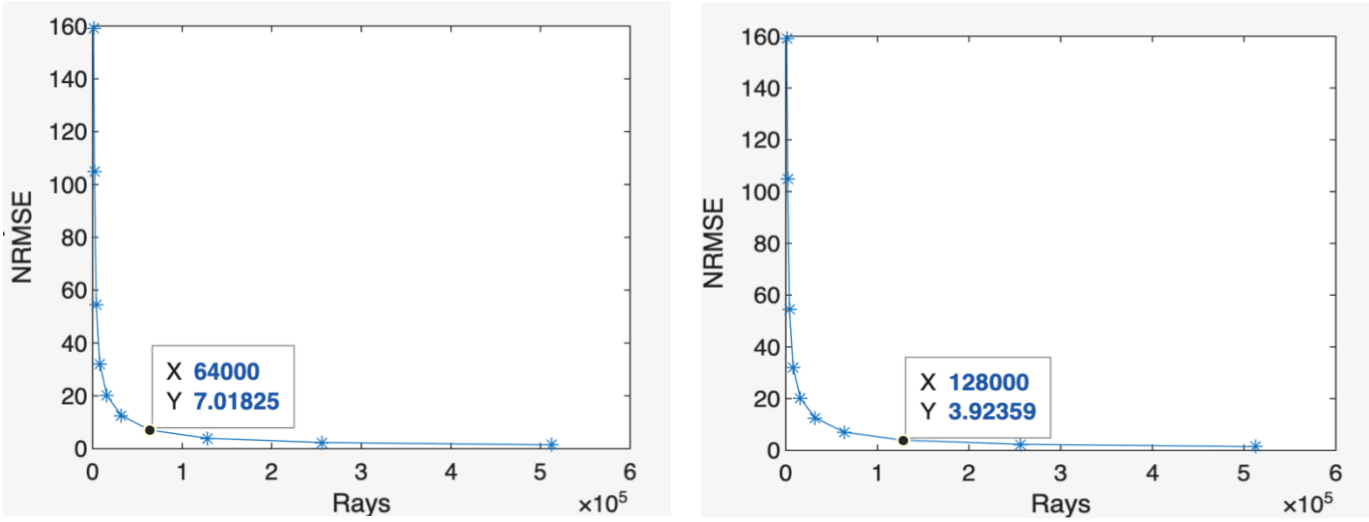

Figure 67: Convergence analysis NRMSE_k (Eq. 5.2.1) as a function of the number of rays for a fixed mesh size of 0.5 cm.

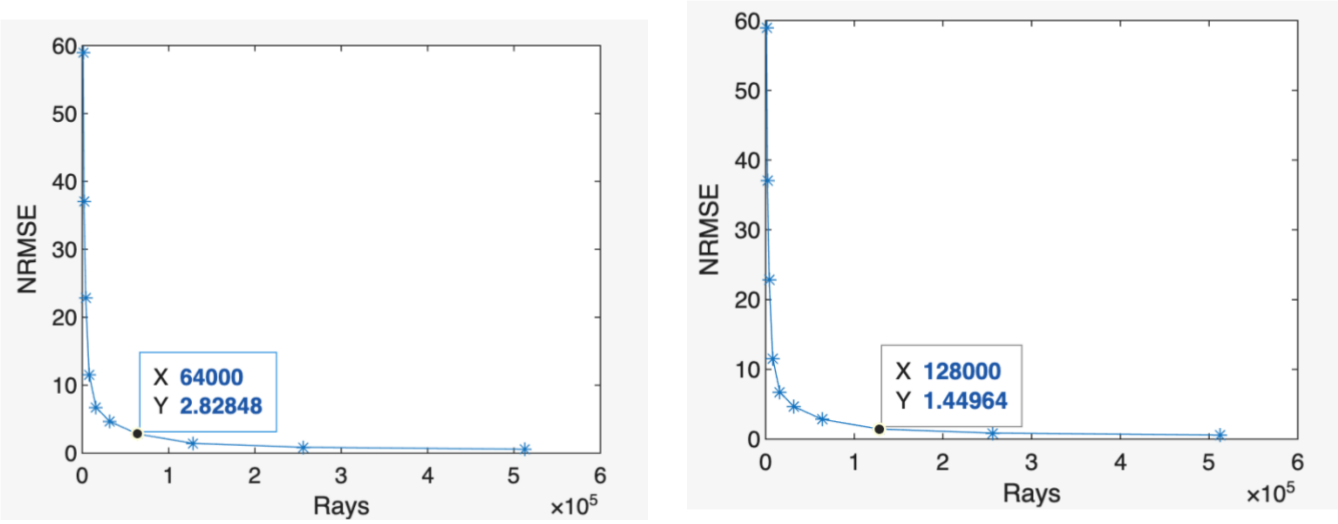

Figure 68: Convergence analysis NRMSE_k (Eq. 5.2.1) as a function of the number of rays for a fixed mesh size of 1 cm.

The graphs shown in Figure 67 and Figure 68 illustrate the trend of the NRMSE as a function of the number of rays for the two spatial discretisation's considered (mesh steps of 0.5 cm and 1 cm). In both cases, the error exhibits a clearly decreasing exponential behaviour, indicating rapid numerical convergence as the number of rays used in the simulation increases. This behaviour confirms the robustness of the adopted discretization procedure and the progressive stabilization of the results with increasing numerical resolution.

The graphs highlight the points corresponding to 64,000 and 128,000 rays, which represent two operational thresholds of particular interest. For the finer mesh (0.5 cm), the NRMSE value at 64,000 rays is approximately 7%, while at 128,000 rays it decreases to below 4%. In the case of the coarser mesh (1 cm), the error at 64,000 rays is already below 2.5% and drops below 1.5% at 128,000 rays. These results confirm that increasing the number of rays leads to a significant reduction in error, with a clear convergence trend toward negligible values.

Based on this evidence, 128,000 rays were adopted as the reference value for all subsequent analyses concerning the characterization of the filtering surface and metallic walls, in order to ensure an adequate level of accuracy and a negligible residual error. However, for large-scale simulations in which all sources are simultaneously active (entire lamp), a compromise between accuracy and computational cost was chosen, with 64,000 rays adopted as the operational value. This choice allows the error to remain within acceptable limits while significantly reducing computation time.

Interestingly, and somewhat counterintuitively, the error appears to be lower in the case of the coarser mesh. This aspect will be specifically addressed in the following section, in order to investigate its causes and implications from both numerical and physical perspectives.

To evaluate the effect of both spatial and angular discretization in the computation of the illuminance field, a rigorous and systematic methodology was followed. The fundamental steps and the physical-mathematical rationale behind the adopted choices are outlined below.

After fixing the number of rays for the discretization of the emission solid, the filtering surface was discretized with increasing mesh resolution, reducing the element size from 2.5 cm to 0.125 cm in steps of 0.25 cm. This process was repeated for various numbers of rays, ranging from 4,000 to 256,000, to assess how the simulation quality depends on both spatial and angular resolution.

To quantitatively compare the results obtained with meshes of different resolutions, all illuminance distributions were linearly interpolated onto a common grid of points. This procedure is essential to ensure that the comparison between different configurations is consistent and free from bias due to the differing positions of mesh nodes.

For quantification purposes, the Normalized Root Mean Square Error (NRMSE) was again used, as previously described.

The trends of NRMSE is a function of the element seize, corresponding to 64,000 and 128,000 rays, are reported in figure 69 and 70 respectively.

Number of rays: 64000

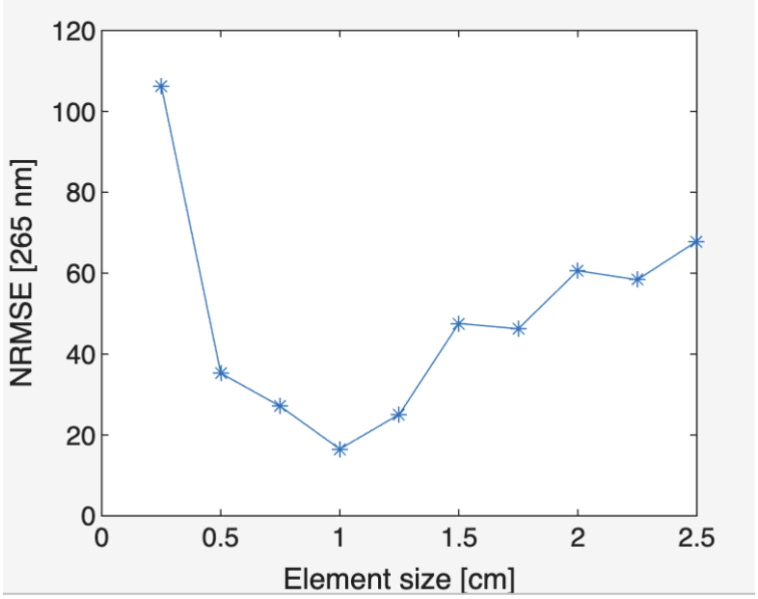

Figure 69: Convergence analysis NRMSE_k (Eq. 5.2.1) as a function of the element size for a fixed number of rays of 64000.

Number of rays: 128000

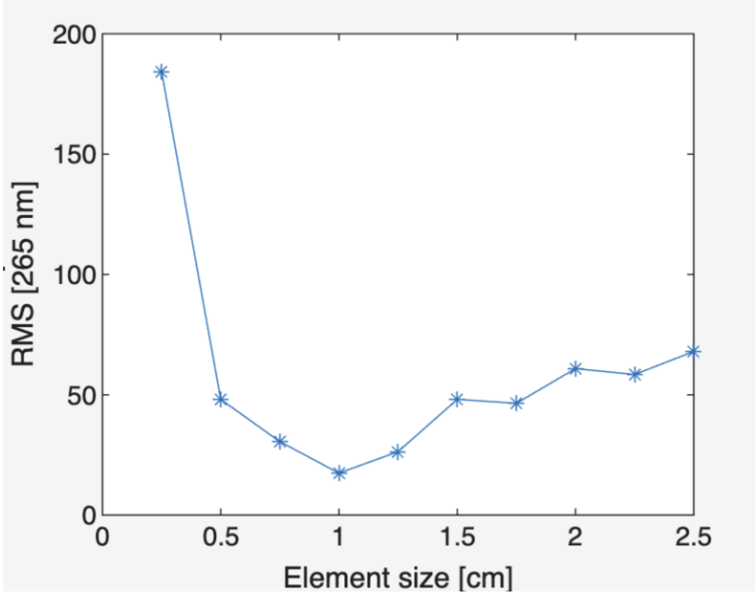

Figure 70: Convergence analysis NRMSE_k (Eq. 5.2.1) as a function of the element size for a fixed number of rays of 128000.

A key result, also observed in the literature, is that the error does not always decrease monotonically as the mesh is refined, but may exhibit a local minimum. This phenomenon can be explained by considering that the effective spatial resolution depends not only on the grid spacing (Δx), but also on the angular density of the rays, that is the spatial distance between the impact points of adjacent rays on the filtering surface.

The characteristic distance between the ray impact points can be estimated as:

$$dr \approx L \cdot \Delta\theta \tag{5.2.2}$$

where $L$is the distance between the source and the filtering surface, and $\Delta\theta$is the solid angle between two adjacent rays. In order for the discretization to be physically accurate and to avoid the introduction of numerical artifacts (aliasing), the grid element size must be greater than or equal to d_r:

$$\Delta x \gtrsim dr\Delta x \gtrsim d_r\Delta x \gtrsim dr \tag{5.2.3}$$

If this condition is not met, there is a risk of introducing systematic errors due to angular undersampling, resulting in the appearance of non-physical light and shadow patterns [120-122].

In conclusion, the optimal choice of discretization requires a balance between the spatial resolution of the mesh and the angular density of the rays, in order to ensure solution convergence and the absence of numerical artifacts. This aspect is crucial for accurately modeling the illuminance field.

To support the above discussion, illuminance maps obtained for different mesh element sizes are presented in figure 71, 72, 73 and 74, referring to the central LED, for element equal to 2, 1, 0.5 and 0.125 cm respecctively. These visualizations highlight the impact of discretization on the spatial distribution of illuminance, empirically demonstrating the importance of an appropriate choice of numerical parameters in the simulation process.

For each case, both the full illuminance maps on the target surface and the corresponding one-dimensional plots of power density along the vertical axis are provided. The latter is chosen to represent the points located directly in front of the source, i.e., those for which the angle between the source normal and the direction of the measurement points is zero. This configuration allows for a direct analysis of the effect of discretization along the main direction of light energy propagation.

- Elements size - 2 cm

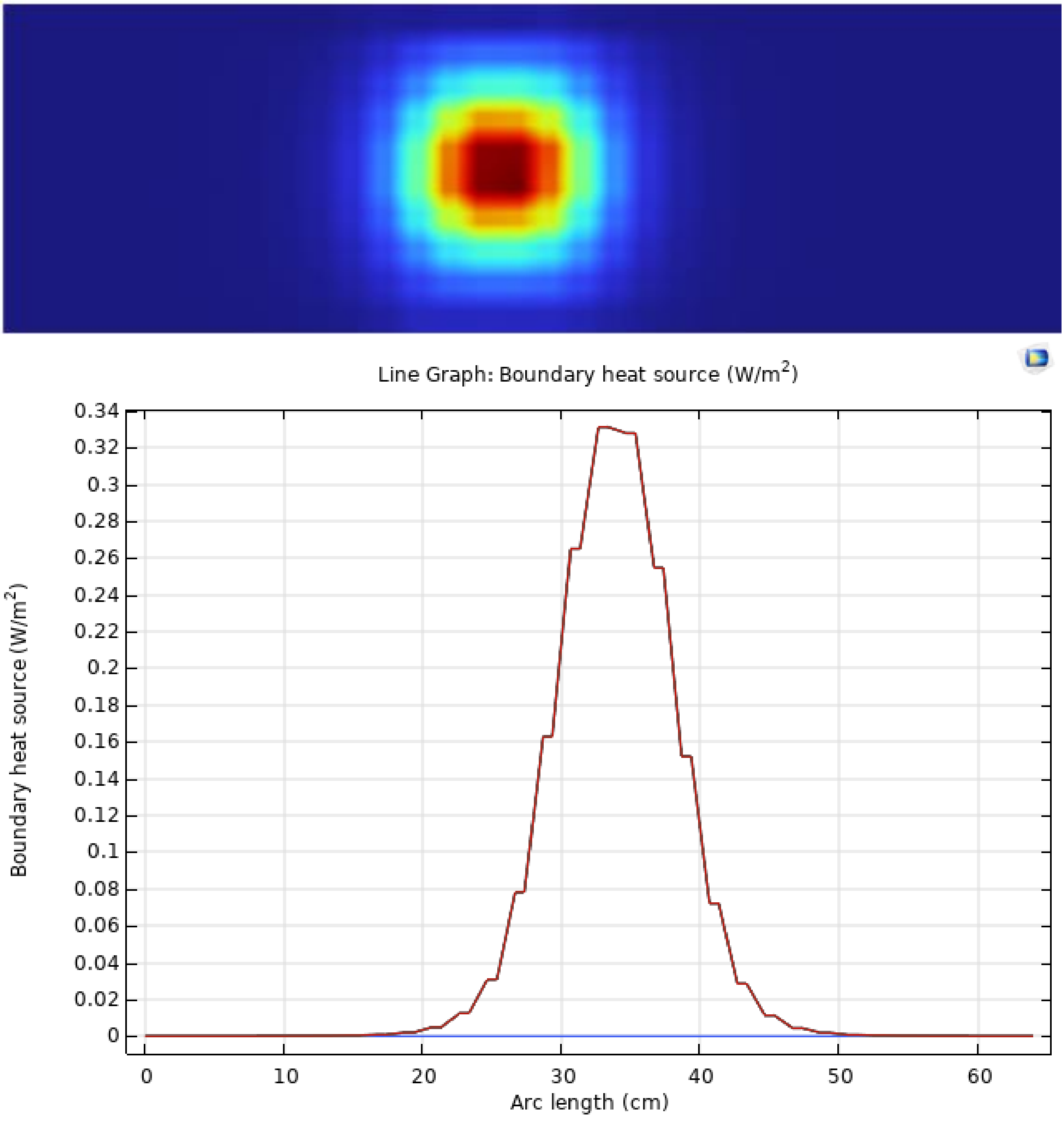

Figure 71: Simulated power density map on the target surface with 2 cm mesh resolution and 128,000 ray traces.

- Elements size - 1 cm

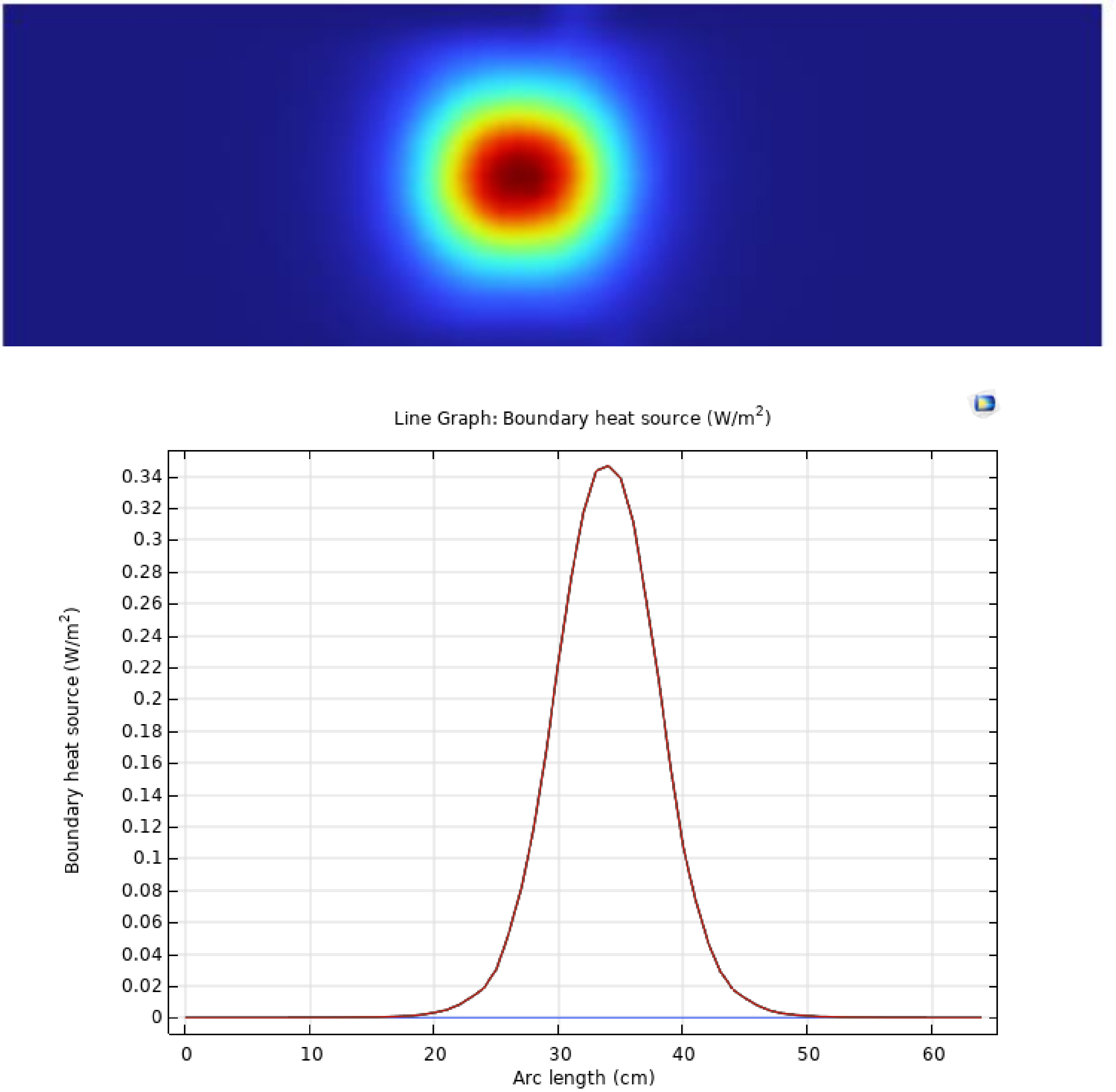

Figure 72: Simulated power density map on the target surface with 1 cm mesh resolution and 128,000 ray traces.

- Elements size - 0.5 cm

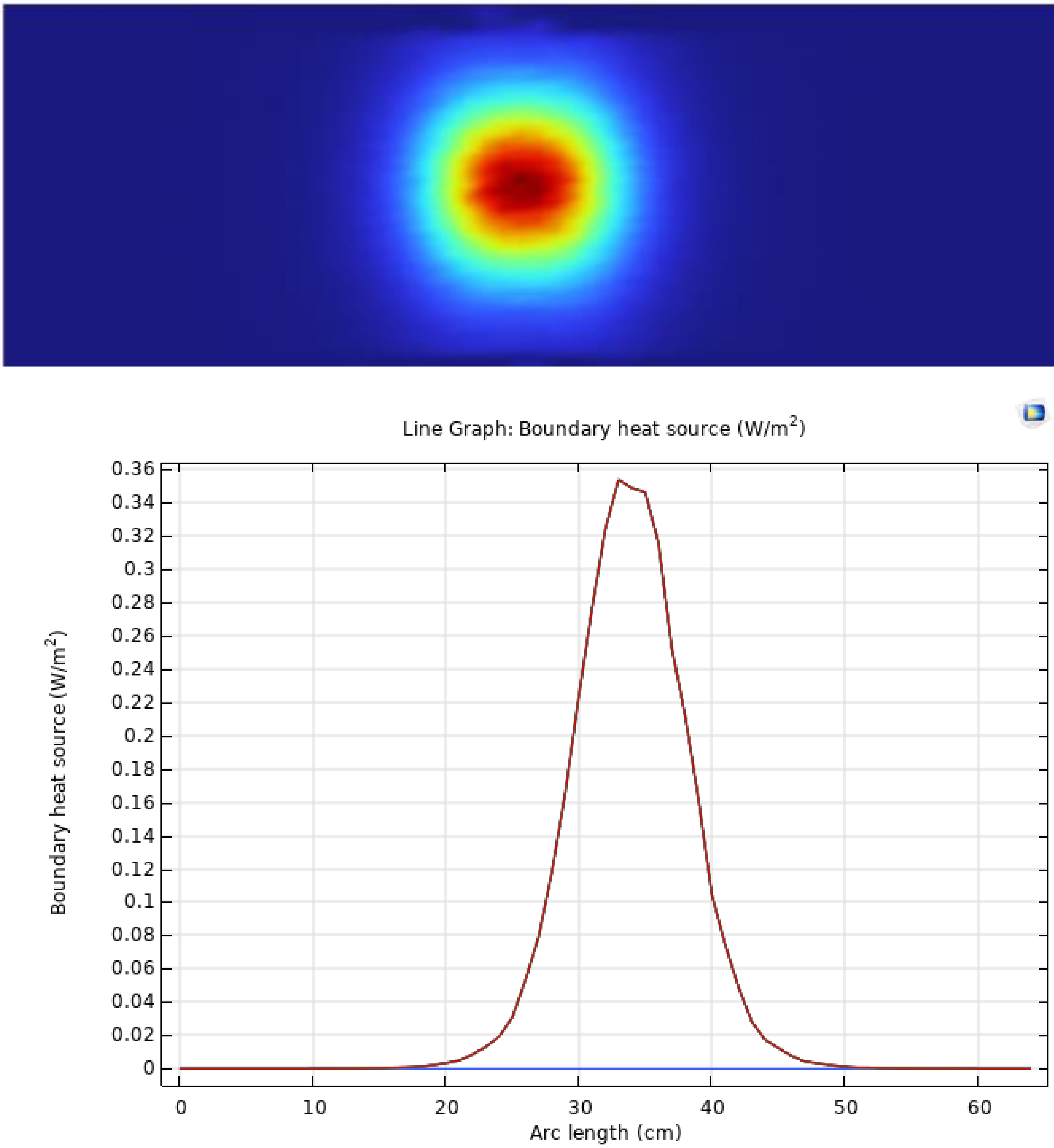

Figure 73: Simulated power density map on the target surface with 0.5 cm mesh resolution and 128,000 ray traces.

- Elements size - 0.125cm

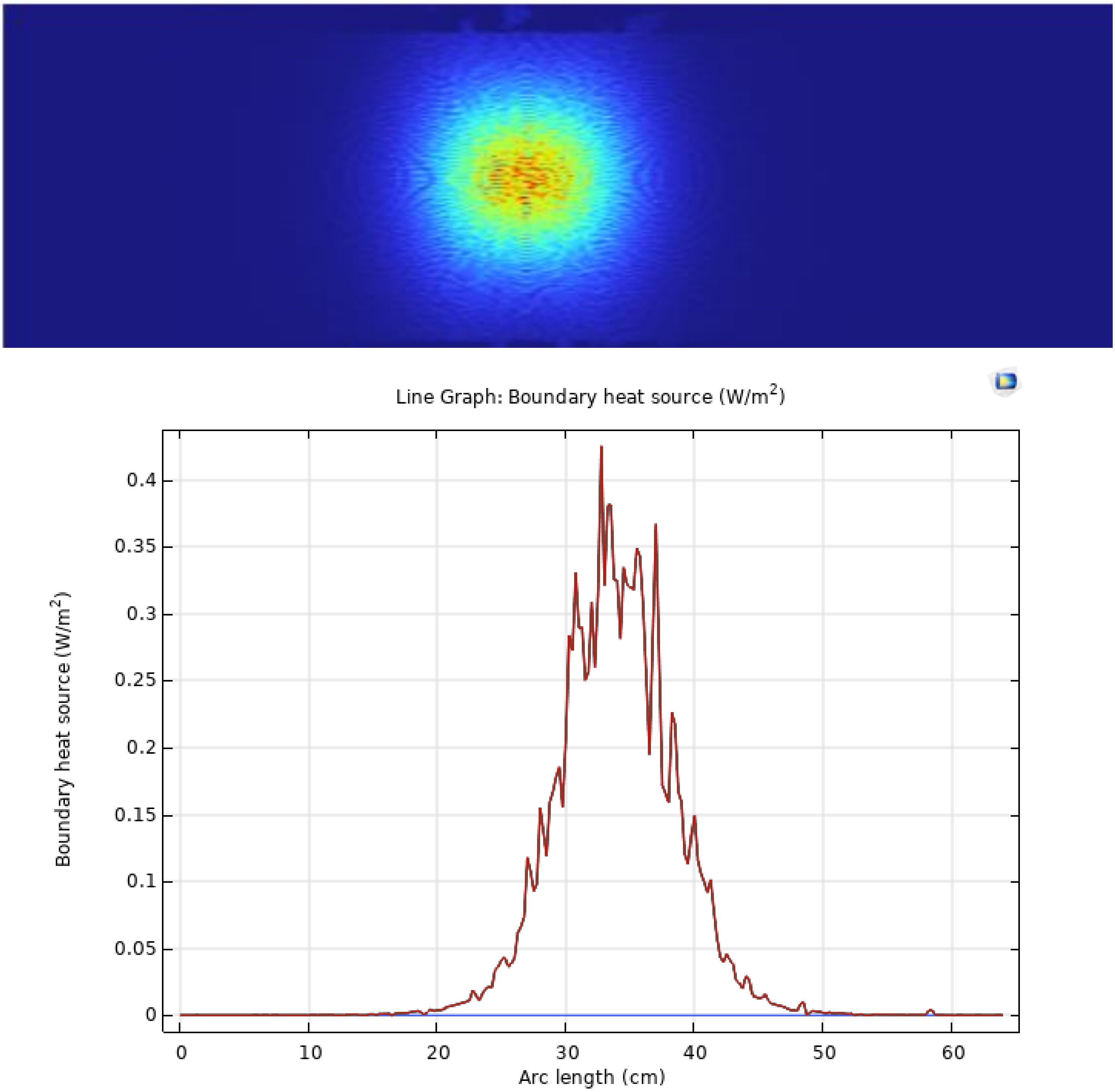

Figure 74: Simulated power density map on the target surface with 0.125 cm mesh resolution and 128,000 ray traces.

5.3 Characterization of Walls

Once an optimal mesh size of 1 cm was identified for the target surface, a similar approach was applied to the walls of the device. The filtering surface, modeled as a rectangle, was discretized using a square mesh, chosen for its regularity and ease of implementation in planar geometries. In contrast, the metallic structure, characterized by a more complex and three-dimensional geometry, was discretized using a tetrahedral mesh, which is more suitable for representing irregular and volumetric domains.

The tetrahedral mesh is well-suited for complex geometries due to its geometric flexibility and ability to adapt to arbitrary three-dimensional domains. However, it typically offers lower per-element accuracy compared to hexahedral or square meshes and may require a larger number of elements to achieve the same level of precision. The square mesh, on the other hand, ensures higher local accuracy in regular geometries but is less suitable for curved or irregular surfaces.

To validate the discretization choice, an additional mesh convergence analysis was conducted. For the optical characterization of the device, simulations were performed over two distinct time intervals. Initially, a duration of 1 second was considered, under the assumption that, with an LED-to-surface distance of 8 cm, the light rays would have already reached the target surface. This assumption is based on the law of light propagation, where the speed in vacuum is approximately $c = 3 \times 10^8 \text{ m/s}$, implying a travel time on the order of nanoseconds.

However, the results obtained showed strong oscillations in the simulated signal (as shown in Figures 75 and 76), suggesting the presence of transient phenomena or multiple reflections that had not yet stabilized. For this reason, the simulation time was extended to 60 seconds, resulting in a noticeable attenuation of the oscillations and greater signal stability. The values obtained at 60 seconds were also consistent with simulations extended to 10 minutes, indicating that a steady-state regime had been reached after a certain period.

5.3.1 Determination of the Reflection Coefficient

The second analysis focused on determining the reflection coefficient of the material composing the device. This parameter, also known as spectral reflectance, represents the ratio between the intensity of the reflected radiation and that of the incident radiation. It strongly depends on the refractive index of the material and the angle of incidence of the light.

The simulations were based on Fresnel's equations, which describe reflection for polarized waves (S and P) and allow the reflection coefficient to be calculated as a function of angle and polarization. For metallic materials, such as anodized aluminum or sandblasted steel, reflectance values were extracted from regional databases and integrated into the numerical model to accurately simulate the optical behavior of the device.

Whereas the previous analysis, aimed at identifying the optimal mesh size, was conducted under conditions that minimized the contribution of reflective walls (while keeping it non-zero), this second phase adopted the opposite approach. The objective was to characterize the reflective behavior of the material composing the device walls, and to this end, the analysis focused on the light sources closest to these surfaces.

Specifically, the variation in incident power density was evaluated as a function of the degree of geometric refinement. The sources considered were the LEDs of the upper and lower bars, located approximately 8 cm from the walls. Unlike the previous analysis, the NRMSE (Normalized Root Mean Square Error) coefficient was not used; instead, the variation in illuminance as a function of mesh refinement was directly observed.

The procedure involved using the minimum element size proposed by the simulation software, which was progressively halved at each iteration. The resulting irradiation distributions are shown in the figures 75 and 76, referring to the condition in which the first LED of the upper bar is activated.

For this type of analysis, particular attention was not paid to the region adjacent to the source, as the variations observed in that area were not significant from an evaluative standpoint. Instead, the focus was placed on the available extraction region, comparing experimental and numerical data in the illuminated zone, where the interaction between light and the reflective surface is more pronounced and representative of the system's overall behavior.

Figure 76 refers to the simulation time of one second, whereas Figure 77 shows the results obtained for a simulation time of sixty seconds.

Simulation Time 1s

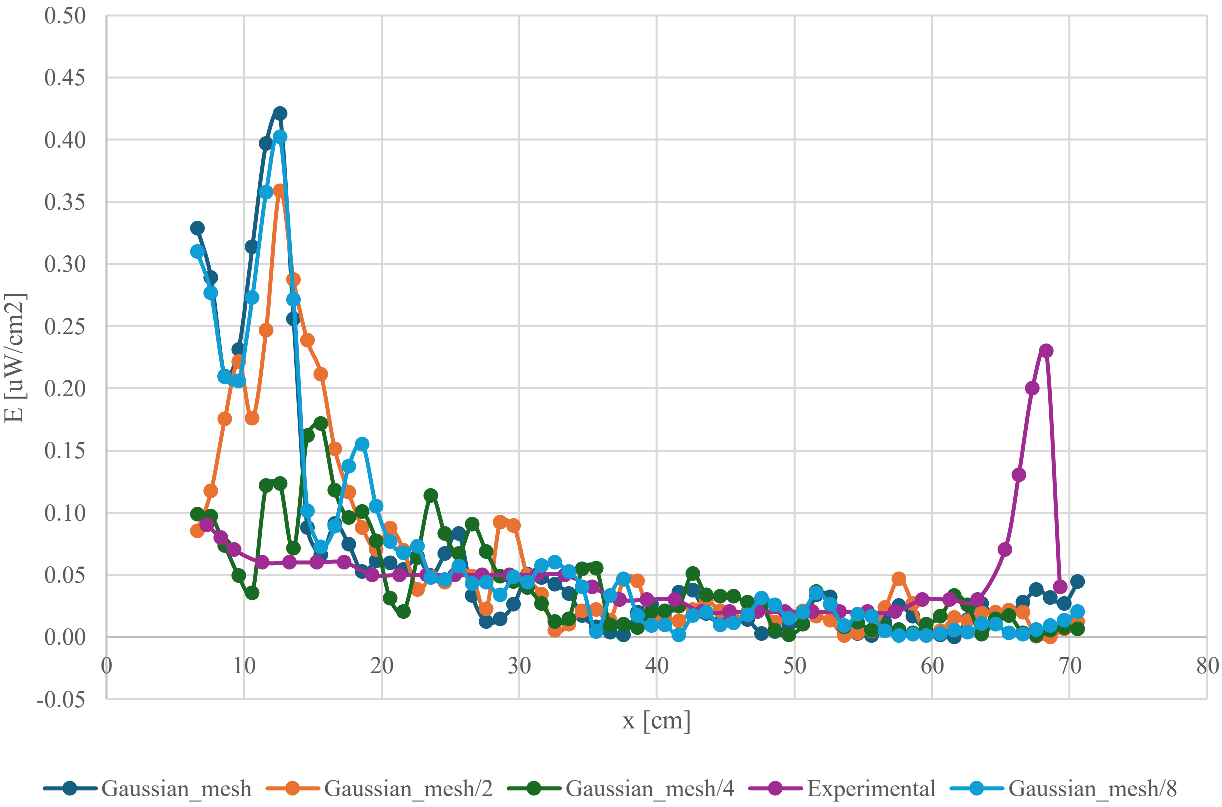

Figure 75: Comparison between power density profile along the x-axis for different wall size elements in 1s.

Simulation Time 60s

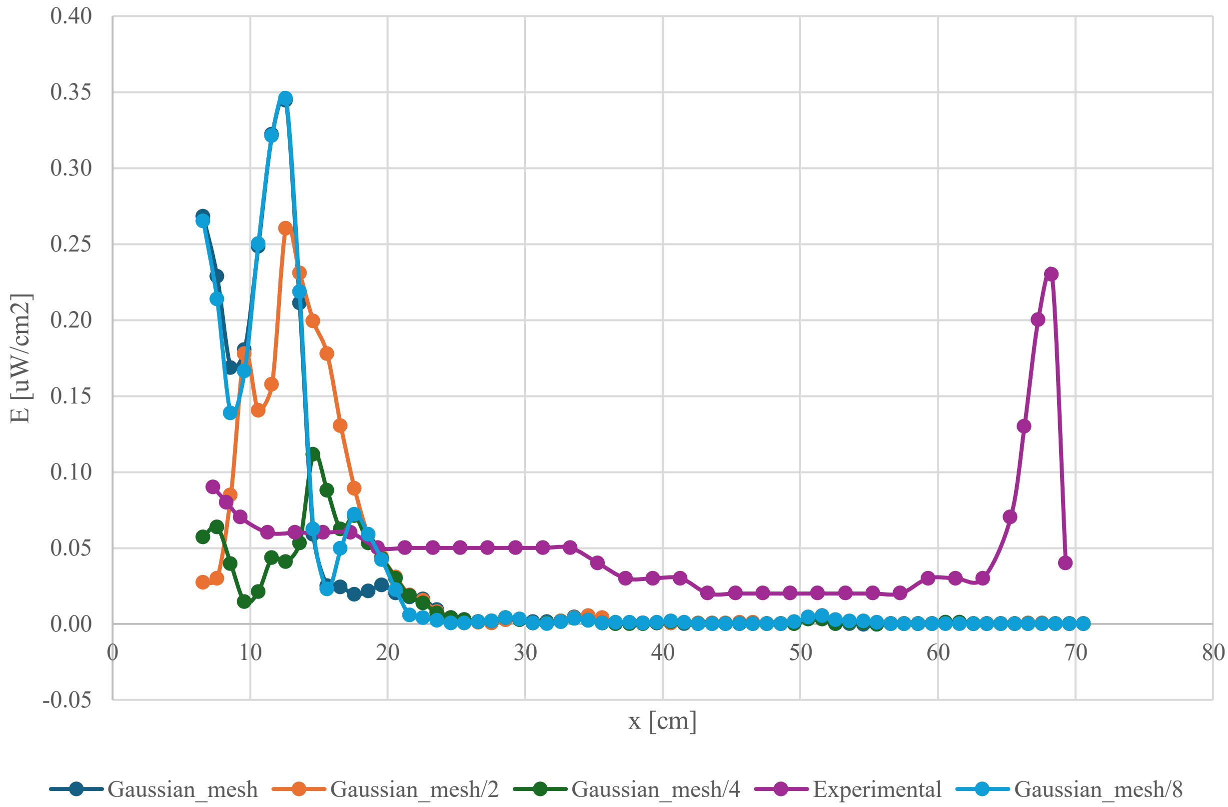

Figure 76: Comparison between power density profile along the x-axis for different wall size elements in 1min.

As previously mentioned, it can be observed that, in the one-second case, significantly higher oscillations are present compared to those observed in the sixty-second simulation, indicating a condition of transient instability.

By focusing on the second graph, a clear correspondence can be noted with the mesh convergence analysis related to the target surface. In particular, a progressive attenuation of the power density is observed as the degree of mesh refinement increases. However, once the optimal size is exceede, corresponding in this case to the initial mesh reduced by a factor of eight, the power density tends to return to values comparable to those obtained with the original mesh.

This behavior can be explained by considering that the effective spatial resolution depends not only on the mesh size, but also on the distance between the impact points of adjacent rays, which is determined by the angular density. If the mesh is too fine relative to this distance, numerical artifacts such as aliasing may be introduced, resulting in non-physical light and shadow patterns.

For this reason, the mesh corresponding to the initial configuration reduced by a factor of eight was adopted as the optimal size, as it represents the best compromise between numerical accuracy and the stability of the simulated signal.

Finally, it is noted that the peak observed on the left side of the distribution may be attributed to external light leakage or to reflections from uncontrolled ambient sources, which locally interfere with the measured field.

To describe the optical behavior of the device walls, a statistical diffuse reflection model, as available in the COMSOL Ray Optics module [109], was adopted. This model is suitable for opaque and slightly structured surfaces, such as the treated metals, where incident light is scattered in multiple directions rather than reflected according to the law of incidence. Diffuse reflection produces a more uniform illumination distribution and allows realistic definition of wall boundary conditions, accounting for the combination of specular and diffuse components and the angular distribution of reflected light. In this way, the propagation of light and its interactions with the surfaces are simulated accurately. Previous studies [113] have shown that similar surfaces can be effectively modeled using diffuse reflection approaches.

In the present study, several values of the reflection coefficient were analyzed: 1.0, 0.9, 0.8, 0.7, and 0.5. For each case, the resulting illuminance was evaluated by activating the first LEDs of the upper and lower bars, focusing on the regions farthest from the source installation position, in order to isolate the reflected contribution from the direct one.

The graphs shown in the following figures 77 and 78 display the simulated illuminance trends for each coefficient, both for the lower and the upper lamp, respectively. The comparison with the experimental data allowed the identification of the reflectance value most consistent with the observed behavior, contributing to the optical calibration of the numerical model.

Power density – upper lamp

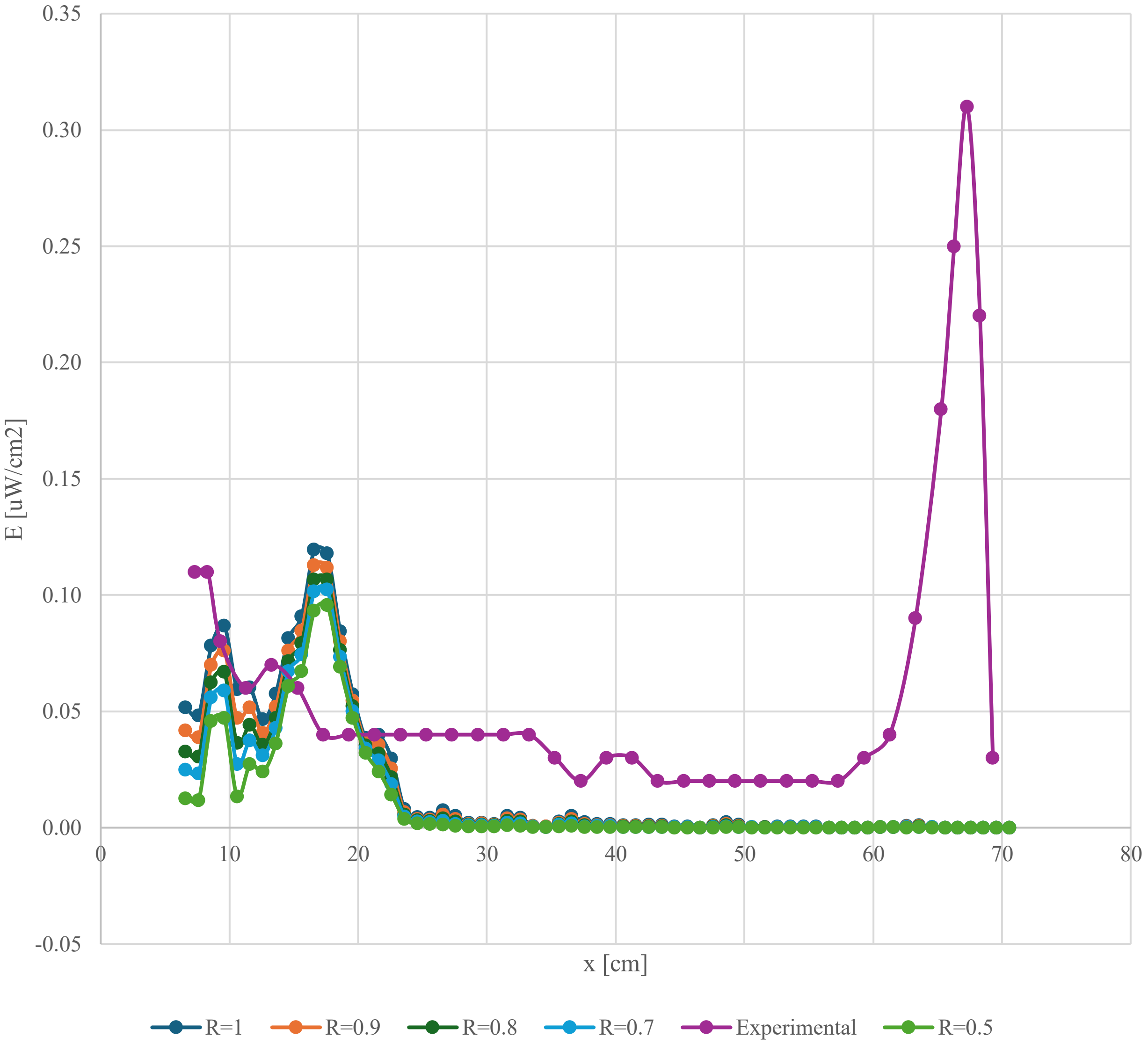

Figure 77: Comparison between power density profile along the x-axis for different material reflection coefficient in case of upper lamp on.

Power density – lower lamp

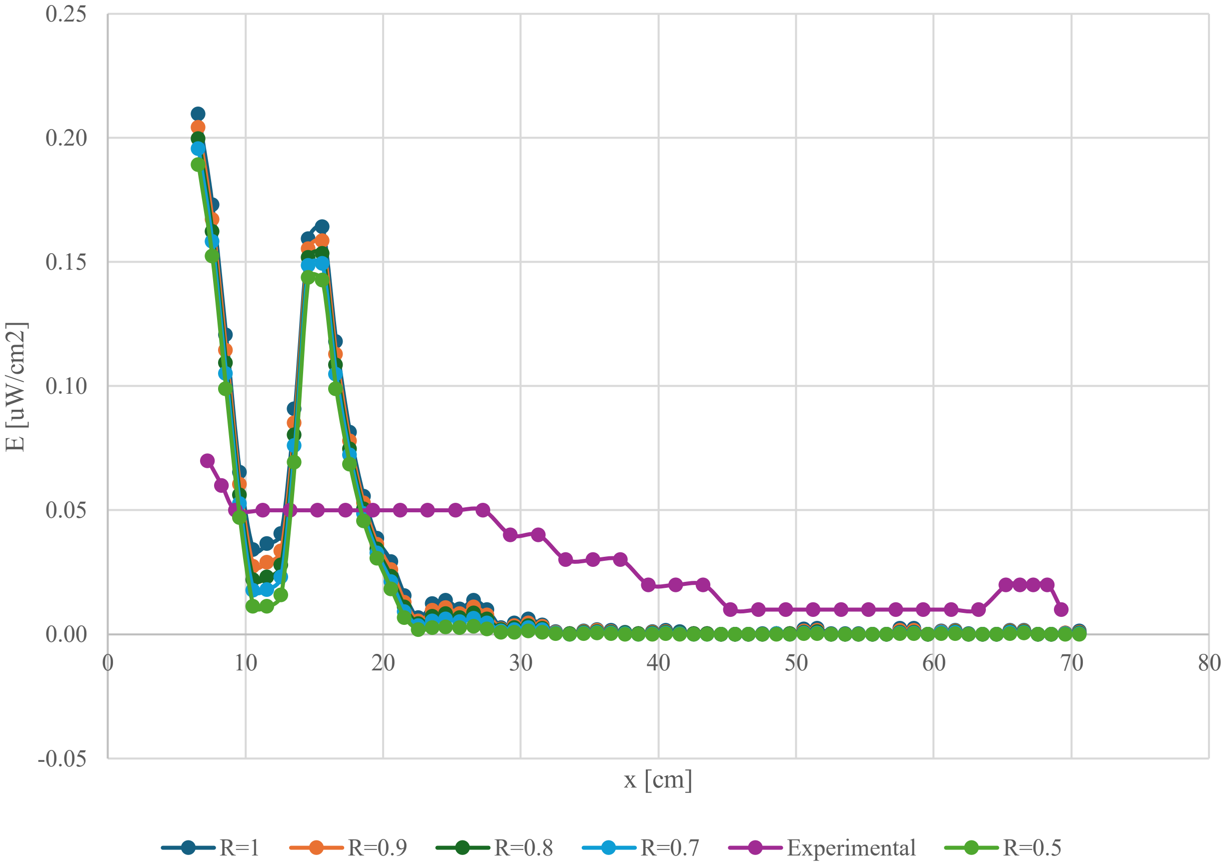

Figure 78: Comparison between power density profile along the x-axis for different material reflection coefficient in case of lower lamp on.

As can be observed from the resulting graphs, as the reflection coefficient decreases, the illuminance curve maintains the same spatial distribution but is progressively shifted downward. This behaviour suggests that reflectance primarily acts as a scalar factor on the overall intensity, without significantly altering the shape of the light field. It is worth noting that this effect may be related to the simplified nature of the adopted model, in which reflection is treated as isotropic and independent of the incident direction.

For this reason, based on both the graphical analysis and the comparison with the literature, a reflectance value of 0.8 was selected. Lower values, such as 0.7 or 0.5, tend to underestimate the reflected contribution, while maintaining the coefficient at 1.0 introduces an excessive systematic error, which is not compatible with the experimental measurements. The choice of $R = 0.8$ therefore represents a physically justified compromise between numerical accuracy and consistency with the observed behavior.

Figures 79 show the final configuration of the discretized structure, with the finite element sizes defined according to the adopted modeling criteria. This representation summarizes the discretization process previously described and reflects the design choices made in terms of geometry, mesh density, and element characteristics.

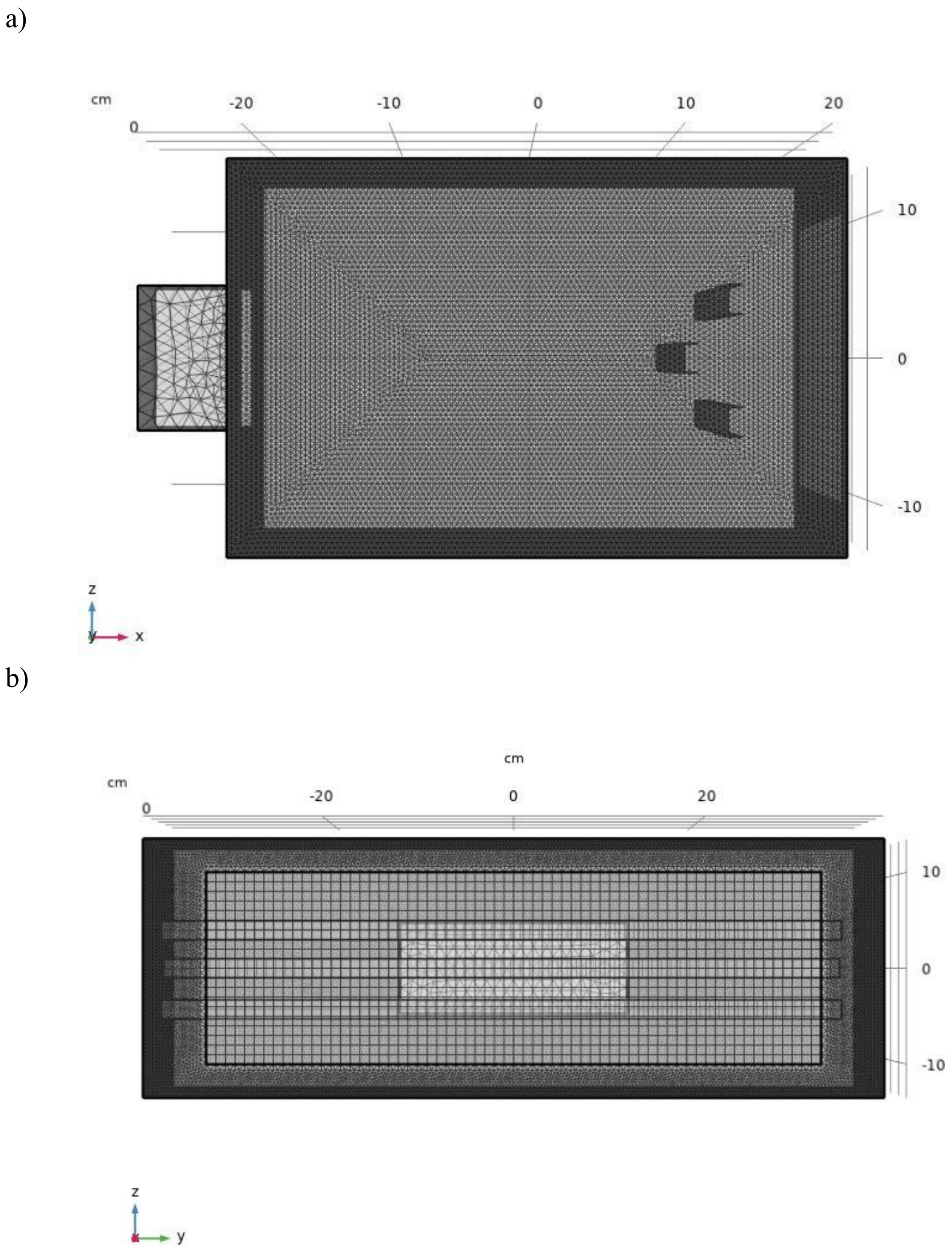

Figure 79: Final mesh configuration used for the test device simulation: a) lateral view of the reconstructed device, b) lateral view of the reconstructed device.

The air inlet duct, although made of the same material as the walls, was discretized using coarser elements. This choice was motivated by its limited influence on the reflection phenomenon and allowed for a significant reduction in computational load without compromising the overall quality of the simulation.

5.4 Numerical Simulation

Once the illuminated domain was discretized, comprising both the light source, modelled through its emission solid, and the geometry of the structure of interest, the numerical simulation phase was carried out. This phase was followed by a direct comparison with the experimental data, conducted across different activation scenarios: individual LEDs turned on, entire bars activated one at a time, and finally, three bars turned on simultaneously.

Particular attention was devoted to the simulation of individual active LEDs, with the aim of analyzing in detail the contribution of each light source to the overall irradiance. In particular, the behaviour of the sixteenth LED (out of a total of 32), positioned at the center of the lamp, was studied with reference to the three bars: upper, lower, and central. In addition to the central LED, the first source of each bar was also analyzed, in order to evaluate the effect of the sources located at the ends of the geometry.

This targeted selection allowed for a deeper investigation of the irradiance distribution and the internal reflection phenomena within the structure, in scenarios already validated numerically. The results obtained from these simulations contributed to a more detailed understanding of the optical behaviour of the system, confirming the consistency between the numerical model and the experimental observations.

Figure 80 shows the structure of the lamp, highlighting the reference LED that will be used in the graphs presented in the following sections.

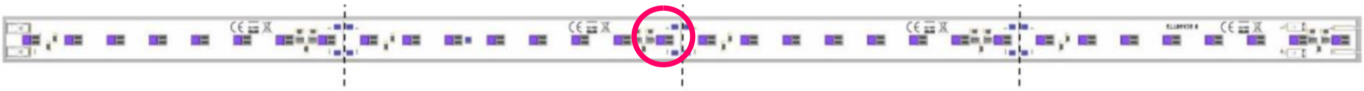

Figure 80: Lamp structure with highlighted simulated source (LED – 16).

Based on the graph nomenclature, it can be observed that the positions obtained through numerical simulation do not coincide with the experimental ones, but are shifted by a small Δy, with the exception of the central position, which shows a more accurate correspondence.

The misalignment observed between the numerical and experimental positions is attributable to the fact that the manual mapping system does not perfectly match the grid used for the discretization of the filtering surface.

The positions for which the sensor is perfectly aligned with the source, as in the case of the central position, or located in its immediate vicinity, as for the upper and lower LEDs, will be represented with larger markers, in order to highlight their relevance in the analysis.

Sixteenth middle led of central lamp

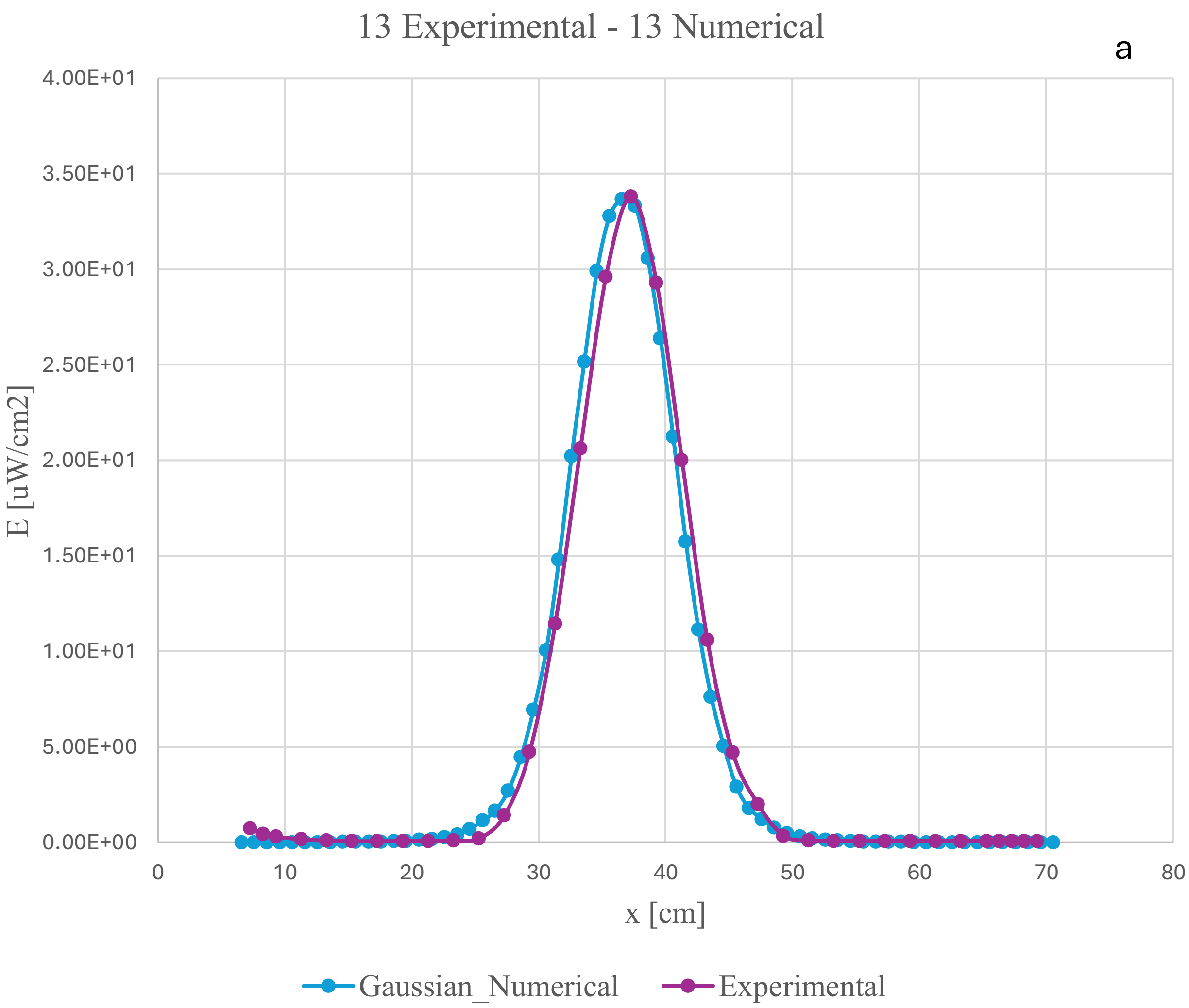

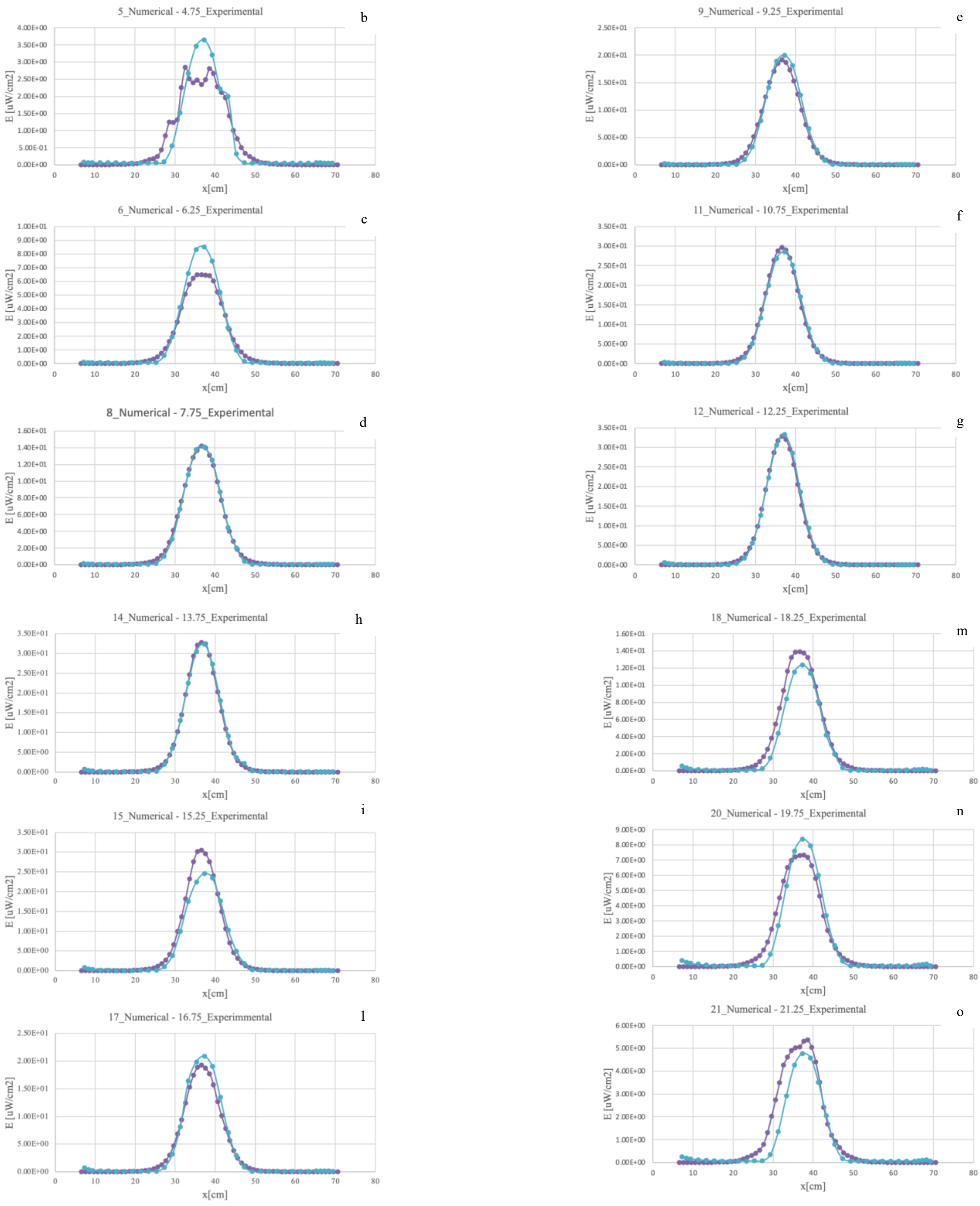

Figure 81: Comparison between the power density profile along the x-axis on the target surface from a numerical pure gaussian emission distribution and experimental data from the central 16-LED lamp for different ordinates: a) 13 cm numerical ordinate – 13 cm experimental ordinate, b) 5 cm numerical ordinate – 4.75 cm experimental ordinate, c) 6 cm numerical ordinate – 6.25 cm experimental ordinate, d) 8 cm numerical ordinate – 7.75 cm experimental ordinate, e) 9 cm numerical ordinate – 9.25 cm experimental ordinate, f) 11 cm numerical ordinate – 10.75 cm experimental ordinate, g) 12 cm numerical ordinate – 12.25 cm experimental ordinate, h) 14 cm numerical ordinate – 13.75 cm experimental ordinate, i) 15 cm numerical ordinate – 15.25 cm experimental ordinate, l) 17 cm numerical ordinate – 16.75 cm experimental ordinate, m) 18 cm numerical ordinate – 18.25 cm experimental ordinate, n) 20 cm numerical ordinate – 19.75 cm experimental ordinate, o) 21 cm numerical ordinate – 21.25 cm experimental ordinate.

Sixteenth middle led of upper lamp

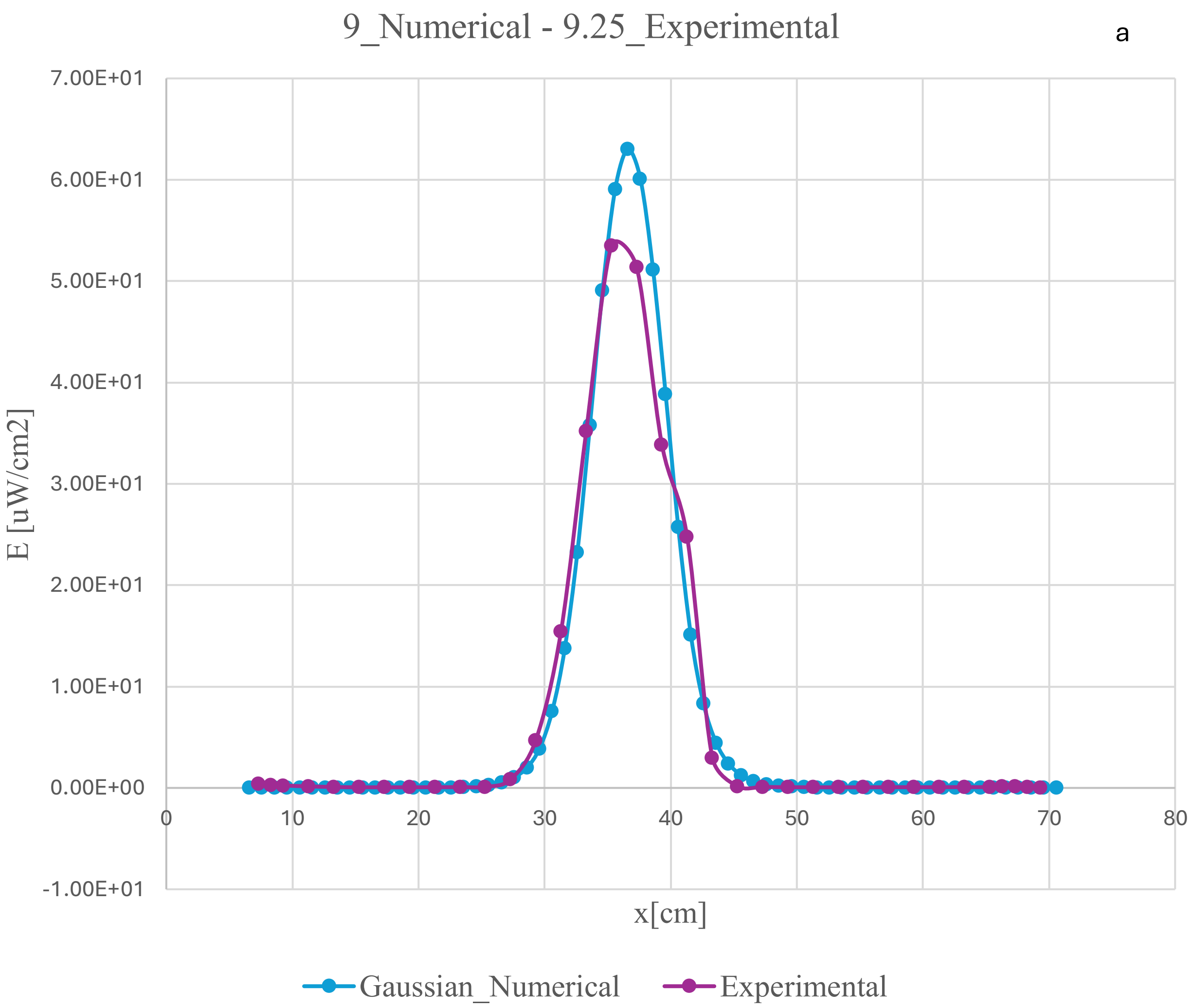

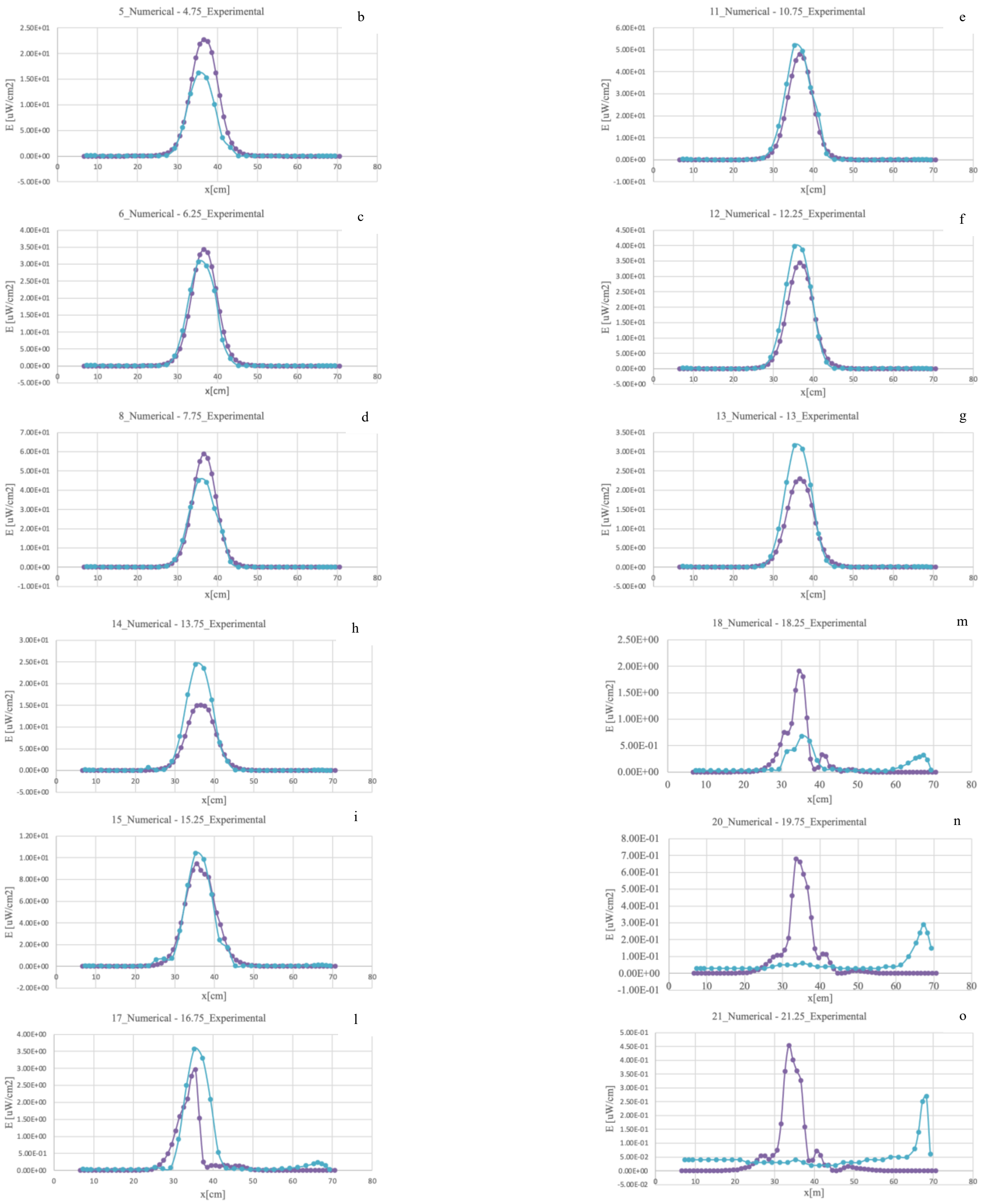
5_Numerical - 4.75_Experimental

6_Numerical - 6.25_Experimental

8_Numerical - 7.75_Experimental

14_Numerical - 13.75_Experimental

15_Numerical - 15.25_Experimental

17_Numerical - 16.75_Experimental

11_Numerical - 10.75_Experimental

12_Numerical - 12.25_Experimental

13_Numerical - 13_Experimental

18_Numerical - 18.25_Experimental

20_Numerical - 19.75_Experimental

21_Numerical - 21.25_Experimental

Figure 82: Comparison between the power density profile along the x-axis on the target surface from a numerical pure gaussian emission distribution and experimental data from the upper 16-LED lamp for different ordinates: a) 9 cm numerical ordinate – 9.25 cm experimental ordinate, b) 5 cm numerical ordinate – 4.75 cm experimental ordinate, c) 6 cm numerical ordinate – 6.25 cm experimental ordinate, d) 8 cm numerical ordinate – 7.75 cm experimental ordinate, e) 11 cm numerical ordinate – 10.75 cm experimental ordinate, f) 12 cm numerical ordinate – 12.25 cm experimental ordinate, g) 13 cm numerical ordinate – 13 cm experimental ordinate h) 14 cm numerical ordinate – 13.75 cm experimental ordinate, i) 15 cm numerical ordinate – 15.25 cm experimental ordinate, l) 17 cm numerical ordinate – 16.75 cm experimental ordinate, m) 18 cm numerical ordinate – 18.25 cm experimental ordinate, n) 20 cm numerical ordinate – 19.75 cm experimental ordinate, o) 21 cm numerical ordinate – 21.25 cm experimental ordinate.

Sixteenth middle led of lower lamp

In the case of the position corresponding to the lower bar, due to the imperfect symmetry of the installation, the source is located exactly halfway between two sensor positions. For this reason, in order to correctly represent the distribution, both corresponding graphs are reported.

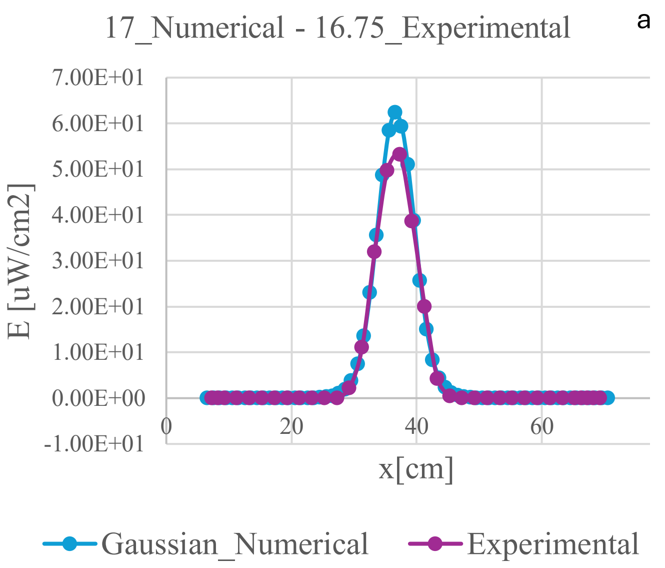

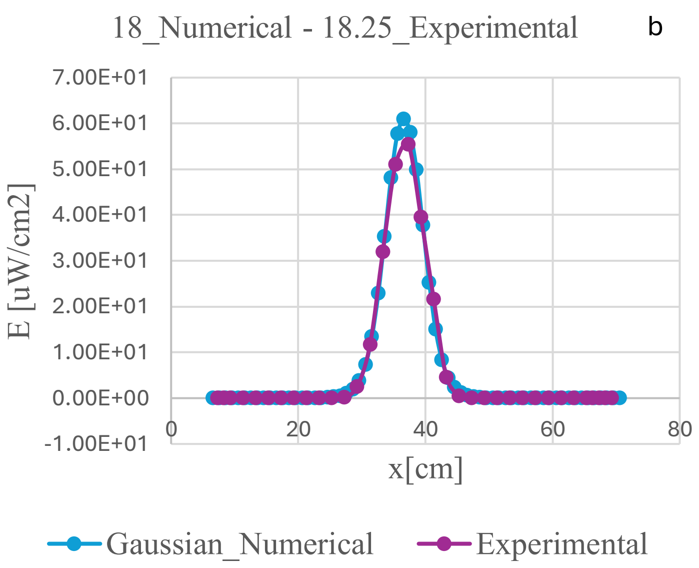

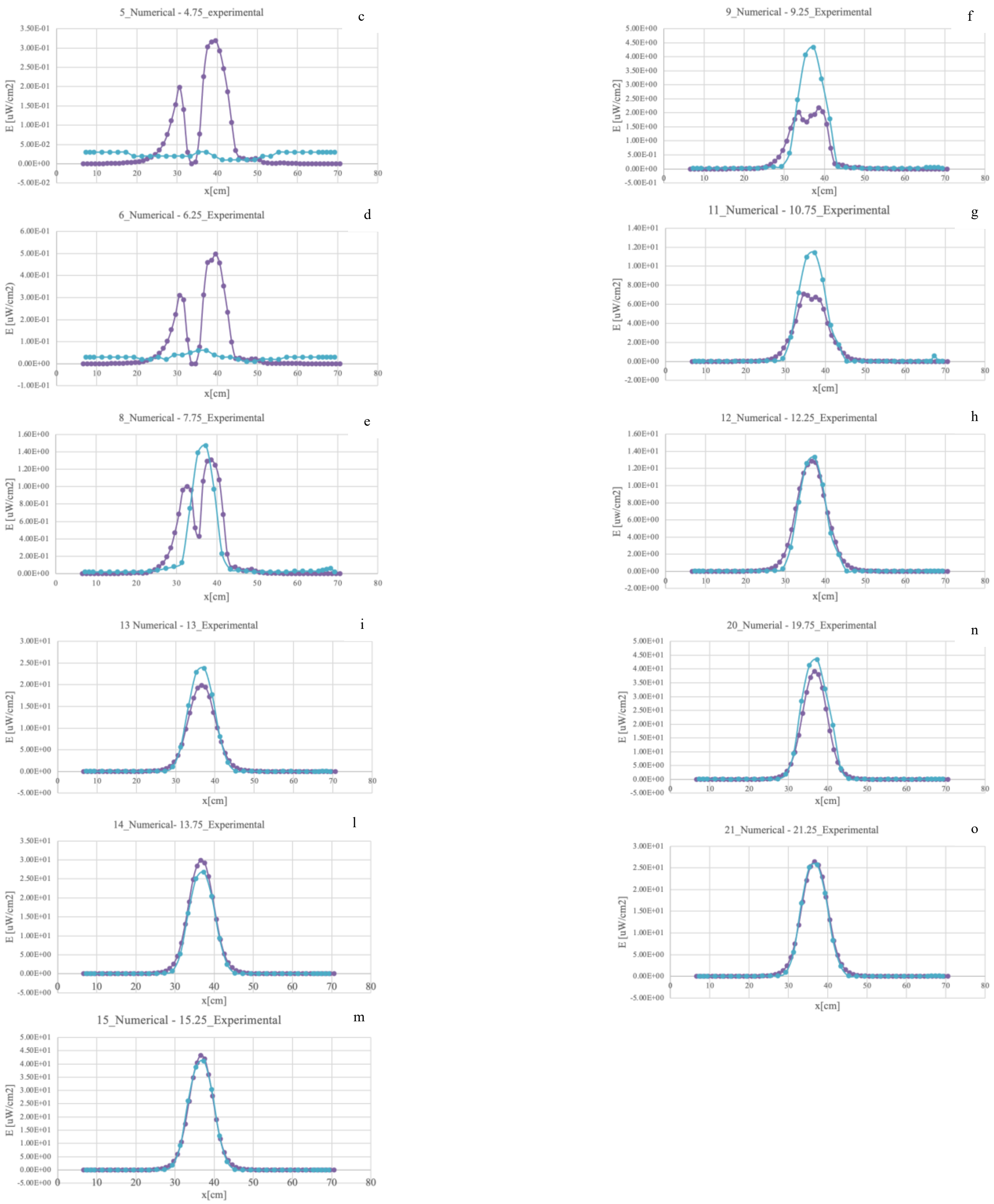

Figure 83: Comparison between the power density profile along the x-axis on the target surface from a numerical pure gaussian emission distribution and experimental data from the lower 16-LED lamp for different ordinates: a) 17 cm numerical ordinate – 16.75 cm experimental ordinate, b) 18 cm numerical ordinate – 18.25 cm experimental ordinate c) 5 cm numerical ordinate – 4.75 cm experimental ordinate, d) 6 cm numerical ordinate – 6.25 cm experimental ordinate, e) 8 cm numerical ordinate – 7.75 cm experimental ordinate, f) 9 cm numerical ordinate – 9.25 cm experimental ordinate, g) 11 cm numerical ordinate – 10.75 cm experimental ordinate, h) 12 cm numerical ordinate – 12.25 cm experimental ordinate, i) 13 cm numerical ordinate – 13 cm experimental ordinate, l) 14 cm numerical ordinate – 13.75 cm experimental ordinate, m) 15 cm numerical ordinate – 15.25 cm experimental ordinate, n) 20 cm numerical ordinate – 19.75 cm experimental ordinate, o) 21 cm numerical ordinate – 21.25 cm experimental ordinate.

After analyzing the graphs related to the central LEDs of the three bars, the examination now proceeds with the peripheral LEDs, which also belong to the same bars. In this case as well, for the positions where the angle between the normal of the sensor and that of the source is zero or close to zero, the comparisons between numerical and experimental data will be represented with larger markers, in order to highlight their relevance.

The following section presents comparison of the illuminance generated by the first lamp source. Figure 84 highlights the source under investigation.

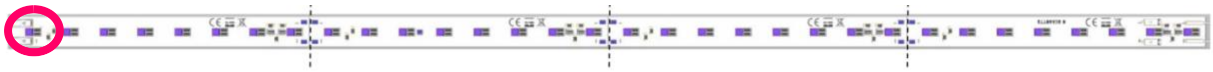

Figure 84: Lamp structure with highlighted simulated source (LED – 1).

First led of central lamp

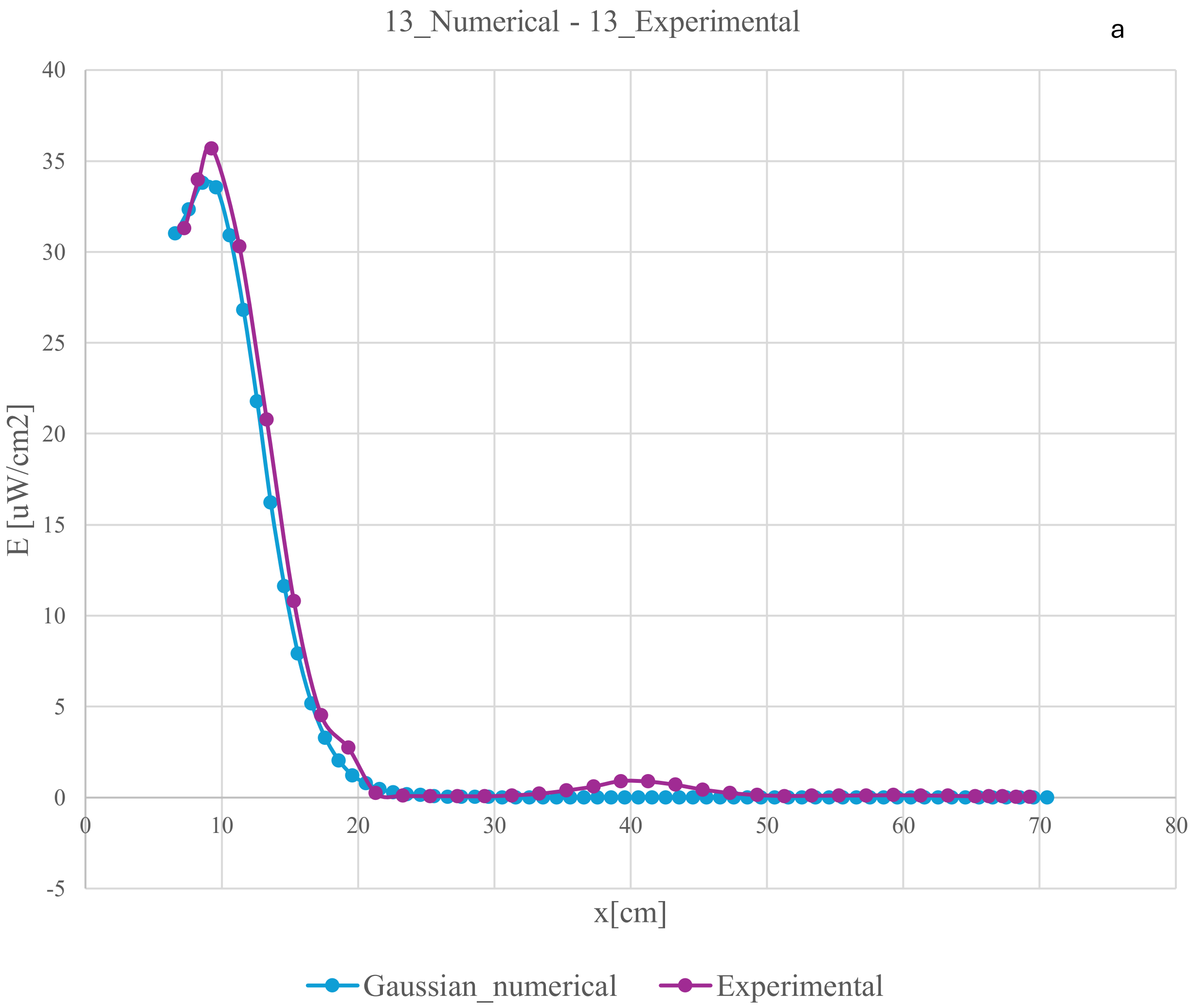

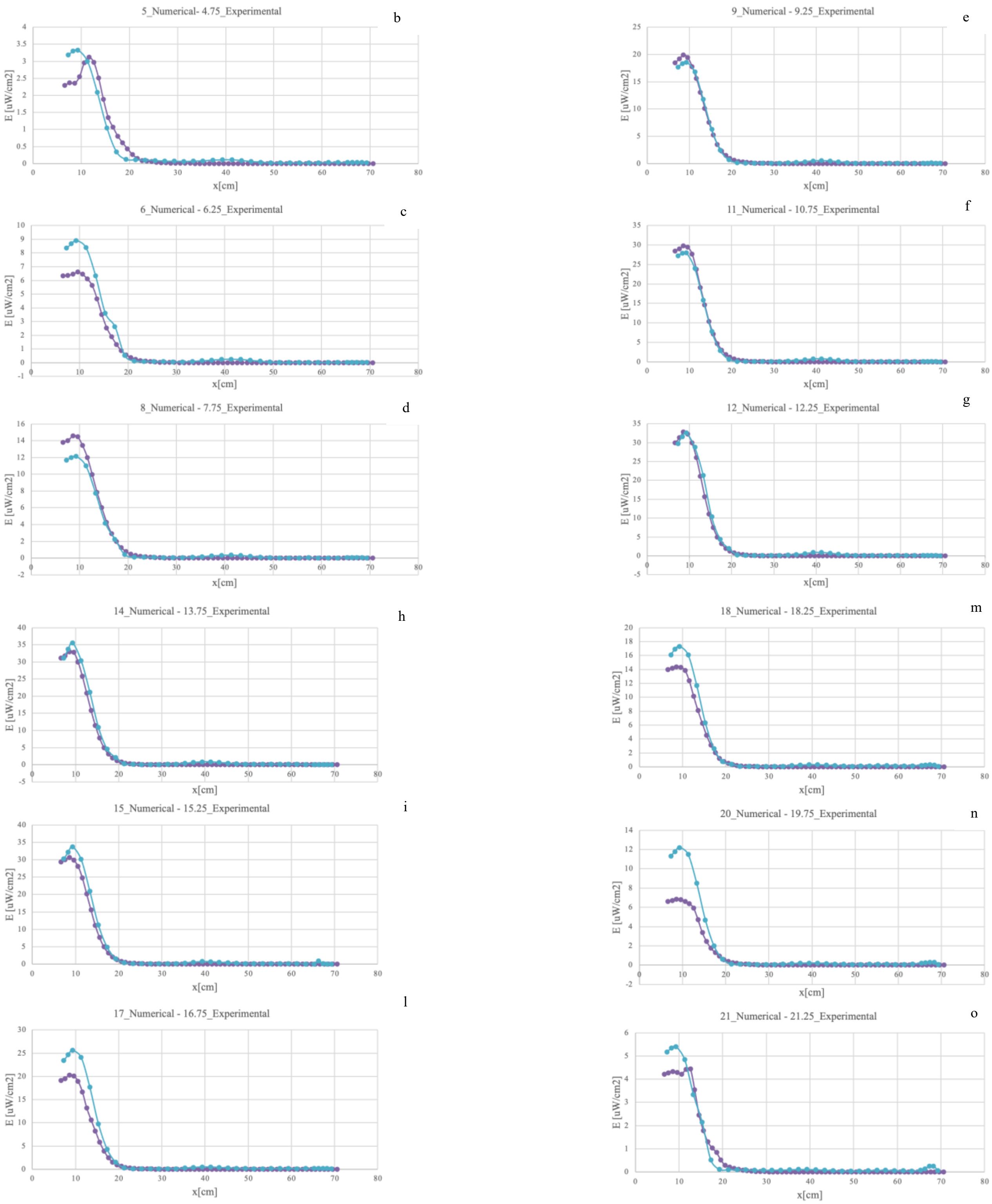

Figure 85: Comparison between the power density profile along the x-axis on the target surface from a numerical pure gaussian emission distribution and experimental data from the central 1-LED lamp for different ordinates: a) 13 cm numerical ordinate – 13 cm experimental ordinate, b) 5 cm numerical ordinate – 4.75 cm experimental ordinate, c) 6 cm numerical ordinate – 6.25 cm experimental ordinate, d) 8 cm numerical ordinate – 7.75 cm experimental ordinate, e) 9 cm numerical ordinate – 9.25 cm experimental ordinate, f) 11 cm numerical ordinate – 10.75 cm experimental ordinate, g) 12 cm numerical ordinate – 12.25 cm experimental ordinate, h) 14 cm numerical ordinate – 13.75 cm experimental ordinate, i) 15 cm numerical ordinate – 15.25 cm experimental ordinate, l) 17 cm numerical ordinate – 16.75 cm experimental ordinate, m) 18 cm numerical ordinate – 18.25 cm experimental ordinate, n) 20 cm numerical ordinate – 19.75 cm experimental ordinate, o) 21 cm numerical ordinate – 21.25 cm experimental ordinate.

First led of the upper lamp

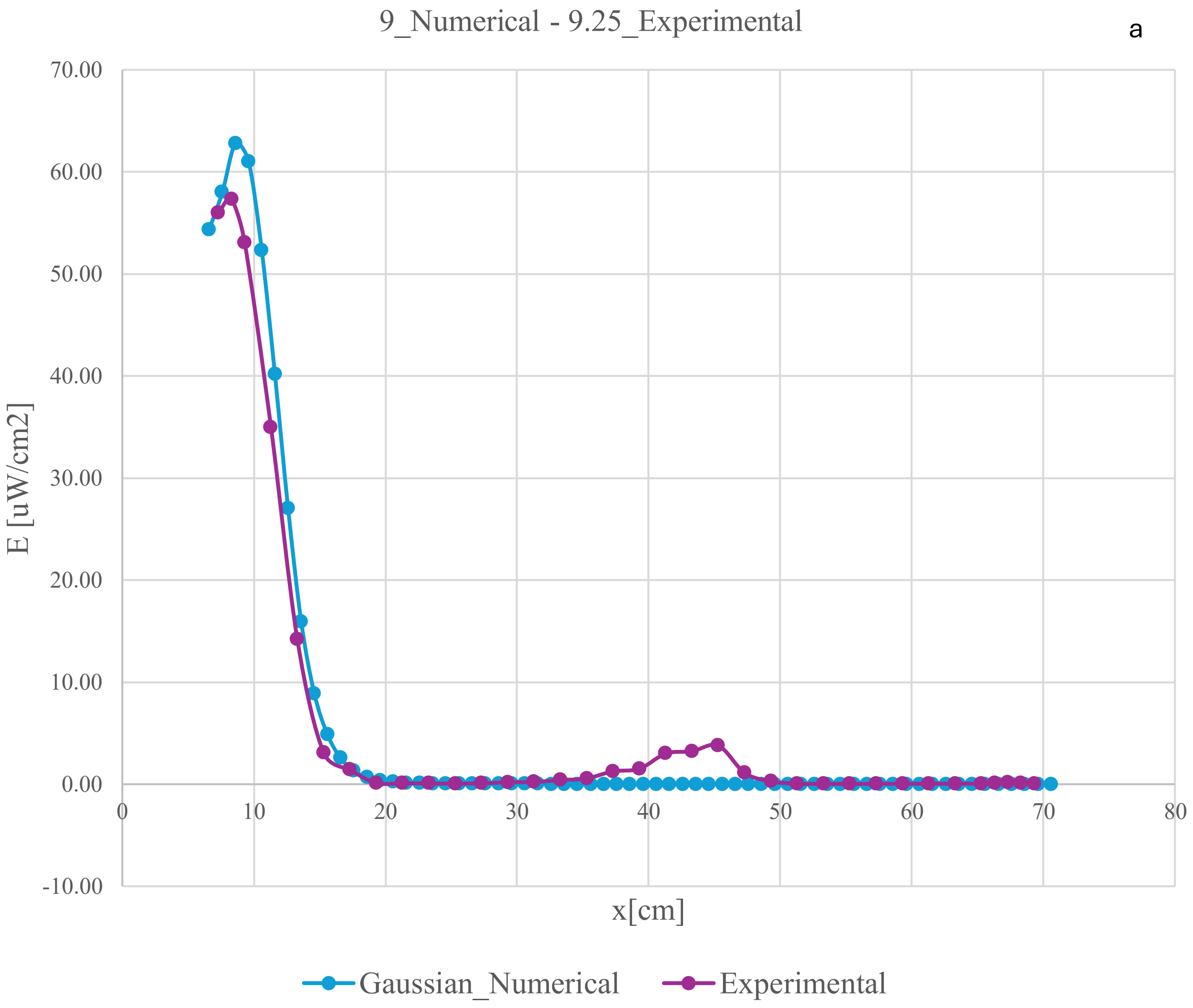

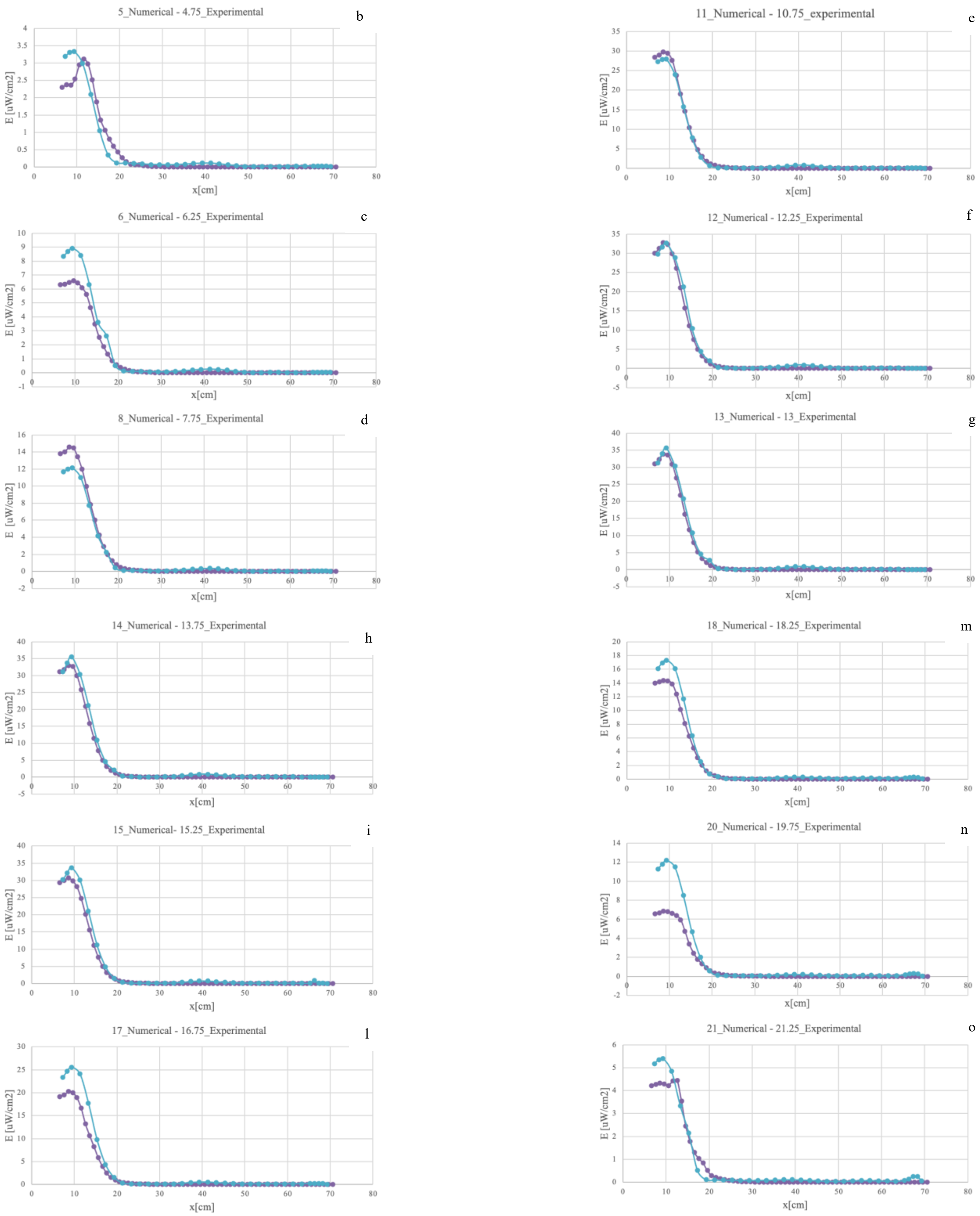

Figure 86: : Comparison between the power density profile along the x-axis on the target surface from a numerical pure gaussian emission distribution and experimental data from the upper 1-LED lamp for different ordinates: a) 9 cm numerical ordinate – 9.25 cm experimental ordinate, b) 5 cm numerical ordinate – 4.75 cm experimental ordinate, c) 6 cm numerical ordinate – 6.25 cm experimental ordinate, d) 8 cm numerical ordinate – 7.75 cm experimental ordinate, e) 11 cm numerical ordinate – 10.75 cm experimental ordinate, f) 12 cm numerical ordinate – 12.25 cm experimental ordinate, g) 13 cm numerical ordinate – 13 cm experimental ordinate h) 14 cm numerical ordinate – 13.75 cm experimental ordinate, i) 15 cm numerical ordinate – 15.25 cm experimental ordinate, l) 17 cm numerical ordinate – 16.75 cm experimental ordinate, m) 18 cm numerical ordinate – 18.25 cm experimental ordinate, n) 20 cm numerical ordinate – 19.75 cm experimental ordinate, o) 21 cm numerical ordinate – 21.25 cm experimental ordinate.

First led of lower lamp

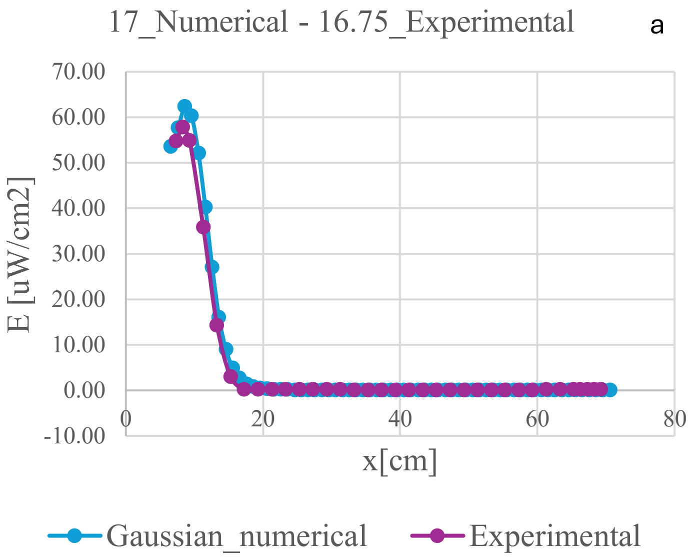
17_Numerical - 16.75_Experimental

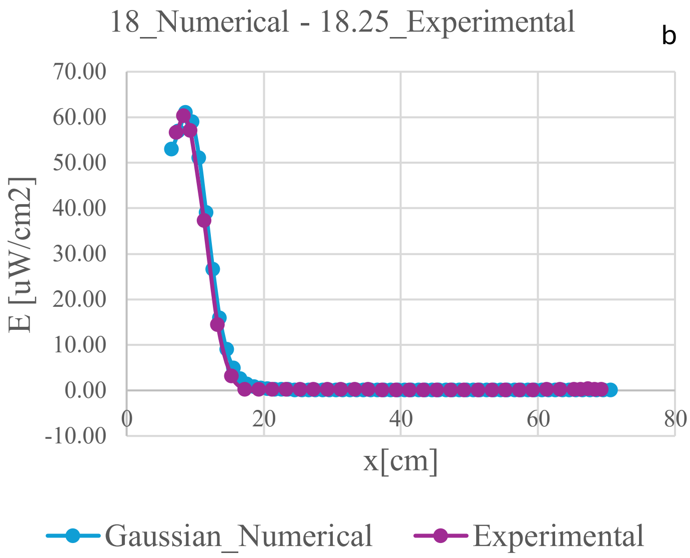
18_Numerical - 18.25_Experimental

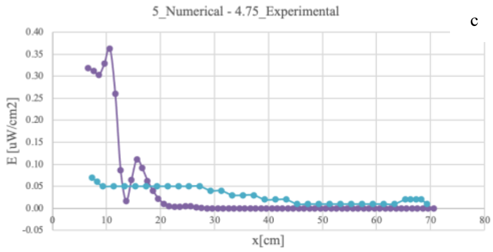
5_Numerical - 4.75_Experimental

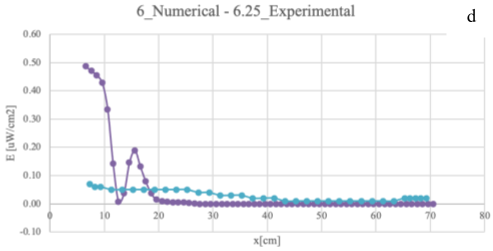
6_Numerical - 6.25_Experimental

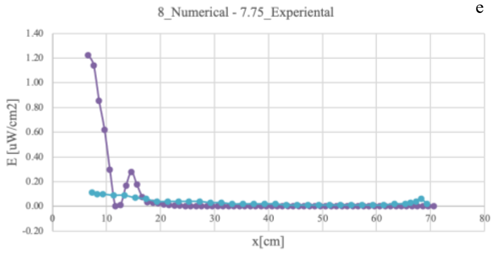
8_Numerical - 7.75_Experiental

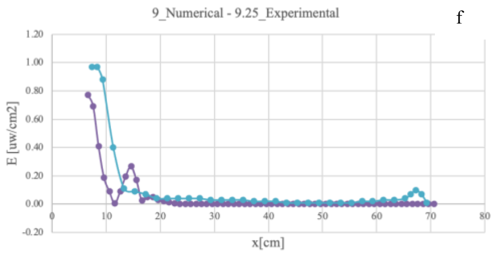
9_Numerical - 9.25_Experimental

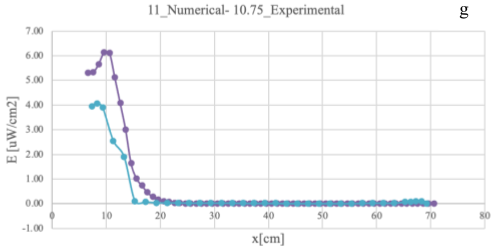
11_Numerical- 10.75_Experimental

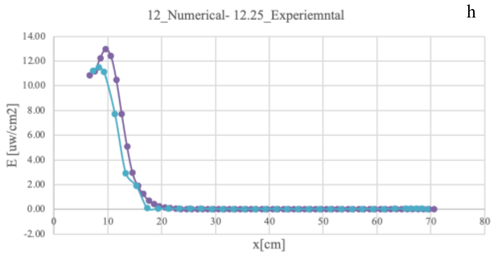
12_Numerical- 12.25_Experiemntal

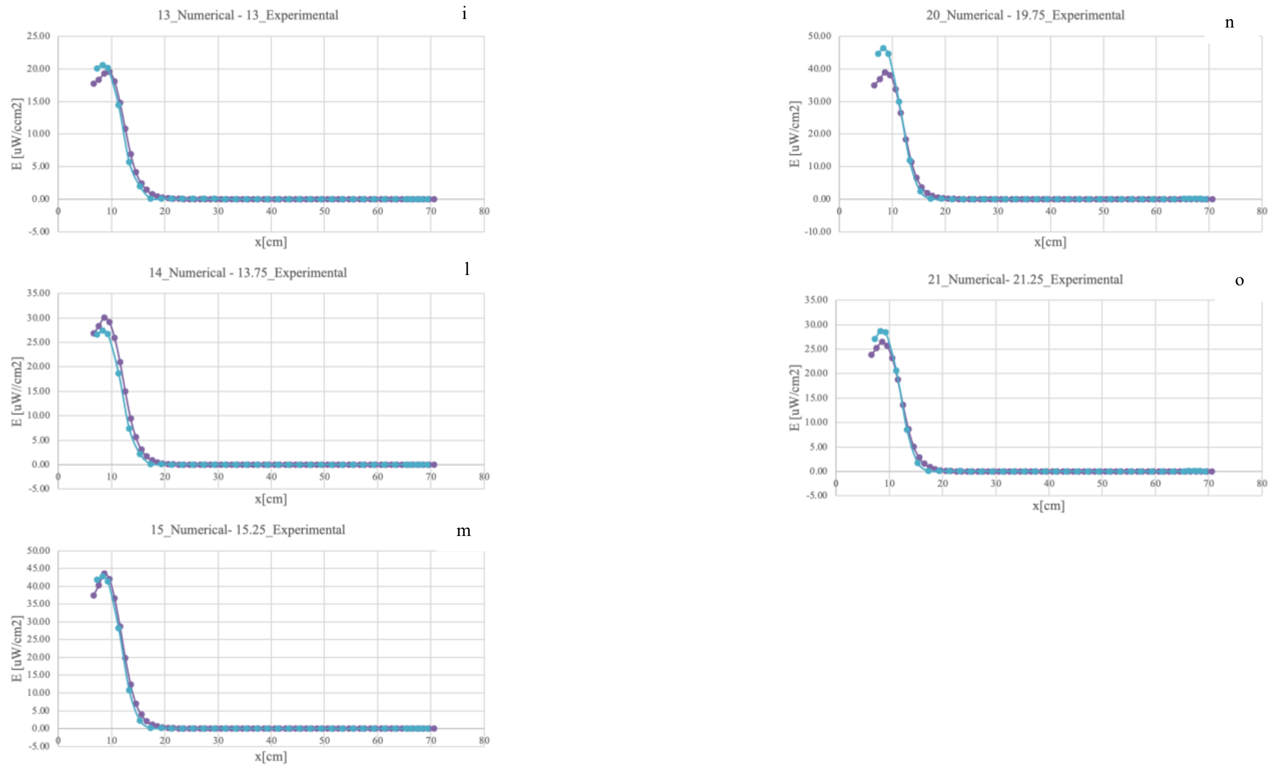

Figure 87: Comparison between the power density profile along the x-axis on the target surface from a numerical pure gaussian emission distribution and experimental data from the lower 1-LED lamp for different ordinates: a) 17 cm numerical ordinate – 16.75 cm experimental ordinate, b) 18 cm numerical ordinate – 18.25 cm experimental ordinate c) 5 cm numerical ordinate – 4.75 cm experimental ordinate, d) 6 cm numerical ordinate – 6.25 cm experimental ordinate, e) 8 cm numerical ordinate – 7.75 cm experimental ordinate, f) 9 cm numerical ordinate – 9.25 cm experimental ordinate, g) 11 cm numerical ordinate – 10.75 cm experimental ordinate, h) 12 cm numerical ordinate – 12.25 cm experimental ordinate, i) 13 cm numerical ordinate – 13 cm experimental ordinate, l) 14 cm numerical ordinate – 13.75 cm experimental ordinate, m) 15 cm numerical ordinate – 15.25 cm experimental ordinate, n) 20 cm numerical ordinate – 19.75 cm experimental ordinate, o) 21 cm numerical ordinate – 21.25 cm experimental ordinate.

An initial analysis of the results shows that the numerical model performs effectively in well-illuminated areas, where the irradiated power density is sufficiently high. In contrast, in peripheral regions characterized by low power density, discrepancies are observed between the simulated and experimental values, with tendencies toward either overestimation or underestimation of the parameter of interest.

These differences can be attributed to several factors. From an experimental standpoint, the mapping system used is manual and not automated, which introduces uncertainties in the spatial positioning of the sensor relative to the source, affecting the accuracy of the measurements, particularly in low-intensity regions.

Moreover, the geometry of the numerical model was reconstructed based on manual measurements taken with a tape measure directly on the test device, in the absence of the original CAD file. This geometric approximation may introduce systematic errors in the spatial discretization, which are reflected in the numerical results, especially in peripheral areas where sensitivity to geometric variations is greater.

It should also be noted that, in low-illumination zones, even small discrepancies between the numerical model and the experimental setup become more evident compared to highly illuminated areas, where the dominant intensity tends to mask potential deviations. This effect amplifies both the visual and numerical differences, making the comparison between simulation and measurement more critical.

The analysis now proceeds with the numerical, experimental comparisons related to the three light sources, each activated individually. This phase allows for the evaluation of the model's behavior under isolated emission conditions, highlighting any discrepancies between simulation and measurement for each configuration.

In the case of the maps corresponding to the individual activation of each bar, as well as for the configuration in which all three bars are simultaneously activated, it was necessary to ensure comparability between the experimental and numerical data. To this end, a targeted interpolation of the illuminance data was performed, limited exclusively to the areas near the bars and to the positions corresponding to the source location.

This choice made it possible to include in the datasets the points where the irradiated power density is maximal, namely those for which the normal to the measurement plane is orthogonal to the surface of the bar. Under these conditions, the contribution of the source is more significant and representative, making the comparison between simulation and measurement more reliable.

The interpolation was performed directly on the original data, with the aim of estimating the values at the positions of interest, even when not directly measured. In this way, correspondence between the positions was ensured, and quantitative comparisons could be made at physically relevant points, minimizing errors due to the different spatial distribution of the data.

Central lamp

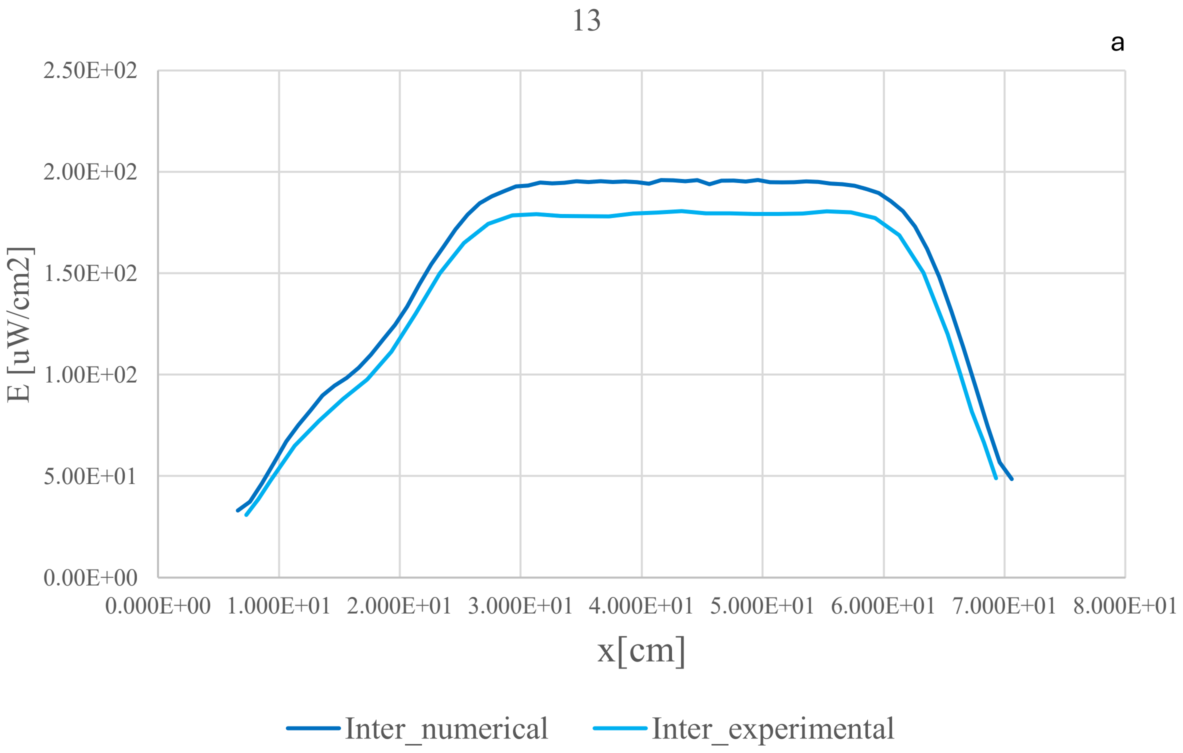

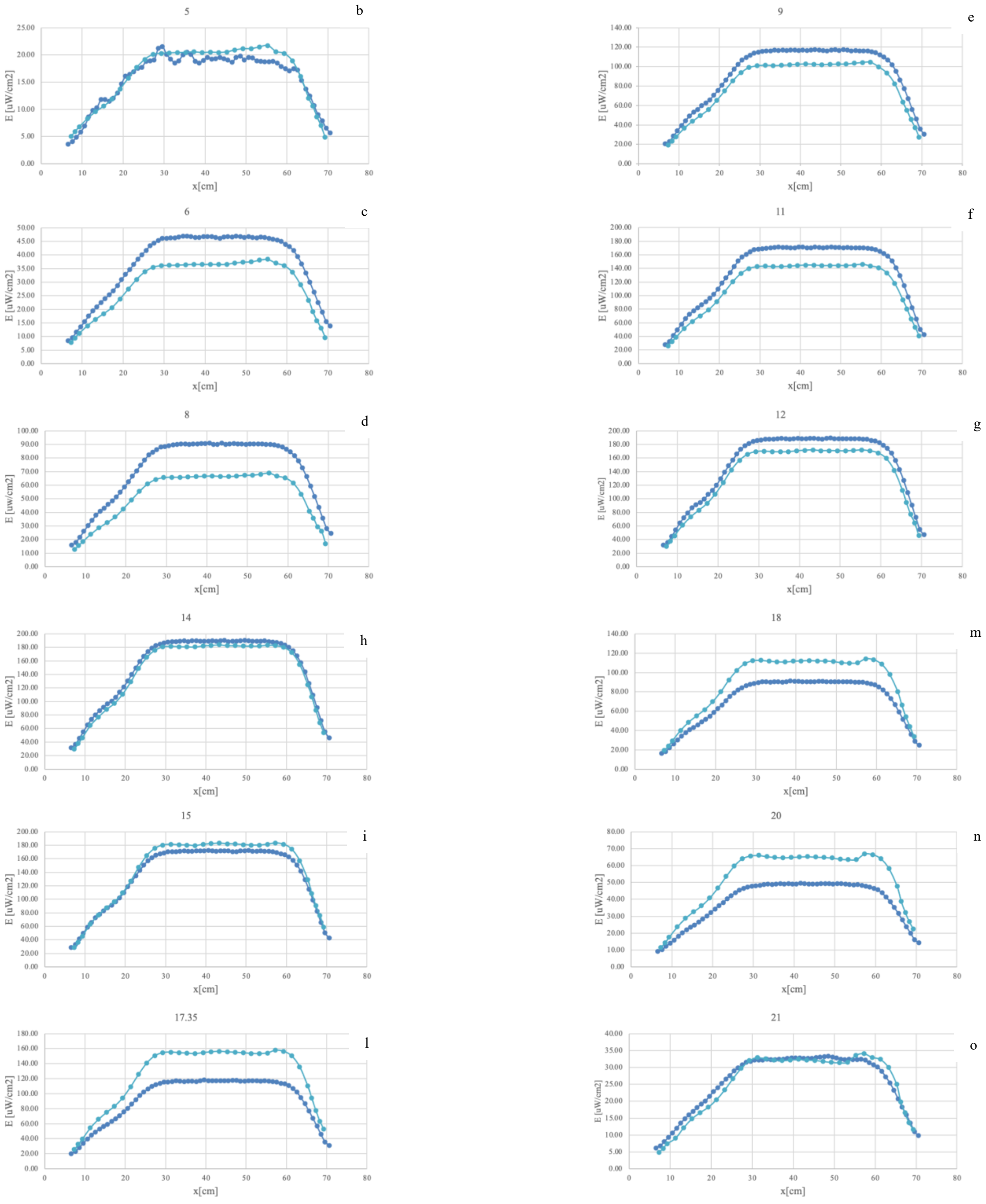

Figure 88: Comparison between the power density profile along the x-axis on the target surface from a numerical pure gaussian emission distribution and experimental data from the central lamp for different ordinates: a) 13 cm numerical ordinate – 13 cm experimental ordinate, b) 5 cm numerical ordinate – 5 cm experimental ordinate, c) 6 cm numerical ordinate – 6 cm experimental ordinate, d) 8 cm numerical ordinate – 8 cm experimental ordinate, e) 9 cm numerical ordinate – 9 cm experimental ordinate, f) 11 cm numerical ordinate – 11 cm experimental ordinate, g) 12 cm numerical ordinate – 12 cm experimental ordinate, h) 14 cm numerical ordinate – 14 cm experimental ordinate, i) 15 cm numerical ordinate – 15 cm experimental ordinate, l) 17.35 cm numerical ordinate – 17.35 cm experimental ordinate, m) 18 cm numerical ordinate – 18 cm experimental ordinate, n) 20 cm numerical ordinate – 20 cm experimental ordinate, o) 21 cm numerical ordinate – 21 cm experimental ordinate.

Upper bar

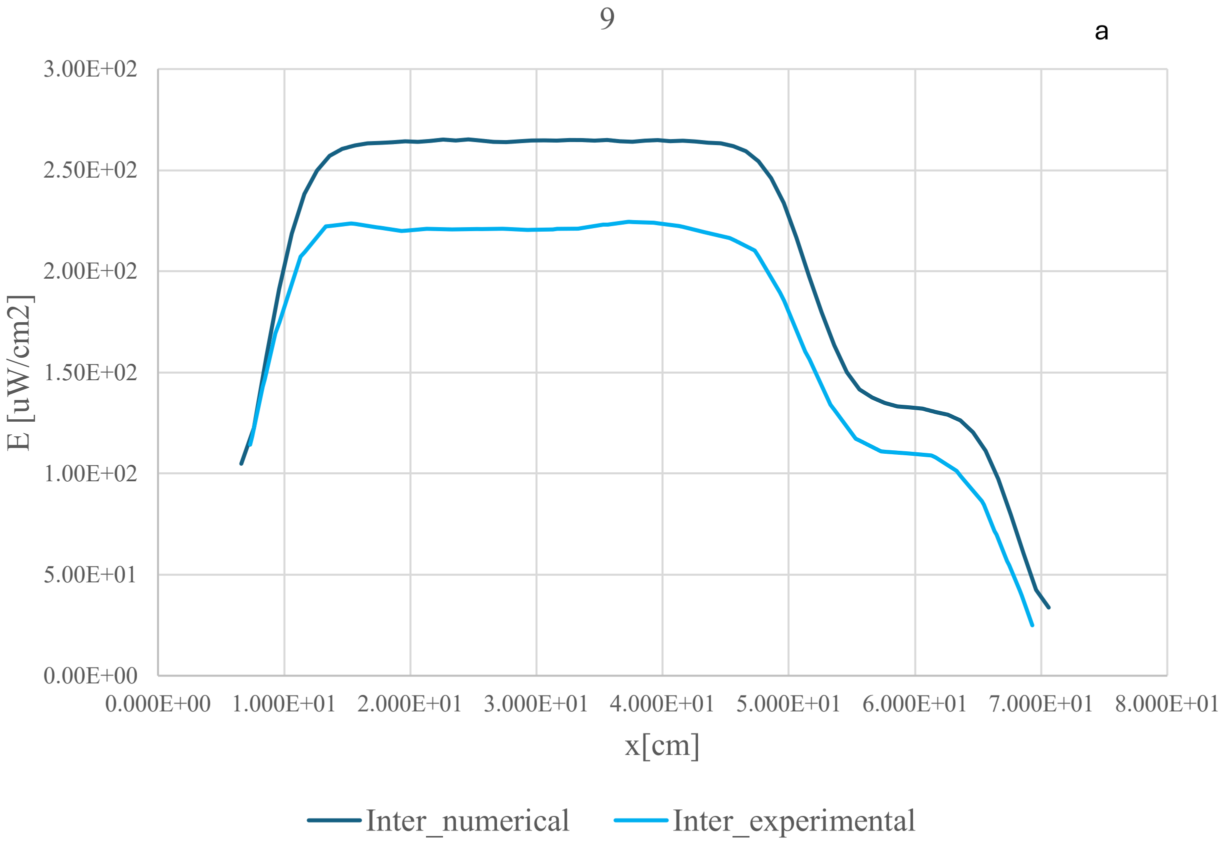
9
a
3.00E+02
2.50E+02
2.00E+02
1.50E+02
1.00E+02
5.00E+01
0.00E+00
E [uW/cm2]
0.000E+00
1.000E+01
2.000E+01
3.000E+01
4.000E+01
5.000E+01
6.000E+01
7.000E+01
8.000E+01
x[cm]
Inter_numerical
Inter_experimental

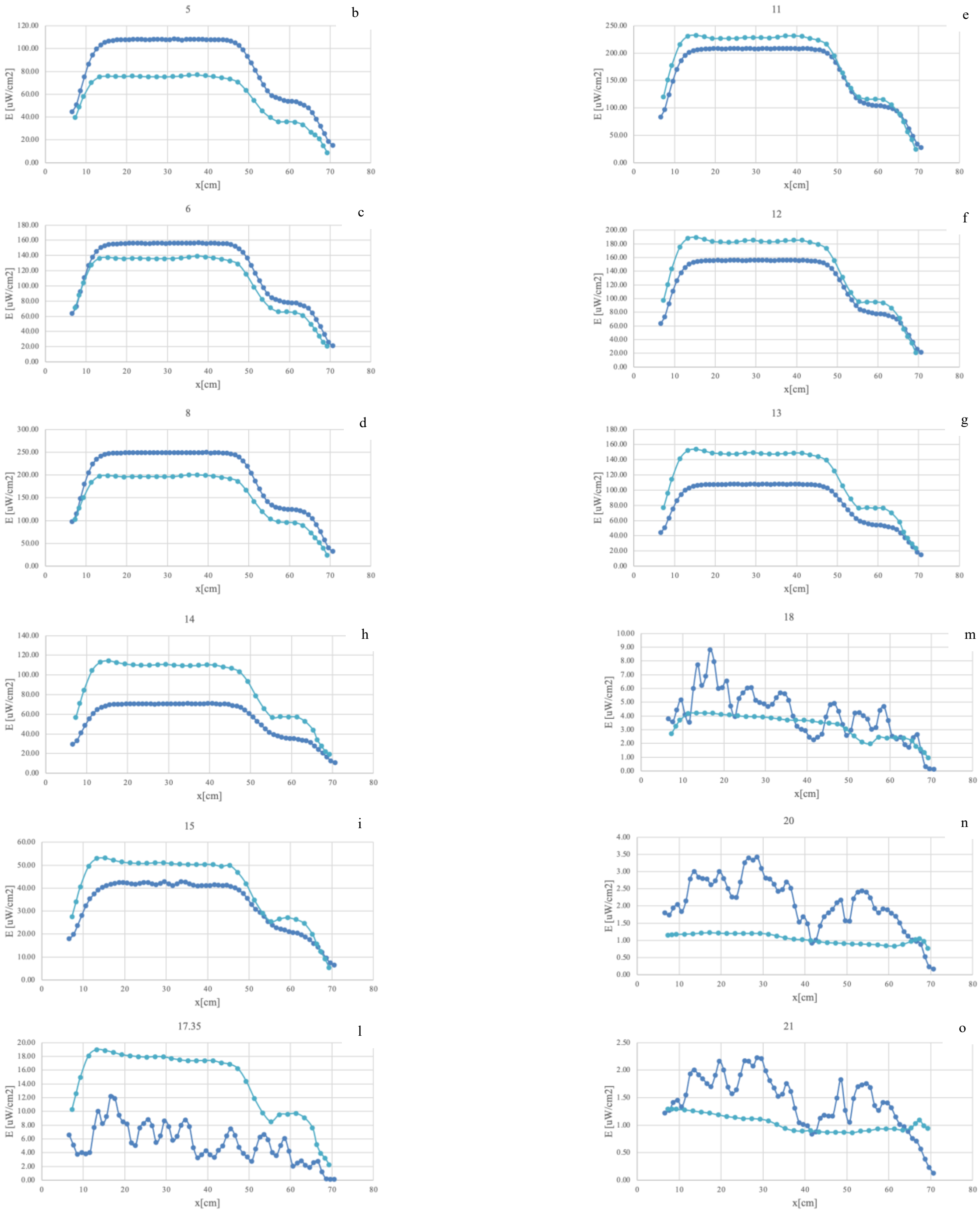

Figure 89: Comparison between the power density profile along the x-axis on the target surface from a numerical pure gaussian emission distribution and experimental data from the upper lamp for different ordinates: a) 9 cm numerical ordinate – 9 cm experimental ordinate, b) 5 cm numerical ordinate – cm 5experimental ordinate, c) 6 cm numerical ordinate – 6 cm experimental ordinate, d) 8 cm numerical ordinate – 8 cm experimental ordinate, e) 11 cm numerical ordinate – 11 cm experimental ordinate, f) 12 cm numerical ordinate – 12 cm experimental ordinate, g) 13 cm numerical ordinate – 13 cm experimental ordinate h) 14 cm numerical ordinate – 14 cm experimental ordinate, i) 15 cm numerical ordinate – 15 cm experimental ordinate, l) 17.35 cm numerical ordinate – 17.35 cm experimental ordinate, m) 18 cm numerical ordinate – 18 cm experimental ordinate, n) 20 cm numerical ordinate – 20 cm experimental ordinate, o) 21 cm numerical ordinate – 21 cm experimental ordinate.

Lower bar

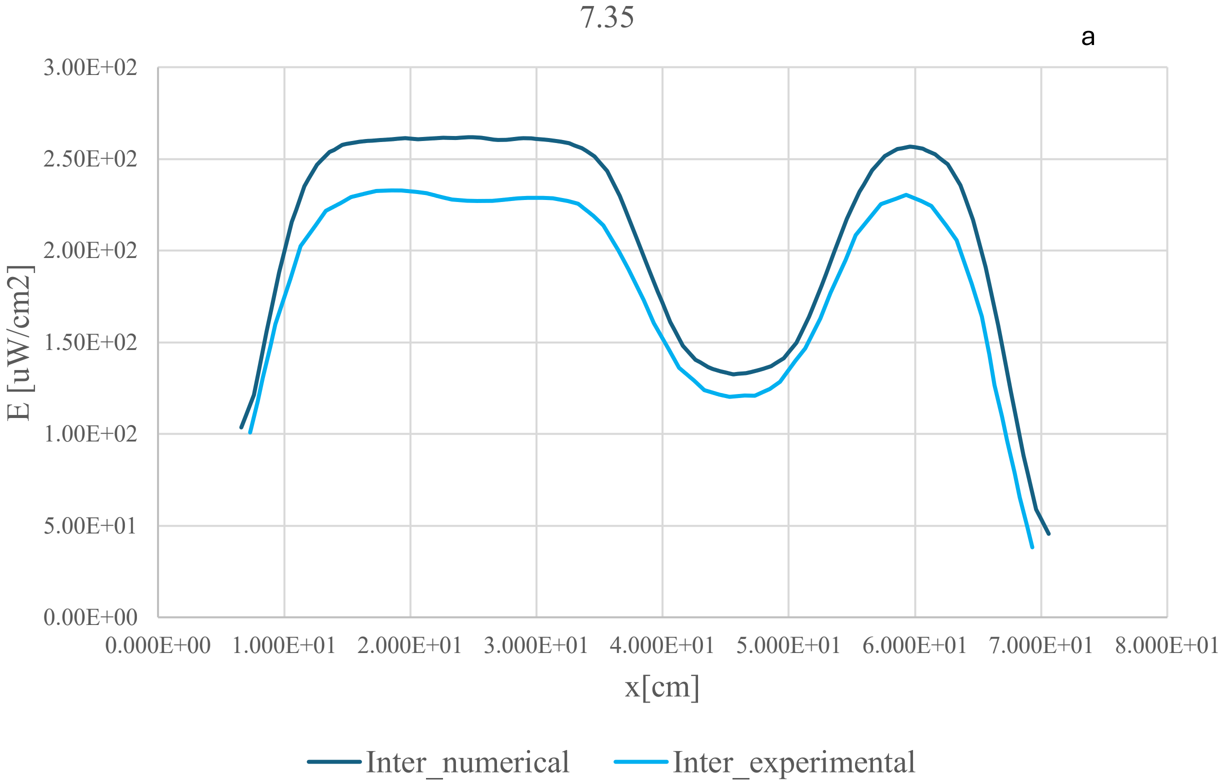
7.35
a
3.00E+02
2.50E+02
2.00E+02
1.50E+02
1.00E+02
5.00E+01
0.00E+00
E [uW/cm2]
0.000E+00
1.000E+01
2.000E+01
3.000E+01
4.000E+01
5.000E+01
6.000E+01
7.000E+01
8.000E+01
x[cm]
Inter_numerical
Inter_experimental

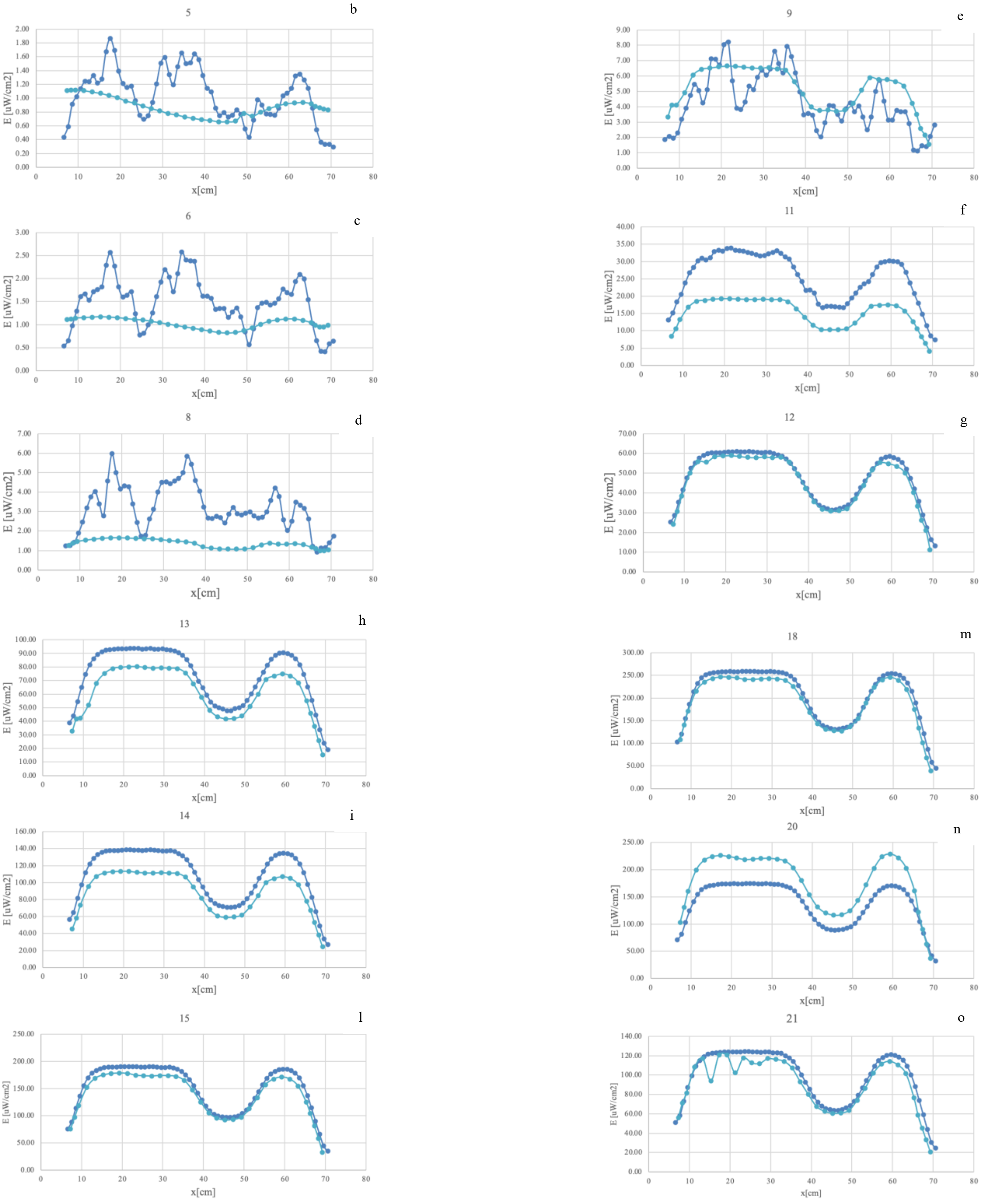

Figure 90: Comparison between the power density profile along the x-axis on the target surface from a numerical pure gaussian emission distribution and experimental data from the lower lamp for different ordinates: a) 17.35 cm numerical ordinate – 17.35 cm experimental ordinate, b) 5 cm numerical ordinate – 5 cm experimental ordinate, c) 6 cm numerical ordinate – 6 cm experimental ordinate, d) 8 cm numerical ordinate – 8 cm experimental ordinate, e) 9 cm numerical ordinate – 9 cm experimental ordinate, f) 11 cm numerical ordinate – 11 cm experimental ordinate, g) 12 cm numerical ordinate – 12 cm experimental ordinate, h) 13 cm numerical ordinate – 13 cm experimental ordinate, i) 14 cm numerical ordinate – 14 cm experimental ordinate, l) 15 cm numerical ordinate – 15 cm experimental ordinate, m) 18 cm numerical ordinate – 18 cm experimental ordinate, n) 20 cm numerical ordinate – 20 cm experimental ordinate, o) 21 cm numerical ordinate – 21 cm experimental ordinate.

As can be observed from the graphs, the numerical model demonstrates a good level of accuracy in the frontal regions and in areas adjacent to the source, that is, in the points where the normal to the measurement plane is orthogonal to the surface of the source itself. Under these conditions, the emission and reception geometry is optimal, and the comparison between simulation and measurement is particularly meaningful.

An analysis of the relative error, defined as:

$$\text{Relative error} = \left(\frac{\text{Experimental} - \text{Numerical}}{\text{Experimental}}\right) \times 100 \tag{5.4.1}$$

shows that, at the frontal position, the error remains limited, ranging between 4% and 7%. This confirms the good agreement between the simulated and measured data in proximity to the source.

However, as shown in the graphs corresponding to the individual activation of the LEDs, the situation changes significantly in the peripheral regions. In these areas, the numerical model exhibits strong oscillations compared to the experimental data, with non-negligible deviations. This behavior can be attributed to several factors:

- Sensor geometry: the active surface of the photodiode is larger than the size of the emitting elements, which may introduce spatial averaging effects not captured by the model.
- External light leakage: the presence of unmodeled diffuse or reflected light may alter the measured values, especially in regions that are not directly illuminated.
- Emission solid quality: potential improvements or variations in the angular distribution of the real source compared to the modeled one may affect the accuracy of the numerical calculation.

In summary, while the numerical model proves to be reliable in the central and directly irradiated regions, further optimizations are required to accurately describe the behavior in peripheral areas, where more complex and less controllable phenomena come into play.

In case of three bars are lit at the same time, the profiles opposite to the central lamp, opposite to the upper lamp and opposite to the lower lamp are shown in figure 91.

The three lamps lit at the same time

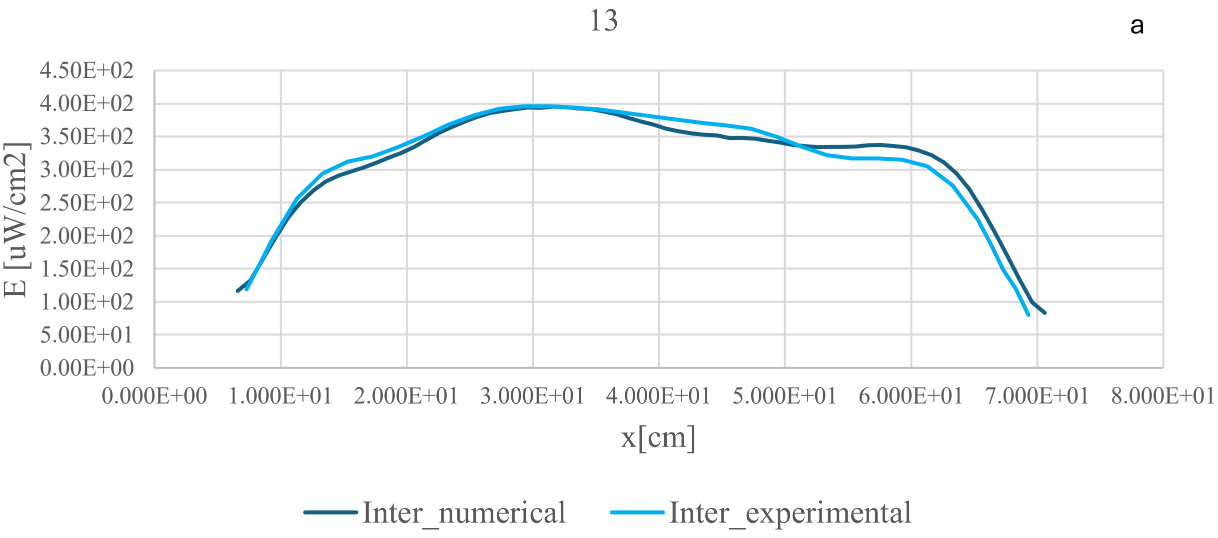

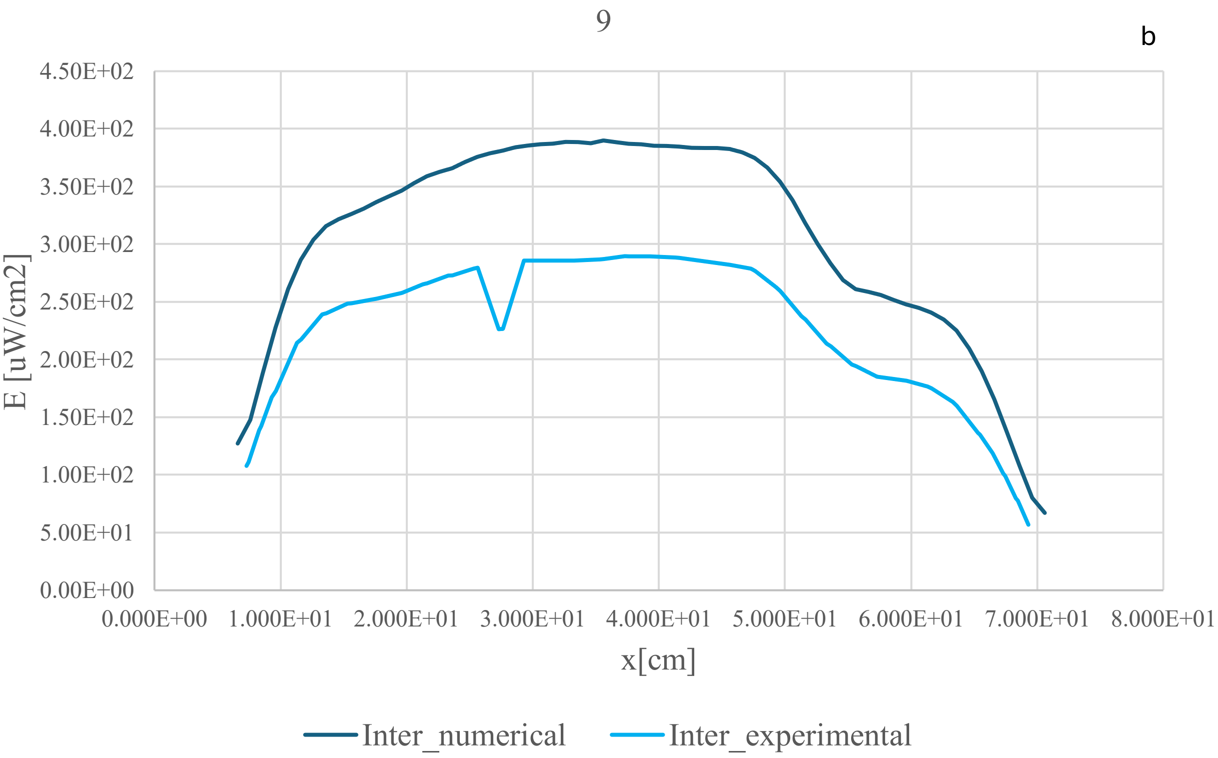

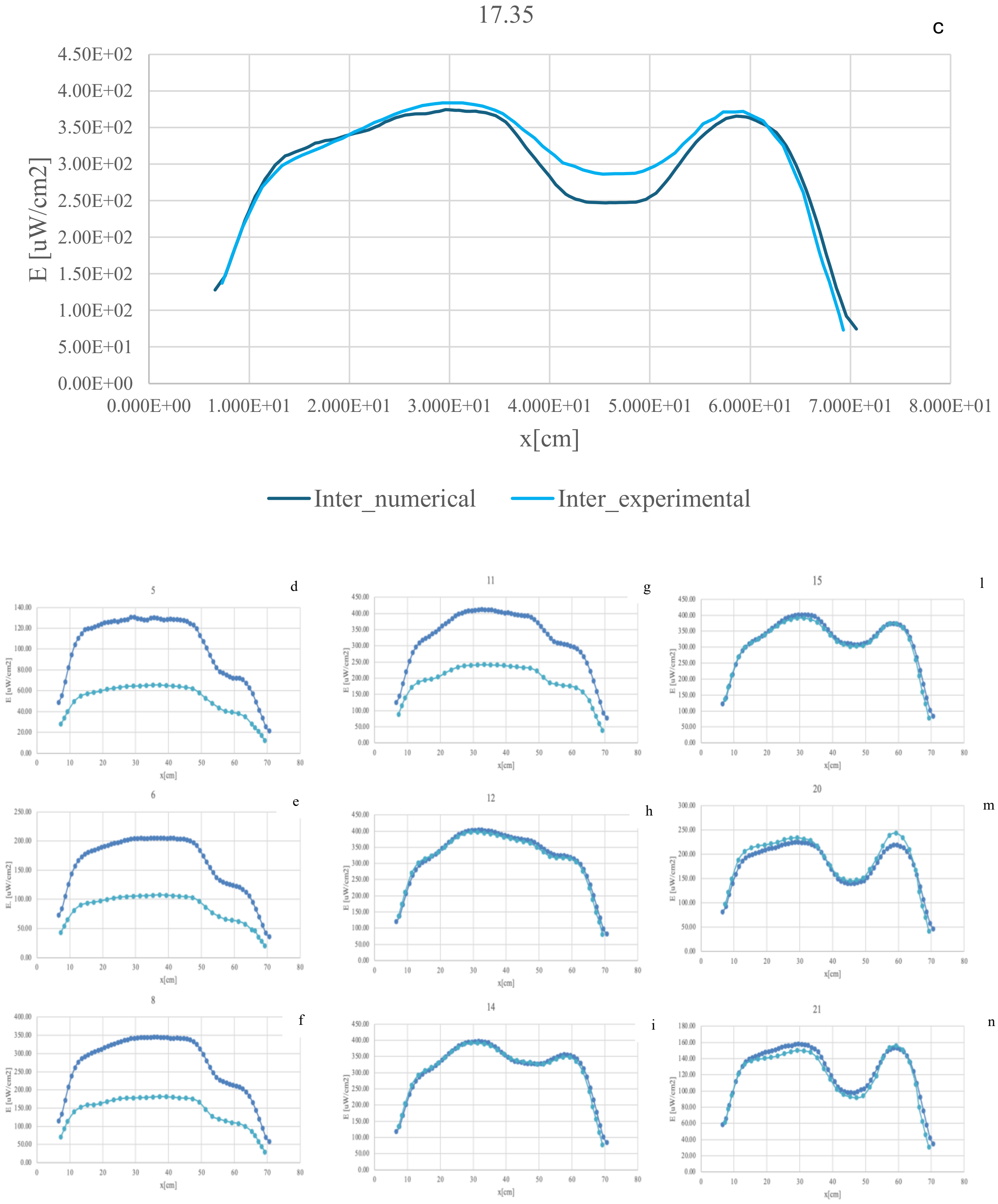

Figure 91: Comparison between the power density profile along the x-axis on the target surface from a numerical pure gaussian emission distribution and experimental data from three lamps lit at the same time for different ordinates: a) 13 cm numerical ordinate – 13 cm experimental ordinate, b) 9 cm numerical ordinate – 9 cm experimental ordinate, c) 17.35 cm numerical ordinate – 17.35 cm experimental ordinate, d) 5 cm numerical ordinate – 5 cm experimental ordinate, e) 6 cm numerical ordinate – 6 cm experimental ordinate, f) 8 cm numerical ordinate – 8 cm experimental ordinate, g) 11 cm numerical ordinate – 11 cm experimental ordinate, h) 12 cm numerical ordinate – 12 cm experimental ordinate, i) 14 cm numerical ordinate – 14 cm experimental ordinate, l) 15 cm numerical ordinate – 15 cm experimental ordinate, m) 20 cm numerical ordinate – 20 cm experimental ordinate, n) 21 cm numerical ordinate – 21 cm experimental ordinate.

From the analysis of the graphs corresponding to the configuration in which all three sources are simultaneously activated, it clearly emerges that the numerical model is capable of accurately describing the system’s behavior, particularly in the frontal regions of the target surface. In these areas, the relative error between simulation and measurement remains low, ranging from 2% to 4%, confirming the validity of the model under conditions of maximum direct incidence.

However, this result contrasts with what is observed in the upper portion of the target surface, where significant discrepancies between the numerical and experimental data are found. This phenomenon can most likely be attributed to a malfunction of the upper source during the measurement phase. Supporting this hypothesis is the observation that the maximum illuminance values recorded in the configuration with all three sources active are not significantly higher than those obtained with only the upper source turned on. This suggests that, in this configuration, the measurement points in the upper region of the target surface are primarily influenced by the contribution of the other two sources, namely the central and lower ones.

Moreover, although the upper and lower sources are not perfectly symmetrical with respect to the central one, their geometric misalignment is not sufficient to justify the magnitude of the observed discrepancy. For this reason, the reported errors refer primarily to the portion of the surface located in front of the central and lower sources, where the radiant contribution is effectively present and correctly modeled.

Chapter 6 – Geometry optimization

Based on the results obtained and discussed in the previous chapter, the developed numerical model was adopted as the reference for the subsequent design phases, despite the critical issues observed in certain experimental configurations. In particular, the good agreement between simulation and measurement under the condition of simultaneous activation of the three sources, with relative errors ranging from 2% to 4%, confirmed the robustness of the model in the central regions of the target surface, making it suitable as a support tool for system optimization.

Building on this foundation, the work focused on improving the optical performance of the prototype, with the aim of enhancing illuminance effectiveness, especially in the peripheral areas where the largest discrepancies had been observed. At this stage, attention was directed toward the internal geometry of the device, under the hypothesis that a targeted modification of the wall shape could positively influence the spatial distribution of UV-C radiation.

As a first step toward system optimization, the spatial arrangement of the LED modules was modified to make the lateral bars symmetrical with respect to the central one. This choice was motivated by the desire to ensure a more balanced distribution of UV-C radiation on the target surface, reducing the asymmetries observed in previous configurations. To this end, two distinct configurations were tested, characterized by a vertical displacement (Δy) of 4 cm and 4.35 cm, respectively, in order to evaluate the impact of this variation on the irradiance distribution.

In these symmetrical configurations, the effect of the distance between the sources and the target surface was also analyzed, considering two specific cases: all bars placed at 8 cm and at 11 cm from the surface. This comparison made it possible to assess how the variation in distance affects beam collimation and illuminance uniformity, providing useful insights for the optical design of the system.

Once a basic symmetrical configuration was defined, the study proceeded with the analysis of the internal geometry of the device, focusing in particular on the shape of the upper and lower walls of the optical chamber. The initial hypothesis was that a properly designed curvature could act as a passive optical guide, contributing to the apparent collimation of the beam emitted by the LEDs and improving the germicidal effectiveness of the system.

Preliminary simulations were therefore conducted on different geometric configurations, analyzing the optical behavior associated with concave (inward-curved) and convex (outward-curved) surfaces. The objective was to evaluate which geometry promotes a more homogeneous radiation distribution and a localized increase in light intensity, thereby contributing to the improvement of the system’s germicidal performance.

This phase represents a crucial step toward the development of an optimized prototype, in which geometry is no longer a secondary element but an integral part of the UV-C beam control and management strategy. The integration between numerical modelling and geometric design thus constitutes the core of the following chapter, dedicated to the optimization of the device.

6.1 Preliminary Optimization of the Source Arrangement

In the process of optimizing the irradiation system, it was considered essential to begin with a reflection on the spatial configuration of the sources. Before intervening on the internal geometry of the device, it was necessary to ensure a condition of symmetry among the LED bars, in order to establish a consistent basis for the subsequent optical analyses. For this reason, the lateral bars were repositioned with respect to the central one, adopting two values of vertical displacement (Δy), equal to 4 cm and 4.35 cm, to evaluate the influence of small geometric variations on the system's response. This phase represented a preliminary but essential step, aimed at isolating the contribution of symmetry in the distribution of the UV-C beam.

This intervention was accompanied by a second alignment operation, aimed at centering the bars longitudinally with respect to the axis of the device. In this way, a uniform distance was ensured between the ends of the bars and the lateral-vertical walls of the optical chamber, a necessary condition to avoid edge effects and asymmetric reflections that could compromise the regularity of the radiant field. The complete symmetrisation, both in the transverse and longitudinal directions, allowed for the definition of a stable and balanced reference configuration, from which to proceed with the subsequent numerical and experimental analyses.

In parallel, the effect of the distance between the sources and the target surface was analyzed, considering two configurations with the bars placed at 8 cm and 11 cm from the filtering plane, respectively. The objective was to understand how the variation in distance affects beam collimation and illuminance uniformity, providing a quantitative basis for the subsequent geometric modifications of the device.

Figure 92 shows the vertical sections of the device, highlighting the alignment of the LED bars with respect to the central axis.

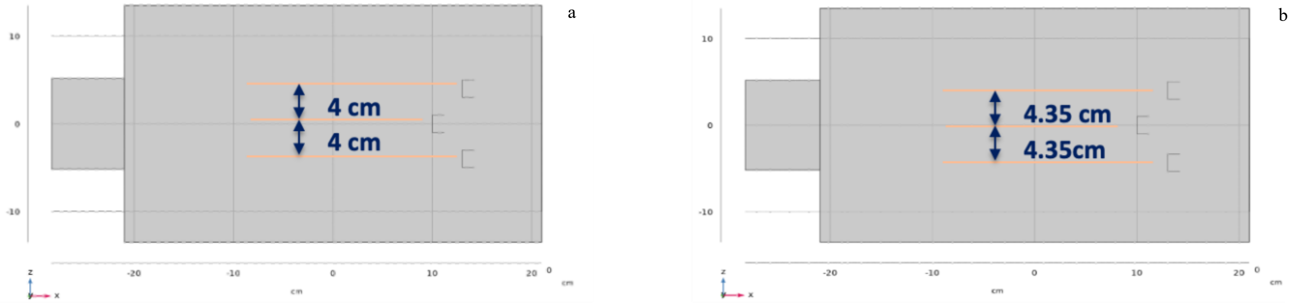

Figure 92: The alignment of the LED lamps: a) 4 cm alignment, b) 4.35 cm alignment.

With regard to the analysis of the irradiated power density curves, the focus was placed on configurations in which the system structure was fully symmetrized. Under these conditions, thanks to the alignment of the LED bars and their symmetrical arrangement with respect to the horizontal central axis of the device, a perfect correspondence is observed between the positive and negative positions relative to this axis. This allows the analysis to be limited to only one half of the domain, simplifying the interpretation of the results without losing significant information.

For the study of the curves, three representative positions were selected:

1. The position where the normal to the sampling point coincides with the normal to the surface of the bar, a condition that ensures the maximum direct contribution from the source.
2. The position corresponding to the edge of the filtering surface, where a lower level of illuminance is expected and where system optimization is more critical to ensure adequate exposure to UV-C radiation.
3. An intermediate position between the two above, useful for observing the transition in the irradiance distribution and for evaluating the system's effectiveness along the entire vertical profile.

These three reference positions will be systematically adopted in all analyses presented in this section, in order to ensure methodological consistency and comparability across the different geometric configurations examined.

Figure 93 shows the sampling positions used for the analysis of the irradiance distribution.

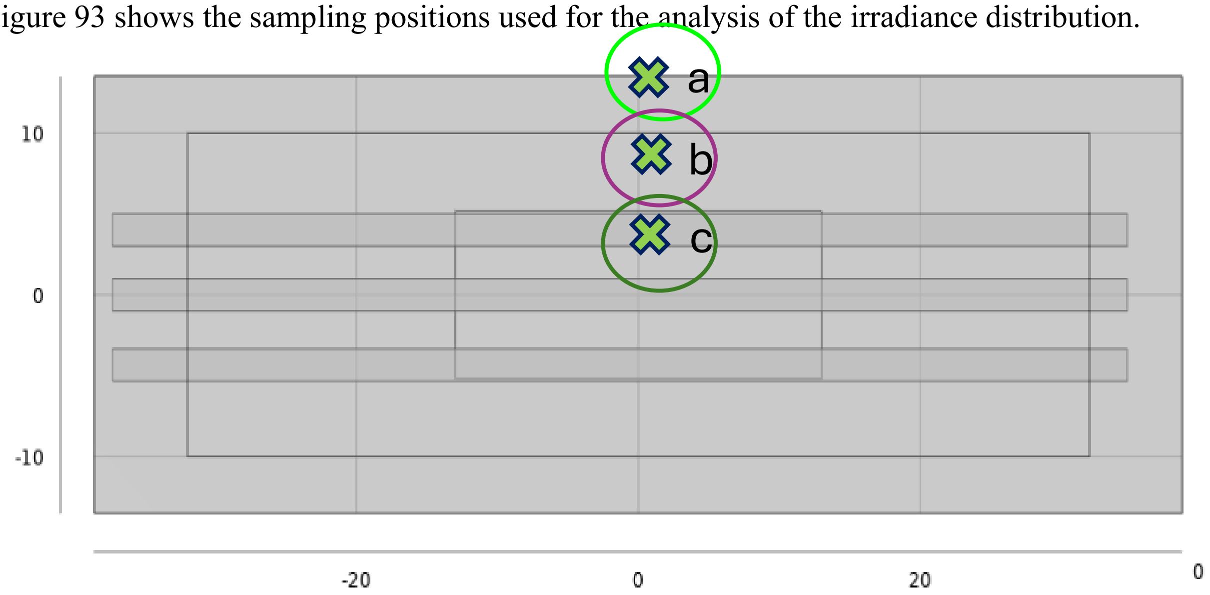

Figure 93: The sampling positions used for the analysis of the irradiance distribution.

Starting from these reference positions, the different trends in the irradiance distribution are analyzed as a function of the spatial arrangement of the LED bars within the device. The objective is to evaluate how the positioning of the sources influences the shape and intensity of the UV-C beam, with particular attention to the peripheral areas of the target surface, where optimization is more critical. In Figure 94, the comparison between the irradiance profiles obtained for the two installation geometries is presented, showing the power density distribution along the x-axis of the target surface when all three lamps are simultaneously activated.

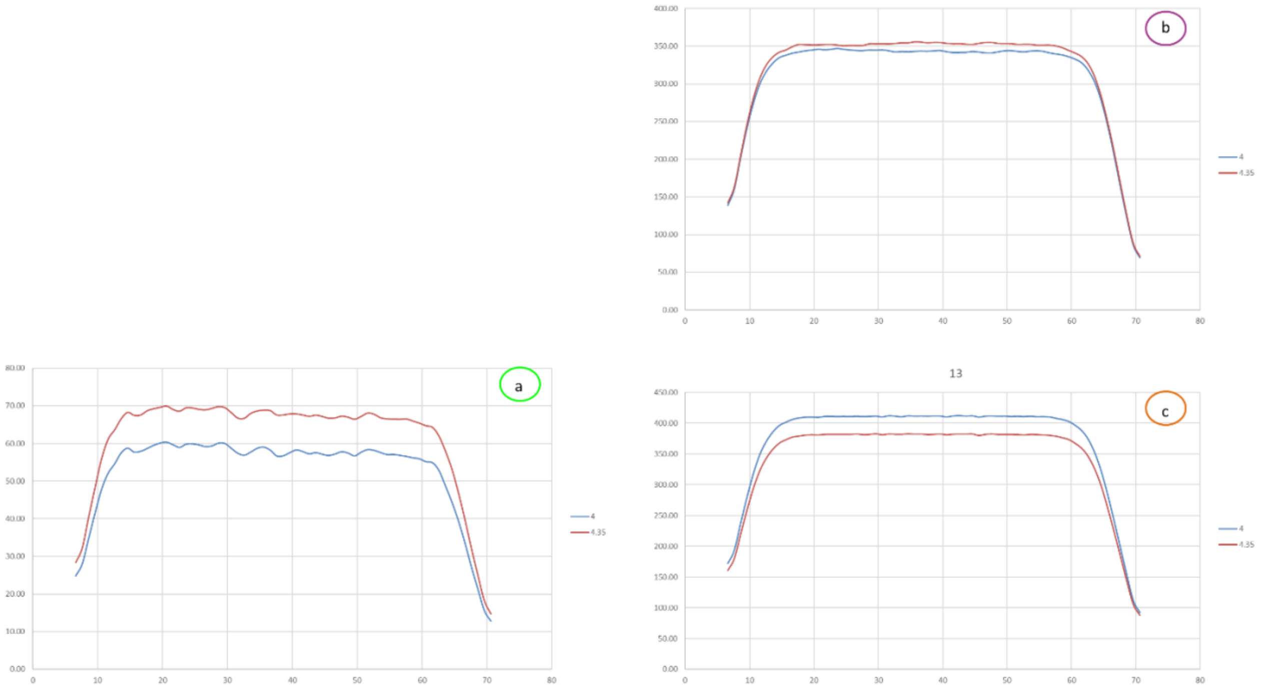

Figure 94: Comparison between the power density profile along the x-axis on the target surface from the 3 three lamps lit at the same time for different lamp installation: a) Trend corresponding to the ordinate "a" in Figure 93 with max error between the curves of 20%, b) Trend corresponding to the ordinate "b" in Figure 93 with max weeroe between the curves of 4%, c) Trend corresponding to the ordinate "c" in Figure 93 with max weeroe between the curves of 20%.

The image clearly illustrates the impact of the relative positioning of the LED bars on the distribution of the irradiated power density, highlighting how even minor geometric variations can lead to significant differences in the optical behaviour of the system.

The two configurations under comparison, characterized by a vertical displacement Δy of the lateral bars with respect to the central one, equal to 4 cm and 4.35 cm respectively, are both symmetric with respect to the central axis of the device. Nevertheless, the effect produced by this slight variation is far from negligible. As observed, increasing the distance between the lateral bars and the central one (Δy = 4.35 cm) results in a noticeable enhancement of irradiance in the peripheral regions of the target surface. This outcome is particularly relevant, as the peripheral areas initially exhibited the lowest illuminance levels and therefore required optimization interventions.

Conversely, the configuration with Δy = 4 cm, in which the bars are positioned closer to the central one, yields an improvement in illuminance within the central region, which was already subject to high irradiation. This contrasting behavior between the central and peripheral zones underscores the high sensitivity of the UV-C beam distribution to the system's geometry and demonstrates that even a variation of merely 0.35 cm can substantially influence the device's effectiveness.

From this analysis, it can be inferred that selecting the configuration with Δy = 4.35 cm provides a greater contribution to peripheral coverage without significantly compromising central illuminance. This balance between peripheral coverage and central intensity constitutes a fundamental criterion for optimal system design, particularly in applications requiring a uniform distribution of germicidal radiation.

To assess the influence of this parameter, two distinct configurations were considered: one with the LED bars positioned 11 cm from the filtering plane, and another with the bars placed at 8 cm. Both configurations were analyzed in conjunction with the two previously studied vertical symmetry variants (Δy = 4 cm and Δy = 4.35 cm), thereby enabling a comprehensive evaluation of the interaction between vertical positioning and source-target distance. In total, four geometric configurations were examined, each defined by a specific combination of Δy and distance from the filter, as it shown in figure 95.

The results obtained were compared with those from the previous analysis, in which the source-target distance was held constant. Comparative graphs of the different configurations are presented in figure 96 and 97, visually illustrating the combined effect of Δy variation and distance from the filtering plane on the irradiance distribution.

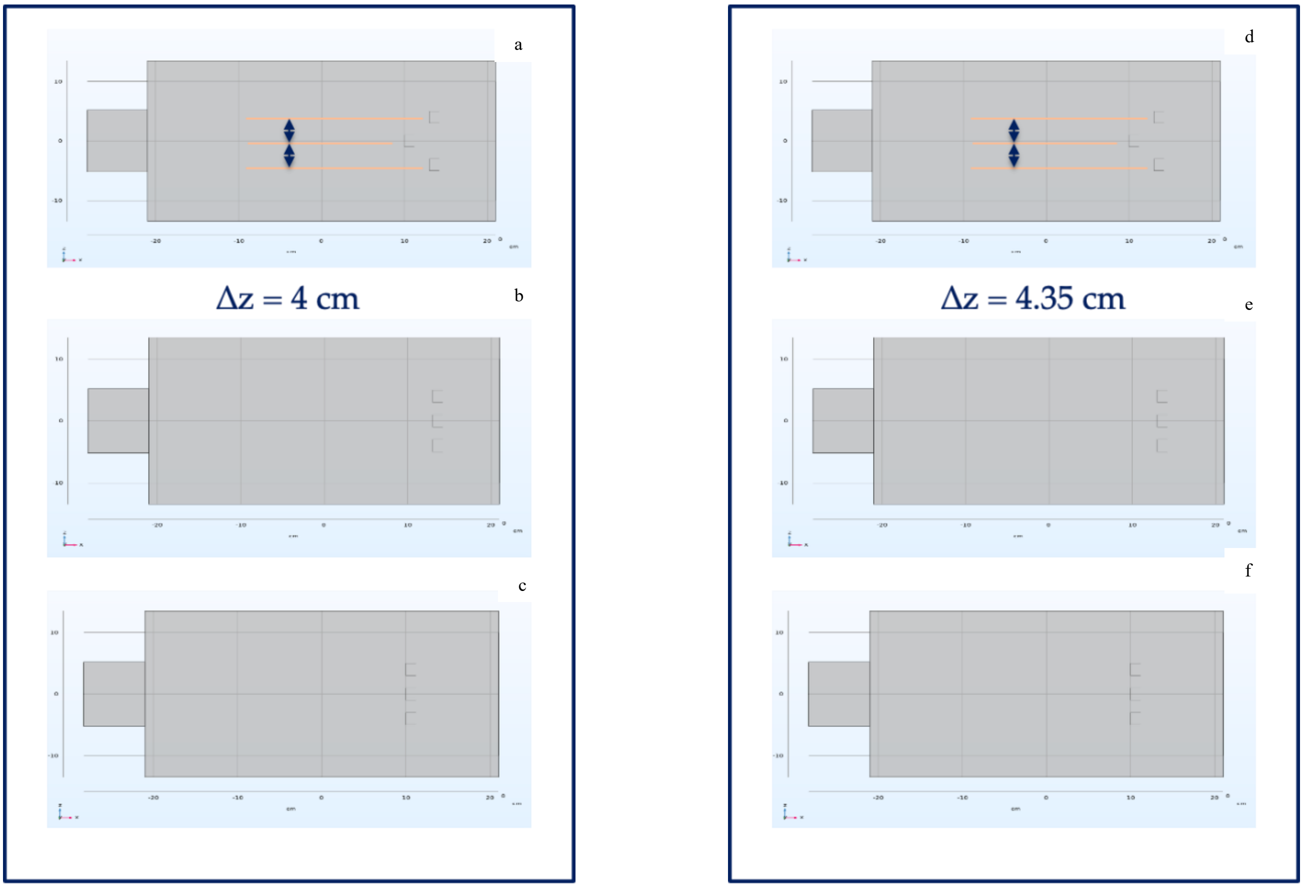

Figure 95: Different lamp configurations: a) Original configuration with external lamps installed at distance of 4 cm from the central source, b) Configuration with lamps spaced 4 cm apart and located 8 cm from the target surface, c) Configuration with lamps spaced 4 cm apart and located 11 cm from the target surface, d) Original configuration with external lamps installed at distance of 4.35 cm from the central source, e) Configuration with lamps spaced 4.35 cm apart and located 8 cm from the target surface, f) Configuration with lamps spaced 4.35 cm apart and located 11 cm from the target surface.

Symmetry Configuration: $\Delta y = 4$ cm

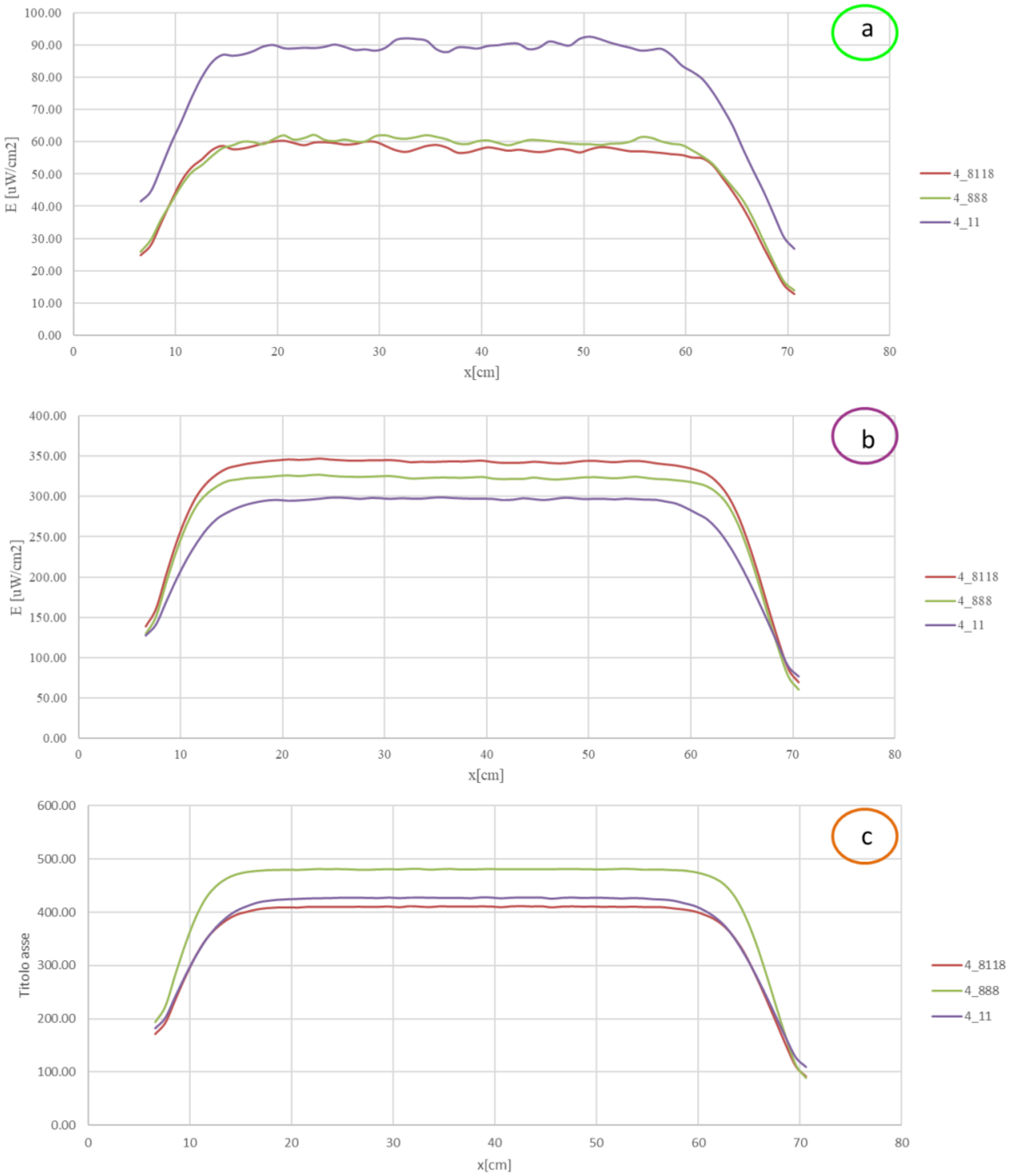

Figure 96: Comparison between the power density profile along the x-axis on the target surface from the 3 three lamps lit at the same time for different lamp installation spaced of 4 cm: a) trend corresponding to the ordinate "a" in Figure 93 with max error between the configurations 4_11 and 4_8118 of 60% at the center and 110% laterally and between the configurations 4_11 and 4_888 of 56% at the center and 92% laterally, b) trend corresponding to the ordinate "a" in Figure 93 with max error between the configuration 4_8118 and 4_11 of 16% at the center and 25% laterally and between the configurations 4_8118 and 4_888 of 6% at the center and 15% laterally, c) trend corresponding to the ordinate "a" in Figure 93 with max error between the configuration 4_888 and 4_8118 of 17% at the center and 20% laterally and between the configurations 4_888 and 4_11 of 13% at the center and 19% laterally.

Symmetry Configuration: Δy = 4.35 cm

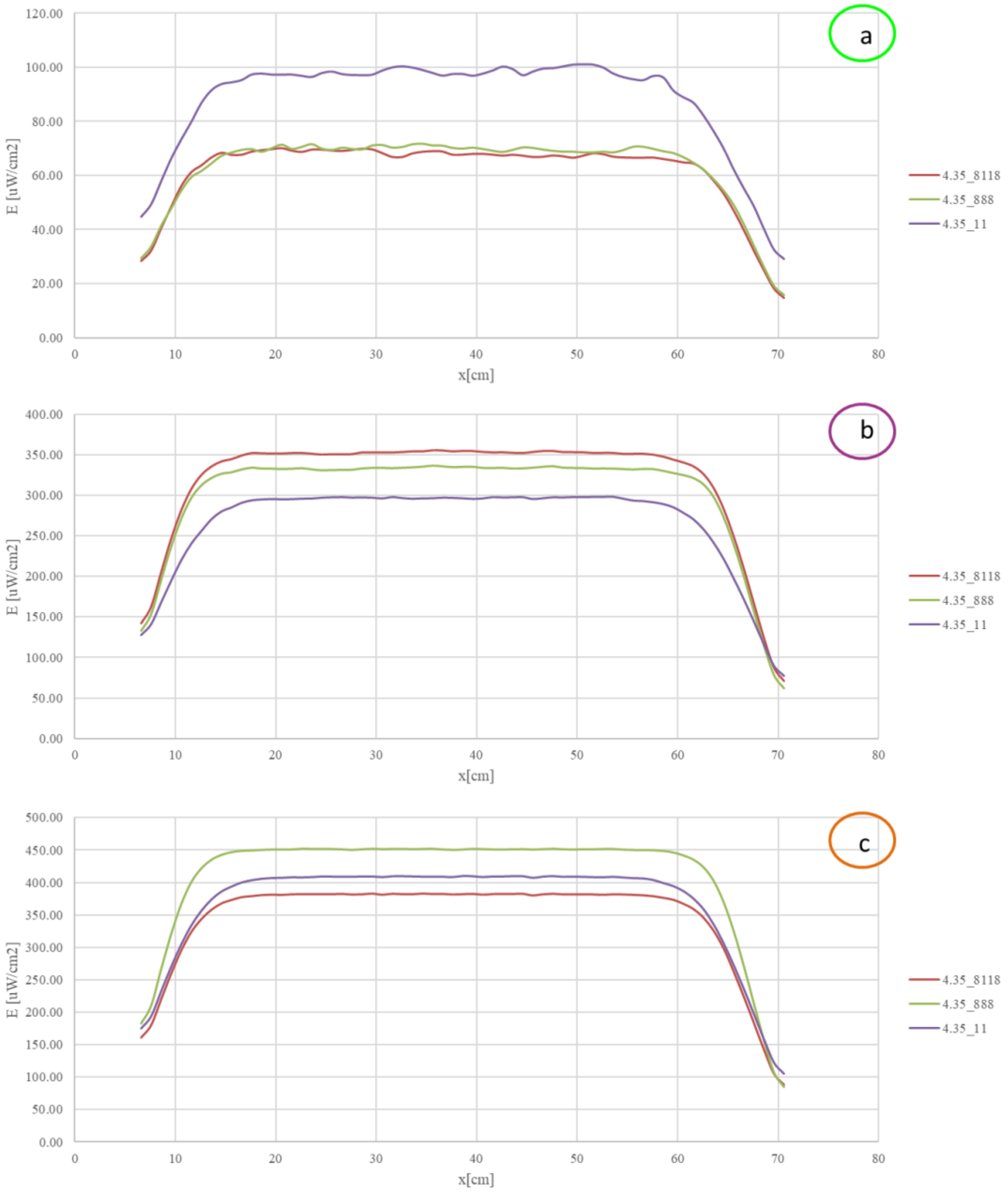

Figure 97: Comparison between the power density profile along the x-axis on the target surface from the 3 three lamps lit at the same time for different lamp installation spaced of 4.35 cm: a) trend corresponding to the ordinate "a" in Figure 93 with max error between the configurations 4_11 and 4_8118 of 52% at the center and 98% laterally and between the configurations 4_11 and 4_888 of 47% at the center and 83% laterally, b) trend corresponding to the ordinate "a" in Figure 93 with max error between the configuration 4_8118 and 4_11 of 20% at the center and 28% laterally and between the configurations 4_8118 and 4_888 of 6% at the center and 15% laterally, c) trend corresponding to the ordinate "a" in Figure 93 with max error between the configuration 4_888 and 4_8118 of 19% at the center and 24% laterally and between the configurations 4_888 and 4_11 of 11% at the center and 21% laterally.

The graphs presented in the figure serve to extend and consolidate the observations derived from previous analyses. In particular, they confirm a behaviour already identified during the study of the vertical displacement Δy: increasing the separation leads to an enhancement of irradiance in the peripheral regions of the target surface, accompanied by a slight reduction in intensity at the center. Conversely, decreasing the distance between the bars strengthens central illuminance at the expense of peripheral coverage.

A similar behavior is observed in the graphs related to the variation of the source-target distance. By longitudinally shifting the LED lamps, i.e., modifying their distance from the filtering plane (from 8 cm to 11 cm), a comparable effect to that of vertical displacement is observed: increasing the distance results in a wider angular spread of the beam and improved irradiance in peripheral zones, whereas reducing the distance intensifies the central contribution.

The error parameters shown in the graphs refer to the curve with the highest intensity, while the colour of the frame highlights which of the lower-intensity curves is being compared to the reference. Visually, a clear improvement in irradiated power density in the peripheral zones is evident for configurations in which all bars are positioned 11 cm from the filtering plane (configurations 4_11 and 4.35_11).

The error analysis reveals that, although reducing the distance between the bars yields a greater contribution in terms of central intensity, this increase is not comparable to the improvement achieved in the peripheral zones, which are particularly critical in terms of germicidal effectiveness.

Finally, having confirmed the superiority of the configuration in which all bars are placed at 11 cm compared to both the configuration with all bars at 8 cm and the initially hypothesized arrangement (8-11-8), a comparison was conducted between the two variants with different Δy values. In this context, contrary to the previous case, the configuration with Δy equal to 4 cm exhibits more favourable behaviour, suggesting that the source-target distance may alter the optimal conditions associated with vertical displacement.

6.2 Geometric Optimization of the Irradiation System

The analysis conducted on the spatial configurations of the LED sources has demonstrated that even minor variations in the vertical and longitudinal positioning of the bars significantly affect the distribution of UV-C irradiance. Specifically, it was observed that increasing the vertical distance of the lateral sources relative to the central one enhances illuminance in peripheral zones, whereas decreasing this distance intensifies the central contribution. Similarly, varying the distance between the sources and the target surface revealed that a greater separation improves peripheral coverage, while a shorter distance concentrates irradiance at the center.

These findings underscore the necessity of intervening not only in the arrangement of the sources but also in the internal geometry of the system, with the aim of improving the directionality of the UV-C beam and optimizing germicidal effectiveness across the entire target surface. To this end, a parallel investigation was initiated focusing on the shape of the internal walls of the device, with particular attention to the upper and lower surfaces that define the optical chamber.

The initial hypothesis posits that a suitably designed curvature may contribute to beam collimation, channelling the rays toward central and peripheral zones in a more controlled manner. To test this hypothesis, preliminary trials were conducted on configurations with concave and convex surfaces, evaluating their impact on irradiance distribution. The objective is to determine whether such geometric modifications can produce a sharper local peak or a more homogeneous radiation spread, thereby enhancing the overall performance of the system.

The first modification introduced to the internal geometry of the system concerned the curvature of the walls surrounding the frame of the filtering surface. In the initial phase, the horizontal walls were modified to be convex, followed by the application of the same transformation to the vertical walls. The goal was to identify which of the two geometric components contributes more significantly to the irradiance distribution, particularly in the peripheral zones of the target surface.

This design choice stems from the hypothesis that a well-defined curvature may facilitate UV-C beam collimation, improving ray directionality and enhancing the germicidal effectiveness of the system. The two configurations were analyzed separately to isolate the contribution of each geometric element and assess their impact on irradiated power density.

Figure 98 presents the two new configurations, corresponding respectively to the curvature of the horizontal walls and that of the vertical walls, used for numerical and experimental analysis.

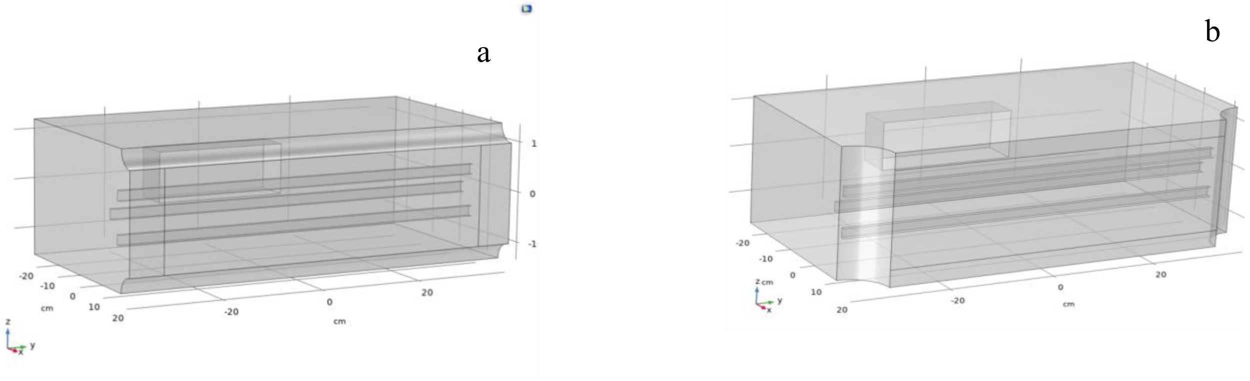

Figure 98: Sections of the new geometric configurations of the device: a) Configuration with convex latero-horizontal walls, b) Configuration with convex latero-vertical walls.

To ensure the comparability of results, the simulations were conducted while maintaining a constant installation configuration for the LED sources; specifically, the upper bar was positioned with a vertical displacement of $\Delta y = 4$ cm, and the lower bar with $\Delta y = 4.35$ cm. This configuration, previously adopted as a reference in earlier analyses, provided a consistent basis for evaluating the effects of the introduced geometric modifications.

Figure 99 presents the comparative graphs related to irradiated power intensity. These comparisons highlight the differences between the new geometries and the baseline configuration, allowing for an assessment of the effectiveness of the proposed modifications in terms of irradiance distribution and improvement of peripheral coverage. For clarity, the following nomenclature is defined: *geom 1* refers to the baseline configuration, *geom 2* to the configuration in which the lateral vertical walls are convex, and *geom 3* to the configuration in which the lateral horizontal walls are compressed. This terminology will be systematically employed in subsequent analyses to facilitate comparison among the various geometric configurations.

.

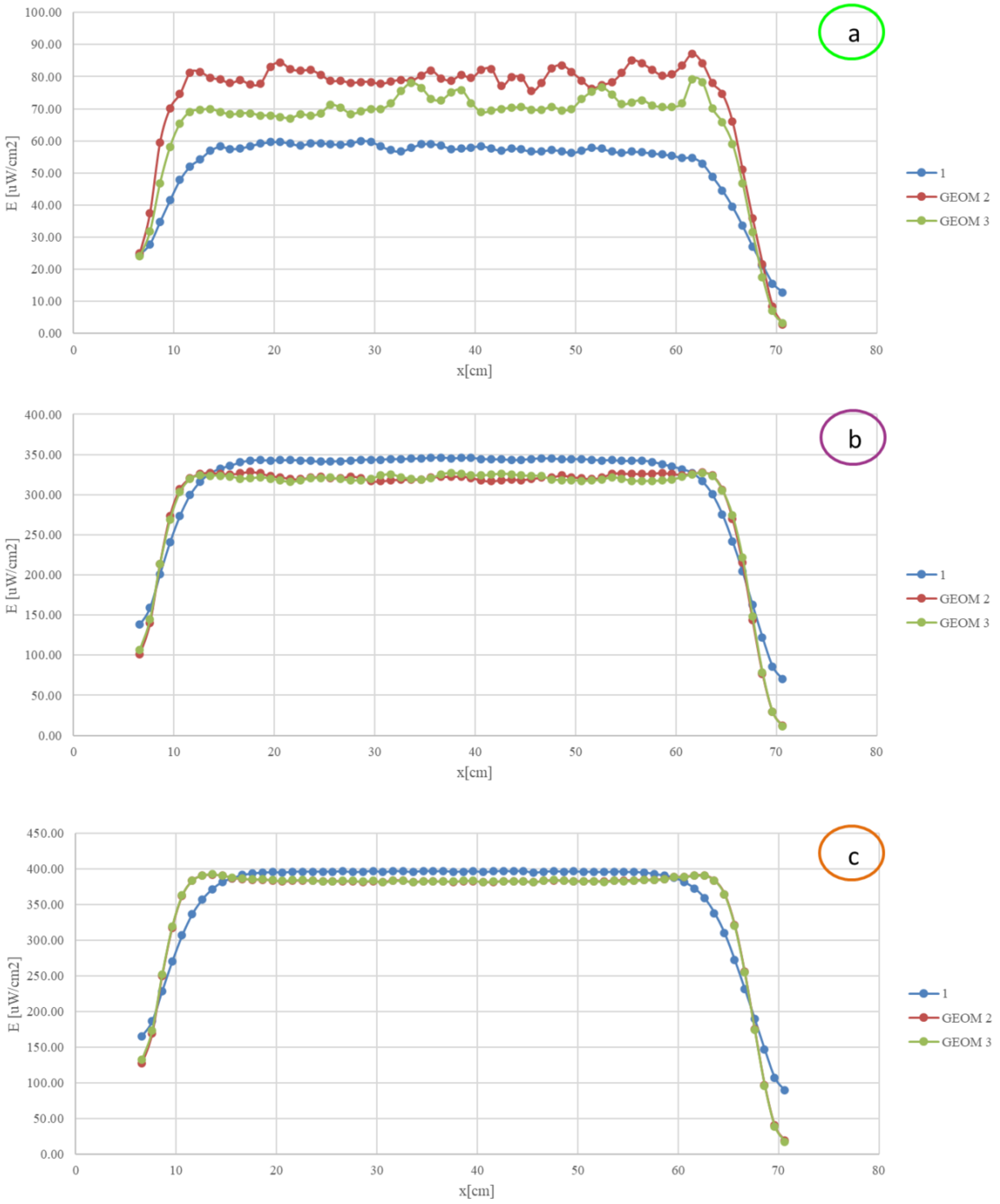

Figure 99: Comparison between the power density profile along the x-axis on the target surface from the 3 three lamps lit for the configurations shown in figure 97: a) trend corresponding to the ordinate "a" in Figure 93 with max error between the configurations GEOM_2 and 1 of 50% at the center and 68% laterally and between the configurations GEOM_2 and GEOM_3 of 18% at the center and 45% laterally, b) trend corresponding to the ordinate "a" in Figure 93 with max error between the configuration 1 and GEOM_3 of 5% at the center and 9% laterally and between the configurations 1 and GEOM_2 of 4% at the center and 9% laterally, c) trend corresponding to the ordinate "a" in Figure 93 with max error between the configuration 1 and GEOM_4 of 3% at the center and 4% laterally and between the configurations 1 and GEOM_2 of 3% at the center and 4% laterally.

The analysis of the graphs corresponding to the three reference planes reveals that, in the central and intermediate zones (represented respectively by graphs b and c), the introduced geometric variations do not yield a significant contribution. Specifically, the central region, already characterized by high irradiance intensity, does not exhibit appreciable sensitivity to the effects of the internal geometric modifications. This suggests that, in these regions, the beam distribution is primarily governed by the position and orientation of the LED sources rather than by the shape of the optical chamber walls.

A different behavior is observed in the peripheral zone, where the system demonstrates greater sensitivity to geometric variations. Notably, the configuration featuring convex lateral vertical walls (*geom 2*) exhibits a more pronounced contribution compared to both the baseline configuration (*geom 1*) and the one with compressed lateral horizontal walls (*geom 3*). This result motivated a deeper investigation into the effect of lateral horizontal curvature, hypothesizing that a convex shape could further enhance beam collimation toward the peripheral regions.

Following these observations, a new comparison was introduced involving three geometric configurations: one with convex lateral vertical walls, one with concave lateral vertical walls, and one with ramp-shaped lateral vertical walls. The objective was to evaluate which of these solutions could provide the most significant improvement in irradiance distribution, particularly in peripheral areas where germicidal effectiveness is most critical.

Figure 100 presents the geometric configurations used for this comparison, along with the corresponding graphs of irradiated power density at the three predefined planes. These results enable a comparative analysis of the effects of different geometries on UV-C beam distribution and guide design decisions toward more effective solutions.

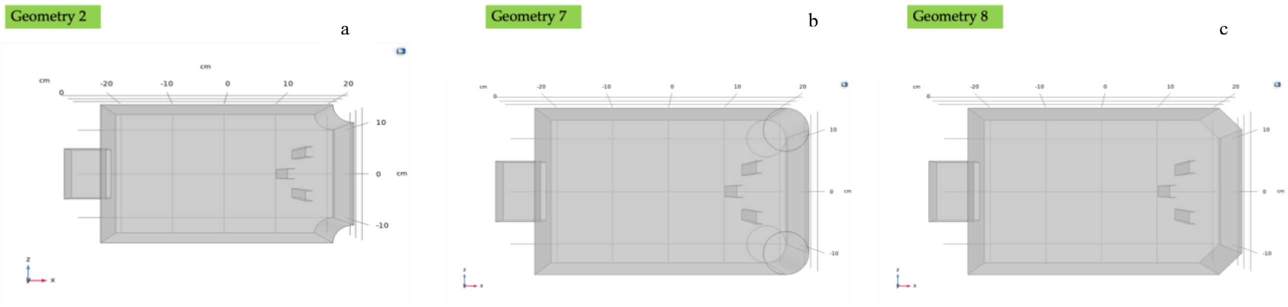

Figure 100: Cross-sectional view of the three geometric configurations: a) convex lateral vertical walls, b) concave lateral vertical walls, c) ramp-shaped lateral vertical walls.

In the analysis of irradiated power density trends, the following nomenclature was adopted: *geom 7* refers to the configuration in which the lateral horizontal walls are convex, while *geom 8* denotes the geometry in which the same walls are shaped as ramps.

The final comparison will be conducted among the three geometric configurations just described (*geom 7*, *geom 8*, and the ramp-shaped lateral vertical wall geometry), also including data from the initial configuration, consistently referred to as *geom 1*. This comparison will enable a systematic evaluation of the effectiveness of the proposed geometric solutions.

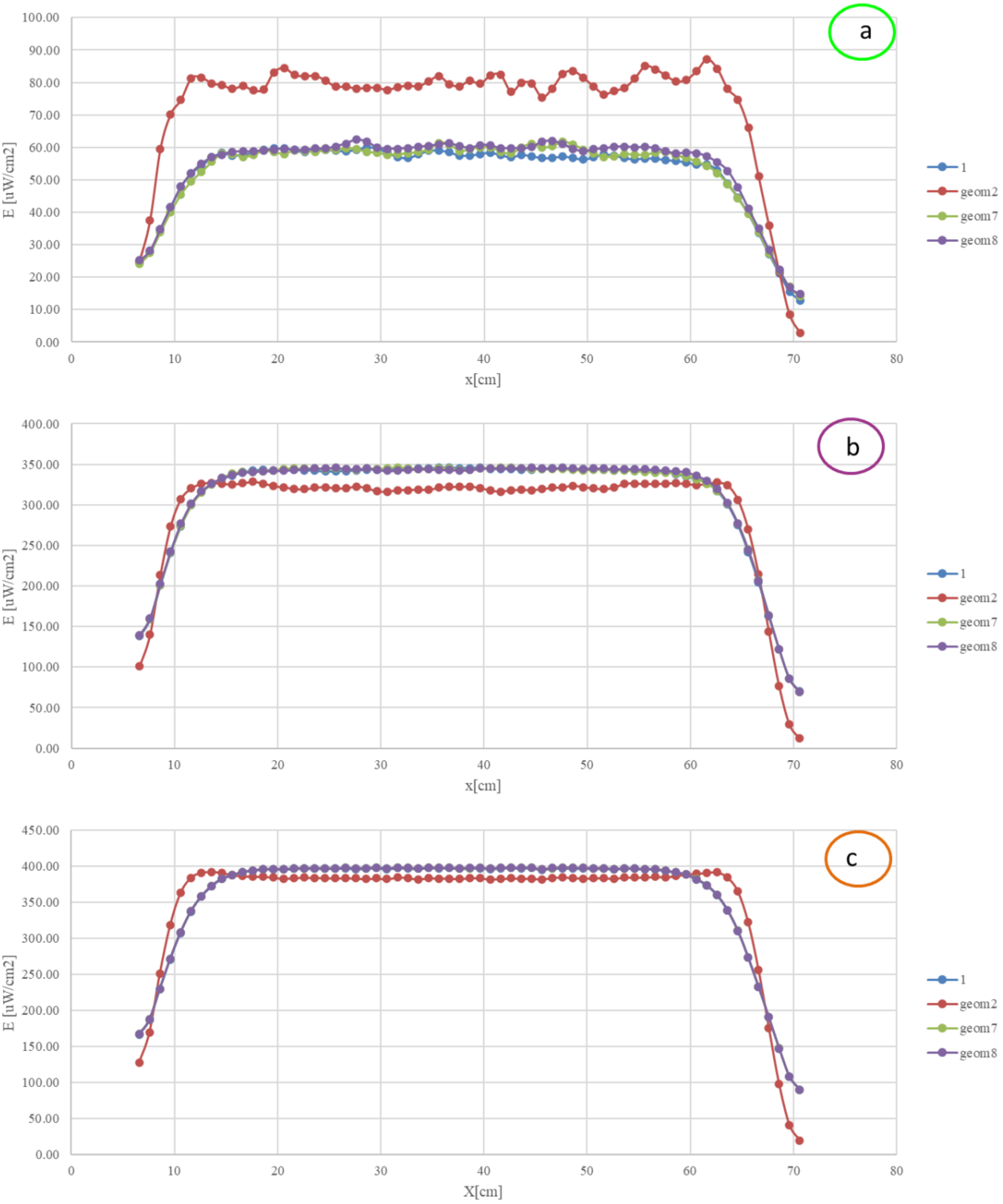

Figure 101: Comparison between the power density profile along the x-axis on the target surface from the 3 three lamps lit for the configurations shown in figure 99: a) trend corresponding to the ordinate "a" in Figure 93 with max error between the configurations geom2 and 1 of 46% at the center, between geom2 and geom7 of 43% at the center and between geom2 and geom8 of 39% at the center, b) trend corresponding to the ordinate "a" in Figure 93 with max error between the configuration geom8 and geom2 of 9% at the center, between geom7 and geom2 of 9% at the center and between 1 and geom2 of 9% at the center, c) trend corresponding to the ordinate "a" in Figure 93 with max error between the geom7 and geom2 of 4% at the center, between geom8 and geom2 of 4% at the center and between 1 anf geom2 of 4% at the center.

The analysis of the graphs corresponding to the three reference planes reveals a behavior consistent with that observed in previous geometric configurations. Specifically, in the central and intermediate zones (graphs b and c), modifications to the internal geometry do not result in significant variations in UV-C illuminance. The central region, already characterized by high irradiance intensity, appears largely insensitive to changes in wall shape, confirming that geometric effects manifest primarily in peripheral areas.

It is precisely in the peripheral zone (graph a) that the most relevant differences emerge. In this case, the configurations with ramp-shaped and convex lateral vertical walls do not exhibit appreciable improvements compared to the baseline geometry (*geom 1*). In contrast, the configuration with concave walls demonstrates a significant contribution, with increased irradiance in the marginal areas of the target surface. This result is particularly relevant, as peripheral zones represent the most critical areas in terms of germicidal effectiveness.

From this analysis, it can be concluded that among the geometries considered, the concave configuration most effectively optimizes illuminance in the peripheral zone, outperforming the convex, ramp-shaped, and baseline geometries. Figure 103 presents the comparative graphs of irradiated power density for the three analyzed geometric configurations, along with the data from the baseline configuration (*geom 1*), used as a reference.

To conclude the geometric optimization process, a final series of analyses was conducted focusing on the progressive introduction of concave surfaces into the frame surrounding the filtering surface. The upper and lower walls were shaped to extend from the filter plane and terminate at various heights, taking into account the positions of the three LED bars. The objective was to assess whether a more targeted curvature could further improve UV-C beam collimation, particularly in peripheral zones where germicidal effectiveness is most critical.

The concave configurations analyzed, shown in Figure 102, include:

- a curvature with a radius equal to the height of the frame (*geom 2*)
- a curvature reaching the height of the upper and lower LED bars (*geom 4*)
- a curvature terminating halfway between the central bar and the upper/lower pair (*geom 5*)
- a curvature extending to the position of the central bar (*geom 6*)

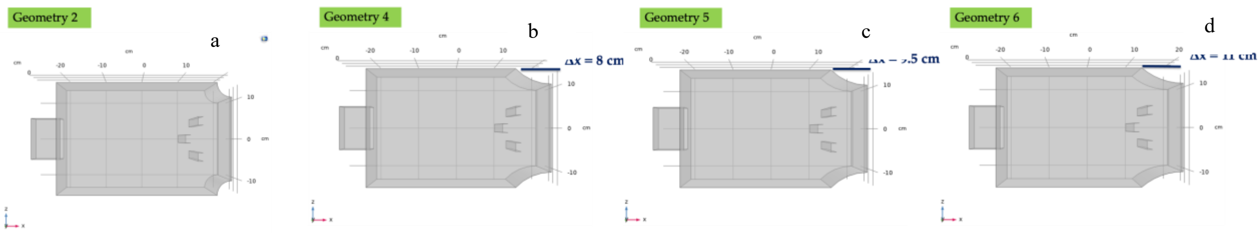

Figure 102: Comparison between four concave configurations with curvatures extending respectively to the frame height (a), the external LED bar height (b), halfway between the central and upper/lower bars (c), and to the central LED bar (d).

The comparative graphs will be generated for the four proposed concave configurations and the baseline configuration, in order to systematically evaluate the effect of the different geometries on the distribution of UV-C irradiance.

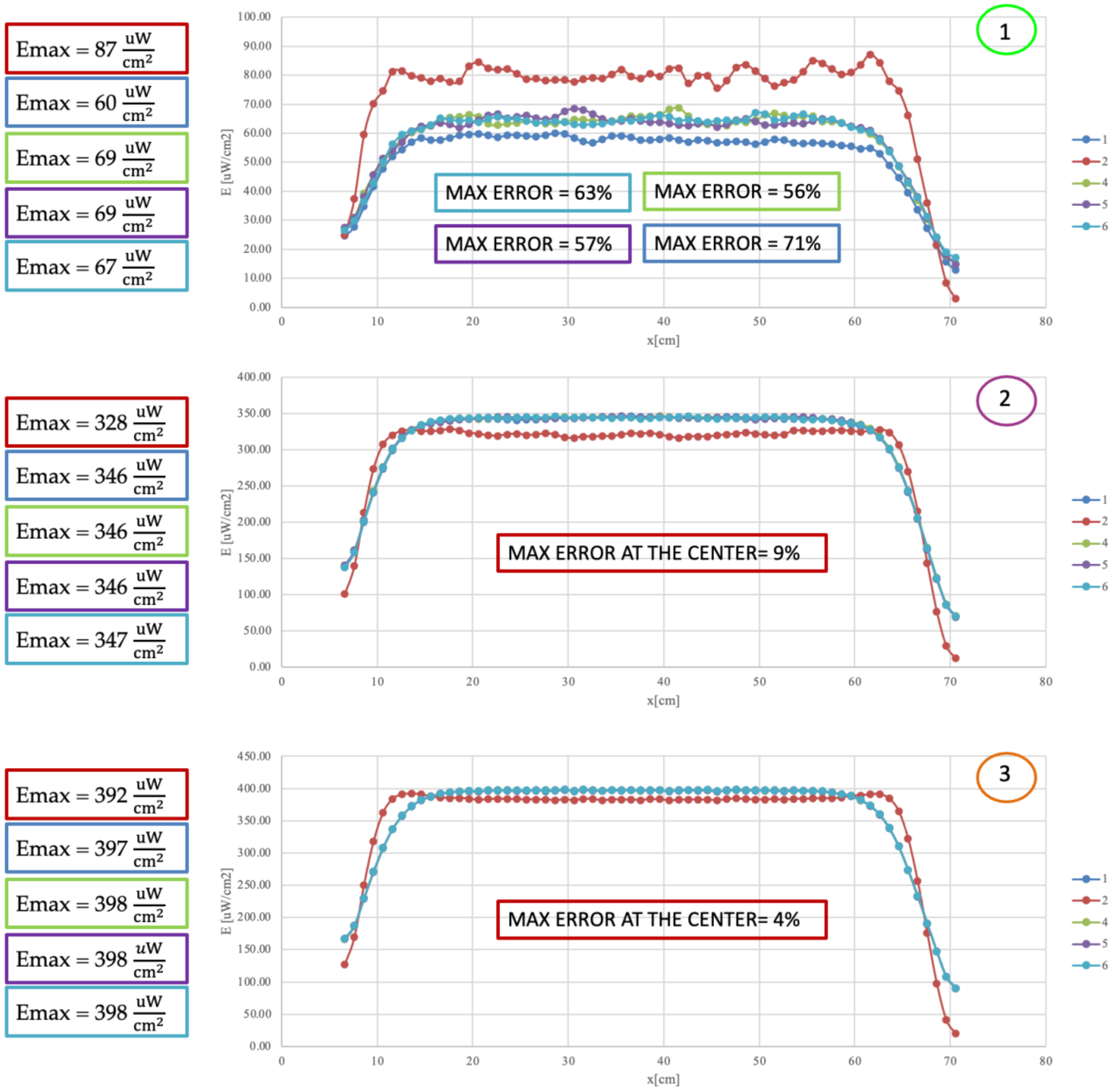

Figure 103: Comparison between the power density profile along the x-axis on the target surface from the 3 three lamps lit for the configurations shown in figure 101: a) trend corresponding to the ordinate "a" in Figure 93 with max error between the configurations 2 and 1 of 71% at the center, between 2 and 6 of 63% at the center, between 2 and 5 of 57% at the center and between 2 and 4 of 56% at the center, b) trend corresponding to the ordinate "a" in Figure 93 with max error between the configurations 1 and 2 of 9% at the center, between 4 and 2 of 9% at the center, between 5 and 2 of 9% at the center and between 6 and 2 of 9% at the center, c) trend corresponding to the ordinate "a" in Figure 93 with max error between the configurations 1 and 2 of 4% at the center, between 4 and 2 of 4% at the center, between 5 and 2 of 4% at the center and between 6 and 2 of 4% at the center.

The analysis of the graphs corresponding to the three reference planes shows that configurations *geom 4*, *geom 5*, and *geom 6* exhibit trends that are nearly identical to those of the baseline configuration (*geom 1*) in the central and intermediate zones, represented respectively by graphs 3 and 2. This behavior indicates that, in these regions, the geometric modifications introduced do not significantly affect irradiance intensity, resulting in only slight improvements over *geom 2*.

In contrast, in the peripheral zone (graph a), there is an increase in illuminance compared to the baseline configuration; however, this rise remains lower than that achieved with *geom 2*. The error analysis related to the maximum irradiance values confirms that *geom 2* is still the most effective setup for optimizing illuminance, especially in peripheral areas where germicidal effectiveness is most important.

The entire analytical process has shown that the distribution of UV-C irradiance is heavily affected by both the spatial arrangement of the sources and the internal shape of the device. In particular, the symmetrization of the LED bars, both vertically and along their length with respect to the normal to the sources, was a crucial step in creating a stable and consistent foundation for later optical assessments. The combined effect of vertical displacement and source-target distance allowed for the identification of a configuration that balances central intensity with peripheral coverage.

Building on this foundation, modifications were made to the internal wall geometry, exploring various solutions such as convex, concave, and ramp-shaped forms to enhance the UV-C system's beam collimation. The analysis indicated that, although geometric changes have little effect on the central and intermediate zones, the concave shape is the most effective at increasing illuminance in peripheral areas, outperforming other configurations and the baseline design.

This thorough comparison has identified an optimized geometric solution that can serve as a reference for future design and experimental validation phases.

Conclusions

The research in this thesis has developed within a scientific field that, in recent years, has become increasingly important: the disinfection of indoor air using non-drug-based technologies, especially UV-C radiation. Interest in these solutions has grown due to global events like the SARS-CoV-2 pandemic, which underscored the need for effective, safe, and easily integrated disinfection systems within existing infrastructures.

The work was divided into several phases, each helping to build a knowledge base and operational framework useful for designing UV-C devices. In the initial phase, a detailed review of scientific literature was carried out to understand how microbial inactivation occurs through ultraviolet radiation, focusing specifically on the UV-C range (100–280 nm), known for its germicidal properties. This analysis helped identify the most effective wavelengths, inactivation kinetics models, and environmental factors that affect treatment effectiveness.

Subsequently, an experimental phase was initiated in collaboration with industrial partners, resulting in the development of a prototype device equipped with UV-C LED sources. Irradiance measurements were performed using high-precision photometric sensors placed at the filtering surface to map the distribution of irradiated power density. This phase involved establishing a strict measurement protocol, calibrating instruments, and controlling environmental factors such as temperature, humidity, and internal reflections.

Meanwhile, a three-dimensional numerical model was created using the Ray Optics module of COMSOL Multiphysics to simulate the system's optical behavior. To input data into the model, it was necessary to reconstruct the emission solid of the LED sources based on experimental data collected from individual modules. This reconstruction involved coordinate transformations, angular analysis of luminous intensity, and defining parametric functions that could approximate the emission profile. Several models (Gaussian, polynomial, Lambertian) were tested and compared for descriptive accuracy and consistency with measured data.

Once the numerical model was validated, simulations were performed on various geometric configurations of the device, changing the position of the sources, the distance from the filtering plane, and the shape of the internal walls. In particular, the impact of concave, convex, and ramp-shaped surfaces was examined, showing that internal geometry can greatly influence irradiance distribution, especially in peripheral areas. Simulations indicated that, in some configurations, peripheral illumination could be enhanced without reducing central intensity.

However, it is important to stress that the results obtained, while promising, should be interpreted carefully. The lack of a detailed CAD model required manual reconstruction of the geometry, which may have introduced approximations. Additionally, the experimental measurements, though carefully performed, showed some variability, especially in low-intensity conditions where the signal is more vulnerable to noise and uncontrolled reflections. The behavior of reflective materials, modeled in a simplified way, may also have contributed to differences between simulation and actual results.

Considering these points, the work is seen as a helpful but not final contribution to designing UV-C systems. Several future paths can be suggested to improve and broaden the research.

a) Enhancing experimental measurement quality by using more advanced acquisition systems that automatically collect data with higher precision. This helps minimize manual errors and yields a more accurate depiction of irradiance distribution.

b) Refining simulation models to make them more representative of real operating conditions, including complex optical phenomena such as irregular reflections and radiation dispersion. The integration of air physical parameters (variations in refractive index as a function of temperature, pressure, and humidity) and the effects of fluid-dynamic and thermodynamic processes on radiant energy distribution is also foreseen, in order to achieve numerical predictions that are more reliable and consistent with the system's actual behavior.

c) Exploring more flexible geometric solutions, such as devices with movable or adjustable components that can adapt to various operating conditions and enhance light distribution in real time.

d) Evaluate the effect of irradiance distribution on the effective dose and on microbiological inactivation under real operating conditions.

e) Expanding the numerical model to include aspects related to material heating and mechanical response will enable assessment not only of germicidal effectiveness but also of the system's durability and long-term sustainability.

These directions not only continue the work already done but also offer a chance to make UV-C technologies more advanced, dependable, and ready for real-world use in places like hospitals, schools, public transportation, and industrial sites.

In summary, the research conducted has helped develop advanced skills in optical modeling, photometric testing, and the geometric design of UV-C systems. Carefully executed, this work is believed to lay not only a strong foundation for future innovations in environmental disinfection, aiding in the development of safer, healthier, and more technologically advanced indoor environments, but also useful support for the prelamination design of UV-C devices devoted to air sanification.

Alongside the main research presented in this thesis, a supplementary study is currently in progress to analyze and compare the performance of low-pressure mercury vapor lamps, a well-established and historically important technology for producing UV-C radiation. This study arises from the need to systematically compare mercury-based radiative sources with solid-state UV-C LEDs, focusing on metrics such as radiometric efficiency, spectral stability, and long-term operational reliability. The ultimate aim is to develop objective criteria for their best use in air and surface disinfection systems.

Mercury vapor lamps generate light through an electric discharge in a low-pressure mercury vapor environment, producing a specific emission spectrum dominated by the 253.7 nm line, which explains their renowned germicidal effectiveness. The current study includes quantitative irradiance measurements, spectral power distribution (SPD) analysis, and the evaluation of radiant flux reduction over time to assess the devices' photometric performance, thermal stability, and effective lifespan under controlled operating conditions.

Particular attention is given to the relationships among electrical input parameters, thermal equilibrium, and radiative output, as these factors significantly influence the stability and uniformity of the emitted UV-C flux. The research also examines how lamp geometry, fill gas composition, and envelope materials, especially synthetic quartz, affect ultraviolet transmittance, internal reflection phenomena, and resistance to photochemical degradation.

The comparative framework established by this study will enable the development of benchmark models for germicidal performance and energy efficiency of mercury vapor lamps versus UV-C LED systems. While the latter offer benefits such as compactness, modular design, and environmental safety because they do not contain mercury, traditional mercury vapor lamps still demonstrate higher radiant output, consistent spectral properties, and advantageous cost-to-performance ratios. This makes them suitable for applications requiring high irradiance and wide-area coverage.

From an applicative perspective, the ongoing work aims to enhance the integration of mercury vapor lamps into Heating, Ventilation, and Air Conditioning (HVAC) systems and Air Handling Units (AHUs) by developing multiphysics models that describe the combined optical, thermal, and fluid-dynamic behaviors of these systems. The goal is to find a rational balance between disinfection effectiveness and energy efficiency, supporting the design of next-generation hybrid UV-C systems (mercury-based and LED-based) with improved performance and reduced environmental impact.

This parallel research project should not be seen as an ancillary activity, but rather as a natural and coherent extension of the scientific path established by this dissertation. It reinforces the main goal of developing innovative, reliable, and sustainable technologies for indoor air and surface disinfection, ultimately helping to create safer, healthier, and more technologically advanced built environments.

References

1. Subri, M.S.M.; Yahya, E.; Mohd Yunus, N.A.; Daar, M.; Abu Hassan, F.A. *The Parameter of the Sick Building Syndrome: A Systematic Literature Review. Heliyon* **2024**, *10*(12), e32431. https://doi.org/10.1016/j.heliyon.2024.e32431
2. Aziz, N.; Abdul Shukor, S.F.; Hassan, N. *Indoor Air Quality (IAQ) and Related Risk Factors for Sick Building Syndrome (SBS) at the Office and Home: A Systematic Review. [Journal information pending]* **2023**.
3. Tran, V.V.; Park, D.; Lee, Y.-C. *Indoor air pollution, related human diseases, and recent trends in the control and improvement of indoor air quality. Int. J. Environ. Res. Public Health* **2020**, *17*(8), 2927. https://doi.org/10.3390/ijerph17082927
4. Chatkin, J.M.; Correa, L.; Santos, U.P. *External environmental pollution as a risk factor for asthma. Clin. Rev. Allergy Immunol.* **2021**, *62*(3), 375–389. https://doi.org/10.1007/s12016-021-08856-2
5. Kim, K.-H.; Kabir, E.; Kabir, S. *A review on the human health impact of airborne particulate matter. Environ. Int.* **2015**, *74*, 136–143. https://doi.org/10.1016/j.envint.2014.10.005
6. Collins, D.B.; Farmer, D.K. *Unintended consequences of air cleaning chemistry. Environ. Sci. Technol.* **2021**, *55*(19), 12276–12284. https://doi.org/10.1021/acs.est.1c02582
7. Hodgson, A.T.; Destaillats, H.; Sullivan, D.P.; Fisk, W.J. *Performance of ultraviolet germicidal irradiation and filtration for air cleaning in an office environment. Indoor Air* **2007**, *17*(4), 305–317. https://doi.org/10.1111/j.1600-0668.2007.00477.x
8. Van Durme, J.; Dewulf, J.; Sysmans, W.; Leys, C.; Van Langenhove, H. *Abatement and degradation pathways of toluene in indoor air by positive corona discharge. Chemosphere* **2007**, *68*(10), 1821–1829. https://doi.org/10.1016/j.chemosphere.2007.02.007
9. Xu, T.; Peccia, J.; Hernandez, M.; Miller, S.L. *Effects of UVGI on airborne bacteria in full-scale ventilation systems. Appl. Environ. Microbiol.* **2002**, *68*, 340–345.
10. Xu, T. *Upper-room UVGI effectiveness in indoor air disinfection. Environ. Eng. Policy* **2001**, *3*, 101–107.
11. Zhao, B.; Liu, Y.; Chen, C. *Air purifiers: A supplementary measure to remove airborne SARS-CoV-2. Build. Environ.* **2020**, *177*, 106918.
12. Bolashikov, Z.D.; Melikov, A.K. *Methods for air cleaning and protection of building occupants from airborne pathogens. Build. Environ.* **2009**, *44*(7), 1441–1448.
13. Van Boeckel, T.P.; Brower, C.; Gilbert, M.; Grenfell, B.T.; Levin, S.A.; Robinson, T.P.; Teillant, A.; Laxminarayan, R. *Global trends in antimicrobial use in food animals. Proc. Natl. Acad. Sci. USA* **2015**, *112*(18), 5649–5654. https://doi.org/10.1073/pnas.1503141112
14. Silva, M.R.F.; Alves, M.F.R.P.; Cunha, J.P.G.Q.; Costa, J.L.; Silva, C.A.; Fernandes, M.H.V.; Vilarinho, P.M.; Ferreira, P. *Nanostructured transparent solutions for UV-shielding: Recent developments and future challenges. Mater. Today Phys.* **2023**, *29*, 101131. https://doi.org/10.1016/j.mtphys.2023.101131
15. Sinha, R.P.; Häder, D.-P. *UV-induced DNA damage and repair: A review. Photochem. Photobiol. Sci.* **2002**, *1*(4), 225–236. https://doi.org/10.1039/B201230H
16. Von Sonntag, C. *Mechanisms of DNA damage induced by UV radiation. Photochem. Photobiol.* **2004**, *80*(3), 183–190. https://doi.org/10.1562/0031-86552004.080<0183:MODDIU>2.0.CO;2
17. Bolton, J.R.; Cotton, C.A. *The Ultraviolet Disinfection Handbook. Am. Water Works Assoc.* **2008**.
18. Hijnen, W.A.M.; Beerendonk, E.F.; Medema, G.J. *Inactivation credit of UV radiation for viruses, bacteria and protozoan (Oo)cysts in water: A review. Water Res.* **2006**, *40*(1), 3–22. https://doi.org/10.1016/j.watres.2005.10.030
19. Oguma, K. *Inactivation of viruses and bacteria by ultraviolet light-emitting diodes (UV-LEDs). Water Sci. Technol. Water Supply* **2016**, *16*(3), 877–883. https://doi.org/10.2166/ws.2015.188
20. Kim, D.-K. *Inactivation of bacterial endospores and viruses by UV-LED irradiation. Appl. Environ. Microbiol.* **2017**, *83*(5), e02486–16. https://doi.org/10.1128/AEM.02486-16
21. Song, K.; Mohseni, M.; Taghipour, F. *Application of ultraviolet light-emitting diodes (UV-LEDs) for water disinfection: A review. Water Res.* **2016**, *94*, 341–349. https://doi.org/10.1016/j.watres.2016.02.068
22. Knudson, G.B. *Photoreactivation of UV-inactivated bacteria and viruses. Microbiol. Rev.* **1985**, *49*(4), 436–451. https://doi.org/10.1128/mr.49.4.436-451.1985
23. **23.** Sommer, R. *Inactivation of microorganisms in water by ultraviolet light: Comparison of disinfection by low and medium pressure mercury lamps. Water Res.* **1998**, *32*(8), 2633–2640. https://doi.org/10.1016/S0043-1354(98)00042-5
24. Mamane-Gravetz, H.; Linden, K.G. *Impact of particle aggregation on UV disinfection of viruses. Appl. Environ. Microbiol.* **2005**, *71*(12), 7581–7588. https://doi.org/10.1128/AEM.71.12.7581-7588.2005
25. Beck, S.E.; Ryu, H.; Boczek, L.A.; Cashdollar, J.L.; Jeanis, K.M.; Rosenblum, J.S.; Lawal, O.; Linden, K.G. *Evaluating UV-C LED disinfection performance and energy efficiency for water treatment. Appl. Environ. Microbiol.* **2016**, *82*, 1813–1820.
26. Sun, W.; Li, X.; Ma, Q.; Zhang, L.; Li, Y.; Shi, H. *Inactivation efficiencies, action spectra, and mechanisms of UV-LEDs for microbial disinfection. Environ. Sci. Technol.* **2023**, *57*, 4211–4220.

27. Buonanno, M.; Welch, D.; Shuryak, I.; Brenner, D.J. *Far-UVC light (222 nm) efficiently and safely inactivates airborne human coronaviruses. Sci. Rep.* **2020**, *10*, 10285.
28. Green, B.J.; McCarthy, L.; Kearney, A.; Lyon, G.; Graham, T.; Kearns, A.; Staffa, S.; Schaberg, D.; Carney, D.; Smith, C. *Inactivation of the multi-drug-resistant pathogen Candida auris by ultraviolet C (UVC) light. Emerg. Infect. Dis.* **2020**, *26*, 811–813.
29. Dai, T.; Vrahas, M.S.; Murray, C.K.; Hamblin, M.R. *Ultraviolet C irradiation: An alternative antimicrobial approach to control emerging viral and bacterial infections. Future Microbiol.* **2012**, *7*, 495–507.
30. Smith, A.B.; Johnson, C.D. *Ultraviolet (UV) radiation technology for water purification: Applications and advancements. J. Environ. Eng.* **2024**, *150*(4), 04024012. https://doi.org/10.1061/(ASCE)EE.1943-7870.0001745
31. Zhang, Y.; Li, X.; Wang, Z. *Low-pressure mercury vapor lamps for disinfection: Mechanisms and applications. J. Environ. Manag.* **2025**, *300*, 113629. https://doi.org/10.1016/j.jenvman.2021.113629
32. Patel, J. *Improved method for UV lamps irradiance measurement. J. Environ. Eng.* **2025**, *151*(5), 04023012. https://doi.org/10.1061/(ASCE)EE.1943-7870.0001745
33. Cattai, M.; D'Orazio, A.; Sbardella, F. *Application of UV-C radiation in HVAC systems: A review of current challenges and standardization needs. Build. Environ.* **2023**, *237*, 110391. https://doi.org/10.1016/j.buildenv.2023.110391
34. World Health Organization (WHO). *Mercury and health: Key facts.* **2023**. https://www.who.int/news-room/fact-sheets/detail/mercury-and-health
35. International Energy Agency (IEA). *Energy efficiency and emerging lighting technologies report.* **2025**.
36. Nunayon, S.S.; Wang, M.; Zhang, H.H.; Lai, A.C. Evaluating the efficacy of a rotating upper-room UVC-LED irradiation device in inactivating aerosolized Escherichia coli under different disinfection ranges, air mixing, and irradiation conditions. *J. Hazard. Mater.* **2022**, *440*, 129791. https://doi.org/10.1016/j.jhazmat.2022.129791.
37. Li, P.; Koziel, J.A.; Macedo, N.; Zimmerman, J.J.; Wrzesinski, D.; Sobotka, E.; Balderas, M.; Walz, W.B.; Paris, R.V.; Lee, M.; et al. Evaluation of an Air Cleaning Device Equipped with Filtration and UV: Comparison of Removal Efficiency on Particulate Matter and Viable Airborne Bacteria in the Inlet and Treated Air. *Int. J. Environ. Res. Public Health* **2022**, *19*, 16135. https://doi.org/10.3390/ijerph192316135.
38. Zhu, S.; Lin, T.; Wang, L.; Nardell, E.A.; Vincent, R.L.; Srebric, J. Ceiling impact on air disinfection performance of Upper-Room Germicidal Ultraviolet (UR-GUV). *Build. Environ.* **2022**, *224*, 109530. https://doi.org/10.1016/j.buildenv.2022.109530.
39. Lai, P.Y.; Liu, H.; Ng, R.J.H.; Wint Hnin Thet, B.; Chu, H.S.; Teo, J.W.R.; Ong, Q.; Liu, Y.; Png, C.E. Investigation of SARS-CoV-2 inactivation using UV-C LEDs in public environments via ray-tracing simulation. *Sci. Rep.* **2021**, *11*, 22612.
40. Biasin, M.; Bianco, A.; Pareschi, G.; Cavalleri, A.; Cavatorta, C.; Fenizia, C.; Galli, P.; Lessio, L.; Lualdi, M.; Tombetti, E.; Ambrosi, A. UV-C irradiation is highly effective in inactivating SARS-CoV-2 replication. *Sci. Rep.* **2021**, *11*, 6260.
41. Blatchley, E.R., 3rd; Dumoutier, N.; Halaby, T.N.; Levi, Y.; Lainè, J.M. Bacterial response to ultraviolet irradiation. *Water Sci. Technol.* **2001**, *43*, 179–186.
42. Miller, D. Theoretical survival curves for radiation damage in bacteria. *J. Theor. Biol.* **1970**, *26*, 383–398. https://doi.org/10.1016/0022-5193(70)90091-3.
43. Kowalski, W.J.; Bahnfleth, W.P.; Witham, D.L.; Severin, B.F.; Whittam, T.S. Mathematical Modeling of Ultraviolet Germicidal Irradiation for Air Disinfection. *Quant. Microbiol.* **2000**, *2*, 249–270. https://doi.org/10.1023/a:1013951313398.
44. Frigerio, F.; Borra, M.; Cottica, D.; Grignani, E.; Militello, A.; Mansi, A.; Tirabasso, A.; Tranfo, G.; Sisto, R. Interim indications for the use of UV germicidal irradiation in the conjuncture of COVID-19 pandemic. *Ital. J. Occup. Environ. Hyg.* **2020**, *11*, 1–51.
45. Liberati, A.; Altman, D.G.; Tetzlaff, J.; Mulrow, C.; Gøtzsche, P.C.; Ioannidis, J.P.A.; Clarke, M.; Devereaux, P.J.; Kleijnen, J.; Moher, D. The PRISMA statement for reporting systematic reviews and meta-analyses of studies that evaluate healthcare interventions: Explanation and elaboration. *BMJ (Clin. Res. Ed.)* **2009**, *339*, b2700.
46. Al-Rawi, M.; Ikutegbe, C.A.; Auckaili, A.; Farid, M.M. Sustainable technologies to improve indoor air quality in a residential house—A case study in Waikato, New Zealand. *Energy Build.* **2021**, *250*, 111283.
47. Al-Rawi, M.; Farid, M.M.; Jones, R.J.; Louie, K. Evaluation of a Polyester Filter and UV Light (PFUV) Dehumidifier to Improve Indoor Environmental Quality: Preliminary Results. *Sustainability* **2022**, *14*, 4504. https://doi.org/10.3390/su14084504.
48. Anderson, D.J.; Gergen, M.F.; Smathers, E.; Sexton, D.J.; Chen, L.F.; Weber, D.J.; Rutala, W.A. Decontamination of Targeted Pathogens from Patient Rooms Using an Automated Ultraviolet-C-Emitting Device. *Infect. Control Hosp. Epidemiol.* **2013**, *34*, 466–471. https://doi.org/10.1086/670215.
49. Arora, A.; Bhardwaj, K.; Esmail, N.; Dubey, P.D. Design, Fabrication, and Testing of a Solar Powered Air Purifier with UV Sterilization Capability. In *Lecture Notes in Mechanical Engineering*; Springer: Singapore, 2023; pp. 261–272.
50. Atci, F.; Cetin, Y.E.; Avci, M.; Aydin, O. Evaluation of in-duct UV-C lamp array on air disinfection: A numerical analysis. *Sci. Technol. Built Environ.* **2021**, *27*, 98–108. https://doi.org/10.1080/23744731.2020.1776549.

51. Baldelli, G.; Aliano, M.P.; Amagliani, G.; Magnani, M.; Brandi, G.; Pennino, C.; Schiavano, G.F. Airborne Microorganism Inactivation by a UV-C LED and Ionizer-Based Continuous Sanitation Air (CSA) System in Train Environments. *Int. J. Environ. Res. Public Health* **2022**, *19*, 1559. https://doi.org/10.3390/ijerph19031559.
52. Bang, J.-I.; Park, J.; Choi, A.; Jeong, J.-W.; Kim, J.Y.; Sung, M. Evaluation of UR-UVGI System for Sterilization Effect on Microorganism Contamination in Negative Pressure Isolation Ward. *Sustainability* **2018**, *10*, 3192. https://doi.org/10.3390/su10093192.
53. Brockmann, G.; Brandt, S.; Kriegel, M. Numerical approach to improve UVC radiation for air disinfection and investigation of the scalability. *E3S Web Conf.* **2023**, *396*, 03002. https://doi.org/10.1051/e3sconf/202339603002.
54. Bui, C.M.; Phan, N.D.M.; Tran, N.Q.H.; Doan, L.A.; Vo, Q.T.; Tran, D.C.; Nguyen, T.T.V.; Nguyen, D.L.; Huynh, V.S.; Ho, T.A.N. Disinfection performance of an ultraviolet lamp: A CFD investigation. *Acta Polytech.* **2022**, *62*, 418–426. https://doi.org/10.14311/ap.2022.62.0418.
55. Capetillo, A.; Noakes, C.J.; Sleigh, P.A.; Khan, A. In-duct uvgi air sterilisation: Optimisation study for high performance energy efficient systems. *Indoor Air 2014—13th Int. Conf. Indoor Air Qual. Clim.* **2014**, 594–599.
56. D'Orazio, A.; D'Alessandro, D. Air bio-contamination control in hospital environment by UV-C rays and HEPA filters in HVAC systems. [Controllo della biocontaminazione dell'aria negli ambienti ospedalieri con l'impiego combinato di raggi UV-C e di filtri HEPA negli impianti di condizionamento]. *Ann. Di Ig. Med. Prev. E Di Comunita* **2020**, *32*, 449–461.
57. Davidson, B.L. Bare-bulb Upper-Room Germicidal Ultraviolet-C (GUV) Indoor Air Disinfection for COVID-19†. *Photochem. Photobiol.* **2021**, *97*, 524–526.
58. De Matteis, L.; Cullinan, M.F.; McGinn, C. Numerical model of the irradiance field surrounding a UV disinfection robot. *Biomed. Phys. Eng. Express* **2022**, *8*, 055025.
59. de Souza, S.O.; Cardoso, A.A., Jr.; Sarmento, A.S.C.; d'Errico, F. Effectiveness of a UVC air disinfection system for the HVAC of an ICU. *Eur. Phys. J. Plus* **2022**, *137*, 37. https://doi.org/10.1140/epjp/s13360-021-02240-y.
60. Feng, Z.; Cao, S.J.; Haghighat, F. Removal of SARS-CoV-2 using UV+Filter in built environment. *Sustain. Cities Soc.* **2021**, *74*, 103226.
61. Firrantello, J.; Bahnfleth, W. Simulation and monetization of collateral airborne infection risk improvements from ultraviolet germicidal irradiation for coil maintenance. *Sci. Technol. Built Environ.* **2018**, *24*, 135–148.
62. Gilkeson, C.A.; Noakes, C.J.; Khan, M.A.I. Computational fluid dynamics modelling and optimisation of an upper-room ultraviolet germicidal irradiation system in a naturally ventilated hospital ward. *Indoor Built Environ.* **2014**, *23*, 449–466. https://doi.org/10.1177/1420326x14532933.
63. Glyva, V.; Nazarenko, V.; Burdeina, N.; Leonov, Y.; Kasatkina, N.; Levchenko, L.; Tykhenko, O.; Krasnianskyi, G.; Petrunok, T.; Biruk, Y. Determining the efficiency of using led sources of ultraviolet radiation for ionization and disinfection of room air. *East.-Eur. J. Enterp. Technol.* **2023**, *3*, 23–29. https://doi.org/10.15587/1729-4061.2023.282784.
64. Hsu, L.-H.; Huang, C.-K. The Application of Cyclone Structure with UVC Equipment on the Analysis of Indoor Air Quality. In Proceedings of the 2022 IEEE International Conference on Consumer Electronics—Taiwan, Taipei, Taiwan, 6–8 July 2022; pp. 555–556.
65. Jones, H.L.; Braly, H.L.; Parsley, B.S.; Gonzalez, J.L.; Ausborn, V.A.; Noble, P.C. Do Ultraviolet Air Disinfection Units Reduce Contamination by Particulates in Total Knee Replacement Procedures? *J. Arthroplast.* **2022**, *37*, S301–S305. https://doi.org/10.1016/j.arth.2022.02.070.
66. Kanaan, M.; Ghaddar, N.; Ghali, K.; Araj, G. Upper room UVGI effectiveness with dispersed pathogens at different droplet sizes in spaces conditioned by chilled ceiling and mixed displacement ventilation system. *Build. Environ.* **2015**, *87*, 117–128. https://doi.org/10.1016/j.buildenv.2015.01.029.
67. Kanaan, M.; Ghaddar, N.; Ghali, K. Localized air-conditioning with upper-room UVGI to reduce airborne bacteria cross-infection. *Build. Simul.* **2016**, *9*, 63–74. https://doi.org/10.1007/s12273-015-0250-7.
68. Kanaan, M. CFD optimization of return air ratio and use of upper room UVGI in combined HVAC and heat recovery system. *Case Stud. Therm. Eng.* **2019**, *15*, 100535. https://doi.org/10.1016/j.csite.2019.100535.
69. Kanaan, M.; Ghaddar, N.; Ghali, K.; Araj, G. New airborne pathogen transport model for upper-room UVGI spaces conditioned by chilled ceiling and mixed displacement ventilation: Enhancing air quality and energy performance. *Energy Convers. Manag.* **2014**, *85*, 50–61. https://doi.org/10.1016/j.enconman.2014.05.073.
70. Kotov, M.A.; Shemyakin, A.N.; Solovyov, N.G.; Yakimov, M.Y. Symmetrization and Amplification of Germicidal Radiation Flux Produced by a Mercury Amalgam UV Lamp in Cylindrical Cavity with Diffusely Reflective Walls. *Symmetry* **2022**, *14*, 125. https://doi.org/10.3390/sym14010125.
71. Kouropoulos, G. The effect of reynolds number of air flow during the air sterilization process with ultraviolet germicidal irradiation lamp. *ASEAN Eng. J.* **2021**, *11*, 1–12. https://doi.org/10.11113/aej.v11.16868.
72. Krishnamoorthy, G.; Tande, B.M. Improving the effectiveness of ultraviolet germicidal irradiation through reflective wall coatings: Experimental and modeling based assessments. *Indoor Built Environ.* **2016**, *25*, 314–328. https://doi.org/10.1177/1420326x14547785.
73. Lee, B.; Bahnfleth, W.P. Effects of installation location on performance and economics of in-duct ultraviolet germicidal irradiation systems for air disinfection. *Build. Environ.* **2013**, *67*, 193–201. https://doi.org/10.1016/j.buildenv.2013.05.019.

74. Lee, L.D.; Delclos, G.; Berkheiser, M.L.; Barakat, M.T.; Jensen, P.A. Evaluation of multiple fixed in-room air cleaners with ultraviolet germicidal irradiation, in high-occupancy areas of selected commercial indoor environments. *J. Occup. Environ. Hyg.* **2022**, *19*, 67–77. https://doi.org/10.1080/15459624.2021.1991581.
75. Liu, J.; Liu, J.; Fan, Y.; Wang, P. Combination of UV radiation with 3D structure media filter for indoor air disinfection. *E3S Web Conf.* **2022**, *356*, 05054. https://doi.org/10.1051/e3sconf/202235605054.
76. Luo, H.; Zhong, L. Development and experimental validation of an improved mathematical irradiance model for in-duct ultraviolet germicidal irradiation (UVGI) applications. *Build. Environ.* **2022**, *226*, 109699. https://doi.org/10.1016/j.buildenv.2022.109699.
77. Luongo, J.C.; Miller, S.L. Ultraviolet germicidal coil cleaning: Decreased surface microbial loading and resuspension of cell clusters. *Build. Environ.* **2016**, *105*, 50–55. https://doi.org/10.1016/j.buildenv.2016.05.024.
78. Luongo, J.C.; Brownstein, J.; Miller, S.L. Ultraviolet germicidal coil cleaning: Impact on heat transfer effectiveness and static pressure drop. *Build. Environ.* **2017**, *112*, 159–165. https://doi.org/10.1016/j.buildenv.2016.11.022.
79. Mariita, R.M.; Davis, J.H.; Lottridge, M.M.; Randive, R.V.; Witting, H.; Yu, J. Towards a Healthy Car: UVC LEDs in an Automobile's HVAC Demonstrates Effective Disinfection of Cabin Air. *Atmosphere* **2022**, *13*, 1926. https://doi.org/10.3390/atmos13111926.
80. Messina, G.; Spataro, G.; Catarsi, L.; De Marco, M.F.; Grasso, A.; Cevenini, G. A mobile device reducing airborne particulate can improve air quality. *AIMS Public Health* **2020**, 7, 469–477.
81. Noakes, C.J.; Khan, M.A.I.; Gilkeson, C.A. Modeling infection risk and energy use of upper-room Ultraviolet Germicidal Irradiation systems in multi-room environments. *Sci. Technol. Built Environ.* **2015**, *21*, 99–111. https://doi.org/10.1080/10789669.2014.983035.
82. Nunayon, S.S.; Zhang, H.H.; Lai, A.C. A novel upper-room UVC-LED irradiation system for disinfection of indoor bioaerosols under different operating and airflow conditions. *J. Hazard. Mater.* **2020**, *396*, 122715. https://doi.org/10.1016/j.jhazmat.2020.122715.
83. Nunayon, S.S.; Zhang, H.; Lai, A.C.K. Comparison of disinfection performance of UVC-LED and conventional upper-room UVGI systems. *Indoor Air* **2020**, *30*, 180–191. https://doi.org/10.1111/ina.12619.
84. Pan, Y.; Xia, T.; Guo, K.; An, Y.; Chen, C. Predicting spatial distribution of ultraviolet irradiance and disinfection of exhaled bioaerosols with a modified irradiance model. *Build. Environ.* **2023**, *228*, 109792. https://doi.org/10.1016/j.buildenv.2022.109792.
85. Pichurov, G.; Srebric, J.; Zhu, S.; Vincent, R.L.; Brickner, P.W.; Rudnick, S.N. A validated numerical investigation of the ceiling fan's role in the upper-room UVGI efficacy. *Build. Environ.* **2015**, *86*, 109–119. https://doi.org/10.1016/j.buildenv.2014.12.021.
86. Qiao, Y.; Yang, M.; Marabella, I.A.; McGee, D.A.; Aboubakr, H.; Goyal, S.; Hogan, C.J., Jr.; Olson, B.A.; Torremorell, M. Greater than 3-Log Reduction in Viable Coronavirus Aerosol Concentration in Ducted Ultraviolet-C (UV–C) Systems. *Environ. Sci. Technol.* **2020**, *55*, 4174–4182. https://doi.org/10.1021/acs.est.0c05763.
87. Randive, R.; Mariita, R.; Davis, J.; Schwegler, T.; Franchy, M.; Kamtekar, S.; Rother, H. Demonstrating UVC LEDs inside Automobile HVAC Chambers for Clean Cabin Air and Airborne Transmission Risk Reduction. *SAE 2022 Annu Tech. Pap.* **2022**.
88. Rudnick, S.N.; McDevitt, J.J.; Hunt, G.M.; Stawnychy, M.T.; Vincent, R.L.; Brickner, P.W. Influence of ceiling fan's speed and direction on efficacy of upperroom, ultraviolet germicidal irradiation: Experimental. *Build. Environ.* **2015**, *92*, 756–763.
89. Jayakantha, D.R.; Bandara, H.; Gunawardana, N.M.; Rajapakse, R.J.; Thilakarathne, D.S.; Comini, E.; Gunawardhana, N.; Karunarathne, S. Design and construction of a low cost air purifier for killing harmful airborne microorganisms using a combination of a strong multi-directional electric-field and an ultra violet light. *HardwareX* **2022**, *11*, e00279. https://doi.org/10.1016/j.ohx.2022.e00279.
90. Singh, D.; Soorneedi, A.R.; Vaze, N.; Domitrovic, R.; Sharp, F.; Lindsey, D.; Rohr, A.; Moore, M.D.; Koutrakis, P.; Nardell, E.; Demokritou, P. Assessment of SARS-CoV-2 surrogate inactivation on surfaces and in air using UV and blue light-based intervention technologies. *J. Air Waste Manag. Assoc.* **2023**, *73*, 200–211.
91. Song, L.; Li, W.; He, J.; Li, L.; Li, T.; Gu, D.; Tang, H. Development of a Pulsed Xenon Ultraviolet Disinfection Device for Real-Time Air Disinfection in Ambulances. *J. Health Eng.* **2020**, *2020*, 6053065. https://doi.org/10.1155/2020/6053065.
92. Srivastava, S.; Zhao, X.; Manay, A.; Chen, Q. Effective ventilation and air disinfection system for reducing coronavirus disease 2019 (COVID-19) infection risk in office buildings. *Sustain. Cities Soc.* **2021**, *75*, 103408. https://doi.org/10.1016/j.scs.2021.103408.
93. Vijeta; Kapri, R.K.; Saha, S.; Jaiswal, V.K.; Sharma, P. Theoretical Simulation for Evaluating Error in Irradiance Measurement Using Optical Detectors Having Different Cosine Responses. *Mapan—J. Metrol. Soc. India* **2021**, *36*, 473–480. https://doi.org/10.1007/s12647-021-00486-6.
94. Wang, M.; Zhang, H.; Chan, C.; Lee, P.; Lai, A. Experimental study of the disinfection performance of a 222-nm Far-UVC upper-room system on airborne microorganisms in a full-scale chamber. *Build. Environ.* **2023**, *236,* 110260. https://doi.org/10.1016/j.buildenv.2023.110260.

95. Wang, C.; Lu, S.; Zhang, Z. Inactivation of airborne bacteria using different UV sources: Performance modeling, energy utilization, and endotoxin degradation. *Sci. Total. Environ.* **2019**, *655*, 787–795. https://doi.org/10.1016/j.scitotenv.2018.11.266.
96. Wang, S.-N.; Li, J.-J.; Liu, Y.-X.; Lin, Z.; Qiao, J.-J.; Chen, L.-H.; Li, Y.; Wu, Y.; Wang, M.-M.; Liu, Y.-B.; et al. Pulsed xenon ultraviolet and non-thermal atmospheric plasma treatments are effective for the disinfection of air in hospital blood sampling rooms. *Photodiagnosis Photodyn. Ther.* **2019**, *27*, 137–140. https://doi.org/10.1016/j.pdpdt.2019.05.034.
97. Wang, Y.; Sekhar, C.; Bahnfleth, W.P.; Cheong, K.W.; Firrantello, J. Effectiveness of an ultraviolet germicidal irradiation system in enhancing cooling coil energy performance in a hot and humid climate. *Energy Build.* **2016**, *130*, 321–329. https://doi.org/10.1016/j.enbuild.2016.08.063.
98. Xie, Y.; Zhu, X.; Zhang, P.; Wang, S.; Yang, J.; Li, J. Cost-effective instant air disinfection for building ventilation system by a combination of UV and micro-static electricity. *Chem. Eng. J.* **2023**, *454*, 140231. https://doi.org/10.1016/j.cej.2022.140231.
99. Yang, Y.; Zhang, H.; Nunayon, S.S.; Chan, V.; Lai, A.C. Disinfection efficacy of ultraviolet germicidal irradiation on airborne bacteria in ventilation ducts. *Indoor Air* **2018**, *28*, 806–817. https://doi.org/10.1111/ina.12504.
100. Yang, Y.; Lai, A.C.; Wu, C. Study on the disinfection efficiency of multiple upper-room ultraviolet germicidal fixtures system on airborne microorganisms. *Build. Environ.* **2016**, *103*, 99–110. https://doi.org/10.1016/j.buildenv.2016.04.004.
101. Yang, Y.; Zhang, H.; Lai, A.C. Lagrangian modeling of inactivation of airborne microorganisms by in-duct ultraviolet lamps. *Build. Environ.* **2021**, *188*, 107465. https://doi.org/10.1016/j.buildenv.2020.107465.
102. Yang, Y.; Zhang, H.; Chan, V.; Lai, A.C. Development and experimental validation of a mathematical model for the irradiance of in-duct ultraviolet germicidal lamps. *Build. Environ.* **2019**, *152*, 160–171. https://doi.org/10.1016/j.buildenv.2019.02.004.
103. Yarahmadi, R.; Soleimani-Alyar, S.; Darvishi, M.-M. Inactivation of airborne SARS-Co-V2 using NTP-UVGI hybrid process. *Int. J. Environ. Sci. Technol.* **2023**, *20*, 209–218. https://doi.org/10.1007/s13762-022-04399-y.
104. Yildirim, G.; Kilic, H.; Karakas, H.M. The antimicrobial efficacy of shielded ultraviolet germicidal irradiation in CT rooms with intense human circulation. *Diagn. Interv. Radiol.* **2021**, *27*, 293–301. https://doi.org/10.5152/dir.2021.20688.
105. Zhang, H.; Lai, A.C.K. Evaluation of Single-Pass Disinfection Performance of Far-UVC Light on Airborne Microorganisms in Duct Flows. *Environ. Sci. Technol.* **2022**, *56*, 17849–17857. https://doi.org/10.1021/acs.est.2c04861.
106. Zhu, S.; Srebric, J.; Rudnick, S.N.; Vincent, R.L.; Nardell, E.A. Numerical modeling of indoor environment with a ceiling fan and an upper-room ultraviolet germicidal irradiation system. *Build. Environ.* **2014**, *72*, 116–124. https://doi.org/10.1016/j.buildenv.2013.10.019.
107. CIE 155:2003; Ultraviolet air disinfection. International Commission on Illumination: Vienna, Austria, **2003**.
108. UNI EN 1822:2019. 2019. High-efficiency air filters (HEPA and ULPA) – Classification, performance, and testing. Ente Nazionale Italiano di Unificazione, 1–64. https://www.uni.com
109. Wikipedia contributors. Rappresentazione schematica di un filtro HEPA. *Wikipedia: The Free Encyclopedia*. Wikipedia. Ultimo aggiornamento: 20 October 2025. URL: https://en.wikipedia.org/wiki/HEPA_filte
110. Rosenberg Ventilatoren GmbH. 2017. Fiche technique GDSV8 180x180L. Rosenberg Ventilatoren GmbH. https://rosenbergusa.com/wp-content/uploads/pdfs/Q37-B1%20GDSV8%20180x180L%20Standard%20Airflow.pdf
111. C-LED. 2024. *Moduli LED UVC 32 LED 24V*. C-LED. https://www.c-led.it/prodotti/lighting/moduli-led-uvc-32-led-24vù.
112. Newport Corporation. 2010. *Manuale utente della serie 918D – Sensori a fotodiodo calibrati*. Newport Corporation, 1–144. https://www.newport.com/medias/sys_master/images/images/he2/h50/8797036511262/918D-Manual-RevD.pdf.
113. Testo S.p.A. 2025. *Strumenti di misura professionali e sistemi di misura*. Testo S.p.A. https://www.testo.com/it-IT/
114. L. Dettwiller; Short review on the refractive index of air as a function of temperature, pressure, humidity and ionization, *arXiv preprint*, **2024**. doi: 10.48550/arXiv.2204.02603.
115. M. E. Shaheen, S. T. Abdelhameed, N. M. Abdelmoniem, H. M. Hashim, R. A. Ghazy, S. A. Abdel Gawad, and A. R. Ghazy; Determination of the refractive index of air and its variation with temperature and pressure using a Mach–Zehnder interferometer, *Journal of Optics*, vol. 53, pp. 2219–2228, **2023**. doi: 10.1007/s12596-023-01486-2.
116. COMSOL. 2025. *Ray Optics Module User's Guide*. COMSOL. https://doc.comsol.com/6.2/doc/com.comsol.help.roptics/RayOpticsModuleUsersGuide.pdf.
117. The MathWorks, Inc. 2025. *Curve Fitting Toolbox™ User's Guide*. The MathWorks, Inc. https://www.mathworks.com/help/curvefit/index.html (accessed 20 October 2025).
118. Born, M.; Wolf, E. 1999. *Principles of Optics: Electromagnetic Theory of Propagation, Interference and Diffraction of Light*, 7th edition. Cambridge University Press, Cambridge, UK.
119. Moreno, I.; Sun, C.-C. 2008. Modeling the radiation pattern of LEDs. Optics Express, 16(3), 1808–1821. https://doi.org/10.1364/OE.16.001808.
120. Belcour, L.; Poulin, P.; Drettakis, G. Antialiasing Complex Global Illumination Effects in Path-Space. Comput. Graph. Forum 2017, 36, 45–58. https://doi.org/10.1111/cgf.13245

121. Giroux, B.; Dupuis, J. C. Task-parallel implementation of 3D shortest path raytracing. J. Comput. Phys. 2013, 290, 123–137. https://doi.org/10.1016/j.jcp.2015.01.014
122. Wang, C.; Chen, N.; Heidrich, W. dO: A Differentiable Engine for Deep Lens Design of Computational Imaging Systems. IEEE Trans. Comput. Imaging 2022, 8, 1–13. https://doi.org/10.1109/TCI.2022.3150231

Acknowledgements

To my supervisor, Prof. Annunziata D’Orazio, for her availability and support.
To my family for their encouragement.
To the company Sagicofim S.p.a for partially founding my PhD and supporting our research.